SURFACE REACTIONS OF BIOMASS DERIVED OXYGENATES ON LEWIS ACIDIC METAL OXIDES

A Dissertation
Presented to
The Academic Faculty

by

Sean Najmi

In Partial Fulfillment
of the Requirements for the Degree
Doctor of Philosophy in the
School of Chemical & Biological Engineering

Georgia Institute of Technology

December 2021

SURFACE REACTIONS OF BIOMASS DERIVED OXYGENATES ON LEWIS ACIDIC METAL OXIDES

Approved by:

Dr. Carsten Sievers, Advisor
School of Chemical and Biomolecular Engineering
Georgia Institute of Technology

Dr. J. Will Medlin
Department of Chemical and Biological Engineering
University of Colorado, Boulder

Dr. Andrew J. Medford, Advisor
School of Chemical and Biomolecular Engineering
Georgia Institute of Technology

Dr. Charles Liotta
School of Chemistry and Biochemistry
Georgia Institute of Technology

Dr. Christopher W. Jones
School of Chemical and Biomolecular Engineering
Georgia Institute of Technology

Date Approved: November 29th 2021

"A scientific man is a true index and representative of humanity, for through processes of inductive reasoning and research he is informed of all that appertains to humanity, its status, conditions and happenings. He studies the human body politic, understands social problems and weaves the web and texture of civilization. In fact, science may be likened to a mirror wherein the infinite forms and images of existing things are revealed and reflected. It is the very foundation of all individual and national development. Without this basis of investigation, development is impossible. Therefore, seek with diligent endeavor the knowledge and attainment of all that lies within the power of this wonderful bestowal."

`Abdu'l-Bahá - The Promulgation of Universal Peace

Acknowledgements

If you had asked me at the end of 2019 whether I'd want to finish my PhD during the COVID-19 pandemic, I would first ask, "What's COVID-19?" Then I'd think for a bit and conclude that yes, I would like to finish my degree. These acknowledgements to all the people who have been there for me during graduate school is a testament to my conviction in this response. First, my advisors Carsten and AJ have been truly supportive of me pursuing what piques my interest and have always provided valuable guidance. Carsten has gotten me to fall in love with chemistry again and made me think outside the box. AJ has challenged me to rigorously apply the scientific method, to think about my hypotheses, and to evaluate my assumptions. Together, they have made me into the scientist I am, to which I am forever grateful.

I would also like to thank Will who has become a pseudo-advisor of mine. I have greatly enjoyed collaborating with him and receiving all the mentorship he has provided. Like Carsten and AJ, Will has had significant influence in how I think about science and conducting research. Chris and Dr. Liotta have been terrific committee members who always provide me with valuable feedback on my work, thank you both for agreeing to serve on my committee.

My time in graduate school was challenging, but the people I got to work with always made me cherish being in the lab regardless the circumstance. I was fortunate to share office space with Andrew and Yimeng and enjoyed working alongside them on various projects during our time together. Even more, the diverse conversations we would have on culture, politics, sports, and occasionally philosophy were always something I looked forward to. In addition, working with Jenn, Giada, Qandeel, Mike, Bryan, Olivia and Karoline has been a wonderful experience and they have been very supportive group mates. I'll really miss spending time with them both in and out

of the lab. I would also like to thank Ben, Chaoyi, Gabriel and Jagriti for always answering my random DFT questions on slack for when I would play pretend computational chemist.

Along with these group mates at Georgia Tech, I would like to thank Mat who has become a wonderful colleague and friend. Working with him on the molybdenum projects has been a real pleasure and I look forward to what the future holds for both of us. Although not featured here, the zeolite work with Dr. Jungseob So, Dr. David Sholl, Dr. Will McDermott, and Dr. Ive Hermans was a wonderful experience and I enjoyed being a part of that with them. Special shootout to Mary who was a phenomenal building manager for RBI and always there to help me and the group out whenever needed.

I had a great group of undergraduates that I got to mentor during my time in graduate school and some of their work is featured here. Thanks to Somto (Chapter 2), Madison (Chapter 4), Jason and Kathryn for being helpful, curious and diligent researchers. Mentoring you all was a great experience for me, and I learned a lot from teaching you the ins and outs of research.

Several collaborators have helped me get to where I am. Hanno Leisen has been a great resource for me concerning all things NMR and I am grateful for him training me into the NMR spectroscopist that I am. I would like to thank Dr. Eli Stavistki, Dr. Simon Bare, and Dr. Adam Hoffman for their assistance with work done at BNL and SLAC, respectively. Dr. James Collins has been helpful running NMR experiments at MagLab to which I am grateful. My time at PNNL was a useful experience and I would like to acknowledge Dr. Andy Lipton for teaching me everything I ever wanted to know about solid state NMR. I would also like to thank Dr. Sungmin Kim and Julian Schmid for helping me navigate the national lab environment. Thanks to Sam, Jacob, and Sten for being such great friends during my time in Washington.

Living in Atlanta has been the best and I am so fortunate to have met so many incredible people. Rodd, Danny, Justin, Tyler, Amanda (and of course Phoebe!), Josh, Rayan, Jeffrey, Arezou and many others have truly been incredible people and I will always enjoy the time we got to spend together during my tenure in graduate school. Friends away from Atlanta have always been there to listen to me and motivate/encourage me to continue on. Special thanks to Aarti, Aida, Alejandra, Andrew, Apurva, Daniel, DeeDee, Pearl and others who continue to be there for me and for always sharing endless laughs.

I want to finally acknowledge my family who have always been there for me. My sister, Natasha, is always there willing to talk with me and remind me of my capacity to succeed. My parents have always shown me so much unconditional love, allowing me to forge my own path by letting me do whatever I am passionate about. The resilience my baba showed after struggling mightily coming to this country as a young immigrant but yet never giving up will always serve as inspiration to me. I am so lucky to have been raised by a man who can so effortlessly combine a conscientious, hard working attitude with compassion and love. Along with my mom who always encourages me to not always get carried away and enjoy the moment, they have both been the best parents I could ever ask for.

Table of Contents

List of Tables

List of Figures

List of Symbols & Abbreviations

FTIR	Fourier Transform Infrared Spectroscopy
ν	Stretching Vibrational Mode
δ	Scissoring Vibrational Mode
ρ	Rocking Vibrational Mode
ω	Wagging Vibrational Mode
SSNMR	Solid State Nuclear Magnetic Resonance
CPMAS	Cross Polarization Magic Angle Spinning
DPMAS	Direct Polarization Magic Angle Spinning
ppm	Parts per Million
$T_{1\rho}$	Spin Lattice Relaxation Time in Rotating Frame
BAS	Bronsted Acid Site
LAS	Lewis Acid Site
CUS	Coordinatively Unsaturated Site
TOF	Turnover Frequency
eV	Electron volt
Å	Angstrom
BET	Brauaner Emmett Teller
BJH	Barret Joyner Halenda
DRIFTS	Diffuse Reflectance Infrared Spectroscopy
EDS	Energy Dispersive X-Ray Spectroscopy
EXAFS	Extended X-ray Absorption Fine Structure
HPLC	High Performance Liquid Chromatography
STEM	Scanning Transmission Electron Microscopy
TGA	Thermogravimetric Analysis
TPD	Temperature Program Desorption
XANES	X-ray Absorption Near Edge Structure
XAS	X-ray Absorption Spectroscopy
XPS	X-ray Photoelectron Spectroscopy
XRD	Powder X-ray Diffractometry

Summary

Mitigating humanity's dependence on fossil resources will be one of the largest challenges of this century. The effects of rising CO_2 emissions caused by industrialization has resulted in increasing global temperatures which have led to environmental hardship that are affecting our everyday lives. Thus, the need for developing a sustainable energy sector that incorporates aspects of a circular economy will be crucial for the combating this problem. One strategy would be to switch to a bio-based refinery model where lignocellulosic biomass would be sourced as a feedstock as opposed to oil. Instead of hydrocarbons, oxygenated compounds would be sourced from the three main biomass constituents: cellulose, hemicellulose, and lignin. Upgrading these components will be challenging and due to their high oxygen content and likelihood to undergo various kinds of reactions. Heterogeneous catalysts can be used for the upgrading process and help control selectivity to desired products. Specifically, Lewis acidic catalysts can be used to transform biomass derived oxygenated compounds into platform chemicals and other value-added chemicals. There is knowledge gap in how these Lewis acidic catalysts interact with oxygenates, particularly from the surface science perspective. This dissertations seeks to elucidate the surface interactions within certain catalytic systems and provide insight into how specific factors of Lewis acidic catalysts affect reaction pathways.

The first study considered molybdenum oxide and the consequences of pretreatments had on the oxidation states of molybdenum and what the effects were on the aldol condensation of ethanol and acetaldehyde. As the oxidation state of molybdenum decreased from Mo(VI) to Mo(IV) the capacity of the catalyst oxide to adsorb ethanol and acetaldehyde increased. Crotonaldehyde was the main product detected as a result of the aldol condensation reaction. The increased in adsorption capacity was due to the formation of oxygen vacancies that acted as

coordinatively unsaturated sites (CUS). These defects were crucial to increasing yields of crotonaldehyde. The reaction was shown to proceed via a tautomerization of ethanol and acetaldehyde to form their respective enolates. The reduction of molybdenum oxide was also shown to occur when the catalyst was exposed to alcoholic solvents, although the reduction of molybdenum atom was not as severe as pretreating in hydrogen gas at high temperatures.

The second study builds off the knowledge from the first study and instead of using bare, unsupported molybdenum oxide, introduces molybdenum oxide particles (MoO_x) onto silica and alumina supports. The aldol condensation of acetaldehyde to crotonaldehyde was the reaction of focus in this study to get an understanding of how the weight loading of molybdenum affects the reaction along with the support. When SiO_2 was the support, the conversion increased monotonically as the weight loading of the support increased. This trend was not consistent with Al_2O_3 as the support. A maximum conversion was achieved with only 1 wt% MoO_x and as the weight loading increased, the conversion began decreasing heading towards the conversion achieved with just the bare Al_2O_3. Quenching of Al active sites by the MoO_x was likely responsible for this decreasing activity. High concentration of strong and medium strength Lewis acid sites positively correlated with higher conversion of acetaldehyde to crotonaldehyde.

Moving away from molybdenum-based catalysts, the third study pivots to investigating the surface interactions of two polyoxygenated compounds (3-hydroxybutanal and 4-hydroxy-2-butanone) with four Lewis acidic metal oxides: γ-Al_2O_3, CeO_2, Nb_2O_5, and TiO_2. Dehydration of 3-hydroxybutanal to crotonaldehyde was the dominant reaction occurring on γ-Al_2O_3 mainly because of the strong Al (III) Lewis acid sites. On the other three catalysts, the retro-aldol condensation to acetaldehyde and its enolate equivalent was observed. Although all catalysts had high concentrations of Lewis acid sites, this finding points to some other factor that is responsible

for this reaction. For 4-hydroxy-2-butanone, the dehydration to methyl vinyl ketone was observed on γ-Al_2O_3, CeO_2, and TiO_2. Interestingly, Nb_2O_5 showed evidence of acetone formation on the surface as evidenced by the presence of its enol form. Acetone and formaldehyde would be the two products formed from retro-aldol condensation of 4-hydroxy-2-butanone. Nb_2O_5 was the only catalyst with Brønsted acidity present and may be an important factor for the retro-aldol condensation of ketone containing compounds. The bifunctional acidic property of this material is certainly an advantage for a catalytic system like this.

The last study in this work details the upgrading of a model sugar compound, erythrose, using Lewis acidic metal oxides. This was done by employing operando solid-state nuclear magnetic resonance (NMR) and observing what surface species form. NMR relaxometry was also used to study the adsorption strength and mobility of the species formed. Erythrose primarily exists as a ring in solution and on the oxides tested, carboxyl moieties were observed at room temperature. This indicates on the surface, ring opening can occur and varies significantly in quantity depending on the oxide tested. When looking at the mobility of the functional groups that formed on the surface, the alkoxy groups had the highest average relaxation time indicating they were most strongly bound to the surface regardless of the surface. Interestingly, the spectra of species on TiO_2 had very sharp peaks and the relaxation times of the carbon nuclei present were the lowest of those measured on any catalyst. After washing the spent catalyst, product was detected indicating this catalyst is active even under mild conditions. The amount of carboxyl nuclei present, a clear indicator of ring opened erythrose present, was positively correlated to the size of the ionic radii of the cation of the metal. This suggests that this descriptor can be a strong indicator for catalyzing ring opening and stabilizing the formed species.

Chapter 1 Introduction

1.1 Fossil Fuels: Then, Now & the Future

Societal dependence on fossil fuels throughout the years should not be underemphasized nor ignored. Although used by many cultures for centuries, coal was popularized as a fuel source in the 18th century when it was used by James Watt to power steam engines.[1] This was a major breakthrough for the world as coal powered steam engines were soon used for ships and locomotives thereby revolutionizing the way in which humans and resources are transported. Soon after, the refining of crude oil to gasoline was used for the internal combustion engine further improving the transportation sector. In the middle of the 20th century, applications of fossil fuels were further expanded when plastics made from hydrocarbons began to burgeon as a major consumer good. Again, the rapid growth of the fossil fuel industry can be attributed to innovative applications and developments brought on by the need for both energy and goods.

Currently, the refinery industry provides chemicals crucial to our daily lives through reactive process such as fluidized catalytic cracking (FCC), hydrodesulfurization (HDS), aromatization and many others. All these processes involve materials known as heterogeneous catalysts to help drive the reaction forward. Catalysts lower the activation barrier for the reaction path and are not consumed in the reaction. Catalyst discovery and innovation was a crucial aspect to the expansion of the refinery industry. These examples include: the zeolite known as ZSM-5 developed by Mobil Co. for FCC,[2] supported molybdenum sulfides for HDS,[3] and SAPO-34 developed by UOP/HYDRO for methanol to olefins.[4] One major driving force for innovation in the realm of catalysis is the rising global population and subsequent demand for carbon derived goods. The US is projected to reach a population of 400 million by 2058[5] and China is predicted to steadily maintain its population of 1.4 billion for the next few decades while increasing its

standard of living, thus consuming more resources.[6] In addition to the populations of these two important economies, the total global population is projected to reach almost 10 billion by 2050.[7] These numbers point to the need towards continuous production of petrochemicals and plastics that will have to meet the demand for these goods. This, however, will be incredibly challenging due to the finite nature of the sources needed for production of these goods. Thus, a total reorganization and change in thinking of how we source and distribute energy and chemicals will need to take place if we are to improve the lives of human beings.

In 2020, the total amount of energy produced from fossil fuels that was consumed in the US was around 73 quadrillion BTU, the lowest in almost 30 years.[8] While this is a positive in the alleviation of our dependence on fossil fuels, there is still innovation and research needed to further phase out the role of fossil resources in our daily lives. A breakdown of the energy consumption in the US by source is shown in Figure 1.1 The advent of natural gas production has certainly proved to create energy independence for America along with a "cleaner" energy source, but it is still a nonrenewable resource and emits carbon dioxide (CO_2) into our atmosphere. It is forecasted that natural gas reserves will run out in the year 2100.[9] This should create a sense of urgency within the energy community to develop sustainable energy technologies and further move away from fossil fuels. On top of that, increasing CO_2 emissions are contributing to rising temperatures and climate change. This environmental impact will continue to harm our environment and overall health unless we create alternatives that can mitigate the impact of CO_2.

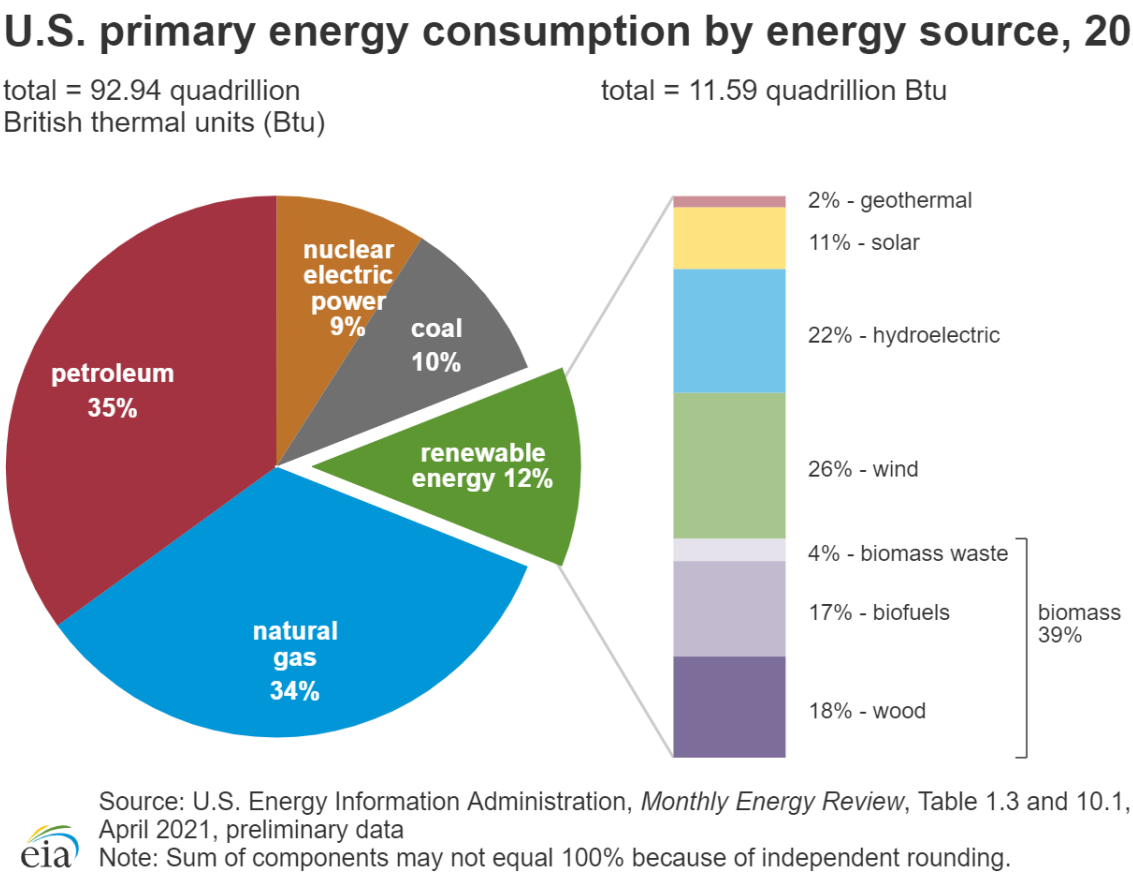

Figure 1.1 US Energy consumption in 2020 broken down by energy source[8]

As shown in Figure 1.1, the amount of energy that is sourced from renewables is small compared to that of fossil fuel sources (coal, natural gas, and petroleum). The cost of renewable energy sources, such as photovoltaics and wind, has slowly but steadily decreased making them viable options.[10] Solar energy from photovoltaics suffers from intermittency although storage of energy through what are known as solar fuels can solve this problem.[11] Wind powered electricity is also viewed as a viable renewable energy resource but, like solar, it has a problem with intermittency. Other challenges include improving the understanding of wind power plant physics and the dynamics of the turbine response over its lifetime, along with more sophisticated integration of wind power plants into our future electric grid.[12] This certainly can be done within the next few decades but moves entirely away from the refineries model that has proven to be

robust and profitable. This argument puts biorefineries, refineries focused on sustainable processing of biomass to marketable goods and energy, at the forefront as a solution to solving the sustainable energy dilemma.

1.2 Biorefineries as a Sustainable Alternative

Unlike petroleum-based refineries which use fossil fuels as the feedstock, biorefineries use lignocellulosic biomass (referred to as biomass from hereon) as the starting material. Biomass consists of three main constituents: cellulose, hemicellulose, and lignin. Cellulose consists of glucose molecules connected by a glycosidic bonds, which can be broken by hydrolysis.[13] Hemicellulose is another polymer made up of sugars but instead of just glucose it includes other C5 and C6 sugars. Lignin is a heterogeneous aromatic polymer that consists of various different aromatic compounds, and major challenges into valorization of lignin persist.[14] Although full realization of biomass as a sustainable feedstock has not been reached, the potential upside from its implementation would be enormous. The passing of the Energy Independence and Security Act in 2007 legitimized biomass as a source of sustainable energy by creating funding to study development of biofuels.[15] It is estimated that by 2040 there will be around 82 million dry tons of biomass available.[16] If this supply were to increase it has the chance to meet the target of 1.3 billion tons of biomass to replace a third of transportation fuels and a quarter of all organic chemicals.[17] This push and upside serve as motivation for the body of this work.

The output of biorefineries and biobased goods is still miniscule in comparison to the output of the petroleum industry. Commercialization of chemicals sourced from biomass is paltry, but promise does exist. For example, production of acetic, lactic, and levulinic acids from biomass are currently being done by private companies with acetic and lactic having estimated market values of 837 and 684 million USD/year respectively.[18] High operational and capital costs make

these endeavors expensive and there still exist many complexities associated with scale-up, availability and mechanization.[18] As time goes on, changes in consumer behavior towards "greener" products and legislation/regulation surrounding energy infrastructure will occur. For example, the European Union has recently proposed the ban of production of new gasoline and diesel vehicles by the year 2035. The US is planning on implementing a similar ban by the year 2040. This will further push the need for valorization of biomass.

Thermal processing of raw biomass to value added streams has been conducted and includes processes like pyrolysis and gasification. The flow diagram in Figure 1.2 depicts thermal upgrading methods and the potential products that can be obtained from it. Fast pyrolysis uses temperatures around 500 °C in the absence of oxygen and short residence times to produce mostly bio-oil with some amount of solid gas products.[19] These distributions can change depending on the conditions used (temperature, TOS, etc.) and the actual biomass source (softwoods vs hardwoods, corn stover vs wheat straw).[20] Regardless, bio-oil typically has a high moisture content (15 %) and is present with significant amount of oxygenated compounds (ketones, aldehydes, esters etc.).[20] This makes it challenging to integrate bio-oil with standard hydrocarbon fuel streams.

As implied by the name, gasification yields more gaseous products than pyrolysis and operates at higher temperatures. Gasification primarily produces syngas (H_2 and CO) which can be used to power turbines, engines, and other machinery. Syngas can also be used as a feedstock for catalytic upgrading to ethanol which has a variety of applications such as a liquid hydrogen carrier for fuel cells and industrial solvent.[21] Syngas is most popular for the Fischer-Tropsch reaction which has traditionally used coal derived syngas as the reactant to produce hydrocarbons. Gasification of biomass is more attractive than coal gasification due to the lower operating temperatures and less potential emissions of sulfur oxides into the atmospheres. As with fast

pyrolysis, the scale-up and cost of natural resources has kept this method from becoming fully realized.

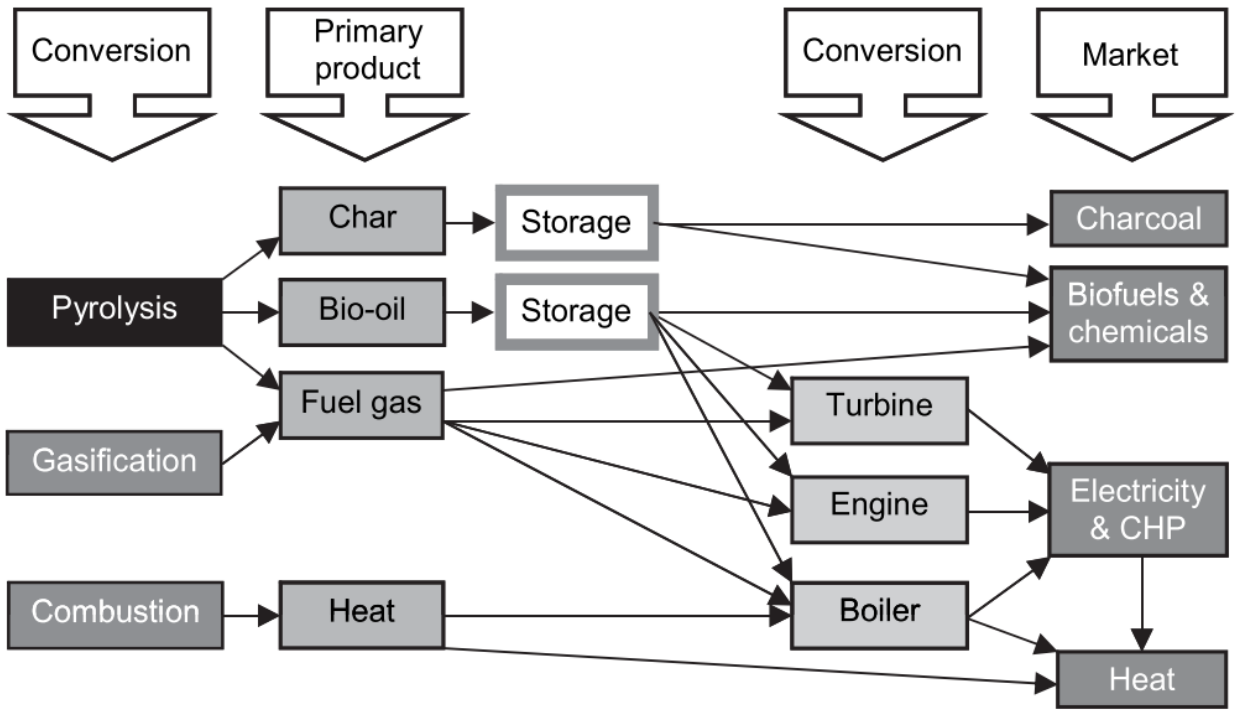

Figure 1.2 Products from thermal biomass conversion[19]

Catalytic upgrading of biomass solutions, essentially the same strategy used currently in the chemical industry, provides a unique strategy that can be furthered through innovative research and development. The three biomass constituents are feedstocks from which intermediates can be derived, such as sugars from cellulose and hemicellulose. Sugars can be further upgraded to chemicals like 5-hydroxymethylfurfural and other value-added products.[22,23] This presents sugar upgrading as a valuable strategy towards biomass valorization. As previously mentioned, glucose monomers can be obtained from cellulose hydrolysis making glucose the most abundant biomass derived sugar. Thus, significant focus has been given to catalytic conversion of glucose into platform chemicals. The ubiquity of sugars within nature also garners interest in the fields of

glucose sensor monitoring and abiogenesis. A major challenge of sugars processing is their low inherent volatility. Unlike hydrocarbons, sugars must be dissolved in aqueous solutions or other polar solvents which poses another set of difficulties. For example, increasing concentrations of sugars in solution increases the likelihood of sugar caramelization. This can be alleviated by operating at low temperatures, but at low temperatures kinetics will be exponentially slower and thermodynamics may become unfavorable. Another issue is understanding the complex nature of the solute-solvent interactions thus making it challenging to select an appropriate catalytic system. This complication is accentuated by the fact that sugars have various functional groups which can lead to many reaction paths. Using heterogeneous over homogeneous catalysts can reduce the level of complexity in terms of dynamics within a single phase but significant work remains to fully comprehend the totality of interactions within these catalytic systems.

1.3 Lewis Acidic Catalysts for Oxygenate Upgrading

Acid catalyzed reactions constitute a wide class of important reactions within organic chemistry such as oligomerization, isomerization, and alkylation. The two types of acids, Lewis and Bronsted, are both able to catalyze these reactions but sometimes one is preferred over the other. The body of this work will almost exclusively focus on the transformation of oxygenates using heterogeneous Lewis acidic catalysts. Lewis acids are defined as electron acceptors which makes them ideal for converting oxygenates with electron-rich oxygen-based functional groups. Reduced metals and other cationic species can act as Lewis acids. Brønsted acids are defined as species that can donate a proton (H^+).

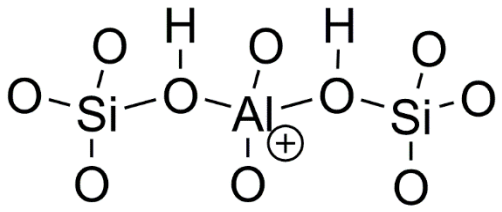

Figure 1.3 Examples of Lewis acid (Al^{4+}) and Bronsted acid (H) sites on a portion of a zeolite

Zeolites are well ordered, crystalline materials that possess both Lewis and Bronsted acidity and an example depicting both is shown in Figure 1.3. Metal oxides are also prime examples of acidic heterogeneous catalysts. The catalysts listed in Section 1.1 used for traditional reactions within refining all have some major component that is a metal oxide. Other examples widely used in industry include: CoO_x, Fe_2O_3 for Fischer-Tropsch, MoVTeNbO for direct propane to acrylic acid oxidation, and Cu-ZnO/Al_2O_3 for methanol synthesis from H_2 and CO.[24] The robustness and cheap cost exemplifies metal oxides as suitable candidates for research in biomass upgrading. The cationic metal sites can act as Lewis acids and can catalyze relevant reactions such as isomerization, retro aldol condensation, and dehydration. Although some oxides may catalyze the same reactions, the kinetics are different because of the discrepancies of metal itself. These effects can be rationalized by the characteristics of the metal cation such as ionic radius, electronegativity and hardness.[25–27] The size of the metal ion can impact the moieties that can accommodate to the active site. For example, C-C bond coupling reactions may need the two adsorbates on the same active site, thus bringing into light whether the site is large enough to accommodate both.[28] Electronegativity, especially as it relates to Lewis acids, is an important descriptor because it measures the tendency of an atom to attract electrons. Hardness/softness relates to the size, charge, and polarizability of a species. Hard species are small with high charges and are weakly polarizable. Soft species are larger with low charge states and strongly polarizable.

These descriptors demonstrate that solid Lewis acids will inherently have different characteristics that will dictate the reactions they catalyze.

Introducing metals into zeolite frameworks has been effective for probing the reactivity of specific metal sites in well-defined environments where characteristic properties of the metal can be better isolated. For example, Sn-BEA is effective for isomerization of glucose to fructose in water at mild conditions.[29] Framework Sn sites were necessary to catalyze the isomerization, and it was hypothesized that hydrolyzed Sn sites known as "open" sites were active for this reaction and glucose-mannose epimerization.[30] This study highlights the advantage of introducing new Lewis acid sites (LAS) into already catalytically active materials to adjust the reaction pathway. Besides the cation, defects within catalysts such as oxygen vacancies can be LAS and take on the role of the active site for the reaction. A reaction involving interaction with an oxygen vacancy could follow a reverse Mars Van Krevelen reaction where an oxygen atom from the reactant is removed and incorporated into the catalyst lattice. Hydrodeoxygenation (HDO), an important reaction for biomass upgrading, is a prime example of an oxygen vacancy catalyzed reaction. Gaining a sense of the Lewis acid nature of the catalyst is key to better understanding surface reactions of biomass derived compounds. By elucidating the effect of surface acidity, new catalytic materials can be developed based on these learnings and used for other relevant reactions.

1.4 Objectives, Organization and Outcomes

The body of this work deals with Lewis acid catalyzed reactions of various biomass derived oxygenates. Metal oxides will serve as solid Lewis acidic catalysts in this case for reasons mentioned in section 1.3. This work specifically seeks to understand how surface reactions are geared towards certain pathways based on the nature of the metal oxide catalyst. To probe what is happening on the catalyst surface, *in-situ* spectroscopy techniques will be employed. These include

Fourier transformed infrared spectroscopy (FTIR), ultraviolet-visible (UV-VIS) spectroscopy, and solid state nuclear magnetic resonance (SS-NMR) spectroscopy. FTIR is a rovibrational technique that can be used to observe molecule vibrations and can identify functional groups of adsorbed molecules. UV-VIS shows electronic transitions and can reveal oxidation states and coordination environments of metals. SS-NMR provides similar information as FTIR where the presence of certain moieties can be revealed, but it also can be used for relaxometry which can be correlated to determine adsorbate strength. These techniques in combination with other characterization methods will serve as the primary methods for understanding the surface interactions of biomass-derived oxygenates on Lewis acidic metal oxides.

Chapter 2 investigates the role of oxygen vacancies on molybdenum trioxide (MoO_3) for the aldol condensation of ethanol and acetaldehyde. This study was done with FTIR and supported by temperature programmed desorption – mass spectrometry (TPD-MS) measurements, density functional theory (DFT) calculations and X-ray absorption (XAS) spectroscopy. MoO_3 is known for being a highly reducible catalyst and in combination with Sn-MFI recently showed promise for alkyl lactate production from glucose.[31] The appearance of MoO_3 as blue after reaction prompted the investigation described here on the role of the reduced MoO_3 for certain reactions. Aldol condensation is a particularly relevant reaction to study because it is efficient for C-C bond formation. With this serving as motivation, the effect of pretreating MoO_3 under reducing, inert and oxidizing conditions was tested for the adsorption of ethanol, acetaldehyde, and crotonaldehyde. Higher amounts of each were observed in the following order of treated surfaces: reduced>inert treated>oxidized. Coordinatively unsaturated sites (CUS) formed during the reduced and inert pretreated catalysts were responsible for catalyzing aldol condensation. The reaction proceeds via an enolate intermediate formed by tautomerization. Several other

characterization techniques were used to understand the sensitive behavior of MoO_3 depending on its environment.

Chapter 3 builds off the insight provided from Chapter 2 and investigates the activity of MoO_x supported on SiO_2 and Al_2O_3 for aldol condensation of acetaldehyde. Pretreating MoO_x/Al_2O_3 in H_2 versus O_2 resulted in a similar trend as for bulk MoO_3.There was a higher amount of acetaldehyde that adsorbs when the catalyst was reduced. Interestingly, pretreatment had no effect on the steady state conversion for either pretreated catalyst suggesting the oxidation state of these supported catalysts is governed primarily by reaction conditions. Strong and medium strength acid sites as determined by pyridine FTIR measurements were responsible for catalyzing aldol condensation. For MoO_x/SiO_2 based catalysts, increasing weight loading of MoO_x resulted in higher conversions whereas for MoO_x/Al_2O_3 low loading of MoO_x resulted in the highest conversion and subsequent loadings gave rise to lower conversions. Active sites on the Al_2O_3 support were quenched by increased loading thus resulting in the lower conversions. Further characterization was done on these materials to understand their intrinsic physical properties.

Chapter 4 pivots away from molybdenum-based catalysts and instead focused on other Lewis acidic oxides: γ-Al_2O_3, CeO_2, Nb_2O_5 and TiO_2. Two isomers were chosen as candidates for studying the retro-aldol condensation reaction: 3-hydroxybutanal and 4-hydroxy-2-butanone. *In-situ* transmission FTIR was used to study surface species that formed from adsorption of the two probe molecules. This allowed for understanding which reaction pathways may be occurring at relevant reaction temperatures and also determining how strongly the formed species are bound to the surface. Adsorption of 3-hydroxybutanal primarily resulted in the RAC to acetaldehyde on CeO_2, Nb_2O_5 and TiO_2 while on γ-Al_2O_3 there was primarily dehydration to crotonaldehyde. For 4-hydroxy-2-butanone, dehydration to methyl vinyl ketone was observed on γ-Al_2O_3, CeO_2, and

TiO_2 while RAC to acetone and formaldehyde was observed on Nb_2O_5. This indicates Nb_2O_5 is best suited for RAC of both aldehyde and ketone containing functional groups and may be due to the presence of BAS which can help creating bifunctional configurations that allow for the C-C bond breaking to occur more readily.

Chapter 5 looks at the upgrading of the C4 sugar erythrose which was chosen due to its structural similarity to glucose. Motivated by the numerous findings regarding glucose, this chapter delves into a surface science perspective of how erythrose reacts on the surface of different oxide catalysts. These were Al_2O_3, CeO_2, Nb_2O_5, SiO_2, SnO_2, TiO_2, and ZrO_2. SS-NMR was used as the primary technique to investigate the formation of different surface species on these materials. Ring opening of erythrose, as evidence by carbonyl nuclei, was prevalent on CeO_2 and Nb_2O_5 at room temperature indicating these may be suitable catalysts for erythrose upgrading. At higher temperatures, ring opening of erythrose became more prominent on SnO_2, TiO_2 and ZrO_2. The catalysts had acid sites quantified through pyridine FTIR and were further characterized through other techniques. The size of the ionic radius was shown to be an important descriptor for whether ring opening of erythrose would occur. This points to having a larger metal cation is necessary for stabilizing larger sugar molecules and catalyzing ring opening of larger cyclic compounds. The surface species on TiO_2 were shown to be weakly bound as seen by direct polarization and NMR relaxometry. Alkoxy bonds on the surface were the functional groups found to be most strongly interacting with the catalyst surface.

Chapter 2 Pretreatment Effects on the Surface Chemistry of Small Oxygenates on Molybdenum Trioxide

This work contains contributions from Mathew J. Rasmussen, PhD

2.1 Introduction

Developing processes for producing oxygen-containing commodity chemicals from biomass has garnered considerable attention. Biomass-derived sugars have the potential to revolutionize the way chemicals, such as lactic acid and ethylene glycol, are produced by offering a more efficient pathway compared to conventional processes.[32–35] A major challenge remains the design of heterogeneous catalysts that promote selective transformations of sugars.[36]

Solid catalysts containing Lewis acid sites have shown promise for many desired reactions of sugars, including isomerization, retro-aldol condensation and the Cannizzaro reaction.[31,37,38] These sites can accept electrons and therefore activate reactant molecules. Several descriptors, such as hardness, electronegativity, and ionic radii, have been proposed to better characterize the nature of Lewis acid properties in different materials.[39–41] However, the influence of these factors on catalytic activity and selectivity remains only partly understood. One solid Lewis acid catalyst, tin-containing zeolite Beta (Sn-BEA), was shown by Davis and coworkers[29,37] to isomerize glucose to fructose through a 1,2-intramolecular hydride shift in the presence of water as the solvent, but this catalyst showed limited activity for the desired subsequent retro-aldol condensation (RAC). The Sn sites in the zeolite are isolated Lewis acid sites that hypothetically bond with the α-hydroxyl group of glucose and then transfer the hydrogen to the carbonyl group to become fructose. In contrast, molybdenum (VI) trioxide (MoO_3) is an effective catalyst for RAC of fructose to

dihydroxyacetone (DHA) and glyceraldehyde (GLA), which could then be converted to alkyl lactates.[31] They also found that the overall carbon yield increased when ethanol was used as a solvent rather than water under the same conditions. However, the nature of the active sites on molybdenum oxide and the origins for their high retro-aldol activity remain unknown.

Recently, density functional theory (DFT) was employed to calculate the thermodynamics and kinetics of reactions involving MoO_3. Rellán-Piñerio and López studied the Formox process (methanol oxidation to formaldehyde) with DFT calculations and found that Mo(VI) cycles to Mo(IV) during reaction, with oxygen vacancy formation being a key step in the catalytic cycle.[42] Vlachos and coworkers used DFT to obtain the free energy profile of the retro-aldol fragmentation of fructose to DHA and GLA.[43] They proposed a monodentate intermediate, in which the oxygen atom of the carbonyl group binds to a single Mo(VI) site. López and coworkers also used DFT to describe the epimerization of glucose to mannose on both a fully oxidized and defective MoO_3 surface.[44] These modeling studies provide additional atomic-scale predictions of the nature of the active site on MoO_3, but additional confirmation regarding the behavior MoO_3 under relevant conditions through in-situ and/or operando experiments is currently lacking.

In addition to being an important solvent for sugar chemistry and other biomass transformations, ethanol has been extensively studied as a feedstock for biorefineries due to well-established processes for its production, its cheap cost, and ease of implementation into current technologies.[45–47] Moreover, ethanol is a useful probe molecule for studying aldol processes on metal oxide surfaces.[48] One such aldol reaction, known as the Lebedev process, transforms ethanol into 1,3-butadiene, a valuable chemical for rubber production.[49] It was recently shown that there is an optimal density of Lewis acid sites for the selective reaction to butadiene.[50,51] Another example of aldol condensation, the Guerbet reaction, converts primary alcohols to longer chain

alcohols, which can often be used as fuel additives.[52]. For example, Barta and coworkers[53] found that nickel- and copper-doped porous metal oxide catalysts were able to transform ethanol to butanol with significant yields. These important developments make ethanol an attractive reactant for further study and highlight the role of Lewis acid sites on the conversion of ethanol.

In this work, the effect of reduction during typical thermal pretreatments of MoO_3 in H_2, N_2, and O_2 and their consequences for aldol reactions were studied. Adsorption and reactions of the probe compounds ethanol, acetaldehyde, and crotonaldehyde were analyzed and discussed considering the nature of active sites during reaction conditions (see Scheme 2.1). The effect of alcoholic solvents as a reducing agent to the surface of MoO_3 is also investigated.

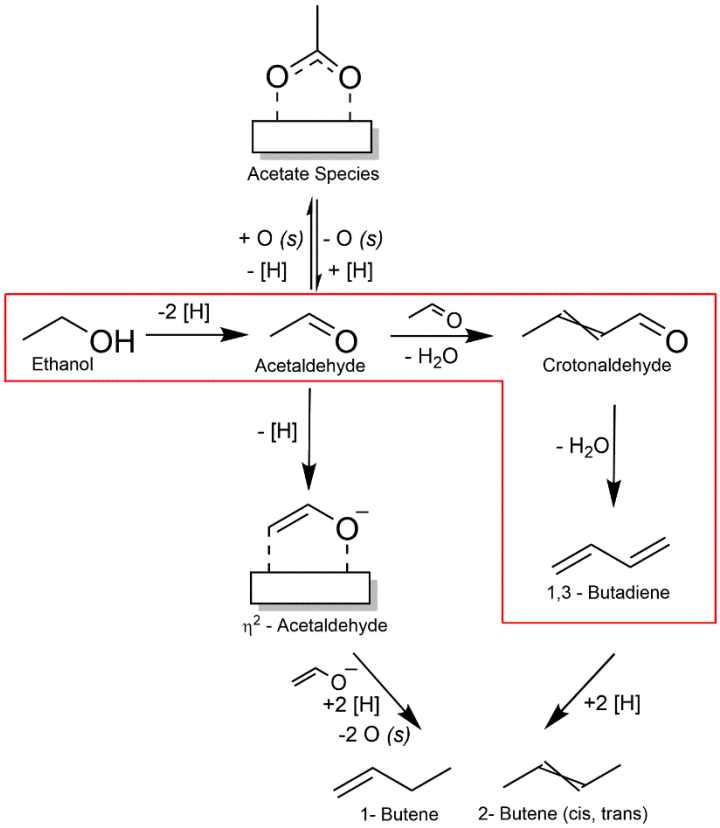

Scheme 2.1 Reaction pathways for conversion of ethanol. The boxed route is Toussaint's mechanism of aldol condensation.[54]

2.2 Methodology

2.2.1 Materials

Commercial MoO_3 (≥99.5%, Sigma-Aldrich) was calcined in dry air at 450 °C for 4 hours and utilized for all experiments. Pretreatment gases included H_2 (99.999%, Airgas), He (99.999%, Airgas), and O_2 (99.994%, Airgas). Ethanol (≥99.5%), acetaldehyde (≥99.5%), crotonaldehyde (≥99%, predominately trans) and potassium bromide (≥99.0%), were purchased from Sigma-Aldrich for FTIR experiments. For TPD experiments, ethanol (200 Proof, Decon Labs), acetaldehyde (99.5%, Acros Organics), crotonaldehyde (>99% predominately trans, Sigma-Aldrich), 1,3-butadiene (≥99%, Sigma Aldrich) and 1-butene (≥99%, Sigma Aldrich) were used.

2.2.2 Catalyst Characterization

2.2.2.1 N_2 Physisorption

A Micromeritics® Accelerated Surface Area and Porosity (ASAP) 2020 system was used for N2 physisorption followed by BET analysis.26 Before analysis, samples were degassed at 110 °C and held at this temperature for 4 hours. Adsorption-desorption measurements of nitrogen were carried out at -196°C. After being calcined in air at 450 °C for 4 h in air, the sample was sieved >90 μm and one gram was used for the experiment.

2.2.2.2 XRD

Powder XRD patterns were measured on a Philips X'pert diffractometer equipped with an X'celerator module. Diffractograms were obtained with Cu Kα radiation for $2\theta = 10-80°$ with a step size of 0.0167°. In situ X-ray diffraction data were collected at the Quick Absorption and

Scattering beamline (QAS, 7-BM) at the National Synchrotron Light Source II (NSLS-II). The samples were placed in the Clausen cell and hydrogen was flowed through the glass at the rate of 20 sccm. The patterns were collected using 19 keV photons with Perkin Elmer flat panel detector. The energy was calibrated using a LaB_6 standard, and the 2D patterns were integrated using Dioptas software.

2.2.3 XANES

Mo L_3-edge X-ray absorption near edge spectroscopy (XANES) experiments were performed at beamline 4-3 at the Stanford Synchrotron Radiation Laboratory (SSRL). The Si(111) monochromator was calibrated by setting the edge energy of a Mo foil reference to a standard value of 2520.0 eV. For the in-situ experiments, the Mo L_3 edge was analyzed in fluorescence mode using a passivated implanted planar silicon (PIPS) detector. The sample was prepared by diluting MoO_3 with BN to create a mixture with roughly 11 wt.% MoO_3. This mixture was packed into a sample holder and placed in a specially designed cube reactor cell[55] for analysis. XANES of the Mo L_3 edge was collected continuously during a series of treatments performed consecutively on the same sample. First, the sample was heated at 10 °C/min in 40 sccm He from room temperature to 450 °C and held at that temperature for 30 min. The sample was then cooled to room temperature and the flow was switched to 40 sccm of 10% H_2 in He. The sample was then heated at 10 °C/min from room temperature to 450 °C for 30 min. Subsequently, the sample was cooled to 350 °C, and the flow was switched to 40 sccm O_2 and held at this temperature for 30 min before cooling down to room temperature again in 40 sccm He. The XANES data were processed using Athena.[56]

To understand catalyst changes due to solvent effects, X-ray absorption spectra were recorded at the National Synchrotron Light Source II (NSLS-II) (Brookhaven National Laboratory,

NY, USA) at a damping wiggler/Inner Shell Spectroscopy beamline using a cryogenically cooled double crystal Si(111) monochromator. The beam spot on the sample was 0.9 mm × 0.9 mm. The X-ray absorption near-edge structure (XANES) spectra was recorded at the Mo K-edge (20000 eV) in transmission geometry mode using ion chambers as detectors. Spectra were acquired at room temperature using self-supporting pellets of the catalyst powder mixed with boron nitride.

2.2.4 XPS

XPS experiments were carried out in a Multiprobe ultrahigh vacuum (UHV) system with a base pressure $<5 \times 10^{-10}$ Torr, equipped with a hemispherical electron energy analyzer (SPECS, PHOIBOS 100) and a twin anode X-ray source (SPECS, XR50). The XPS spectra were fitted using the add-on function XPST in Igor. Due to spin orbit coupling, the ratio between the Mo $3d_{5/2}$ and Mo $3d_{3/2}$ peaks was constrained to 3/2. Because only a partial reduction was expected, the fit was performed assuming no Mo(IV) was present in the sample. The locations and widths of the peaks were constrained based on literature values compiled elsewhere,[57] and the areas of these peaks were fit based on these parameters.

2.2.5 DFT Calculations

A model surface based on the (100) facet of α-MoO3 (space group *Pnma*) was selected as the most stable bulk structure and surface facet.[42–44] All density functional calculations were performed with Quantum ESPRESSO,[58] and exchange-correlation interactions were treated with the BEEF-vdW functional.[59] The BEEF-vdw functional is parameterized for surface adsorption and does not require material-specific parameters, so we elected to use it instead of the +U correction. There are numerous studies of MoO_3 with[60,61] and without +U[43], and there is no consensus on its necessity for adsorption properties or the appropriate U value[61,62], so the correction was omitted for simplicity. A Monkhorst-Pack k-point sampling[63] of 5x5x1 with a

planewave cutoff of 450 eV was used for all MoO_3 calculations.[42] A Fermi-Dirac electron smearing width of 0.1 eV was used for convergence (results extrapolated to 0 K) with spin polarization and dipole correction[64]. The slab was modeled using 20 Å of vacuum between slabs, and the lower two layers were fixed to bulk positions.The L-BFGS algorithm implemented in the Atomic Simulation Environment (ASE)[65] was applied for geometry optimization (maximum force of 0.05 eV/Å). The adsorption energies were calculated as follows:

$$E = E_{slab+ads} - E_{slab} - E_{ads}$$

where E is the adsorption energy with $E_{slab+ads}$, E_{slab} and E_{ads} as the DFT energy of the adsorption complex, slab, and adsorbate respectively. Free energies were computed in a similar way, with Gibbs free energies used in place of DFT energies.

Vibrational modes were estimated with the normal mode analysis by using a finite difference approximation of the Hessian matrix (Δr = 0.01Å) using ASE. Free energies were computed using the ideal gas approximation for gas-phase species and the harmonic approximation for adsorbates. A temperature of 300 K and a pressure of 1 bar were used in the free energy calculations. These corrections were also computed with the thermochemistry package of ASE, and a low-frequency cutoff of 50 cm^{-1} was used for adsorbed species.[66] Initial guesses for adsorbate geometry and binding site were based on structures from previously reported DFT calculations.[42]

2.2.6 In-situ DRIFTS Studies

DRIFTS spectra were collected using a Nicolet 8700 FT-IR equipped with a liquid nitrogen cooled MCT/A detector and the Praying Mantis (Harrick Scientific) accessory with a high temperature reactor for in-situ studies. Spectra were averaged at 64 scans with a resolution of 4

cm^{-1}. All spectra were treated using the Thermo Scientific Omnic Software. A background of dried potassium bromide at 50 ℃ was used for all spectra. The sampling cup was filled with catalyst and then smoothed across several times to ensure an even layer. The reactor was sealed and flushed with 100 sccm N_2 for 5 min to settle the sample bed. Additional catalyst powder was added to fill any voids. The catalyst was pretreated in 40 sccm of H_2, N_2 or O_2 for 1 h at 450 ℃ at a ramp rate of 10 ℃ /min and then cooled in an N_2 atmosphere for 1 h to bring the temperature of the sample back to 50 ℃. An initial spectrum of the catalyst was collected at this temperature for spectral subtraction against the catalyst with species adsorbed. Ethanol was bubbled in 40 sccm of N_2 for 3 minutes, acetaldehyde in 5 sccm of N_2 for 1 minute, and crotonaldehyde in 10 sccm of N_2 for 1 minute. All probe molecules were introduced to the catalyst bed at 50 ℃. After introducing the probe molecule, the feed was switched to 40 sccm of N_2 and held at 50 ℃ for 30 minutes and then ramped to 100, 150 and 200 ℃ at 10 ℃/min and held at those temperatures for 30 minutes. All the spectra were collected at 50°C after the sample had been heated to the respective reaction temperature.

2.2.7 TPD Studies

For each experiment, about 500 mg of MoO_3 was loaded into a quartz reactor tube packed with quartz wool. Samples were pretreated in a flow of 36 sccm of either H_2 or He at 450 °C for 1 h. After cooling the sample down to room temperature, probe molecules were dosed on the surface by flowing 9 sccm of He through a bubbler containing the desired compound and then over the catalyst bed for 80 min. The bubbler was kept at room temperature when dosing ethanol and crotonaldehyde but was cooled to 10 °C for acetaldehyde. Following dosing, the reactor tube was purged with a 9 sccm flow of He for approximately 8 hours. After purging, the temperature was ramped from room temperature to 715 °C at a heating rate of 10°C/min. Fragmentation and ion

collection were performed by a Pfeiffer Prisma quadrupole mass spectrometer downstream of the reactor.

Calibration curves were generated to correlate mass spectrum peak areas to molar amounts for each reactant/product. Controlled volumes of each molecule were injected into the mass spectrometer while monitoring the peak response. Desorption product signals were normalized using the calibration curves according to the following characteristic fragments: ethanol (m/z = 31), acetaldehyde (m/z = 29), 1,3-butadiene (m/z = 54), 1-butene (m/z = 56), and crotonaldehyde (m/z = 70). For masses associated with multiple products, molecular desorption rates were deconvoluted by subtracting contributions of heavier products using mass fragmentation patterns obtained on our system. Total molar quantities of each desorption product were calculated by integrating the normalized spectra of the relevant characteristic mass fragment with respect to time.

2.3 Results

2.3.1 Catalyst Pretreatment and Characterization

Samples reduced in H_2 are noted as R-MoO_x, samples exposed to an inert gas (either N_2 or He) are noted as I-MoO_x, and samples pretreated with oxygen are noted as O-MoO_3. XRD showed that only orthorhombic MoO_3 was present before and after calcination of MoO_3 for 4 h in air (Figure A1). Peak locations were shifted slightly after calcination, and the d spacing of the crystals decreased (Table A1). This was most likely due to the removal of water during calcination. In-situ XRD showed that at higher temperatures in the presence of hydrogen, the bulk crystal structure of the catalyst did not change (Figure A1B). The surface area of the catalyst was below 2 m^2/g according to N_2 physisorption. Delporte reported that as extent of reduction increases, the surface area of MoO_3 increased from 4 m^2/g to 11 m^2/g.[67] Thus, a higher surface area is a possible contributor to enhanced rates of product formation on reduced samples.

The evolution of the color of MoO_x during the pretreatment gave a first indication of its oxidation state. Heating in an oxygen flow produced no noticeable color change up to 450°C. Heating in inert flow caused the sample to turn slightly blue at around 250 °C, which continued to intensify up to the final temperature of 450°C indicating progressive reduction. In hydrogen flow, the sample turned a dark violet shade similar to MoO_2.[68]

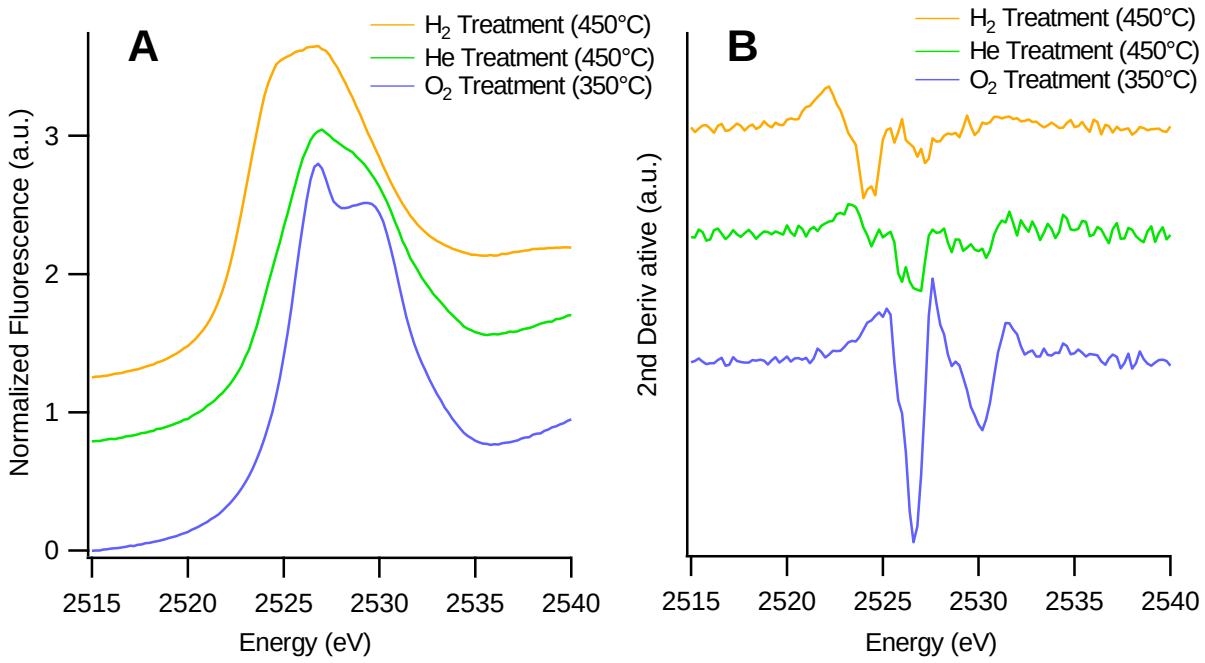

Figure 2.1 Normalized Mo L3 edge XANES data (A) and the second derivative (B) for MoO_3 after treatment with O_2, He, and H_2

The Mo L_3 edge structure is derived primarily from the transition of core electrons in the $2p_{3/2}$ orbital to empty 4d orbitals. However, these vacant d orbitals can be split into e_g and t_{2g} states due to ligand interactions in octahedrally coordinated molybdenum oxides.[69–76] This crystal field splitting causes a doublet peak shape in the white line, as seen clearly in the MoO_3 sample after O_2 treatment (Figure 2.1A). Differences in the splitting energy can be seen more clearly by plotting the second derivative of the signal intensity (Figure 2.1B).[77] Local minima in this plot correspond to peak maxima in the fluorescence data. Another key feature of the XANES spectra, the

absorption edge energy, is often interpreted as the first inflection point in the white line. This edge energy is expected to move to lower energy with decreasing oxidation state.[72,78,79] The shape and position of the edge are also influenced by the symmetry of the coordination sphere around the

Table 2.1 Mo L3 edge and splitting energies

	Edge Position (eV)	*Splitting Energy (eV)*
O_2 Treatment	2525.6	3.6
He Treatment	2524.2	3.4
H_2 Treatment	2523.1	3.2

absorbing atom.[80,81] The absorption edge energy along with the splitting energy difference for the MoO_3 sample after each treatment are compiled in Table 2.1.

Following the oxidative treatment, the Mo L_3 edge energy was determined to be 2525.6 eV with a d-orbital splitting difference of 3.6 eV, which is indicative of fully oxidized MoO_3.[75,82,83] After heating in He, the edge position and splitting energy were shifted downward by 1.4 eV and 0.2 eV, respectively. The high temperature H_2 treatment had a similar effect on both the edge position and splitting energy shifting them further downward by a similar increment. Previous research demonstrated that decreases in both the splitting energy and edge position of metal oxides tend to correlate with reduction in the oxidation state of the metal ion.[72,78,79] As such, it appears that the He treatment causes a slight reduction in Mo(VI) centers, and this effect is enhanced by high temperature treatment in H_2.

Previously published XANES profiles of MoO_3 and MoO_2 from Kashiwabara et al. were used as standards to obtain relative edge positions of the Mo(VI) and Mo(IV) oxidation states (see Figure A2).[69] In this study, the Mo L_3 edge was shifted down by 1.4 eV and 2.5 eV after high

temperature exposure to He and H_2 respectively. This compares to a shift of approximately 2.2eV between MoO_3 and MoO_2 standards (Fig. S2). Using the relationship between edge position and oxidation state obtained from the digitized spectra, this may indicate that the He treated sample is slightly reduced to an intermediate oxidation state around Mo(V), while the H_2 treated sample is highly reduced to a Mo(IV) or lower state.

Several groups have shown that the reduction of bulk MoO_3 with hydrogen can result in the formation of hydrogen molybdenum bronzes under mild conditions.[84,85] In this study, the higher ramp rates and reduction temperatures used during pretreatment would likely have suppressed the formation of these structures. Aritani et al. found that the XANES peaks for type I and type II bronzes were shifted down slightly compared to MoO_3. In contrast, the shifts in peak positions seen between MoO_3 and the H_2 treated sample in this study were much larger. In addition, the in-situ XRD (Fig S1B) of MoO_3 in H_2 at elevated temperatures does not reveal changes in the original diffractogram that would correspond to the formation of a bronze phase. As such, while there is no evidence to suggest the presence of hydrogen molybdenum bronzes after H_2 treatment, their presence cannot be ruled out.

Changes of the oxidation state of MoO_3 through reactions with methanol were probed by XPS and XANES. When MoO_3 was exposed to methanol and then held under vacuum overnight, the color of the catalyst changed from light green to gray-blue, indicating a reducing interaction between the solvent and the MoO_3 surface. This change was verified through XANES of MoO_3 before and after exposure to methanol at the K-edge as reported in Figure A3. A slight decrease in the near edge peak is seen at 20002 eV. Since this near edge peak does not exist for Mo(IV)[86], this result suggests that methanol exposure produced a slight decrease in the average oxidation state of

Mo. The fits of the Mo 3d doublet in the XPS spectra before and after exposure to methanol (Figure A4) indicated that the abundance of Mo(V) increased from 8% to 15% during this treatment.[57,87]

2.3.2 Reaction of Oxygenates on Different Surfaces

2.3.2.1 DFT Calculations

DFT calculations were used to investigate how the presence of oxygen vacancies on MoO_3 influences the binding of ethanol and acetaldehyde. The optimized adsorption geometries for ethanol and acetaldehyde on O-MoO_3 indicate only non-directional bonds and relatively low adsorption energies of roughly -0.20 eV (Figure 2.2). The results provide evidence that both molecules are physisorbed on O-MoO_3. In contrast, there was a clear directed interaction between the alcohol/aldehyde group and the oxygen vacancy site, and binding energies were substantially more exergonic (< -0.75 eV), indicating strong chemisorption at the vacancy sites. This suggests that defect sites are critical to activating alcohol and aldehyde functionalities and corroborates the enhanced reactivity of partially reduced surfaces described below. Vibrational frequencies are shown in Table A2-S4 for both types of surfaces and the three adsorbate molecules. For ethanol, the defect site generally induced a slight blueshift of 0-50 cm^{-1} for most modes, although the O-H stretch is significantly more redshifted by around 150 cm^{-1}. For acetaldehyde, the effects of the defect site are more ambiguous. Most modes were slightly blue shifted (0-50 cm^{-1}), while the C-C and C-H stretch of the CH group was red shifted by 45 and 116 cm^{-1}, respectively.

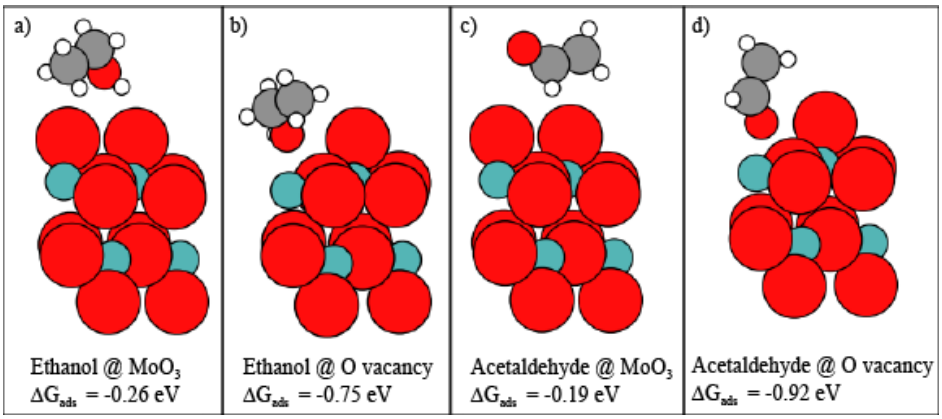

Figure 2.2 Adsorption geometries of ethanol (a, b) and acetaldehyde (b, c) adsorbed on a pristine MoO3 (100) surface (a, c) and an oxygen vacancy defect (b, d). The Gibbs free energy of adsorption is included for each system.

2.3.2.2 DRIFTS Studies

DRIFTS was used to further illustrate the role of oxygen vacancies in strong adsorption and conversion of ethanol, acetaldehyde, and crotonaldehyde at ambient conditions and subsequent heating. Figure 2.3A shows the DRIFTS spectra of ethanol on the three differently pretreated surfaces at 50 °C, and Table 2.2 gives vibrational assignments for the relevant peaks labeled in Figure 2.3A. While the relative absorbance for R-MoO_x were less intense, it is likely the reduced intensities were due to a higher infrared absorbance (darker color) of the sample, and not necessarily due to the adsorbate concentration.

The region above 3200 cm^{-1} is classified as the hydroxyl stretching region.[88,89] For the reduced sample, adsorption of ethanol resulted in a broad, unresolved peak at 3331 cm^{-1}. The poor signal-to-noise ratio for this sample is likely due to the stronger IR absorbance (darker color) of pre-reduced MoO_3. In contrast, the inert and oxidative pretreatments produced samples with several distinct hydroxyl bands. Bands at 1479 and 1447 cm^{-1} suggested the presence of acetate species on the surface.[90,91] Previous studies have shown that acetate species are produced on different metal oxides after ethanol exposure.[91–98] There was a shoulder to the peak marked 1625

cm^{-1} on the R-MoO_x that appeared around 1645 cm^{-1}. As discussed below, this peak is most likely the υ(C=C) mode of crotonaldehyde. Two other bands appeared at 1268 and 1624 cm^{-1} and are attributed to the υ(C-O) and υ(C=C) vibrations of surface bound enolates, respectively. These peaks were retained up to 150 °C (Figure A6) suggesting that the enolates are strongly bound. Idriss et al. referred to this species as η^2-acetaldehyde due to the coordination of both the primary carbon and oxygen atom to the surface (Scheme 1).[93,94] The presence of this species suggests that keto-enol tautomerization of surface species readily occurs on the catalyst, similar to what was observed in the case of dehydration products of glycerol on niobia.[99]

The C-H stretches of ethanol gave rise to peaks near 2978, 2935, and 2902 cm^{-1} that are attributed to $\nu_{as}(CH_3)$, $\nu_{as}(CH_2)$, $\nu_s(CH_2)$ modes, respectively.[97,98] This suggests that significant amounts of ethanol were still present on the surface as either ethoxide groups or in a molecularly adsorbed state. The C-H stretching modes of surface species on the R-MoO_x sample decreased significantly when the temperature was increased above 50 °C, while they remained resolved on the I-MoO_x sample even at 150 °C. Looking at the OH and CH stretching region, it appears that ethanol adsorbs differently based on the pretreatment for the catalyst given more surface hydroxyl groups appear on the I-MoO_x and O-MoO_3 surface due to higher presence of oxygen on the surface.

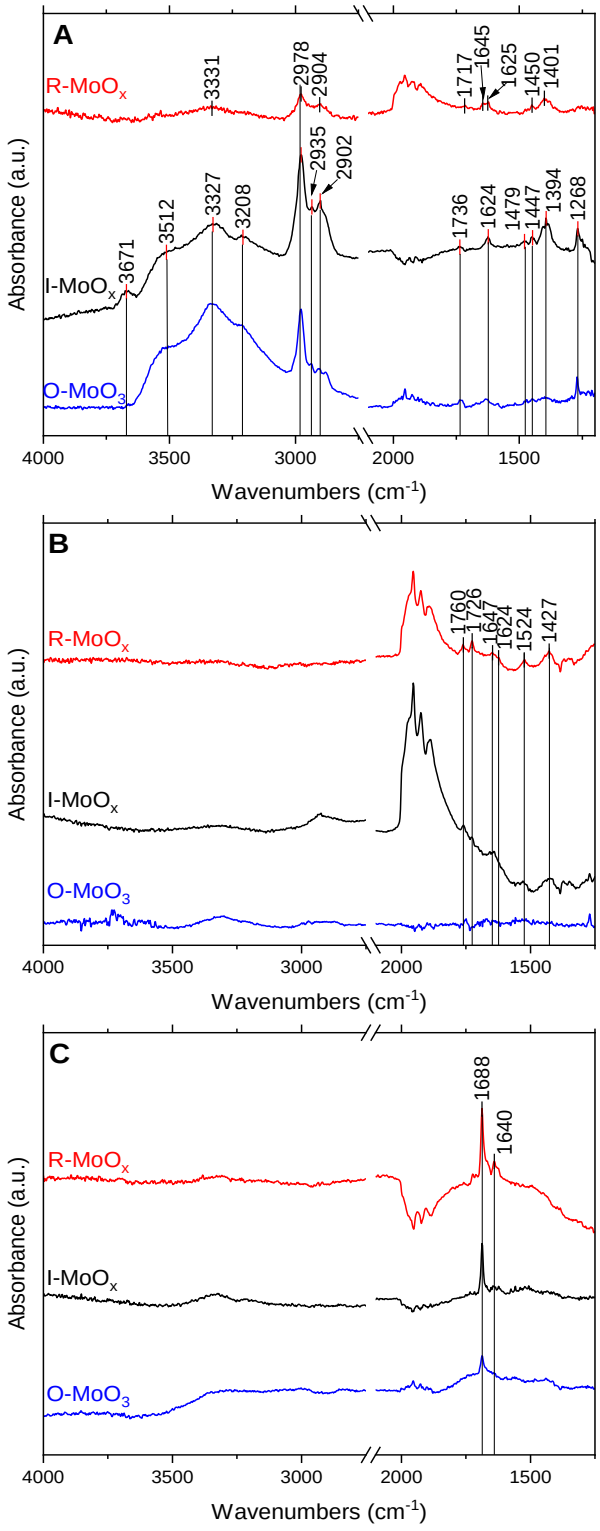

Figure 2.3 Spectral subtraction DRIFTS of (A) ethanol adsorbed onto R-MoO_x, I-MoO_x, and O-MoO_3 sample at 50 °C. (B) acetaldehyde adsorbed onto R-MoO_x, I-MoO_x, and O-MoO_3 sample at 100 °C. (C) crotonaldehyde adsorbed onto R-MoO_x, I-MoO_x, and O-MoO_3 sample at 100 °C.

Table 2.2 Vibrational mode assignments from labeled peaks in Figure 2.3A for species other than ethanol

Mode (cm^{-1})	***Vibration***	***Species***
1268	υ(C-O)	Enol
1393	$\delta_{as}(CH_3)$	Acetaldehyde
1427	$\delta(CH_x)$	Various
1447	$\delta_{as}(CH_3)$, $\upsilon_s(COO)$	Various
1479	$\delta_{as}(CH_2)$	Various
1524	$\upsilon_{as}(COO)$	Acetate
1624	υ(C=C)	Enol
1645/7	υ(C=C)	Crotonaldehyde
1726	υ(C=O)	Acetaldehyde (Chemisorbed)
1735	υ(C=O)	Acetaldehyde
1760	υ(C=O)	Acetaldehyde (Physisorbed)

Figure 2.3B shows the spectra of acetaldehyde on the three different pretreated surfaces at 100 °C. One key feature of these spectra is the appearance of Mo=O overtones in the 1800-2000 cm^{-1} region.[100,101] The appearance of these overtones suggests a strong interaction between acetaldehyde and the Mo=O bond. The peaks at 1726 and 1760 cm^{-1} are characteristic of the υ(C=O) for chemisorbed and physisorbed acetaldehyde, respectively.[102] The peak at 1524 cm^{-1} is attributed to surface acetate species.[93,94] The R-MoO_x sample showed additional peaks. The peak at 1624 cm^{-1} was the same as the one shown in Figure 2.3A and is assigned to the υ(C=C) of an enol. The peak at 1647 is assigned to the υ(C=O) of the aldol coupling product crotonaldehyde.[102] This peak was also seen in Figure 2.3A and Figure 2.3C. The broad peak at 1427 cm^{-1} is assigned to $\delta(CH_x)$ modes of various species.[102] As the temperature increased, the peaks diminished at 200 °C suggesting desorption (Figure A7A). This was also observed for the I-MoO_x sample (Figure A7B). The reduced samples had higher affinity for adsorption of acetaldehyde onto its surface than the O-MoO_3 sample. Interestingly, acetaldehyde only adsorbed very weakly on the O-MoO_3 sample. While there was some physisorbed acetaldehyde present on the surface at 50 °C (Figure A7C), after heating to 100 °C, there were no detectable peaks present.

Figure 2.3C shows the spectra of crotonaldehyde on the three differently pretreated surfaces at 100 °C. The sharp peak at 1688 cm^{-1} is assigned to the υ(C=O) stretching mode of crotonaldehyde, which was redshifted from 1725 cm^{-1} in the gas phase. A shoulder was present around 1640 cm^{-1} and is assigned to the υ(C=C) stretching mode of crotonaldehyde.[103] The sustained presence of this band up to 200 °C on R-MoO_x and I-MoO_x (Figure A8A/B) suggests it was chemisorbed. There were two resolved υ(O-H) peaks present at 3215 and 3334 cm^{-1} that persisted up to 150 °C. As the temperature increased, the peak at 1688 cm^{-1} decreased in intensity, and positive peaks of the overtones of the catalyst appeared (Figure A8B). This is similar to the behavior of acetaldehyde on the I-MoO_x sample shown in Figure A7B. The spectrum of crotonaldehyde on R-MoO_x contained the same peaks, but the overtones gradually decreased as the temperature increased (Figure A8A). The spectrum of crotonaldehyde on O-MoO_3 exhibited the same 1688 cm^{-1} peak, but it disappeared after 100 °C, unlike acetaldehyde on the MoO_3 sample which lost its carbonyl peak after 50 °C (Figure A7C). This suggests that crotonaldehyde was more strongly adsorbed on the oxidized surface compared to acetaldehyde on the same surface but still readily desorbed.

2.3.2.3 TPD MS Studies

TPD was used to determine how reduction of MoO_3 influenced product yields and kinetic barriers for reactions of ethanol, acetaldehyde, and crotonaldehyde. During ethanol TPD on the R-MoO_x surface, ethanol desorbed in a broad, asymmetric peak at 183 °C, while the oxidation product acetaldehyde was formed at 230 °C. Several coupling products were also observed for R-MoO_x, including 1,3-butadiene at 233 °C, 1-butene at 247 °C, and crotonaldehyde at 263 °C. In contrast, the signal for molecular ethanol desorption from the I-MoO_x surface was broad and weak (Figure 2.4B). A similarly small and broad peak associated with acetaldehyde was also seen on

the I-MoO_x surface. The same TPD experiment was also carried out on O-MoO_3, which resulted in lower adsorption and conversion of ethanol. Thus, pre-reduction of MoO_3 was found to dramatically increase both the density of strong adsorption sites for ethanol and the yield for coupling products. It is worth noting that 1-butene may readily isomerize on the oxide surface, and it is likely that the signal attributed to 1-butene also contains contributions from 2-butenes (cis and trans).

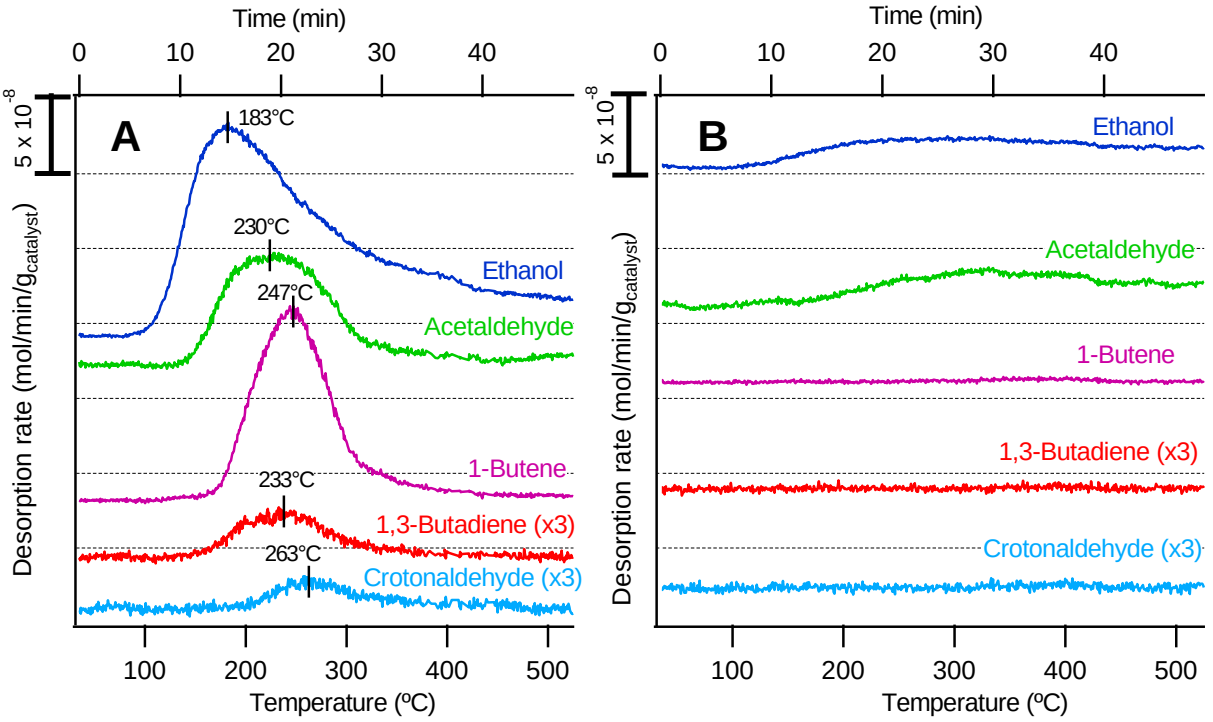

Figure 2.4 TPD profile of products from ethanol dosed on a MoO_3 surface pretreated with 36 sccm of hydrogen (A) or helium (B) at 450 °C for one hour. Assignments of each trace are as follows: ethanol (m/z = 31), acetaldehyde (m/z = 29), 1-butene (m/z = 56), 1,3-butadiene (m/z = 54), and crotonaldehyde (m/z = 70). Contributions from heavier products were subtracted from each trace.

The reactions of acetaldehyde were also examined on MoO_3 to better understand the reaction pathway for the production of C_4 species. On R-MoO_x, a large molecular acetaldehyde desorption peak was observed at 141 °C (Figure 2.5A). Acetaldehyde was detected at a lower temperature here compared to the ethanol TPD, indicating that the kinetic barrier for producing

acetaldehyde from ethanol is higher than the barrier for desorption of molecular acetaldehyde. In other words, the production of acetaldehyde from ethanol is reaction-limited. As expected, coupling products were also observed, with desorption of crotonaldehyde at 199°C, 1,3-butadiene at 238 °C, and acetone at 231°C. Although similar products were observed for the I-MoO_x surface, their yields were significantly lower, and the peak desorption temperatures (266 °C and 279 °C for crotonaldehyde and 1,3-butadiene, respectively) were higher. Desorption yields of acetaldehyde were also significantly lower for I-MoO_3. Again, these results indicate that MoO_3 reduction greatly increases the density of sites able to activate acetaldehyde toward coupling reactions.

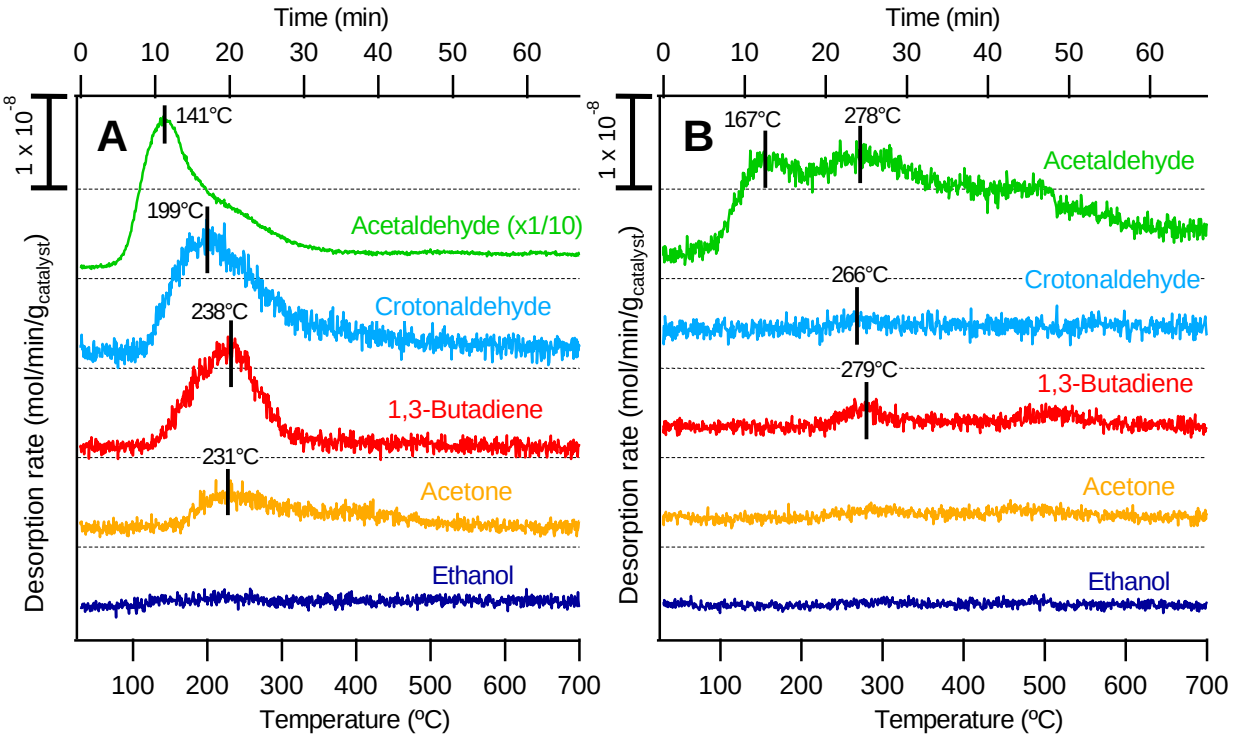

Figure 2.5 TPD profile of products from acetaldehyde dosed on a MoO_3 surface pretreated with 36 sccm of hydrogen (A) or helium (B) at 450 °C for one hour. Assignments of each trace are as follows: acetaldehyde (m/z = 29), crotonaldehyde (m/z = 70), 1,3-butadiene (m/ z = 54), acetone (m/z = 58), and ethanol (m/z = 31). Contributions from heavier products were subtracted from each trace.

A noteworthy difference between the acetaldehyde and ethanol TPD data was the relative concentrations of unsaturated C_4 products (1-butene and 1,3-butadiene). When starting with ethanol, R-MoO_x produced a higher concentration of the more saturated 1-butene when compared to 1,3-butadiene. However, when acetaldehyde was used under the same conditions, the C_4 hydrocarbon product contained almost exclusively 1,3-butadiene. This difference in product selectivity may be caused by the difference in the amount of hydrogen available on the surface. When ethanol is coupled to produce C_4 products, hydrogen is removed through dehydrogenation. The resulting hydrogen may remain on the surface, potentially in the form of surface hydroxyls, and ultimately lead to the production of more saturated species like 1-butene. On the other hand, acetaldehyde does not produce hydrogen during the coupling to C_4 products, so unsaturated species like 1,3-butadiene are presumably more common.

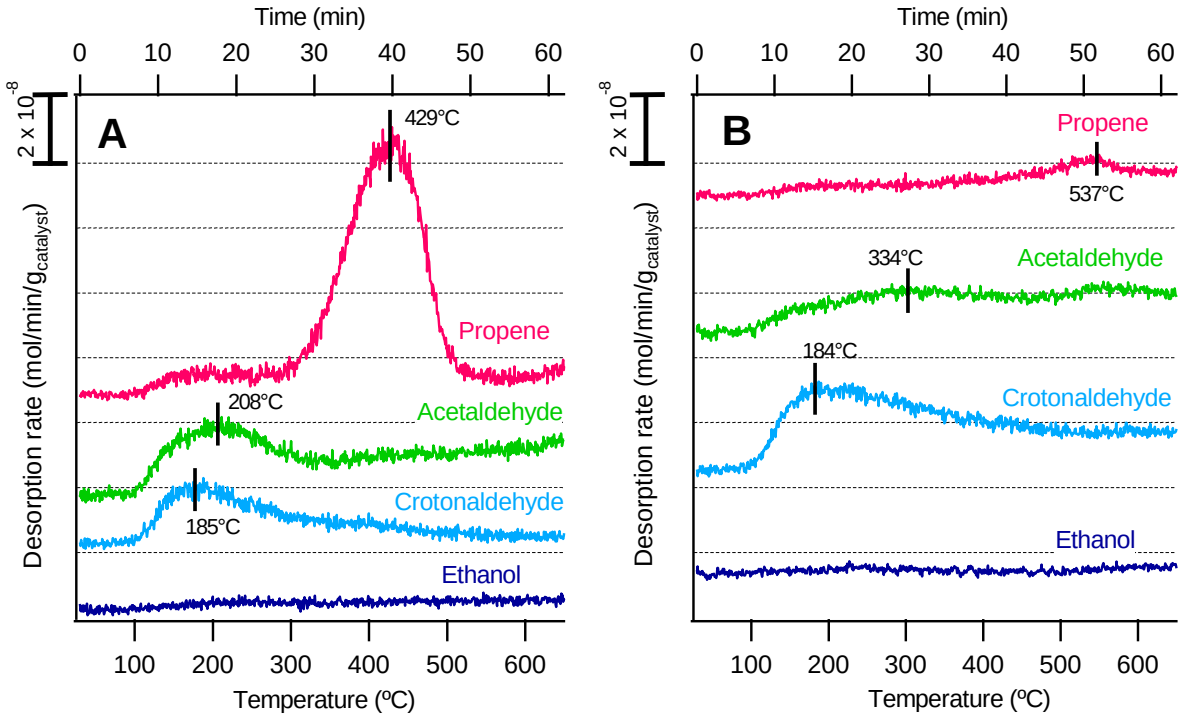

Figure 2.6 TPD profile of products from crotonaldehyde dosed on a MoO_3 surface pretreated with 36 sccm of hydrogen (A) or helium (B) at 450 °C for one hour. Assignments of each trace are as

follows: acetaldehyde (m/z = 29), ethanol (m/z = 31) propene (m/z = 42), crotonaldehyde (m/z = 70). Contributions from heavier products were subtracted from each trace.

To understand how surface reduction influences retro-aldol reactions, TPD studies with crotonaldehyde as a reactant were carried out (Figure 2.6). The peak of crotonaldehyde molecular desorption was similarly broad for both R-MoO_x and I-MoO_x. On the other hand, the desorption profile for the RAC product acetaldehyde showed drastically different behavior for the two treatments. On the I-MoO_x catalyst, the desorption of acetaldehyde from the surface occurred over a broad temperature range, without a clearly resolved desorption peak. However, on the R-MoO_x catalyst, acetaldehyde desorbed with a much sharper and more intense peak at the relatively low temperature of 208°C. This difference most likely indicates that the R-MoO_x surface had a higher concentration of sites that are efficient for RAC at lower temperature. This could also be due to a higher concentration of water on the surface from the reduction step since hydration of crotonaldehyde is a prerequisite for C-C bond cleavage by RAC. It was also found that the R-MoO_x sample catalyzed decarbonylation to produce large amounts of propene at higher temperatures, while the I-MoO_x sample was not particularly active for this reaction pathway. Decarbonylation of crotonaldehyde is often reported as a mechanism for the deactivation of transition metal catalysts[104–106] and is likely catalyzed by the irreversible adsorption of the aldehyde group and subsequent decomposition on reduced Mo sites that are readily available on the R-MoO_x surface.

The integrated total molar desorption quantities for each reaction product in the TPD studies are displayed in Tables S5 (ethanol), S6 (acetaldehyde), and S7 (crotonaldehyde). In all cases, the total moles of desorbed species from R-MoO_x surface was at least twice as high (and in many cases far higher) as that from the I-MoO_x surface. In summary, the cumulative TPD results suggest that the H_2 reduction treatment had two key effects. First, it greatly increased the density

of active sites for the various reactions; as discussed in detail below, we propose that these sites are oxygen vacancies generated during reduction. Second, the reduction treatment decreased the peak temperatures for formation of most products (e.g., acetaldehyde from ethanol), indicating that the generated sites were also more active. We propose that this higher activity is due to an increased Lewis acidity of Mo at greater extents of reduction.

2.4 Discussion

2.4.1 Nature of Active Sites

Many studies have shown that oxidation state and reducibility play a key role in the reactivity of metal oxide catalysts.[107,108] Several groups have hypothesized that the active sites for important reactions on metal oxides are oxygen vacancies, due to their ability to exhibit both Lewis acidic and redox properties.[109–112] This behavior allows them to facilitate the adsorption and reaction of molecules for a wide range of reactions, from hydrodeoxygenation (on CeO_2, MoO_3 and ZnO)[113–115] to aldehyde coupling (on CeO_2)[116,117] and retro aldol condensation.[31,118] Thus, it is critical to properly account for formation and loss of active sites when the catalyst is exposed to pretreatment and reaction conditions. This study shows that oxygen vacancies are formed on MoO_3 at elevated temperatures under inert conditions and, to a much greater extent, under reducing conditions. These reducing conditions are comparable to previous studies of oxygen vacancy formation on MoO_3.[114,119,120] Delporte et al. showed that MoO_3 forms a MoO_2 phase under an n-hexane/H_2 flow at 350 °C for 3 h, as revealed by XRD, and also that a significant increase in surface area occurred.[67] In the present study, XANES in combination with the low surface area of MoO_3 suggested that the partial reduction of MoO_3 must extend into the bulk under inert and reducing conditions, because there are not enough surface sites to account for the reduced average oxidation state of Mo. This increase in the density of reduced sites on the surface is likely

responsible for the increased activity of the R-MoO_x catalyst compared to the I-MoO_x catalyst, as seen in the TPD studies (Figs. 4,5,6). Additionally, probe reactant molecules appear to interact more strongly with these oxygen vacancy sites than on the pristine catalyst. DFT calculations show the adsorption energy of these molecules is lower on the surface with the defect suggesting they are chemisorbed. Although this calculation was only done for the (100) surface, this trend is hypothesized translate to other facets. DRIFTS of acetaldehyde (Figure A7A) exhibited overtone peaks on R-MoO_x which could imply that the Mo site is interacting with the oxygen of the adsorbate now that the corresponding oxygen has been removed. As a result, new Mo=O bonds are formed that were not initially present after reduction. However, these overtones were not observed on the O-MoO_3 sample, suggesting that the different pretreatments affect how adsorbates interact with the surface. The strength of these oxygen vacancy sites also likely plays a role in the activity and selectivity of the catalyst. According to the Sabatier principle, an optimal catalyst requires a balance between the adsorption/activation of the reactant and the ability to desorb products. Volcano plots relating catalytic activity to a descriptive parameter have been demonstrated for a wide variety of reactions.[121,122] While this type of relationship was not observed in this study, it is possible that further reducing the catalyst could lead to excessive coking of the surface from irreversibly adsorbed products. As such, the presence of an optimal density of oxygen vacancy sites for the aldol reaction requires further research.

Interestingly, alcoholic solvents, such as methanol and ethanol, that are commonly used in liquid-phase reactions can also partially reduce and thus activate MoO_3 catalysts for the RAC reaction under mild conditions.[31] In this study, XPS (Fig. S4) and XANES (Fig. S3) both indicated that exposure of MoO_3 to methanol at room temperature resulted in slight reduction, presumably leading to oxygen vacancies on the surface. This also caused a characteristic color change when

the solvents were mixed with the powder. While the mechanism for this reduction is not well-studied in the literature, the deprotonation of these alcohols can cause a higher concentration of protons on the surface, which may lead to an increase in the number of hydroxyls at the surface. Adjacent hydroxyls may then interact to form a water molecule that leaves and a vacancy site. Partial reduction of the surface during reactions in alcoholic solvents could generate active sites for the aldol reaction and thus have a profound impact on catalytic processes.[31] Efforts to rationally improve processes employing these solvents should account for the ability to produce active centers via chemical reduction even in the absence of strong reductants like H_2.

2.4.2 Reaction of Oxygenates on Different Surfaces

Several metal oxides adsorb ethanol through deprotonating the alcohol group creating ethoxide groups on the catalyst surface.[90,93,95,97,123–125] On MoO_3, coordinately unsaturated sites (CUS) in the form of anion-cation pairs at the apical oxygen location (M=O) in the MoO_3 lattice have been hypothesized to stabilize the dissociative adsorption of ethanol into a proton and an ethoxide ion on the surface, as depicted in Figure 2.7. [126–129] This adsorption state is necessary to further dehydrogenate the ethoxide to acetaldehyde through an α-hydride elimination.[130] Several groups have demonstrated that the mechanism for the production of C_4 products from ethanol proceeds through a dehydrogenation to acetaldehyde followed by an aldol coupling reaction.[51,131–133] The promoting effect of the reducing pretreatment most likely derives from an increase in the density of oxygen vacancies at the surface. The specific mechanism for oxygen vacancy formation under hydrogen flow is not clear, but it may occur through hydroxylation and dehydration of surface terminal M=O bonds.[134]

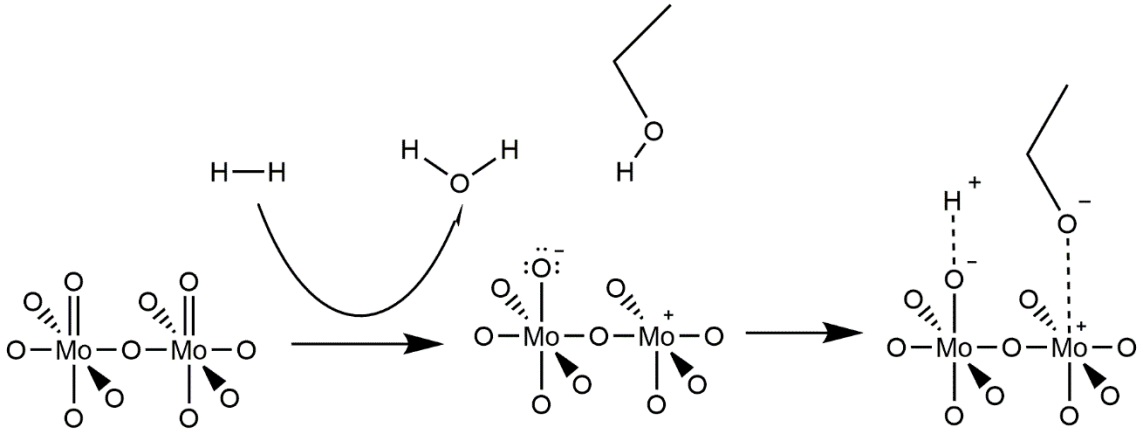

Figure 2.7 Potential mechanism for formation of oxygen vacancies on MoO3 via hydrogen treatment and the stabilization of the ethoxide ion on the surface

Similar to ethanol, acetaldehyde adsorption is likely assisted by CUS sites but to an even greater extent. Other reduced metal oxides have also shown the necessity of CUS sites for acetaldehyde adsorption.[94,102,135–139] High coverage of acetaldehyde and proximity between surface species is important for bimolecular reactions, such as aldol coupling, to occur. Adsorption of acetaldehyde is much stronger when a defect is present as shown by DFT (Figure 2.2). As shown in Figures 4 and 5, there is appreciable production of crotonaldehyde from both ethanol and acetaldehyde on the R-MoO_x and I-MoO_x samples. A reduced MoO_3 state is critical for the forward and reverse aldol condensation reaction. TPD results demonstrated that R-MoO_x was better able to bind and couple both ethanol and acetaldehyde to C_4 products compared to I-MoO_x and O-MoO_3. R-MoO_x facilitated the RAC of crotonaldehyde to acetaldehyde at low temperature, while I-MoO_x did not. Thus, it is suggested that stabilization of both product molecules of the retro-aldol condensation by defects is critical for the reaction to occur effectively. Similarly, the IR spectra indicated that acetaldehyde chemisorbs and reacts on R-MoO_x up to 200°C (Figure A7A), but only adsorbs weakly on O-MoO_3 with complete desorption occurring after 50°C (Figure A7B).

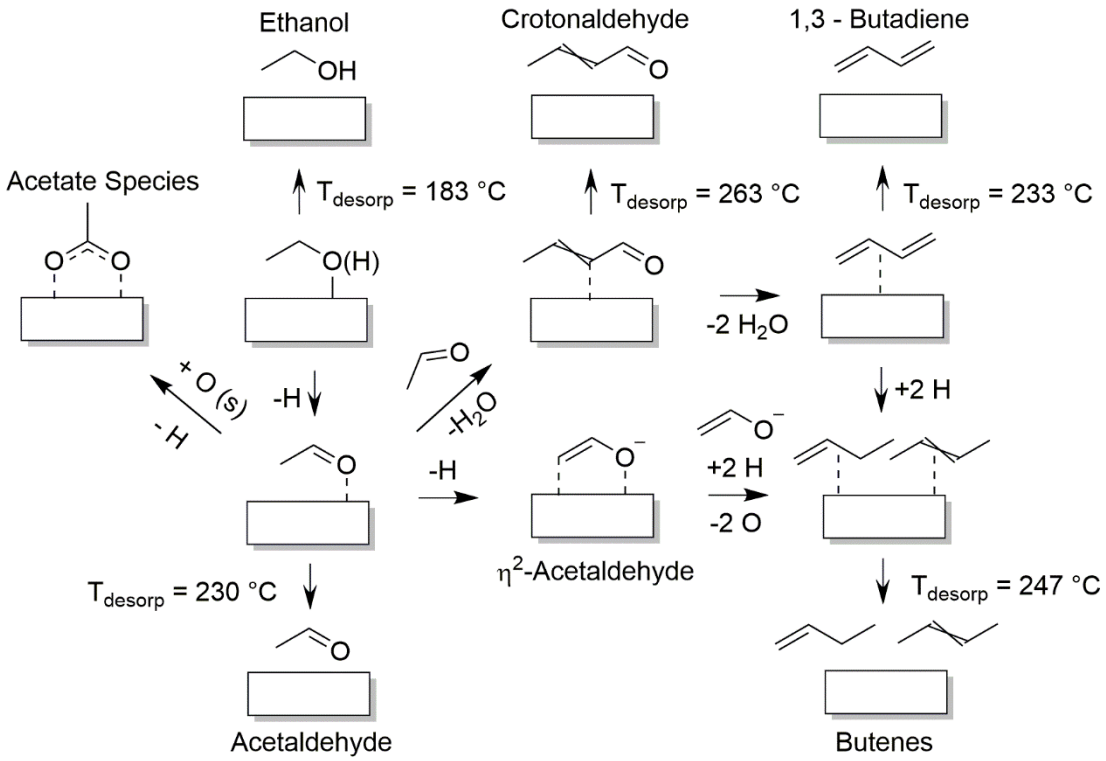

Scheme 2.2 Potential reaction mechanism starting from ethanol with desorption temperatures based on adsorption on R-MoO_x surface (Figure 2.4A).

In parallel to the coupling route, other species were observed. Acetate intermediates were also present on the surface and were similarly observed for different metal oxides after ethanol exposure.[92–98] These species are formed when nucleophilic oxygen atoms from the surface of the catalyst attack the adsorbate. The presence of these acetate species suggests that ethanol is further oxidized when adsorbed on the surface of the catalyst, but only in a surface-bound state since no acetic acid was detected in the TPD. The lack of acetic acid formation can be explained by the weakly basic nature of MoO_3. The peaks at 1269 and 1624 cm^{-1} in Figure 2.3A are characteristic of the enolate form of ethanol as shown in Scheme 2.2. Idriss and coworkers showed that ethanol forms a dihapto structure on the surface of ceria.[93,140] This suggests that the oxidation of ethanol results in the formation of an enolate that is more stable than acetaldehyde. The presence of the enolate indicates that a tautomerization mechanism readily occurs on the surface and the enolate is stabilized by the surface. Interestingly, the enolate was also present on the oxidatively pretreated

catalyst but not the R-MoO_x sample. This suggests that a certain amount of oxygen may be necessary on the surface to strongly bind the adsorbate in this di-hapto configuration. As shown in the proposed mechanism (Scheme 2.2), the enolate is an intermediate for production of other species. Thus, its presence is needed for upgrading to chemicals other than acetaldehyde. It is also noteworthy to point out the tendency of ethanol to undergo dehydrogenation to ethoxide groups/aldehydes over all forms of the pretreated catalyst.

The implications of this work for the field of sugar chemistry are significant. Simple organics with aldehyde and alcohol functionality were observed to behave differently over various pretreated versions of MoO_3. Sugars possess aldehyde, keto and alcohol groups in rather complex molecules. For the simpler model compounds in the present study, it was shown that adsorption and condensation of these groups is greatly facilitated by CUS formed on MoO_3. In the work of Davis and coworkers, Sn-BEA was shown to catalyze the isomerization of glucose to fructose but not the RAC of fructose to dihydroxyacetone and glyceraldehyde.[31] On the other hand, MoO_3 was active for RAC, but had low activity for isomerization. When the solvent was switched from water to methanol, there was a significant increase in alkyl lactate yield, most likely due to defect sites created by the presence of the alcoholic solvent. The results shown here provide support for this finding by suggesting CUS of MoO_3 provide a specific environment with high catalytic activity for RAC sugars. A likely explanation for the stark differences in the reaction paths over Sn-BEA and MoO_x is the steric environment of the active sites in these materials. The Sn sites in Sn-BEA are in framework positions (i.e., zeolitic T-sites) with four-fold coordination, and it is believed that one of the Sn-O-Si bonds is hydrolyzed to form the active "open" site, which should be a little more accessible.[22] This kind of domain lends itself to the formation of a sterically demanding cyclic transition state, in which two functional groups closely interact with the active site to enable

a hydrogen transfer reaction. In contrast, Mo(VI) ions in the bulk of MoO_3 are six-fold coordinated. While surface termination with Mo=O groups and the formation of defect sites will decrease this coordination number, the accessibility of the Mo site will remain much lower compared to LAS in Sn-BEA. Thus, the RAC reaction that only requires one aldehyde or keto group to interact with the LAS should be favored relative to a sterically more demanding isomerization reaction. The accessibility of the Mo site due to reduction is key, as it is possible for a sugar to undergo RAC in an oxygen containing environment, but only if it can interact with the site.[141] Another hypothesis is that CUS effectively stabilize the delocalization of the electron density of the carbonyl, thus leading to a more stable transition state. With this, oxygen atoms adjacent to the vacancy can become more nucleophilic and interact with alkoxide groups more strongly. Specifically, a bifunctional relationship on the surface of the catalyst is created where the CUS acts as an acid and a nearby nucleophilic oxygen becomes more basic. These effects allow the CUS to pull in the electrons of carbonyl oxygen atoms more strongly and the surface oxygen atom to stabilize the adsorbate better. The propensity of MoO_3 to be reduced in alcoholic solvents, thus catalyzing RAC, hints at the extent of reduction of MoO_3 as a key descriptor for their performance.

2.5 Conclusions

This study has shown the role partial reduction of MoO_3 plays in the chemistry of simple oxygenates over MoO_3. Whereas thermal treatment of the catalyst in an inert environment led to partial reduction, treatment in H_2 significantly increased the density of reduced sites. Partial reduction could also be achieved by pretreating the MoO_3 with alcohols commonly used as solvents during (retro) aldol catalysis as shown by XPS and XANES. DFT-computed adsorption energies revealed that defects significantly favor the adsorption of oxygenates. The adsorption of aldehydes over CUS was more favored than alcohols. Furthermore, experimental DRIFTS and

TPD studies showed that more reduced surfaces were far more active for (retro-)aldol coupling reactions. These results provide clear evidence of the importance of surface oxidation state on the catalytic activity and selectivity of MoO_3 catalysts and suggest that catalytic activity can be tuned by solvent selection and/or catalyst pre-treatment. The findings also highlight the importance of in-situ or operando characterization of MoO_3 catalysts, particularly if operating in the presence of reducing solvents.

Chapter 3 Supported Molybdenum Oxides for the Aldol Condensation Reaction of Acetaldehyde

This work contains contributions from Mathew J. Rasmussen, PhD

3.1 Introduction

Consumption of fossils fuels for energy production is the top contributor of greenhouse gas emissions globally.[142] Switching to renewable sources/feedstocks, such as lignocellulosic biomass, can potentially alleviate many of the problems associated with the current energy portfolio.[32] Unlike other sources of renewable energy, lignocellulosic biomass has the unique advantage of being readily converted into liquid fuels which can be easily incorporated into the existing infrastructure for the transportation sector.[143] Cellulose is the most abundant component of biomass and is made up of repeating subunits of glucose molecules bound by glycosidic linkages. These carbohydrate chains can be split into individual glucose monomers through hydrolysis.[13] Sugars, such as glucose, can serve as intermediate feedstocks that can be further upgraded to fuel-grade molecules or valuable specialty chemicals. Some examples include: aqueous phase reforming of sorbitol to alkanes over a Pt/SiAl catalyst[144] and isomerization and retro aldol condensation of glucose to alkyl lactates using Sn-BEA and MoO_3[31]. Recently, there has been increased interest in the transformation of biomass-derived sugars to renewable jet fuel mixtures in the C_9 – C_{16} range through a series of hydrogenation, dehydration, and aldol condensation reactions.[145,146] Careful selection of heterogeneous catalysts is key for selective transformation of sugars to value-added chemicals.

C_2 oxygenates such as ethanol and acetaldehyde are ideal candidates for studying C-C bond formation reactions to higher molecular weight products. The National Renewable Energy Laboratory recently released an overview of their state-of-the-art lignocellulosic biomass

upgrading process and found that several light oxygenates, including acetaldehyde, were produced in significant quantities during the catalytic fast pyrolysis reaction.[147] These volatile compounds are not currently captured by the primary product fuel stream, but coupling reactions like aldol condensation could be utilized to upgrade these molecules into heavier fuel-grade compounds that could be readily incorporated into the liquid fuel product. Several studies have investigated the aldol condensation reaction for ethanol and acetaldehyde over a variety of metal oxide catalysts.[52,135,138,140,148–150] During the aldol condensation of acetaldehyde to crotonaldehyde, an enolate is generated by abstraction of the proton at the α-carbon position followed by addition of an adjacent acetaldehyde molecule and finally dehydration of the aldol addition product.[93] Flaherty and coworkers recently showed that this reaction most likely occurs through a mechanism involving an enolate and acetaldehyde molecule both bound to Lewis acidic Ti sites on anatase TiO_2.[151] Some studies have shown that aldol condensation reactions can lead to significant deactivation of the catalyst at high acetaldehyde pressures due to the formation of heavy, nonvolatile products.[139,152] Strong affinity of acetaldehyde on both solid acid and base sites can also cause deactivation.[152,153] As a result, a deep understanding of interactions between reactants and active sites is necessary for optimizing catalysts for the aldol condensation reaction.

We have previously shown that ethanol and acetaldehyde undergo the retro aldol condensation reaction on MoO_3 and also found that activity is enhanced when a reductive pretreatment is used.[154] A significant disadvantage of bulk MoO_3 is the inherently low surface area. One method to address this is to deposit Mo (as MoO_x) on high surface area supports like Al_2O_3 and SiO_2. Characterization of Mo/Al_2O_3 and Mo/SiO_2 has shown that both materials can achieve high Mo dispersion and high surface area without forming crystalline MoO_3 phases.[155] Such catalysts have been used for many different reactions such as alkane dehydrogenation.[156–162]

MoO_x can be anchored on the acid sites of Al_2O_3, and DFT calculations showed that Mo – O – Al bonds were formed and surface reactivity was enhanced.[163] On the SiO_2 surface, Mo (IV) species likely form two-fold coordinated sites with a mono-oxo ligand.[164] These two different coordination environments of MoO_x will provide insight into how properties of oxide supports may control the characteristic features of Lewis acid sites (e.g., strength, accessibility, hardness) and thus the path of surface reactions.

In this work, we show how the support and weight loading of MoO_x control the activity for aldol condensation of acetaldehyde. To our knowledge, this is the first study that elucidates the aldol condensation of acetaldehyde over Al_2O_3 and SiO_2 supported molybdenum oxide catalysts. Steady state reactions were performed to test the performance of the catalysts. Mo/Al_2O_3 and Mo/SiO_2 were characterized to rationalize how their physical makeup determines the observed reactivity.

3.2 Methodology

3.2.1 Catalyst Synthesis

Supported MoO_x catalysts were prepared through incipient wetness impregnation of Al_2O_3 (99.997% metals basis, Alfa Aesar) and SiO_2 (HPLC grade 99.99%+, Alfa Aesar) porous supports. Ammonium molybdate tetrahydrate (99.98%, Strem Chemicals) precursor was dissolved in water at appropriate concentrations and then mixed with the corresponding support material to create catalyst samples with a variety of Mo loadings. These samples were dried in an oven at 120 °C overnight and then calcined in air at 450 °C for 4 hours. Samples in this study are referred to as xMo/Al_2O_3 or xMo/SiO_2 where x refers to the nominal weight loading of Mo in the sample (in wt%).

3.2.2 Probe Molecule Infrared Spectroscopy

The quantification of Lewis and Brønsted acid sites on the catalysts was performed using *in-situ* pyridine adsorption followed by FT-IR spectroscopy. Measurements were conducted using Thermo Scientific Nicolet iS10 by collecting 64 scans for each spectrum with a resolution of 4 cm^{-1}. Self-supported catalyst wafers were prepared and loaded into a high vacuum setup where the sample was heated to 150 °C under high vacuum for 2 h. The sample then underwent an activation step at 450 °C for 1 h. Then, the temperature was reduced to 150 °C where pyridine was introduced at a pressure of 0.1 mbar for 30 min and then allowed to equilibrate for 1 h. The sample then underwent evacuation after which a spectrum was collected. To probe the strength of acid sites, the samples were subsequently heated to 250, 350, and 450 °C, and spectra of residual pyridine were obtained at 150 °C. After the sample was removed, a 6.45 mm diameter wafer was punched out and weighed to normalize acid site concentrations. Spectra were integrated around 1540 and 1440 cm^{-1} to quantify the amount of pyridine adsorbed on Brønsted and Lewis acid sites, respectively. Molar extinction coefficients were taken from Tamura et al.[165]

These data were also used to group the Lewis acid sites on each catalyst into three general categories (weak, medium, and strong) based on their relative strengths. The number of acid sites in each group was calculated by choosing a temperature range and then subtracting the number of sites retaining pyridine at the higher temperature from the number of sites retaining pyridine at the lower temperature. Weak acid sites were assigned as the number of sites retaining pyridine up to 150 °C but not beyond 250 °C, medium sites as the number of sites retaining pyridine beyond 250 °C but not beyond 450 °C, and strong as the number of sites retaining pyridine above 450 °C.

P-value statistical significance tests and linear regression analysis were performed in Minitab for correlations between the density of weak, medium, strong, and medium + strong acid

sites to the rates of steady-state crotonaldehyde production during reaction tests for each catalyst. A p-value of 0.05 was chosen as the benchmark for statistical significance, and adjusted R^2 values were used for comparing the linear fit models.

3.2.3 Catalyst Evaluation

Catalyst performance was analyzed through steady state reactor experiments involving the aldol condensation of acetaldehyde (99.5%, Acros Organics) to crotonaldehyde. In a typical experiment, approximately 60 mg of catalyst sample was packed into a quartz reactor tube between two layers of quartz wool. Samples were pretreated in 36 sccm H_2 (99.999%, Airgas) at 350 °C for 1 h and purged in 36 sccm He (99.999%, Airgas) at 350°C for 30 min before cooling to 300 °C for reaction. The system was allowed to come to steady-state over 10 hours on stream, and reaction data were collected continuously using an online Agilent 7820A gas chromatograph (GC) with a DB-WAX polar column and flame ionization detector (FID). Comparisons were performed after 10 h on stream because the rate of deactivation had reached a low steady value for crotonaldehyde production at that timepoint (Figure B1B). Comparisons performed at an earlier timepoint (~2.5 hours onstream) exhibited similar trends (Figure B1A). For regeneration experiments, catalyst samples were pretreated normally and then allowed to react for 3-hour intervals before being exposed to a regeneration cycle. Each cycle consisted of either 36 sccm H_2 for 30 minutes at 350 °C or 36 sccm O_2 (99.994%, Airgas) followed by 36 sccm H_2 for 30 minutes each at 350 °C.

Aldol condensation performance was compared through the net rate of crotonaldehyde production. These “mass-time yields” are defined here as the molar flowrate of crotonaldehyde exiting the reactor, determined through online GC analysis, divided by the total mass of the catalyst. Crotonaldehyde may be consumed through further condensation reactions, however,

production of higher order condensation products was small (<20% of GC product area) for the differential conversions used in this study (<10%). All reaction rates discussed in the following sections of this study represent net reaction rates.

Turnover frequencies (TOFs) were calculated using the rate of crotonaldehyde production on the Al_2O_3-supported catalysts after 10 h on stream at 300°C. These values represent an average TOF across the length of the catalyst bed. The number of active sites was estimated as the mass normalized number of medium + strong acid sites present on each catalyst, as determined through pyridine FTIR experiments. The TOF was then calculated by dividing the overall reaction rate by the total number of medium + strong acid sites for each catalyst.

3.2.4 Temperature Programmed Oxidation

Spent catalyst samples were generated using the same conditions listed above for aldol condensation reaction testing (10 h on stream at 300 °C). Samples were then loaded into a separate reactor system with downstream Pfeiffer Prisma quadrupole mass spectrometer for analysis. Samples were purged in a stream of 1 sccm O_2 and 20 sccm He at room temperature for 30 minutes before the temperature was ramped to 700 °C at 10 °C/min. The quantity and reactivity of carbonaceous deposits on each sample were compared by analyzing signals associated with the desorption of CO (m/z = 28) and CO_2 (m/z = 44).

3.2.5 Catalyst Characterization

3.2.5.1 Thermogravimetric Analysis

A small aliquot of the spent sample (~20 mg) was loaded into a thermogravimetric analyzer (TGA, SDT-Q600 by TA) to quantify the carbonaceous deposition. The sample was stabilized at 30 °C for 10 min in 50 sccm of air to desorb potential physisorbed water. Then, the temperature was ramped to 750 °C at 10 °C min^{-1}. That temperature was held for 60 min.

3.2.5.2 Infrared Spectroscopy of Spent Catalysts

Attenuated total reflectance infrared spectroscopy (ATR-FTIR) was used to identify the moieties comprising the carbonaceous species on the catalyst. The IR spectra were recorded without any pretreatment, at room temperature using a Thermo Fisher Scientific Nicolet iS20 instrument equipped with a Smart iTR ATR sampling accessory with a single-reflection ZnSe crystal. The resolution used was 4 cm^{-1}, and 64 scans were recorded. The instrument was equipped with an MCT/A detector cooled at the liquid nitrogen temperature (-196 °C).

3.2.5.3 N_2 Physisorption

Brunauer–Emmett–Teller (BET) surface area measurements were carried out through N_2 physisorption on a Micromeritics 2720 ChemiSorb station. Samples were pretreated in 18 sccm of 30% N_2 in He at 250°C for 30 min before cooling to room temperature. Physisorption measurements were taken during continuous flow of 9 sccm of 30% N_2 in helium, and adsorption/desorption of the flowing N_2 was facilitated by submerging/removing the sample tube from a Dewar filled with liquid nitrogen. Adsorption and desorption cycles were performed three times for each sample to obtain error bars from triplicate measurements.

The nitrogen physisorption isotherms were measured at the liquid nitrogen temperature (-196 °C) using a Micromeritics ASAP 2020 physisorption analyzer. The catalysts were degassed at 200 °C for 4 h before measurement. The surface area and mesopore volume for each sample were calculated by using the BET method and BJH method, respectively.[166,167]

3.2.5.4 Electron Microscopy

The powder sample was dispersed in ethanol, then dropped on holy carbon coated Cu grids after being ultrasonicated for 5 minutes. A Hitachi HD2700 aberration-corrected scanning transmission electron microscope was used to record the high-angle annular dark-field (HAADF)

STEM images. The electron beam convergent angle α was 27 mrad and the HAADF detector collection angle β=70–370 mrad.

3.2.5.5 UV-VIS Diffuse Reflectance Spectroscopy

A Harrick Praying Mantis diffuse reflectance setup with high temperature reactor was used in tandem with ThermoFisher Evolution 300 UV/VIS spectrophotometer. Barium sulfate was used as the 100% transmittance baseline. Al_2O_3 was dehydrated at 450 °C for 1 h before being brought down to room temperature for measurement. The signal from Al_2O_3 was subtracted from the signals obtained for the supported catalysts. Each sample was first calcined in air and brought down to room temperature before reduction under the same temperature program. Tauc plots were generated and linear regions of the plot were fitted with a line of best fit where the x-intercept was taken as the bandgap value.

3.2.5.6 XANES

XANES was performed on beamline 9-3 at the Stanford Synchrotron Radiation Laboratory (SSRL) to determine the effect of H_2 treatment on the oxidation state of a 10Mo/Al_2O_3 sample. Experiments were performed at the Mo K-edge, and all energies were calibrated in reference to a Mo foil standard that was collected during each run and defined as 20000 eV. Edge energies were calculated as the maximum of the 1st derivative. Powder catalyst samples were packed into a capillary flow tube for in-situ analysis during reduction. XAS spectra were collected continually while the reactor tube was purged at room temperature in He for 10 min before ramping to 450 °C at 10 °C/min and being held at this temperature for 1 h. XANES spectra were processed and analyzed using Athena.[56]

3.2.6 Temperature Programmed Desorption

In each experiment, about 100 mg of 10Mo/Al_2O_3 was loaded into a quartz reactor tube between two layers of quartz wool. The sample was then pretreated in 36 sccm of either H_2 or O_2 at 450 °C for 1 hour and then purged in 36 sccm He at 450 °C for 30 minutes before being cooled down to room temperature. Samples were dosed using a stream of 9 sccm He passing through a Pyrex bubbler tube filled with 20 mL of acetaldehyde held at 1 °C and then over the catalyst bed for 30 min. Following dosing, samples were purged in 9 sccm He for approximately 8 hours at room temperature. Subsequently, samples were heated from room temperature to 700 °C at a rate of 10 °C/min. Desorption products were detected with a Pfeiffer Prisma quadrupole mass spectrometer downstream of the reactor.

3.3 Results

3.3.1 Activity and Stability of Supported Catalysts

The performance of Al_2O_3 and SiO_2 supported Mo catalysts with different Mo loadings was analyzed for the steady-state aldol condensation of acetaldehyde to crotonaldehyde. Rates of crotonaldehyde production after H_2 pretreatment and 10 hours on stream are shown in Figure 3.1A. Plots of conversion and crotonaldehyde yield for the same experiments are displayed in Figure B2. Complex product mixtures were produced over all catalysts, including small amounts of various C_4-C_8 condensation products (e.g., 2,4-hexadienal, 2-methyl-2-cyclopenten-1-one, and 2-methylbenzaldehyde) as well as light hydrocarbons from cracking reactions, but the selectivity to crotonaldehyde was high for all catalysts (>80% of GC FID product area) at the low conversions studied here (<10%). For a typical reaction experiment over 10Mo/Al_2O_3, the C_6 product 2-cyclopenten-1-one made up ~5% of the total GC product area, hexadiene made up ~3% of the total GC product area, 2-methyl benzaldehyde made up ~1% of the total product area, and light

hydrocarbons (including C_1 – C_4 compounds) made up ~1% of the total GC product area. Small quantities of other condensation products (totaling ~5% of the total GC product area) were also detected but were not individually quantified. Although crotonaldehyde underwent further condensation to higher products, the direct aldol condensation of acetaldehyde is the focus of this study and can be thought of as an intermediate within a larger reaction network. The presence of Mo generally increased the activity compared to the bare Al_2O_3 and SiO_2 supports, but the optimal weight loading varied. On the Al_2O_3 support, the samples with the lowest Mo loading ($1Mo/Al_2O_3$) exhibited the highest overall activity and catalytic efficiency per Mo site. The activity appeared to decline with increasing Mo loading, with the highest Mo loading sample ($20Mo/Al_2O_3$) demonstrating similar activity to the bare Al_2O_3 support. On the SiO_2 support, the activity of the catalysts increased monotonically with increasing Mo loading up to 10 wt.%. The trend in activity for the Mo/SiO_2 samples appeared to approach the activity of the Mo/Al_2O_3 samples, particularly when extrapolated to high Mo loadings. This suggests that at very high weight loadings, the activity of the catalyst is dominated by the MoO_x phase, and the interactions between catalyst and support become less important. When normalizing production of crotonaldehyde by mass of Mo rather than total catalyst mass (Figure B2), the SiO_2 supported samples displayed similar reaction rates regardless of the Mo loading. Interestingly, on the Al_2O_3 support, the low loading $1Mo/Al_2O_3$ catalyst demonstrated higher Mo-normalized activity than any of the other samples.

Each sample exhibited deactivation over the course of the 10 hours on stream, which can potentially be attributed to a variety of chemical, mechanical, and thermal degradation pathways.[168] One potential means of deactivation for the aldol condensation reaction is site poisoning through the build-up of strongly-bound carbonaceous species over the course of the

reaction. This hypothesis was tested by examining the activity of a $10Mo/Al_2O_3$ sample for the aldol condensation of acetaldehyde while performing oxidation-reduction regeneration cycles at regular 3 h intervals (Figure 3.1B). Each regeneration cycle restored the conversion of the sample, and the deactivation profiles between each cycle appeared to be nearly identical. When a similar experiment was carried out on another $10Mo/Al_2O_3$ sample using reduction-only regeneration cycles, the activity of the sample was not fully regenerated after each cycle (Figure B3). This result implies that some activity can be recovered through thermal desorption and reduction cycles, but an oxidizing environment is needed to fully remove carbonaceous deposits and completely regenerate the initial state of the catalyst surface.

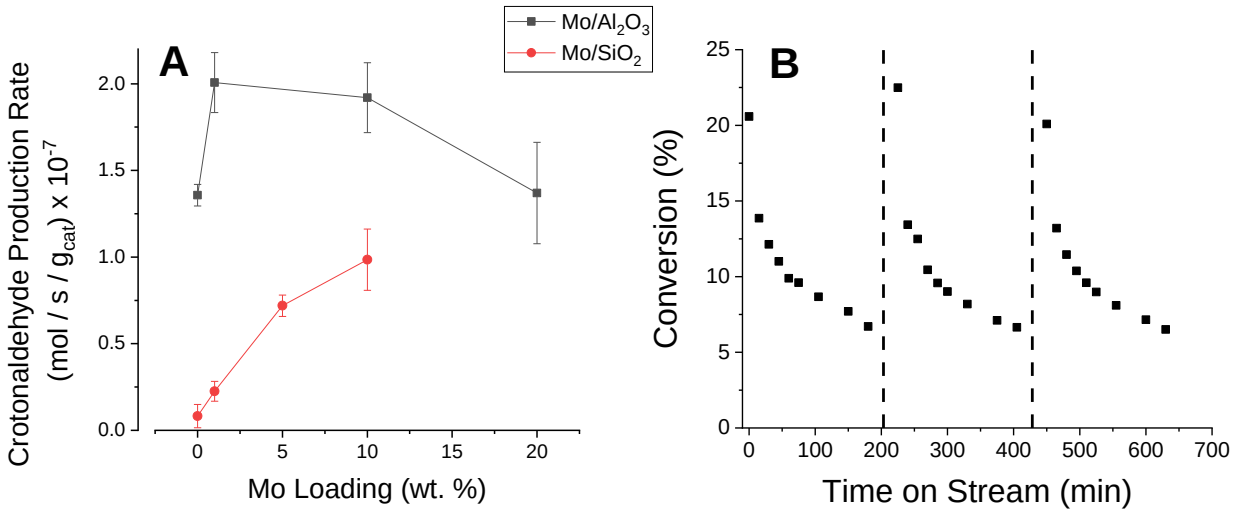

Figure 3.1 Summary of supported Mo catalyst performance. Mass normalized crotonaldehyde formation rate is plotted as a function of Mo loading (A) during the steady state reaction of acetaldehyde on various Mo-modified catalysts at WHSV = 1.4 hr^{-1} after pretreatment in 36 sccm H_2 at 350 °C for one hour and 10 hours reaction at 300 °C. Conversion plotted as a function of time on stream (B) for the aldol condensation of acetaldehyde at 300 °C on a $10Mo/Al_2O_3$ catalyst after pretreatment in H_2 at 350 °C for 1 h. Dotted lines represent regeneration cycles, which involved treatment in O_2 at 350°C for 30 min followed by H_2 at 350 °C for 30 min.

Carbonaceous build-up during reaction was characterized by measuring CO_2 (m/z = 44) evolution during TPO (Figure B4). The areas underneath the desorption profiles associated with both CO and CO_2 were calculated and used to compare the total amount of carbonaceous deposits

on each catalyst (Table B2). Bare SiO_2 showed very little build-up compared to the Al_2O_3 and $10Mo/Al_2O_3$ samples. However, modification of SiO_2 with Mo dramatically increased the amount of CO_2 produced during TPO. Overall, the amount of CO_2 produced by each sample during TPO appears to be correlated to the activity of the catalysts. This may suggest that both the density and efficiency of the active sites are intrinsically linked to the deactivation profile for a given catalyst.

The carbonaceous buildup was also evaluated and quantified by TGA of spent catalyst samples (Figure B5). The derivative of the weight profile was found to be in good agreement with the profiles obtained during TPO experiments reported in Figure B4. The carbonaceous deposits were quantified to be 4.4 wt%, 8.6 wt%, 11.5 wt% and 7.9 wt% for SiO_2, Al_2O_3, $10Mo/SiO_2$ and $10Mo/Al_2O_3$, respectively. Additionally, the composition of the carbonaceous deposits was characterized by ATR-FTIR spectroscopy (Figure B6). Bands at 1715 and 1668 cm^{-1} were detected for surface species on the SiO_2 and were attributed to C=O vibrations of acetaldehyde and crotonaldehyde, respectively.[139,169] The band at 1668 cm^{-1} was not observed on $10Mo/SiO_2$, while a shoulder at 1758 cm^{-1} was detected and attributed to a C=O mode most likely from acetaldehyde on a Mo center.[170] The surface species observed on Al_2O_3 and $10Mo/Al_2O_3$ were different from the ones observed on the SiO_2 supported samples. The two broad features at 1573 and 1450 cm^{-1} were attributed to acetates probably formed by the Tishchenko reaction.[171,172]

The differences in activity trends for Al_2O_3 and SiO_2 supported catalysts suggested that MoO_x-support interactions played an important role in the efficiency of the active site for the aldol condensation reaction. To better understand this phenomenon, a variety of characterization techniques were performed on these samples, and the results were compared to trends in catalyst activity.

3.3.2 Catalyst Structure Characterization

Catalyst surface area was determined through N_2 physisorption (Table 3.1). The bare SiO_2 support had the highest surface area, and deposition of Mo onto the SiO_2 surface reduced this surface area to roughly half of that of the bare support. A similar, large reduction in surface area due to Mo deposition on silica has been shown in other studies.[173,174] Modification of bare Al_2O_3 with Mo did not significantly impact the surface area, and both of these materials showed slightly lower surface areas than the Mo/SiO_2 catalyst.

Table 3.1 BET surface areas of Al_2O_3 and SiO_2 supported Mo catalysts calculated by N_2 physisorption experiments

Sample	*Specific Surface Area (m^2/g)*
Al_2O_3	81 ± 4
$10Mo/Al_2O_3$	81 ± 1
SiO_2	234 ± 10
$10Mo/SiO_2$	109 ± 7

The MoO_x dispersion was studied using transmission electron microscopy (TEM) and energy dispersive x-ray spectroscopy (EDS) (Figure 3.2). The $10Mo/SiO_2$ sample possessed larger MoO_x domains on larger uniform SiO_2 particles. The dispersion of MoO_x particles supported on Al_2O_3 varied depending on the weight loading of Mo (1, 10 or 20%). All samples had MoO_x distributed across the particles as shown in the EDS mapping. The $1Mo/Al_2O_3$ sample showed small, well dispersed particles on an almost atomic scale, while $20Mo/Al_2O_3$ had more agglomerated species present at a higher density. The $10Mo/Al_2O_3$ sample appeared to exhibit intermediate dispersion. Table 3.2 shows that the feature sizes of MoO_x species increased with increasing loading on the Al_2O_3 support. A monolayer coverage of Mo was present on the SiO_2 support of the $10Mo/SiO_2$ sample based on the EDS image. Particle size distributions are shown in Figure B7. Due to the monotonic nature of increasing conversion on Mo/SiO_2 catalysts and the

decreasing conversion on Mo/Al_2O_3, further characterization investigation was done for Mo/Al_2O_3 catalysts at different weight loadings.

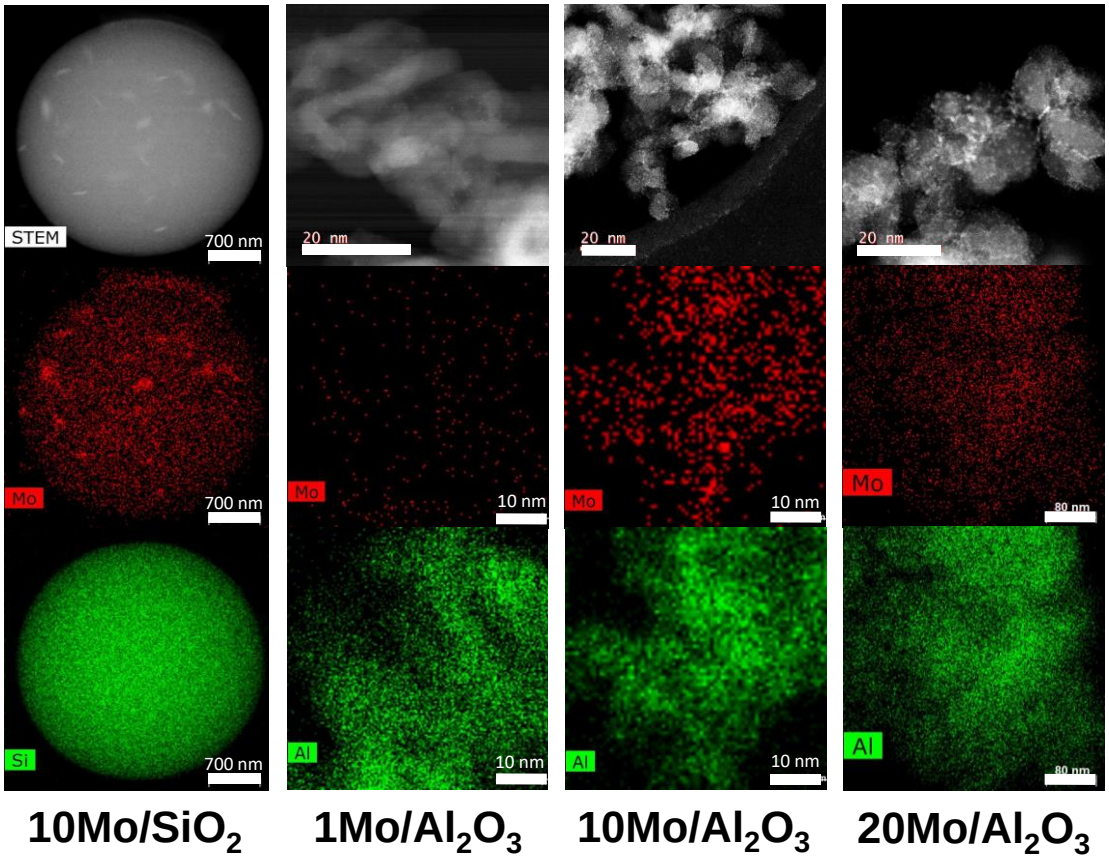

Figure 3.2 TEM and EDS Images of MoO_x supported on SiO_2 and supported on Al_2O_3 at various loadings

Table 3.2 Average particle size of MoO_x species based on TEM images

Sample	*Particle Size (nm)*
$1Mo/Al_2O_3$	0.8 ± 0.1
$10Mo/Al_2O_3$	1.2 ± 0.2
$20Mo/Al_2O_3$	1.5 ± 0.5

The effect of weight loading on the formation of catalytic sites was further investigated with UV-VIS diffuse reflectance spectroscopy to determine bandgaps for Mo/Al_2O_3 (Figure 3.3).

As shown by Chakrabarti and Wachs, lower bandgap values of Mo supported on Al_2O_3 indicate larger molybdenum clusters (> 1 nm) on the surface, and higher bandgaps translate to smaller dimeric and monomeric (< 1 nm) MoO_x species on the support.[175] As weight loading was increased, the bandgap fell, suggesting the particles were clustering with the average particle size increasing from 0.8 to 1.2 to 1.5 nm as weight loading increased from 1 to 10 to 20 wt% (Table 3.2). Interestingly, the reduction also decreased the bandgap, suggesting that either H_2 treatment caused sintering of the MoO_x particles or the oxidation state of Mo for each catalyst decreased.

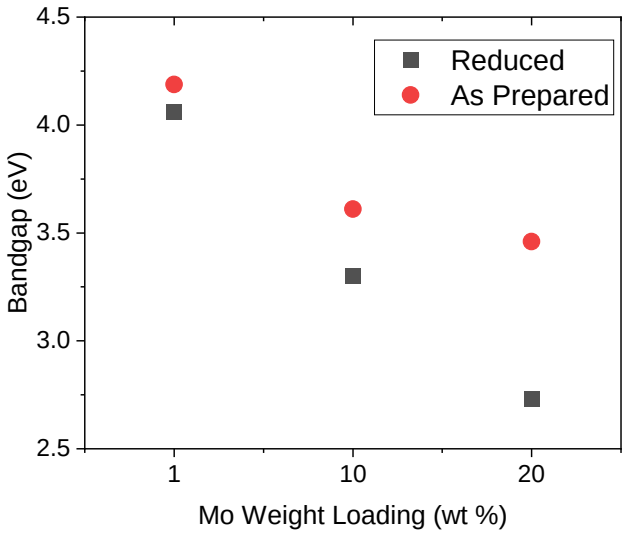

Figure 3.3 Bandgaps of different weight loadings of Mo/Al_2O_3 after reduction and as prepared after calcination.

3.3.3 Acid Site Characterization

Acid sites of the supported catalysts were quantitatively characterized by pyridine adsorption followed by FTIR spectroscopy (Figure 3.4). The concentrations of Lewis and Brønsted acid sites were measured before (Figure 3.4a, b) and after (Figure 3.4c, d) reduction of the catalyst at 450 °C for 1 h in hydrogen. After reduction, the concentrations of both Lewis and Brønsted acid sites were lower compared to the as-prepared samples, but the concentration of Lewis acid sites that retained pyridine at 450 °C was the same or higher for all supported materials.

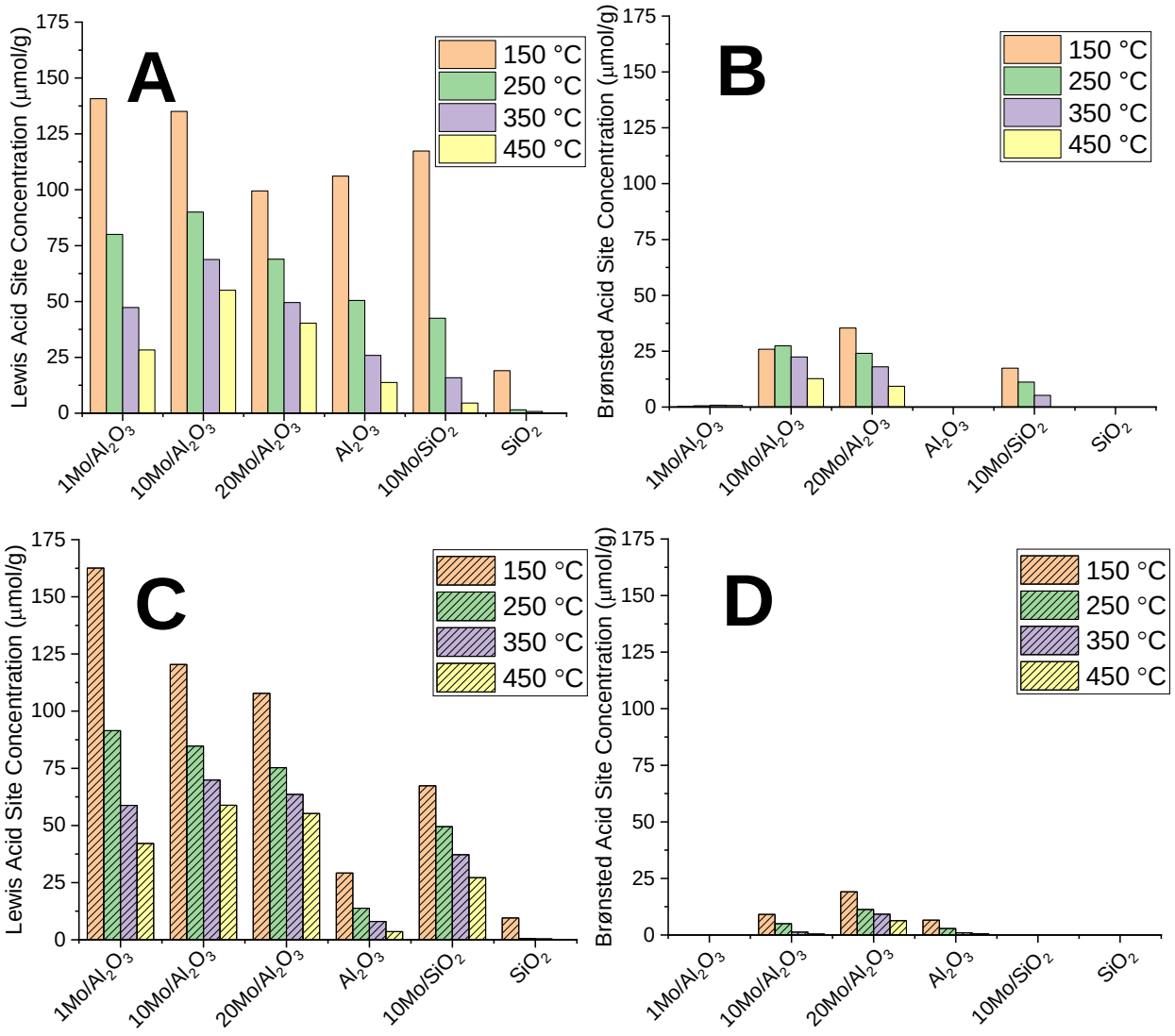

Figure 3.4 Lewis (A and C) and Brønsted (B and D) acid site concentration measured using pyridine transmission FTIR spectroscopy of molybdenum supported catalysts before (A and B) and after reduction (C and D).

The relative strengths of Lewis acid sites were estimated using the pyridine IR data shown in Figure 3.4. The density of Lewis acid sites on each catalyst was categorized into three desorption ranges (Figure 3.5), representing sites associated with relatively weak (150 °C - 250 °C), moderate (250 °C - 450 °C), and strong (450 °C and above) Lewis acid character. SiO_2 and $10Mo/SiO_2$ both showed a relatively high concentration of weak acid sites but contained very few if any strong Lewis acid sites. On the other hand, Al_2O_3 and $10Mo/Al_2O_3$ both contained a higher density of

strong acid sites than medium or weak sites. Modification of SiO_2 and Al_2O_3 with Mo produced catalysts with a higher overall density of acid sites, as well as a larger fraction of strong acid sites in both cases.

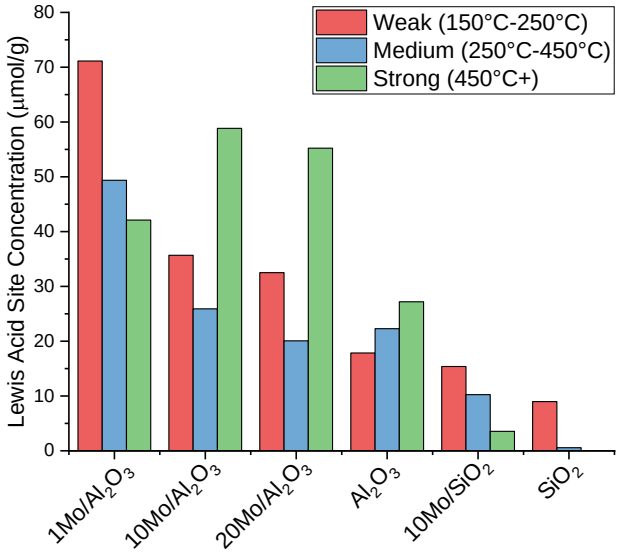

Figure 3.5 Density of Lewis acid sites desorbing pyridine within specific temperature ranges, calculated from data in Figure 3.4

Similar trends with respect to the strength of Lewis acid sites were observed using acetonitrile-d^3 (CD_3CN) adsorption followed by FTIR spectroscopy (Fig. S8). The peak associated with acetonitrile bound to LAS was found to be at a higher frequency on $10Mo/Al_2O_3$ (2320 cm^{-1}) compared to $10Mo/SiO_2$ (2310 cm^{-1}) before reduction, suggesting that the MoO_x sites on the Al_2O_3 support were stronger Lewis acids (Fig S8).[165] Peaks around 2273 cm^{-1} was assigned to surface hydroxyl groups, and peaks near 2111 cm^{-1} associated with physisorbed acetonitrile were also detected.[176,177] For the reduced samples, there was a blueshift from 2320 cm^{-1} (Figure B8A) to 2323 cm^{-1} (Figure B8B) indicating stronger Lewis acidity.

3.3.4 Effect of Pretreatment Conditions on Supported Mo Catalysts

The role of reduced MoO_x sites in the aldol condensation reaction was probed through a variety of temperature programmed characterization techniques. XANES spectra of the Mo K-edge were collected as the sample was resistively heated in flowing H_2 gas (Figure 3.6A) to determine the effect of reducing conditions on the Mo oxidation state. At room temperature, the Mo K-edge structure for the $10Mo/Al_2O_3$ sample closely resembled the MoO_3 standard. As the sample was heated, the pre-edge shoulder began to disappear, and the K-edge shifted to lower energies, indicating that reduction was occurring.

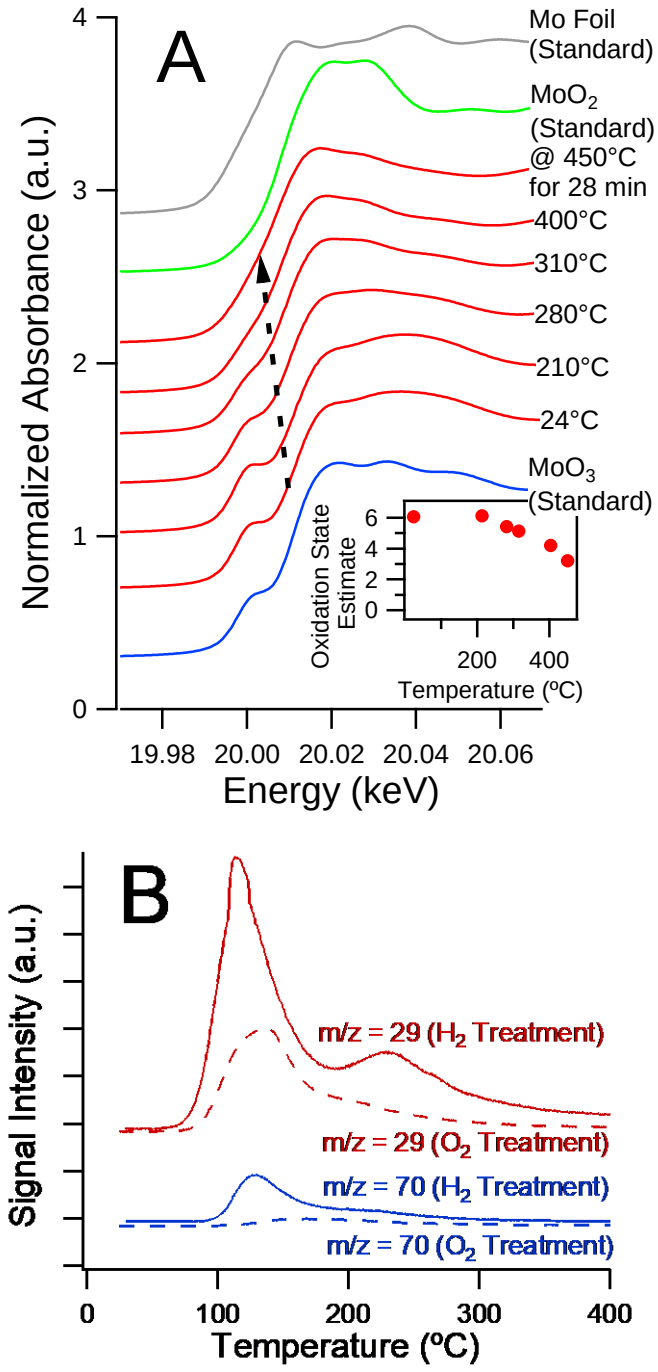

Figure 3.6 XANES spectra (A) and acetaldehyde TPD (B) characterization of the effect of H_2 pretreatments on $10Mo/Al_2O_3$. Mo K edge XANES spectra (A) collected during a temperature ramp in pure H_2 flow. Mo K edge XANES spectra of Mo foil, MoO_2, and MoO_3 standards are also plotted for comparison. Dashed line shows shifts in the adsorption edge energy as the temperature is ramped. Inset: estimated oxidation state of sample as a function of temperature. TPD profiles for acetaldehyde dosed on a $10Mo/Al_2O_3$ catalyst (B) after treatment with 36 sccm H_2 or O_2 at 450 °C for one hour.

For each XANES spectrum collected, the oxidation state of the $10Mo/Al_2O_3$ sample was estimated by comparing the Mo K-edge energy to a linear fit of the K-edge energies for the Mo foil, MoO_2, and MoO_3 standards (Figure B9). The calculated oxidation state of the sample as a function of the sample temperature is shown in the inset for Figure 3.6. As the sample was heated, the oxidation state steadily decreased, ultimately reaching a final value of approximately 3.2 after being held at 450 °C for several minutes. This result indicates that high temperature H_2 pretreatments are highly effective for reducing Mo clusters on supported Mo/Al_2O_3 catalysts. These reduced Mo sites may then act as Lewis acid sites for the aldol condensation reaction as discussed below.

The role of Mo reduction in the aldol condensation reaction was further probed through TPD of acetaldehyde on a $10Mo/Al_2O_3$ sample pretreated with H_2 or O_2 at high temperatures. The desorption traces for masses associated primarily with acetaldehyde (m/z = 29) and crotonaldehyde (m/z = 70) were plotted as a function of temperature (Figure 3.6B). Crotonaldehyde was the main reaction product with a desorption temperature around 120 °C on the H_2 treated surface. On the O_2 treated catalyst, crotonaldehyde desorption shifted to slightly higher temperatures, and the peak intensity was significantly smaller. The ratio of the peak areas associated with crotonaldehyde formation (m/z = 70) on the H_2 and O_2 treated catalyst was approximately a factor of 4 higher, indicating that more crotonaldehyde was formed after H_2 pretreatment compared to the O_2 treatment. Mass fragments associated with other reaction products were also detected (m/z = 54, m/z = 73) at higher temperatures (~230 °C), but the identity of these side products was not determined. The increased desorption signal intensity for both reactants (acetaldehyde) and products (crotonaldehyde), as well as the lower temperature for product formation, suggested that

the reduced MoO_x clusters on the surface of the catalyst were able to bind and activate more acetaldehyde for the aldol condensation reaction.

The effect of pretreatment conditions on the aldol condensation reaction was also analyzed using a packed bed reactor with continuous acetaldehyde feed under steady state conditions. A comparison of the rates of crotonaldehyde production after pretreatment with H_2 or O_2 and 10 hours of reaction on stream at 300 °C is shown in Figure B10. Unlike the TPD results, the steady state reactor data showed no significant difference in aldol condensation activity between the two pretreatments. This suggests that acetaldehyde can also participate in redox reactions with the catalysts, so that the surface structure of the catalysts may equilibrate at an oxidation state that is primarily determined by the reaction conditions, rather than the pretreatment conditions.

3.4 Discussion

Molybdenum oxide (MoO_x) based catalysts have been shown to effectively catalyze various reactions such as olefin metathesis, ethane dehydrogenation and lignin hydrogenolysis.[156,178,179] The active MoO_x phase in these catalysts is typically deposited on high surface area supports due to the low surface area of bulk molybdenum oxides.[67] For many of these reactions, the active phase of MoO_x is a partially reduced Mo center, and as such, the supported MoO_x catalysts are typically activated through reductive pretreatments or reaction conditions. We have previously shown that the reduction of bulk MoO_3 to a lower oxidation state facilitated greater adsorption of ethanol and acetaldehyde and activated these molecules for the aldol condensation reaction.[154] This effect was attributed to the creation of coordinatively unsaturated sites on the MoO_x surface via oxygen vacancies which can then activate oxygen-containing compounds for the aldol reaction. In this study, we deposited MoO_x on high surface area oxides (SiO_2 and Al_2O_3)

and pretreated them under different gases (H_2 and O_2) to understand the role of reductive pretreatments and reaction conditions on the nature of supported MoO_x catalysts. XANES spectra of $10Mo/Al_2O_3$ during heating in H_2 flow (Figure 3.6A) demonstrated that high temperature H_2 treatments can reduce surface Mo clusters to suboxide states. Furthermore, TPD of acetaldehyde on H_2 and O_2 treated $10Mo/Al_2O_3$ samples (Figure 3.6B) showed that the reduced catalyst was able to adsorb and activate a greater quantity of acetaldehyde and convert these molecules via the aldol condensation reaction. These results indicate that reduced Mo sites on supported catalysts, in the form of oxygen vacancies, are able to assist in the adsorption and activation of light oxygenates, similar to what we have seen previously on bulk molybdenum oxides.[154] Similarly, Harlin et al. demonstrated that reduced Mo centers (oxidation state ~4.3) in Mo/Al_2O_3 produced during reductive pretreatments exhibited increased conversion for n-butane dehydrogenation.[158] However, in this study, steady state reactor comparisons of a $10Mo/Al_2O_3$ sample showed no difference in the rate of acetaldehyde condensation to crotonaldehyde after pretreatments in H_2 or O_2 and 10 hours of reaction on stream (Figure B10). This indicates that the structure of the catalyst may equilibrate under reaction conditions regardless of the pretreatment. Similarly, it has been observed for m-cresol hydrodeoxygenation using bulk MoO_3 that prereduction in H_2 has a larger effect on the initial induction period rather than the steady state conversion.[180] The aldol condensation reaction also evolves water, which may be involved in transforming the catalyst surface structure after multiple turnovers. As a result, while pretreatment conditions may have a significant impact on the initial reactivity of the catalyst surface, the reaction process conditions appear to govern the redox state and ultimately the activity of the catalyst under steady-state conditions.

Dispersion of MoO_x particles varied depending on the weight loading and support. Higher dispersion of MoO_x on the catalyst supports led to more efficient use of MoO_x. On the Al_2O_3 support, as weight loading increased, the average particle size also increased (Table 3.2). Interestingly, the same weight loading (10 wt.%) of Mo on Al_2O_3 and SiO_2 resulted in different average particle sizes, as seen in the TEM and EDS images (Figure 3.2). MoO_x is expected to exhibit a weaker interaction with SiO_2 compared to Al_2O_3. A comparison of the structure of these materials has previously shown that crystallization of Mo oxides and poor dispersion occurs on SiO_2 due to weaker Mo-support interactions during impregnation.[181] This is consistent with the particles size within this study. Chakrabarti and Wachs demonstrated that MoO_x supported on Al_2O_3 was anchored as isolated and oligomeric species on basic and surface hydroxyl (OH) sites of the Al_2O_3 support.[175] Overall, particle size characterization in this study as well as literature reports have demonstrated that the strength of Mo-support interactions tends to govern particle size and dispersion for Mo/Al_2O_3 and Mo/SiO_2 catalysts.

We observed that weight loading strongly influences aldol condensation activity and that LAS concentration correlates with this activity. The maximum aldol condensation activity was observed for the sample with the lowest Mo loading – $1Mo/Al_2O_3$. The concentration of LAS on the $1Mo/Al_2O_3$ sample was higher compared to samples with higher weight loadings (Figure 3.4). Thus, highly dispersed oligomeric MoO_x particles seen at low weight loadings are more acidic and contain a higher density of active sites than larger MoO_x agglomerates. This can also affect the steric accessibility of the active site. Prior characterization studies of MoO_3/Al_2O_3 catalysts have shown that the coordination environment of Mo tends to change with MoO_x loading. At low MoO_x loadings, the primary Mo surface configuration has been identified as a tetrahedrally coordinated, isolated dioxo $(O=)_2MoO_2$ species. As the weight loading increases, a higher fraction of

oligomeric mono-oxo $O{=}MoO_4$ species are present, and at high loadings the surface is dominated by crystalline MoO_3 in a distorted octahedral structure.[175,182,183] Both isolated and oligomeric MoO_x species were observed at low and high loadings, as indicated by the bandgaps reported in Figure 3.3. In general, Mo coordination tends to increase with increasing weight loading, from tetrahedral species at low loadings to octahedral crystals at very high loadings. As a result, the Lewis acidic, cationic Mo active site would exhibit a more "open" tetrahedral coordination environment at low loadings, thereby facilitating the accessibility of carbonyl adsorption and ultimately resulting in a higher rate of acetaldehyde condensation. This effect supports the observation that samples with the lowest Mo loading ($1Mo/Al_2O_3$) demonstrated the highest rate of aldol condensation activity (Figure 3.1A).

Another important factor to highlight is the acidity of the support. Since SiO_2 does not possess Lewis acidity (Figure 3.4), increasing MoO_x loading does not block any preexisting active sites. In contrast, the Al_2O_3 support already contains significant Lewis acidity, so blocking Al active sites with MoO_x species will cause a decrease in overall conversion, unless the new MoO_x sites are more efficient for aldol condensation than the bare Al_2O_3. Due to this effect, increasing the MoO_x loading generally tends to drive the conversion on a SiO_2 support up and the conversion on an Al_2O_3 support down (Figure 3.1A). At very high MoO_x loadings we expect that both supports will approach a similar conversion as the surface becomes completely covered by layers of MoO_x, and the interaction with the support becomes less important. When production of crotonaldehyde was normalized to the mass of Mo (Figure B2), the $1Mo/Al_2O_3$ sample exhibited a high value compared to all other samples, but this observation did not account for the existing active sites on bare Al_2O_3. The addition of Mo can therefore be thought of as an enhancement to an already active catalyst.

Acid site strength was considered as a descriptor for aldol condensation on metal oxide catalysts. Several factors previously discussed may influence this Lewis acid strength, such as the geometry of the MoO_x particles, the particle size, the oxidation state under reaction conditions, and interactions with the support. Saraeian et al. demonstrated using NH_3-TPD that as the weight loading of MoO_x increased on an Al_2O_3 support, the concentration of strong acid sites decreased, and the concentration of weak/medium acid sites increased.[184] They also noticed that formation of condensation products from aromatics was highest when stronger LAS were present (lower MoO_x loadings). In the present study, we compared the acetaldehyde steady state aldol condensation activity of a variety of supported Mo catalysts (Figure 3.1A) to their relative acid site strength and density as measured by pyridine FTIR (Figure 3.5). Assuming a P-value of 0.05 for significance, we tested the correlations between the density of weak (Figure B11A), medium (Figure B11B), strong (Figure B11C), and medium + strong (Figure 3.7) acid sites on each catalyst to their crotonaldehyde production rate. Using this analysis, weak acid sites did not show a significant correlation to aldol condensation activity, potentially indicating that weak sites are generally unable to activate carbonyls for aldol addition. Medium, strong, and medium + strong acid sites all demonstrated significant correlations to the crotonaldehyde formation rate, but a linear regression analysis assigned the highest adjusted R^2 value to the medium + strong acid sites combined (Figure 3.7). Assuming medium and strong acid sites are the primary active sites for the aldol reaction, the turnover frequency (TOF) for the production of crotonaldehyde over Al_2O_3-supported samples was calculated to be $2.3\pm0.4 \times 10^{-3}$ s^{-1}. This value is similar to the TOFs reported by Rekoske and Barteau for the consumption of acetaldehyde over anatase TiO_2[185] and Flaherty and coworkers for the production of C_{4+} products from acetaldehyde/ethanol mixtures over anatase TiO_2,[151] albeit with some differences in reaction conditions. Based on these results, we conclude

that Lewis acid site strength is essential for predicting catalyst performance in the aldol condensation reaction, and acid sites of at least moderate acid strength are needed to activate acetaldehyde for this reaction.

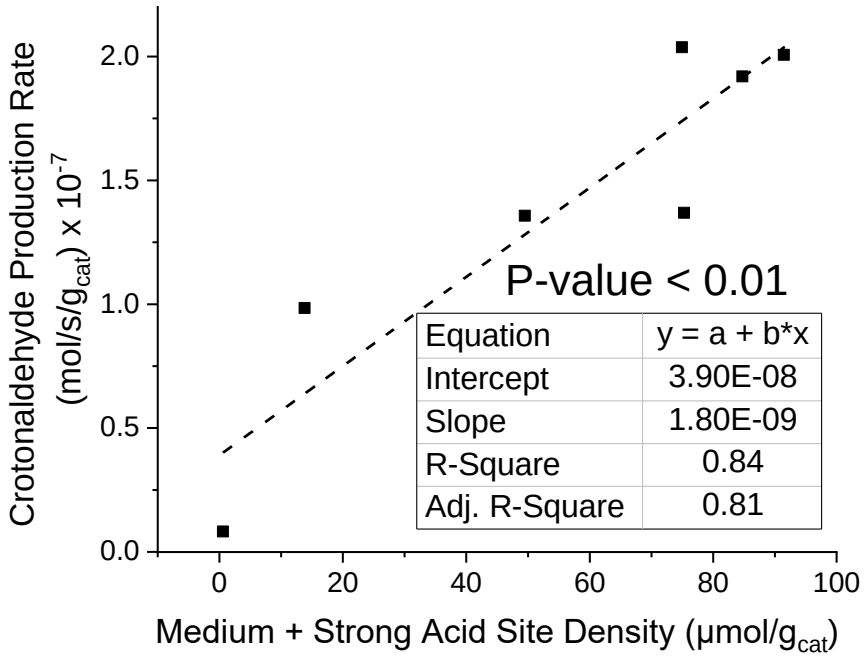

Figure 3.7 Crotonaldehyde production rate from acetaldehyde plotted as a function of medium + strong acid site density for a series of Mo/Al2O3 and Mo/SiO2 catalysts. The calculated P-value and R2 value for a linear correlation between these two variables are displayed on the chart

Coking and deactivation during reaction can be influenced by a variety of different factors, including microporosity, high temperatures and high hydrocarbon pressure.[186] We propose that high concentration of strong Lewis acidic sites is the main factor responsible for the deactivation of our samples. Catalysts with a high density of Lewis acid active sites tend to have higher conversions, but the increased coverage of reactive intermediates on the surface may also increase the probability for coupling reactions to create heavier oxygenates that block active sites. Additionally, strongly Lewis acidic active sites may bind reaction products more strongly, leading to a higher probability of creating heavy, irreversibly bound products that poison the acid site. For

example, the 10Mo/Al_2O_3 sample had stronger LAS than 10Mo/SiO_2 as evidenced by CD_3CN and pyridine FTIR measurements (Figures S8 and 5), and subsequently, the spent catalyst sample displayed a larger CO_2 desorption peak at a higher temperature during TPO (Figure B4). This result may suggest that a Sabatier optimum in Lewis acid site strength exists for the aldol condensation reaction, where high conversion is sacrificed for resistance to carbonaceous buildup. Likewise, catalyst deactivation may simply be controlled by the number of active sites on the surface, which would ultimately manifest in a similar tradeoff between catalyst activity and resistance to deactivation. Overall, our results demonstrate that catalysts with a high density of LAS (Figure 3.4) tend to buildup significant coke deposits (Figure B4) and deactivate substantially over the course of the reaction (Figure B1B). However, these effects can be mitigated through regular oxidation-reduction cycles (Figure 3.1B).

3.5 Conclusion

Both Al_2O_3- and SiO_2-supported MoO_x catalysts are active for aldol condensation of acetaldehyde to crotonaldehyde, but interactions between MoO_x and the SiO_2 and Al_2O_3 supports used in this study are fundamentally different. Dispersion of MoO_x is higher and more uniform on the Al_2O_3 support than the SiO_2 support due to a stronger MoO_x-support interaction. Trends in catalytic activity are also qualitatively different for the SiO_2 and Al_2O_3 supported catalysts. For Al_2O_3-catalysts, the activity is highest at low Mo loadings, indicating significant beneficial particle-support interactions. As the MoO_x loading increases, the aldol condensation activity decreases toward the activity of the bare Al_2O_3 support. On SiO_2, however, the activity increases monotonically with Mo loading, indicating minimal support-particle interactions. Linear regression analysis of aldol condensation activity and pyridine FTIR reveals that the density of medium/strong acid sites are highly correlated with the rate of crotonaldehyde formation from

acetaldehyde. Although the redox state of MoO_x significantly influences the barriers and yields for aldol condensation of acetaldehyde during temperature-programmed studies, under steady-state conditions, the redox character of supported MoO_x catalysts appears to be controlled primarily by the reaction conditions, since use of oxidative versus reducing pretreatments had no measurable effect on activity.

Chapter 4 Elucidating Surface Interactions of C4 Polyoxygenates with Solid Lewis Acid Sites

4.1 Introduction

Chemicals derived from lignocellulosic biomass have the potential to replace current petroleum derived platform chemicals.[32] In 2020, about 12 % of energy consumed in the US was from renewable resources with about 40 % coming from biomass.[8] While this shows promise, switching to a fully sustainable biorefinery will require significant specialized design such as choice of catalyst and producing valuables chemicals from high oxygen content reactants. Solid Lewis acid catalysts have been studied extensively for biomass upgrading reactions.[187] One reaction in particular that can be used for transformation of biomass derived chemicals is the (retro-) aldol condensation reaction in which C-C bonds can be broken/formed. This work will focus on catalyzing the (retro-) aldol condensation reaction of C4 oxygenated compounds over solid Lewis acid catalysts with an emphasis on the surface interactions and reaction of the compounds with the catalyst surface.

Studying the surface interactions of polyoxgenated compounds with solid Lewis acid sites provides critical information for understanding how certain reaction pathways proceed. Two oxygenated compounds will be used as probe molecules, 4-hydroxy-2-butanone (4H2B) and 3-hydroxybutanal (3HB) and are shown in Figure 4.1. 4H2B is an intermediate fine chemical used for manufacturing important chemicals like methyl vinyl ketone (MVK) and can be produced through aldolization of formaldehyde with acetone.[188] 3HB is typically formed as an intermediate from aldolization of acetaldehyde before undergoing retro-Michael dehydration to crotonaldehyde.[189] This makes it an ideal candidate to study for retro-aldol condensation (RAC) to observe whether acetaldehyde forms. Additionally, these compounds are also worthwhile to

investigate because they each contain two different oxygenated functional groups (a ketone and hydroxyl for 4H2B; aldehyde and hydroxyl for 3HB). By introducing compounds with dual oxygen functional groups, adsorption configuration can be determined (monodentate vs bidentate) and serve as a knowledge base for understanding surface interactions of other polyoxygenated compounds.

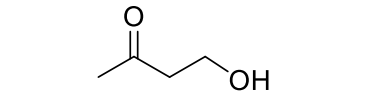

4-hydroxy-2-butanone (4H2B)

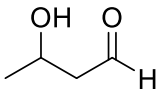

3-hydroxybutanal (3HB)

Figure 4.1 Chemical structures of 4-hydroxy-2-butanone and 3-hydroxybutanal

The following metal oxides will be used in this study: γ-Al_2O_3, CeO_2, Nb_2O_5, and TiO_2. These materials all possess varying degrees of Lewis acidity and some basicity and Bronsted acidity. By focusing on a diverse group of materials, general trends can be made and applied to other catalytic systems. γ-Al_2O_3 is a primarily Lewis acidic catalyst that possess various Al oxidation states (Al^{3+}, Al^{4+}, Al^{5+}) which creates site heterogeneity.[190] Due to this, it has been investigated extensively for alcohol dehydration[191,192] and alkane dehydrogenation.[193,194] Aldol condensation of acetone has been spectroscopically observed on bare γ-Al_2O_3.[195] This provides motivation to study γ-Al_2O_3 for RAC or other relevant reactions. CeO_2 has a high oxygen storage capacity, which allows it to replenish oxygen vacancies easily.[196] This means surface lattice oxygen can become active sites and facilitate base catalyzed reactions. Bare CeO_2 has not been studied before as a catalyst for biomass relevant reactions but has been studied as a support.[197,198] One study found that resistance to formation of carbonaceous deposits on a Ni/CeO_2/Al_2O_3 catalyst

during glucose gasification was mainly due to lattice oxygen species from the CeO_2 surface.[198] This makes CeO_2 an attractive material to study for condensation reactions where heavy carbonaceous species are prone to form. Nb_2O_5 has been studied for aldol condensation of furans, and it was shown that Nb_2O_5 has a strong ability to activate carbonyl moieties and form surface enolates.[199] In addition to this capability, Nb_2O_5 is the only one of the four catalysts in the study that has significant Bronsted acidity present making it interesting to study the bifunctional nature of Lewis and Bronsted acid sites. TiO_2 has been extensively studied for aldol condensation of many smaller (C2, C3) oxygenates.[151,200–202] However, RAC has only been studied for larger molecules like glucose with TiO_2.[203] Using an intermediate sized C4 molecule will serve as a good system to see if one or both reactions can occur on the surface.

This study will invoke *in-situ* transmission Fourier Transformed Infrared Spectroscopy (FTIR) as the main technique for studying the formation of key species on the catalytic surfaces. Our group has previously used this technique for studying the adsorption of glycerol on Nb_2O_5 where it was demonstrated that multidentate glycerol form and undergo dehydration to hydroxyacetone on the Nb_2O_5 surface when high densities of Lewis acid sites (LAS) are present.[99] Other *in-situ* FTIR studies include monitoring Ga speciation at different loadings on Si/Al ratio H-ZSM-5 catalysts[204] and discriminating between spectator species and reactive intermediates by combining *in-situ* FTIR with mass spectrometry.[205] Both studies reveal what is occurring to the state of the catalyst surface under various conditions. This study will fundamentally be doing the same but will instead determine how certain moieties are affected by adsorption on the different catalysts.

In this study, we use ultra-high vacuum (UHV) FTIR to monitor the surface species that form when 4H2B and 3HB are introduced and stabilized on the surface of γ-Al_2O_3, CeO_2, Nb_2O_5,

and TiO_2. Temperature programmed desorption (TPD) will be used after initial adsorption to monitor which functional groups remain and whether new groups form at higher temperatures.

4.2 Methodology

4.2.1 Materials

γ-Al_2O_3 was purchased from Alfa Aesar (99.97% metals basis). Nb_2O_5 was purchased from CBMM International. For CeO_2 synthesis, cerium nitrate (Sigma-Aldrich $Ce(NO_3)_3 \cdot 6H_2O$, 99.999% trace metals basis) was dissolved in deionized water (DI water), and the solution was added dropwise to an ammonium hydroxide solution (ACS reagent, 28.0-30.8 NH_3 basis, Sigma-Aldrich). The deposition was first filtered, and then dried in an oven at 110 °C overnight. TiO_2 was purchased from Evonik (>99%).

4.2.2 FTIR Experiments

FTIR spectroscopy experiments were conducted using ThermoFisher Scientific Nicolet 8700 spectrometer equipped with a liquid nitrogen cooled MCT/A detector. All spectra were collected using the ThermoFisher Scientific software Omnic. The collected spectra were averaged over 64 scans at a resolution of 2 cm^{-1} and an optical velocity of 1.868. An empty cell background was collected using these conditions before samples were loaded for each respective experiment. The sample chamber was equipped with an ultra-high vacuum setup, a diagram for the sample chamber and cell is shown in the SI. Catalyst pellets were made using a hydraulic press after coating a stainless steel anvil with catalyst powder and placing an identical anvil and piston on top. The samples were then loaded to the sample holder and outgassed to 10^{-5} mbar for 20 min at room temperature. The temperature was then raised to 450 ºC and held for 1 h. The sample was then brought down with spectra collected at 450, 350, 250, 150 and 50 ºC to serve as the spectra to be used for subtraction of the catalysts at those temperatures. The two model compound reagents

used in this study, 4-hydroxy-2-butanone (Sigma Aldrich 95%) and 3-hydroxybutanal (Alfa Chemistry, Technical grade), were introduced to the activated catalyst at about 0.3 mbar and allowed to equilibrate at this pressure for 20 min while held at 50 ºC. Afterwards, the sample was outgassed again to 10^{-5} mbar for 20 min before raising the temperature. Each temperature was held for 20 minutes.

Pyridine IR experiments were done using a ThermoFisher Scientific Nicolet iS10 spectrometer equipped with a liquid nitrogen cooled MCT/A detector. Samples were prepared exactly like in the previous section. Instead, after activation, the sample was brought to 150 ºC where a background was collected, and then 0.1 mbar of pyridine (Sigma Aldrich 99.9% HPLC) was dosed to the chamber for 30 min and allowed to equilibrate for 1 h. The sample was then outgassed to 10^{-5} mbar for 1 h before a spectra was collected. The sample subsequently heated to 150, 250, 350, and 450 °C with spectra collected at 150 °C under vacuum. The pellet was then removed, and a 6.35 mm punch-out of the pellet was massed to use for normalizing concentrations to catalyst mass. Peaks at 1440 and 1540 cm^{-1} were integrated for Lewis and Brønsted acid sites respectively with molar extinctions coefficients coming from Tamura.[165]

4.3 Results and Discussion

4.3.1 Acid Site Quantification

Figure 4.2 shows the concentration of Lewis and Brønsted acid sites at various temperatures. TiO_2 had the highest concentration of LAS at temperatures except 450 °C where Nb_2O_5 had an almost identical concentration. CeO_2 had the lowest concentration of LAS of all catalysts measured. Nb_2O_5 had the only significant concentration of BAS, with pyridine being detected up to 450 °C. This makes Nb_2O_5 the only catalyst studied with both LA and BA character.

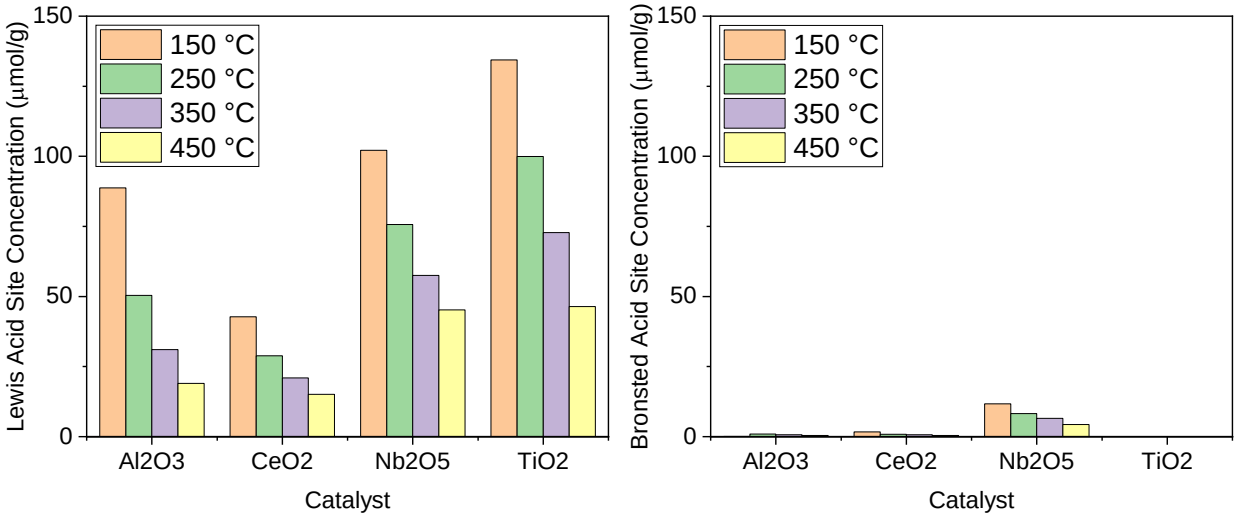

Figure 4.2 Lewis (left) and Brønsted (right) acid site concentration of catalysts studied using pyridine adsorption followed by FTIR spectroscopy.

4.3.2 Adsorption of 4-hydroxy-2-butanone

Figure 4.3 shows the IR spectrum of 4H2B adsorbed on γ-Al_2O_3. There were two negative peaks seen at 3769, 3729 and 3679 cm^{-1} which are most like from interactions of the adsorbate(s) with the surface hydroxyls.[193] There were also two prominent peaks at 2931 and 2871 cm^{-1} due to the $\nu_{as}(CH_3)$ and $\nu_s(CH_3)$ of the methyl group from 4H2B. The presence of these up to 450 °C indicates this group was strongly adsorbed. The strong ν(C=O) peak at 1699 cm^{-1} greatly decreased in intensity as temperature increased. This peak was from the ketone of 4H2B adsorbed on the LAS, a decrease in 30 cm^{-1} from the gas phase equivalent of the ν(C=O) of 4H2B. The peak at 1650 cm^{-1} was the ν(C=C) of a vinylic olefin, formed from dehydration of 4H2B to MVK. A pair of peaks at 1606 and 1502 cm^{-1} began appearing around 250 °C and were due to aromatics forming on the surface. There were two peaks at 1439 and 1361 cm^{-1} which decreased in intensity as temperature increased but remained at 450 °C and were due to the $\delta_{as}(CH_3)$ and $\delta_s(CH_3)$ respectively. Finally, there were two small peaks at 1251 and 1176 cm^{-1} due to a ω(CH) from the vinylic carbon formed in MVK and a ν(C-O) from a secondary alcohol formed of enolization of

the original keto group. Interestingly, there was no primary alcohol (found between 1100-1000 cm^{-1}) detected, indicating the 4H2B immediately undergoes a dehydration step at 50 °C. This is very plausible due to the high activity for alcohol dehydration that γ-Al_2O_3 promotes.

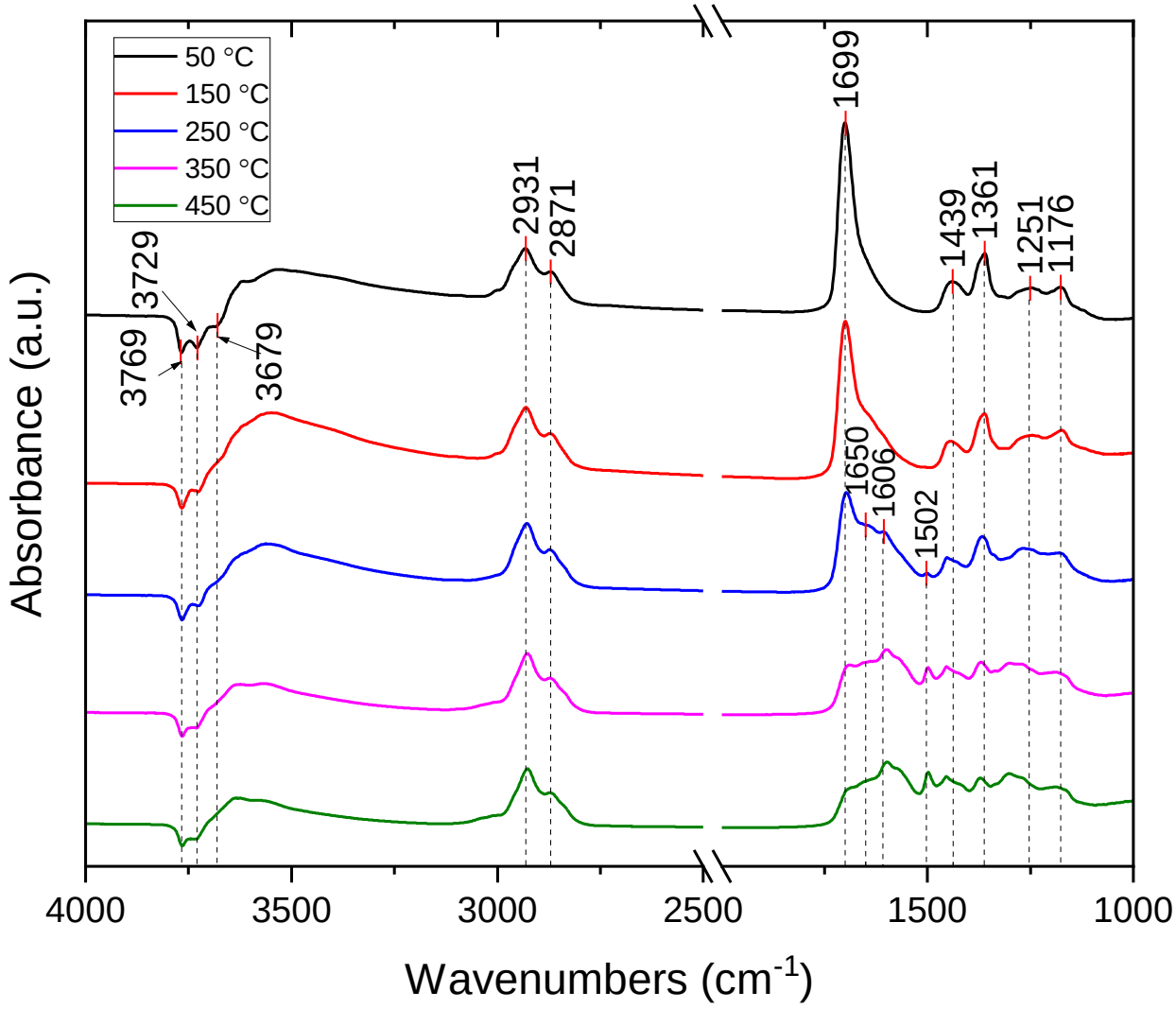

Figure 4.3 FTIR spectra of 4H2B on γ-Al_2O_3 followed by TPD

In the Figure 4.4, the adsorption of 4H2B on Nb_2O_5 is displayed. Negative peaks at 3709 and 3656 cm^{-1} arose from interactions of the adsorbate with the BAS inherent to Nb_2O_5. A peak at 3004 cm^{-1} was observed initially at 50 °C then decreased entirely at 150 °C. There were also two prominent peaks at 2931 and 2871 cm^{-1} due to the $\nu_{as}(CH_3)$ and $\nu_s(CH_3)$ of the methyl group from

4H2B. A peak at 2722 cm^{-1} initially formed and then was completely gone 250 °C. This indicates formation of an aldehyde, most likely from an isomerization of 4H2B to 3HB but the amount detected suggests this was formed in small amounts. This was also supported by the presence of the peak at 1172 cm^{-1} which was due to a secondary alcohol. The peak at 1715 cm^{-1} was due to the ν(C=O) from the ketone interacting with the BAS. This same group interacting with the LAS (Nb atom) was observed at 1673 cm^{-1}. The difference between the two adsorbed sites suggests that carbonyls interact more strongly with LAS than BAS. Interestingly, the ketone adsorbed onto the BAS desorbed almost entirely compared to the LAS at higher temperatures. This again suggests the LAS has a stronger interaction with the carbonyl then the BAS. The peak at 1557 cm^{-1} increased in intensity during the TPD. This mode was from the enolate formed from acetone which has been observed from acetone adsorption on solid LAS before.[28] The formation of acetone is plausible because 4H2B can undergo RAC to form acetone and formaldehyde. Formaldehyde would not be able to stay adsorbed onto the surface at such high temperature making it challenging to observe. The peak at 1085 cm^{-1} was due to the ν(C-O) of the primary alcohol of 4H2B which remains until 350 °C. The dehydration of 4H2B to MVK resulted in the decrease in the intensity of this mode with a shoulder at 1641 cm^{-1} increasing from the ν(C=C) of MVK.

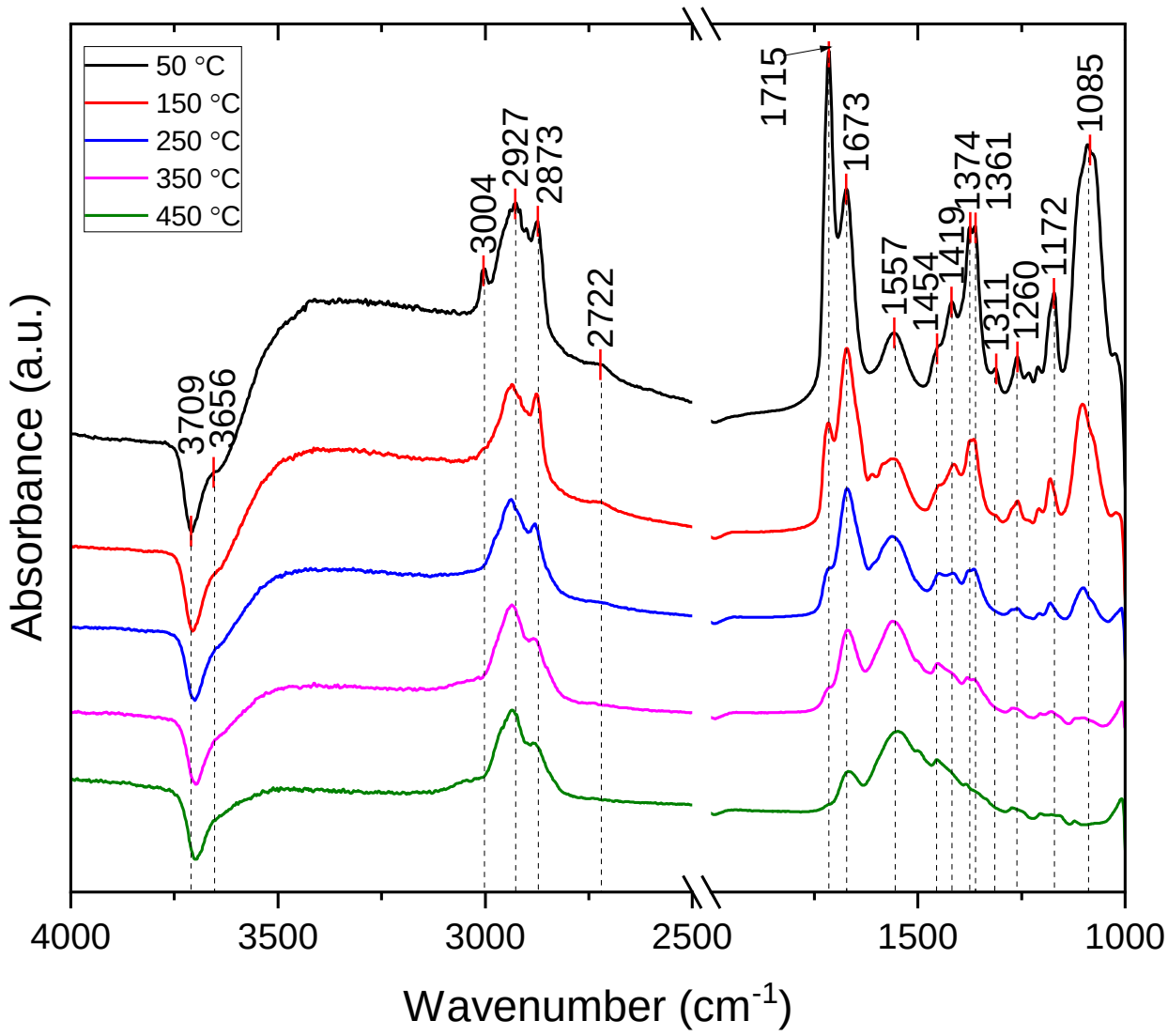

Figure 4.4 FTIR spectra of 4H2B on Nb_2O_5 followed by TPD

Figure 4.5 shows the IR spectrum of 4H2B adsorbed on CeO_2. There were three peaks at 3711, 3689, and 3669 cm^{-1} that all disappeared at 350 °C, which were from the ν(OH) of 4H2B. Peaks at 2965, 2941, 2922, 2868 cm^{-1} were from the $\nu_{as}(CH_3)$, $\nu_{as}(CH_2)$ and $\nu_s(CH_3)$ and $\nu_s(CH_2)$ respectively. This suggests both the CH_2 and CH_3 groups from 4H2B remained and desorbed at 350 °C. At 50 °C, the ν(C=O) peak was 1686 cm^{-1} and was from the ketone of 4H2B, a difference of about 40 cm^{-1} from the gas phase equivalent. This shift suggests the strong interaction of the carbonyl with the CeO_2 surface. CeO_2 tends to reduce at high temperatures, and the peak at 1637

cm^{-1} was from the ν(C=O) adsorbed on a defect site. A group of peaks at 1465, 1410, 1370, and 1294 cm^{-1} were most likely from the $\delta_{as}(CH_3)$, $\delta_{as}(CH_2)$ and $\delta_s(CH_3)$ and $\delta_s(CH_2)$. From these assignments, CeO_2 was not particularly active for catalyzing reactions of 4H2B.

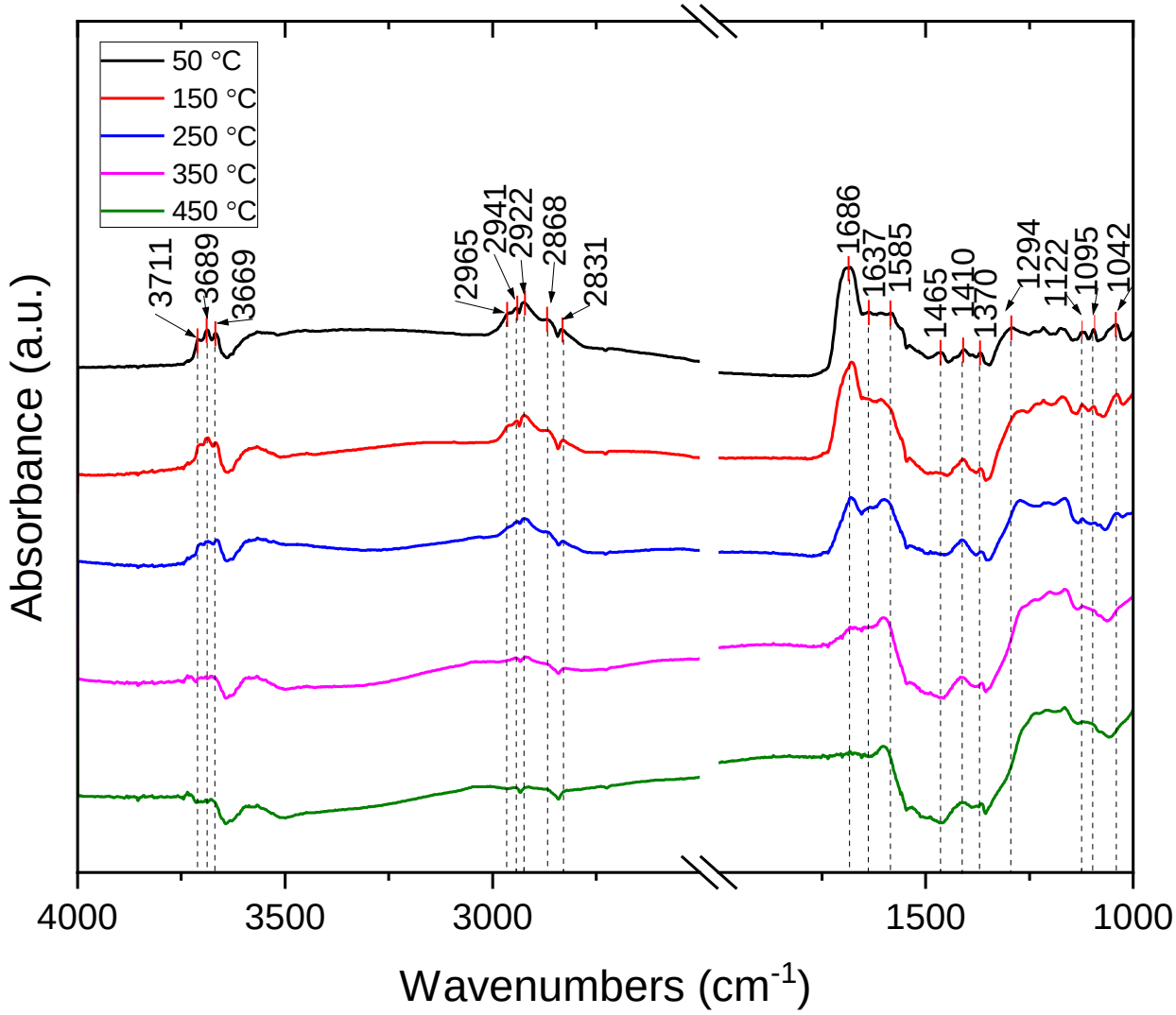

Figure 4.5 FTIR spectra of 4H2B on CeO_2 followed by TPD

Figure 4.6 shows the IR spectrum of 4H2B adsorbed on TiO_2. There were three peaks seen at 2963, 2927, 2866 cm^{-1} and a shoulder at 2840 cm^{-1} were due to the $\nu_{as}(CH_3)$, $\nu_{as}(CH_2)$ and $\nu_s(CH_3)$ and $\nu_s(CH_2)$. There were also two peaks at 1689 and 1642 cm^{-1} from the ν(C=O) of the keto group adsorbed on the metal site and the ν(C=C) formed from dehydration of 4H2B to MVK,

a reaction that has been observed before for the same catalyst.[206] The shoulder present at 1620 cm^{-1} was another ν(C=O) but from the ketone interacting with an oxygen vacancy since TiO_2 is highly reducible like CeO_2. Unlike CeO_2 though, these peaks remained on the surface without major change in intensity up until 450 °C. The ν(C-O) at 1080 cm^{-1} also remained but shifted to lower wavenumbers as temperature increased. This suggests most of 4H2B remained intact on the surface of TiO_2 and did not react much nor desorb. One explanation is there is a bidentate configuration of 4H2B on the surface where defect sites are interacting with the oxygenate moieties. There was a shoulder present at 1460, along with peaks at 1440, 1365, and 1310 cm^{-1} and were due to $\delta_{as}(CH_3)$, $\delta_{as}(CH_2)$ and $\delta_s(CH_3)$ and $\delta_s(CH_2)$. They remained at the highest temperature.

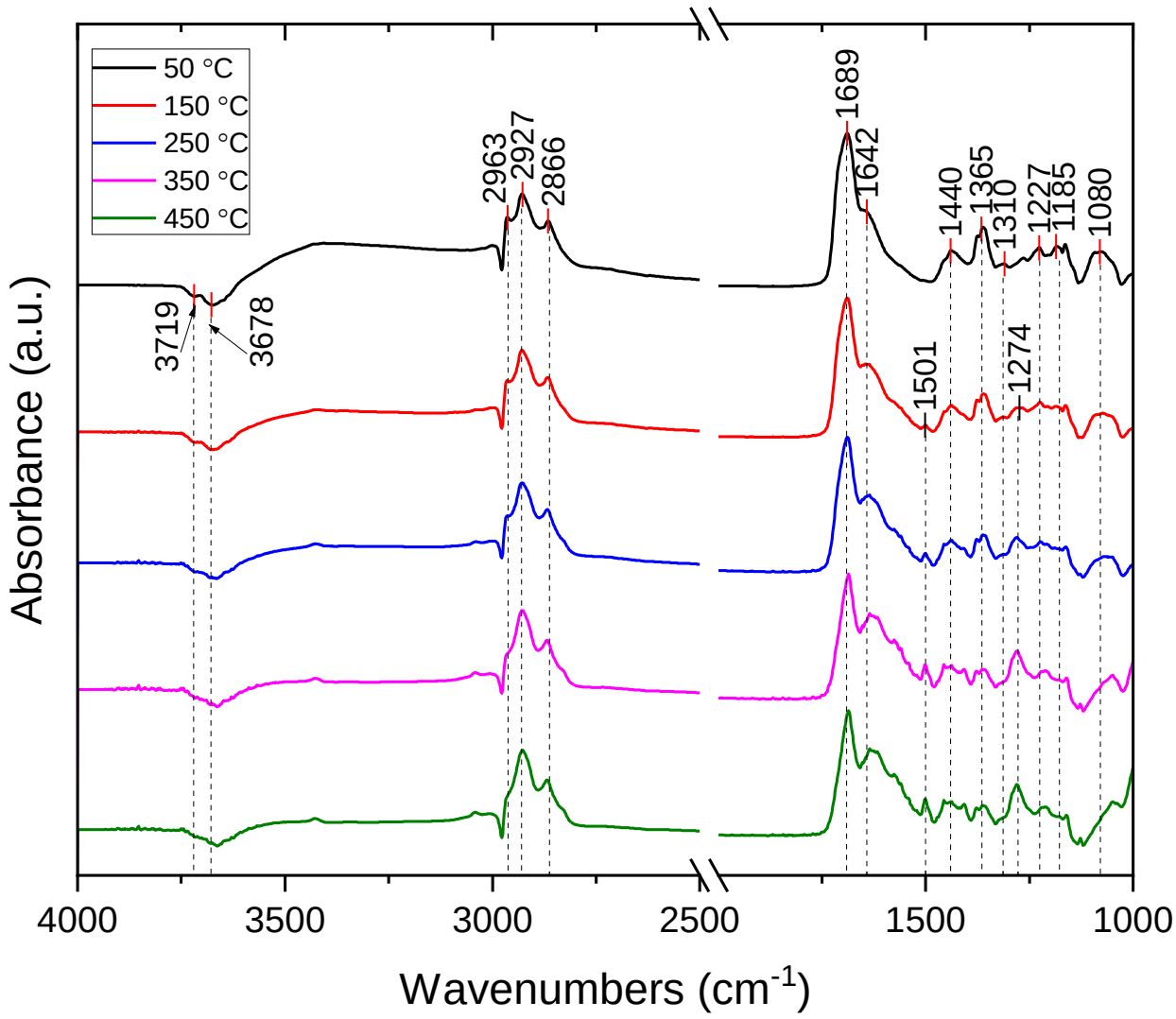

Figure 4.6 FTIR spectra of 4H2B on TiO_2 followed by TPD

4.3.3 Adsorption of 3-hydroxybutanal

Figure 4.7 shows the IR spectrum of 3HB adsorbed on γ-Al_2O_3. A negative peak at 3730 cm^{-1} was seen, likely due to interactions with surface hydroxyl groups. In the 50 °C condition, this peak was not very noticeable, but instead there was a broad peak at 3541 cm^{-1} that disappeared at higher temperatures. This peak was likely due to the formation of water which desorbed at higher temperatures. The formation of water was mostly likely from retro-Michael dehydration of 3HB to form crotonaldehyde. When the strong water peak desorbed, negative peaks associated with

Al_2O_3 surface hydroxyls appeared.[193] There were also peaks at 2966, 2931, and 2876 cm^{-1} in all temperature conditions due to $\nu_{as}(CH_3)$, $\nu_{as}(CH_2)$, and $\nu_s(CH_3)$. The presence of the $\nu_{as}(CH_2)$ up to 450 °C suggests that not all of the 3HB undergoes dehydration. A slight peak from the ν(CH) of the aldehyde was present at 2739 cm^{-1}. At 150 °C, a peak at 3027 cm^{-1} appeared that was from the ν(CH) of a formed aromatic. This peak increased with temperature along with the pair of peaks at 1575 and 1453 cm^{-1}. These were both due to the aromatic stretching caused by the C=C bonds.[207] It is interesting to note that these peaks formed at only 50 °C suggesting aldol condensation of 3HB is occurring at very low temperatures. There were also peaks at 1701 and 1666 cm^{-1} which were due to the ν(C=O) of 3HB and crotonaldehyde respectively. The peak at 1628 cm^{-1} was from the ν(C=C) of crotonaldehyde. Peaks at 1375, and 1286 cm^{-1} were also observed due to the $\delta(CH_3)$ and $\omega(CH_3)$. A peak at 1104 cm^{-1} was most likely formed from the ν(C-O) of the alcohol group of 3HB.

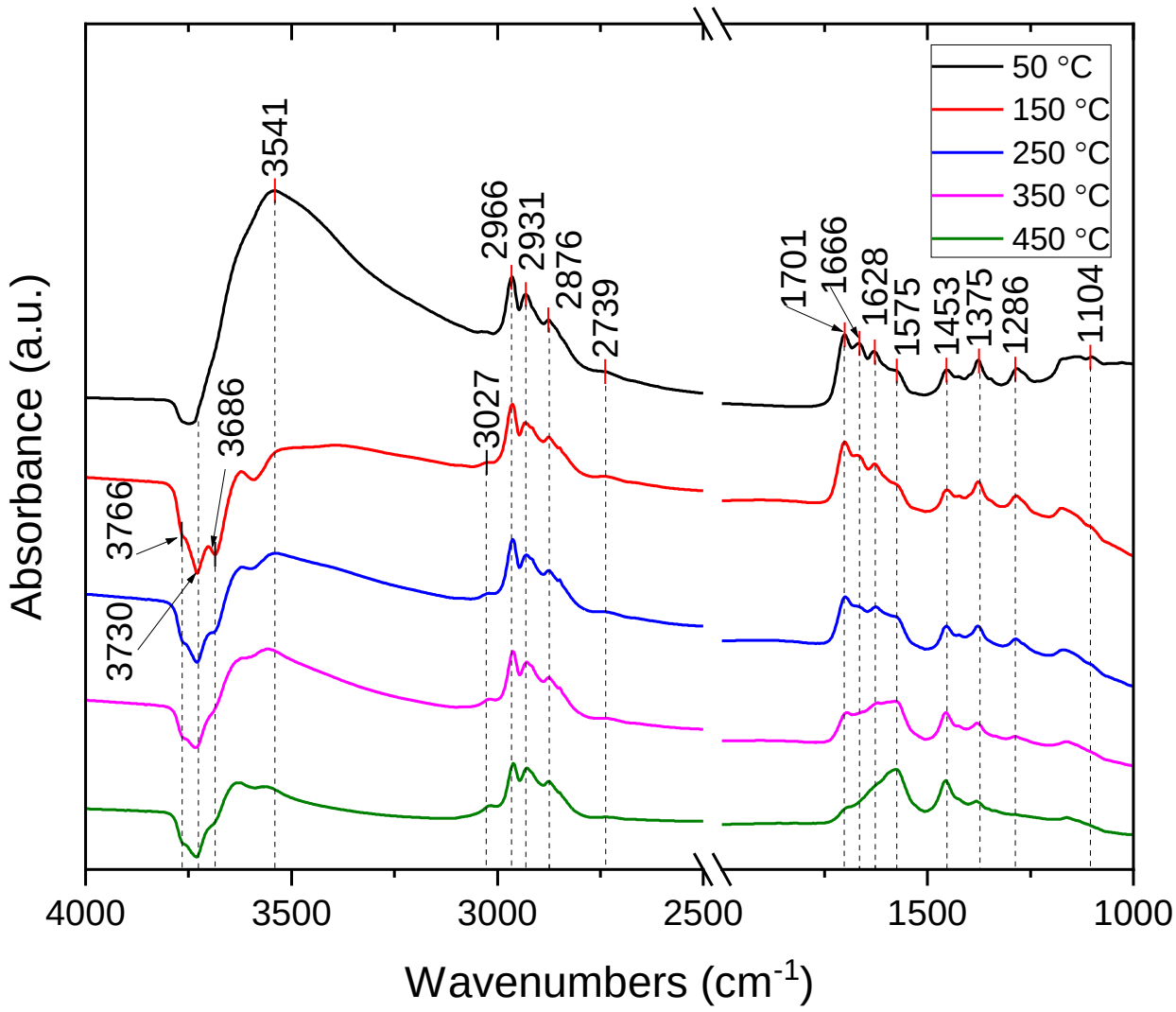

Figure 4.7 FTIR spectra of 3HB on γ-Al_2O_3 followed by TPD

Figure 4.8 shows the IR spectrum of 3HB adsorbed on Nb_2O_5. A negative peak at 3708 cm^{-1} was seen, likely due to interactions of the adsorbate with the BAS. This peak decreased in intensity as the temperature increased due to desorption of adsorbate. At 50 °C, there were two major peaks at 2989 and 2903 cm^{-1}. As temperature increased, these peaks moved towards each other and eventually combined into a single broad peak around 350°C. Peaks at 1697 and 1681 cm^{-1} were due to ν(C=O) of 3HB adsorbed onto the BAS and LAS respectively. As temperature increased, the carbonyl interacting with the BAS disappeared at 250 °C while the LAS site peak was almost completely gone at 450 °C. As with 4H2B, this indicated that adsorbates interacting

with a LAS are more strongly adsorbed. As the temperature increased, the peak at 1681 cm^{-1} shifted to lower wavenumbers and was from the formation of crotonaldehyde. A peak at 1633 cm^{-1} was also present and grew in intensity from 50 to 150 °C. This was from the ν(C=C) of the acetaldehyde enolate. Acetaldehyde was similarly introduced onto the surface of Nb_2O_5 in a separate experiment (Figure C3). A dominant peak at 1638 cm^{-1} was present and like the 1633 cm^{-1} peak in Figure 4.8 disappeared almost completely at 350 °C. In addition, peaks at 1182, 1130 and 1072 cm^{-1} shown when 3HB was adsorbed were also present when acetaldehyde was introduced over Nb_2O_5. The 1182 cm^{-1} peak was the ν(C-C) of acetaldehyde, the 1130 cm^{-1} peak was from the ν(C-O) peak from the secondary alcohol of 3HB, and the 1072 cm^{-1} was due to the ν(C-O) from the enolate of acetaldehyde. Since the secondary alcohol peak was present from the acetaldehyde adsorption on Nb_2O_5, it is plausible that both aldol and retro aldol are actively taking place on this catalyst.

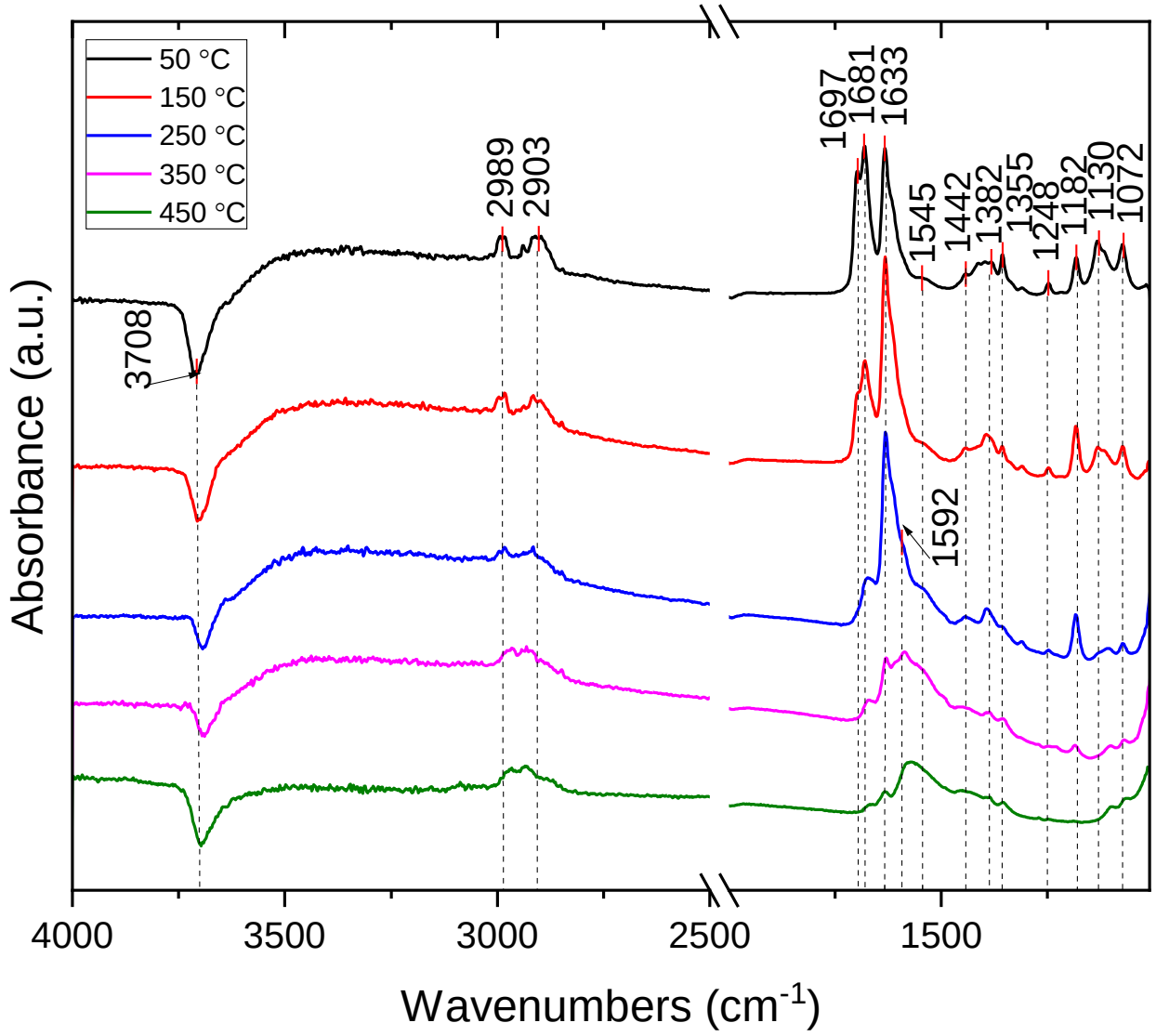

Figure 4.8 FTIR spectra of 3HB on Nb_2O_5 followed by TPD

Figure 4.9 shows the IR spectrum of 3HB adsorbed on CeO_2. At 50 °C, negative peaks at 3717 and 3657 cm^{-1} resulted from interactions of the adsorbate with CeO_2 surface hydroxyls present.[208] Peaks present at 2961, 2926, 2871, and 2830 cm^{-1} represent $\nu_{as}(CH_3)$, $\nu_{as}(CH_2)$, $\nu_s(CH_3)$, and $\nu_s(CH_2)$ respectively. As the temperature increased, these peaks decreased slightly in intensity. At 50 °C, a small peak appeared at 3024 cm^{-1} due to a ν(CH) stretch which suggests formation of an aromatic. There was a peak at 1671 cm^{-1} attributed to the ν(C=O) of the aldehyde of 3HB. As the temperature increased, the intensity drops significantly and was negligible at 450 °C suggesting

full desorption or participating in a reaction. The peak at 1616 cm^{-1} was present at 50 °C and was due to a ν(C=C) most likely from dehydration of the β-hydroxyl. A strong peak was present at 1583 cm^{-1} that maintained the same intensity at elevated temperatures. This peak, in combination with the one at 1437 cm^{-1}, can arise from formation of aromatic compounds. The 1177 cm^{-1} peak was the ν(C-C) of acetaldehyde, the 1122 cm^{-1} peak was from the ν(C-O) peak from the secondary alcohol of 3HB and the 1064 cm^{-1} was due to the ν(C-O) from the enolate of acetaldehyde. This suggests retro aldol condensation along with dehydration of 3HB occurring on the CeO_2 surface.

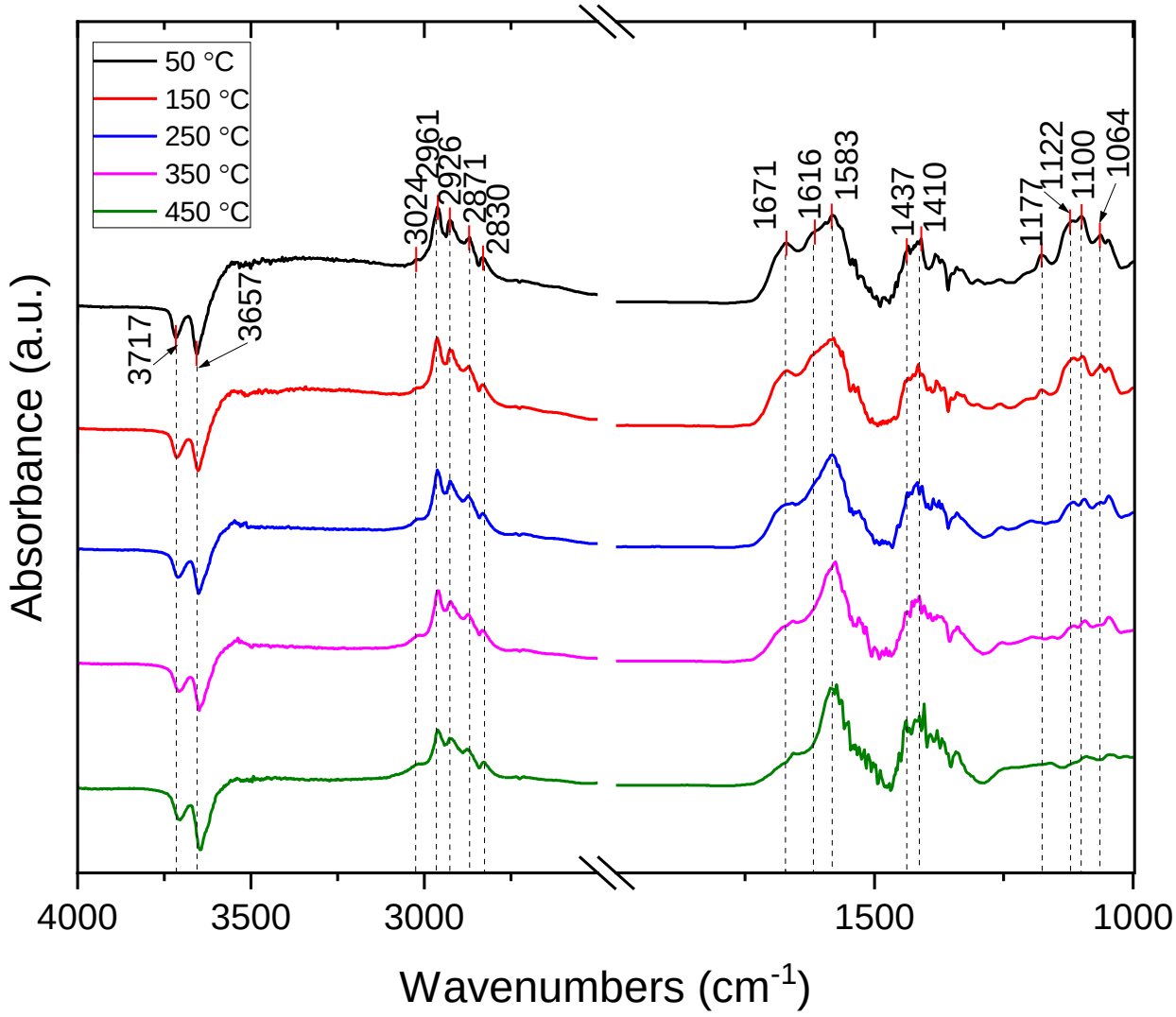

Figure 4.9 FTIR spectra of 3HB on CeO_2 followed by TPD

Figure 4.10 shows the IR spectrum of 3HB adsorbed on TiO_2. Two negative peaks were seen at 3717 and 3673 cm^{-1} due to interactions of the adsorbate with the surface hydroxyls of TiO_2.[209] The intensity of the peaks increased slightly with temperature. In all conditions, there was a small peak at 3024 cm^{-1} which is indicative of the ν(CH) of an aromatic. The peaks at 2964, 2926, and 2874 cm^{-1} remained fairly constant as temperature was increased and were due to the $\nu_{as}(CH_3)$, $\nu_{as}(CH_2)$, and $\nu_s(CH_3)$ respectively. The peak at 1672 cm^{-1} was assigned to the ν(C=O) of 3HB or crotonaldehyde. The peak at 1650 cm^{-1} is from the ν(C=O) of acetaldehyde and was confirmed with adsorption of acetaldehyde on TiO_2 (Figure C4). Similarly, the sharp peak at 1628 cm^{-1} is due to the ν(C=C) of the enolate formed from acetaldehyde tautomerization. The pair of peaks at 1542 and 1442 cm^{-1} increased in intensity as temperature increased meaning the concentration of that species increased. These were most likely from acetate species formed when acetaldehyde was formed.[202] A similar group of overlapping peaks was seen at 1171, 1144, and 1078 cm^{-1} and were assigned to the ν(C-C) of acetaldehyde, the ν(C-O) from the secondary alcohol of 3HB and the ν(C-O) from the enolate of acetaldehyde. This suggests that retro aldol condensation of 3HB is very active on the TiO_2 surface.

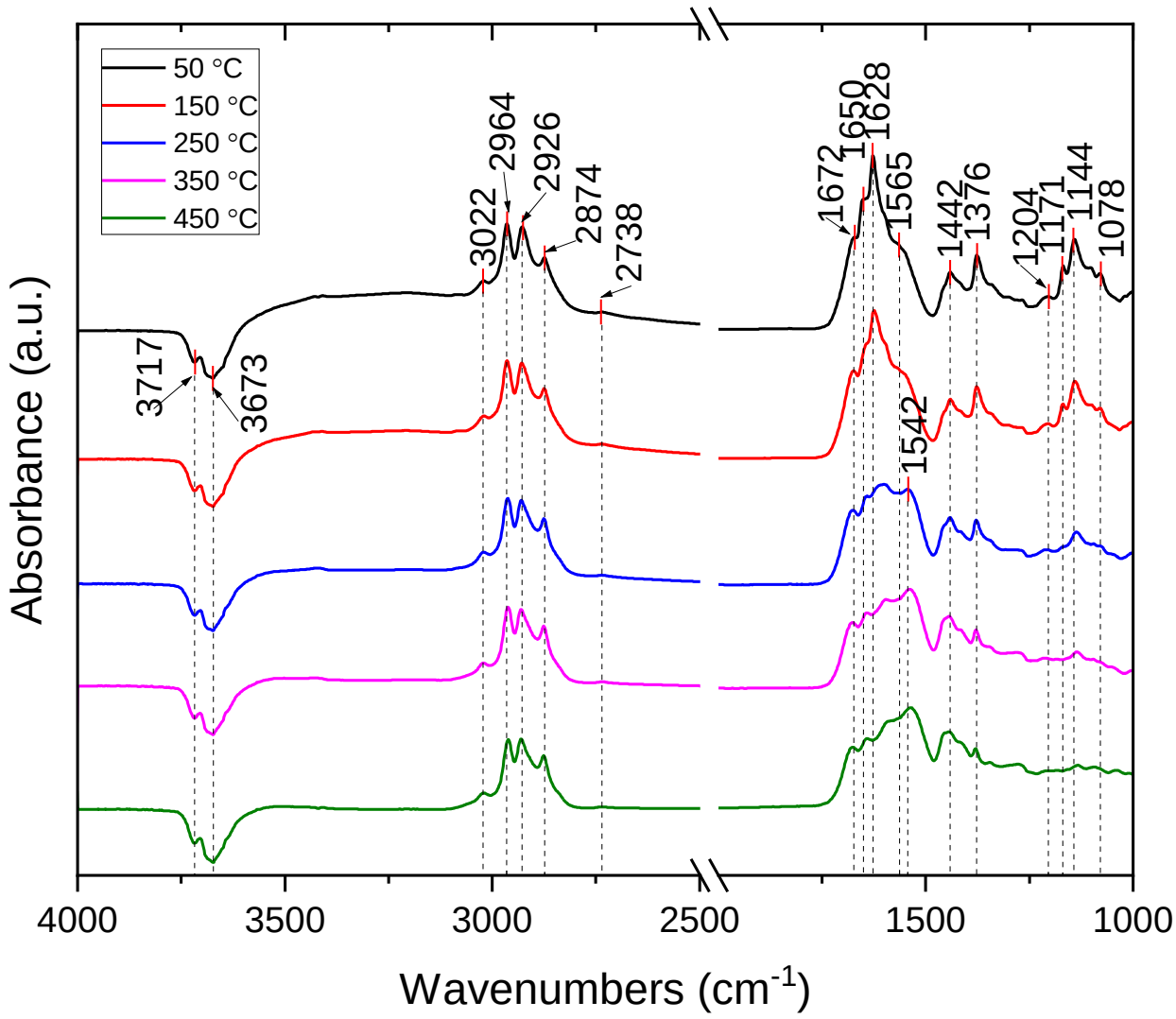

Figure 4.10 FTIR spectra of 3HB on TiO_2 followed by TPD

4.3.4 Implications for Surface Reactions

4.3.4.1 Surface Properties of Metal Oxides

Although there are high concentrations of LAS as shown in Figure 4.2, the surface species derived from adsorption of both model compounds were drastically different depending on the catalyst studied. It is worth noting that although Nb_2O_5 and TiO_2 had practically similar concentrations of strong LAS (defined by concentration of LAS at 450 °C), Nb_2O_5 was able to retain a higher percentage of the original concentration measured at 150 °C. This suggests that Nb_2O_5 may contain the strongest LAS out of all the metal oxides studied because it was able to

retain a higher amount of the original pyridine adsorbed. This is important to note since strong LAS can be beneficial for catalyzing important reactions but can also have detrimental effects on catalyst deactivation by preventing species from desorbing.

One interesting consistency between the various spectra is the appearance of negative bands within the ν(OH) region of the spectra. These are due to the presence of the adsorbate and from its ability to displace surface hydroxyl groups that were previously on the surface or interact with them.[210] Interestingly, this suggests that all these materials are able to dissociate water and create hydroxyls on the surface. The oxygen atom of each oxide can also act as a base by which protons can be abstracted. This can be another way in which surface hydroxyls can be generated *in-situ*. Another consistency between experiments worth mentioning is the formation of aromatics from consecutive aldol condensation reactions. This was especially pronounced at higher temperatures whether carbonaceous buildup tends to accumulate.

4.3.4.2 Surface Reactions of 3-hydroxybutanal and 4-hydroxy-2-butanone

γ-Al_2O_3 was the only catalyst that demonstrated direct dehydration of 3HB to crotonaldehyde at 50 °C. This makes sense since γ-Al_2O_3 has been shown to favor alcohol dehydration, especially for higher substituted carbon centers (secondary, tertiary vs. primary).[192] Given the secondary alcohol of 3HB, dehydration is most likely occurring. Water formed from dehydration on γ-Al_2O_3 strongly adsorbed onto the surface can act as a catalyst poison but does not create BAS.[192] Adsorption of 4H2B on γ-Al_2O_3 was similar in that dehydration was almost immediate since no primary alcohol was detected. The two different carbonyls, aldehyde and ketone, had very similar vibrational frequencies (1699 cm^{-1} for ketone and 1701 cm^{-1} for aldehyde). Relative to the carbonyl vibrational frequencies observed on the other catalysts for the same adsorbates, those on γ-Al_2O_3 were at much higher frequency values meaning a weaker adduct is

formed. This suggests that carbonyl activation is not particularly favorable on the γ-Al_2O_3 surface. This is rather surprising given the fact that hard acids (ie Al^{3+}) are better for carbonyl activation.[211,212] This suggests that when an adsorbate with both alcohol and carbonyl functionality is introduced to γ-Al_2O_3, the dissociation of the alcohol bond is much more active so that RAC cannot strongly compete. As shown when acetaldehyde is adsorbed (Figure C1), the formation of crotonaldehyde occurs because of aldehyde activation. This comes with the caveat that there was no competing alcohol group present, leaving the aldehyde as the oxygenate moiety. Thus, γ-Al_2O_3 is better suited for reactions involving reactants with a singular oxygenate group.

When 3HB was adsorbed onto CeO_2, Nb_2O_5 and TiO_2, there was evidence for RAC given the formation of acetaldehyde derived enolate species. Scheme 4.1 illustrates a potential mechanism for this reaction. The retention of these species at higher temperatures differed depending on the surface. While TiO_2 had presence of carbonyl compounds on the surface up to 450 °C, CeO_2 and Nb_2O_5 did not. Interestingly the locations of ν(C=O) for TiO_2 and CeO_2 were almost identical at 1672 and 1671 cm^{-1} respectively. The vibrational mode of the carbonyl on Nb_2O_5 had two locations with species on both the LAS and BAS. The BAS was at the higher vibrational frequency, most likely because the interaction between a carbonyl and proton is not as strong as a carbonyl and an electron sink, i.e. a transition metal cation. Another reason for the large shift in the vibrational frequency for the ν(C=O) on TiO_2 and CeO_2 may be due to formation of oxygen vacancies generated during the activation step in vacuum.[117,213] Oxygen vacancies can act as active sites, and we have previously shown they are necessary for the aldol condensation of ethanol and acetaldehyde.[154] Thus, it is possible that the creation of oxygen vacancies, which result in CUS, can be responsible for catalyzing RAC.

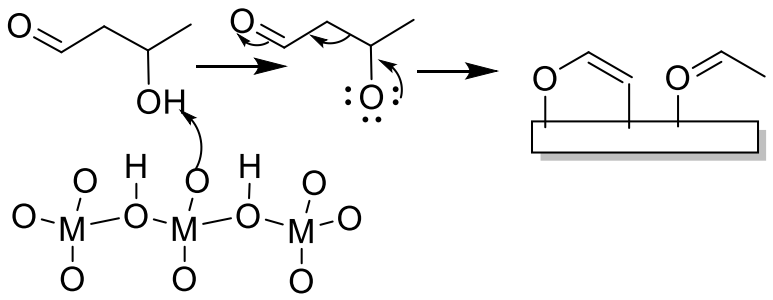

Scheme 4.1. Mechanism for RAC of 3-hydroxybutanal on surface of metal oxide.

The adsorption of 4H2B onto CeO_2, Nb_2O_5 and TiO_2 was again varied depending on the catalyst. CeO_2 not retaining surface species to a high temperature and not forming any MVK from dehydration suggests that it is not particularly active. This is interesting considering CeO_2 was active for RAC under the given conditions. This may be because dehydration of 4H2B involves formation of a primary carbenium that is not well stabilized on a CeO_2 surface. Whereas with 3HB, the dehydration step involves a more stable carbenium in the secondary alcohol position.

For dehydration of 4H2B on TiO_2, the ketone group was strongly bound staying present up to 450 ºC with no change in intensity. The dehydration of 4H2B was studied on both rutile and anatase TiO_2 catalysts in a flow through system.[206] Interestingly from that study, the anatase crystal structure had almost complete conversion at high selectivity to MVK while the rutile structure had a steadily decreasing conversion due to deactivation. The TiO_2 catalyst tested here was mostly anatase structure (>70%). It is interesting to note the large portion of the ketone group present, and this could possibly be due to the rutile crystal structure still interacting with that group. The crystallinity having consequences on the acidity of the catalyst has not been explored thoroughly for many materials. The electrophilicity of rutile and anatase TiO_2 was compared using CO adsorption by DFT calculations, and it was demonstrated the rutile phase is more electrophilic than

the anatase phase.[214] Thus, if pure anatase TiO_2 was used it is hypothesized the relative amount of carbonyl at high temperatures would be less than if pure rutile TiO_2 was used.

Nb_2O_5 interestingly was the only catalyst to demonstrate RAC of 4H2B to acetone and formaldehyde. This may be due to the presence of the BAS which can potentially protonate the carbonyl initially, leaving the alcohol to interact with the LAS resulting in a bifunctional adsorption configuration. The presence of both BAS and LAS thus may have advantages for catalyzing RAC over predominantly Lewis acid catalysts. The vibrational frequency for the ν(C=O) of 4H2B interacting with the BAS was at much higher frequency than that of the ν(C=O) of 3HB interacting with the BAS. This is an interesting caveat given that they are both carbonyls and on a surface will be closer in frequency than in the gas phase. This suggests that BAS may interact differently with ketones vs aldehydes. One reason for this could be steric constraints of access of the BAS to the oxygen atom of the carbonyl. While the aldehyde is in a less steric constrained location, the ketone group may not be as well suited to access this site. The disappearance of the BAS bound ketone group at about 150 ºC suggests it is not as strongly bound to the surface. Still, the presence of acetone enolate at 50 ºC suggests this site is still active for catalyzing RAC but at higher temperature may not be able to retain this species.

4.4 Conclusion

The adsorption of 3-hydroxybutanal on various Lewis acidic catalysts (CeO_2, Nb_2O_5 and TiO_2) showed formation of species derived from retro-aldol condensation while on γ-Al_2O_3 there was almost exclusively dehydration to crotonaldehyde. The dehydration of 4-hydroxy-2-butanone to methyl vinyl ketone was observed on Al_2O_3 CeO_2, and TiO_2. The retro aldol condensation of 4-hydroxy-2-butanone was present on Nb_2O_5 due to presence of Brønsted acid sites. The adsorbate was able to interact with this site while the alcohol group could interact act with the adjacent Lewis

acid site, resulting in a bifunctional configuration. TiO_2 had the highest concentration of Lewis acidity and was able to strongly retain the adsorbates up to very high temperatures, indicating it possesses strong Lewis acidity.

Chapter 5 Surface Interactions of a Model Sugar on Lewis Acidic Metal Oxides: A Solid State NMR Approach

5.1 Introduction

The rising need for sustainable alternatives to fossil fuels has prompted significant research into the area of biomass valorization and transformation.[32] Biomass has three main constituents: cellulose, hemicellulose and lignin. Cellulose is a linear polymer of glucose whereas hemicellulose consists of different C5 and C6 sugars. Sugars can be used as platform chemicals that are upgraded to commodity chemicals using heterogeneous catalysts. One major challenge for developing such processes is understanding how the complex sugar molecules interact with the surfaces of potential catalysts.[36,215] Simpler, smaller compounds with similar functionality, such as the C4 sugar erythrose, can be used in place of glucose to better understand how sugars interact with catalytic surfaces.[216]

Heterogeneous catalysts, such as metal oxides, have revolutionized the way energy is processed. An important property of metal oxides is Lewis acidity. Lewis acidic (LA) catalysts can promote many important sugar reactions, such as isomerization, retro-aldol condensation and the Cannizzaro reaction.[31,37,38] Despite this, a systematic understanding of the factors that promote these reactions occur is missing. One important note is that different LA metal oxides will catalyze different reactions and more specific descriptors are needed to rationalize findings. Some potential descriptors are hardness/softness of metal center, ionic radius, and electronegativity.[26,217,218] In addition to Lewis acidity, Brønsted acidity and basicity are other factors of the catalyst that can affect the overall reaction pathway.

The importance of sugars on the surface metal oxides is not only relevant to the heterogeneous catalysis community but also those who study prebiotic chemistry, sensors, and soil

chemistry.[219–221] For example, several glucose biosensors employ metal oxides as part of detecting concentrations since metal oxides are more stable than enzymes.[222] This provides motivation into further expanding the knowledge basis of how sugars interact with metal oxides.

The investigation of catalytic surfaces and how they interact with organic compounds has been heavily studied through various *in-situ* spectroscopic and other relevant techniques[223] but there has been little to no investigation of the surface interactions of erythrose on relevant materials. One technique that can be utilized for elucidating surface species/interactions is solid state nuclear magnetic resonance (SS-NMR).[224–227] Direct polarization magic angle spinning (DPMAS) is one specific pulse sequence that can be used to identify surface species present in quantifiable manner. Like other *in-situ* techniques, DPMAS NMR spectroscopy can be used to rationalize reaction routes and also observe the behavior of surface species during operando conditions.[228] Cross polarization (CP) is an alternative pulse sequence which can be used to identify surface species in a reduced collection time, but it is not quantifiable like DPMAS. Another capability of CPMAS is to measure the mobility of various moieties based on the rotating frame relaxation time known as $T_{1\rho}$.[229] This type of technique is underutilized in the heterogeneous catalysis community and can provide valuable information regarding the adsorption/confinement of surface species. One consideration when conducting NMR is the presence of paramagnetic species that can attenuate the NMR signal. To overcome this limitation, only catalytically relevant, non-paramagnetic materials were studied.

In this work, we investigate the adsorption of erythrose on the surface of various Lewis acidic metal oxides (γ-Al_2O_3, CeO_2, Nb_2O_5, SiO_2, SnO_2, TiO_2, and ZrO_2) using DPMAS/CPMAS NMR spectroscopy to understand which surface species are present, the mobility of moieties present on the surface, and how these observations are affected by an increase in temperature. It

was found that ring opening of erythrose was present on most materials but the pathway in which the reaction occurred varies depending on the material. The material that produced the most product had the largest atomic radius suggesting this is an important factor for these types of systems.

5.2 Methodology

5.2.1 Materials and Catalyst Synthesis

Fully enriched erythrose (U-13C4, 98%, 0.175 M) 1.2% in water was purchased from Cambridge Isotope Laboratory Inc. Erythrose labeled at the hemiacetal carbon was purchased from Omicron Biochemicals Inc. (1-^{13}C, 99 atom%, 0.096 M). Aluminum oxide (gamma phase, Alfa Aesar 99.97% trace metal basis), niobium pentoxide (CBMM), silicon dioxide (Sigma Aldrich, 99%), and titanium dioxide (rutile phase, Sigma Aldrich, 99.99%) were purchased. Cerium dioxide was synthesized following a co-precipitation procedure described in our previous study.[109,230] Cerium nitrate (Sigma-Aldrich $Ce(NO_3)_3 \cdot 6H_2O$, 99.999% trace metals basis) were dissolved in deionized water (DI water), and the solution was added dropwise to an ammonium hydroxide solution (ACS reagent, 28.0-30.8 NH_3 basis, Sigma-Aldrich). The deposition was first filtered, and then dried in an oven at 110 °C overnight. Tin oxide was synthesized from $SnCl_2$ (Sigma Aldrich, 99.995% trace metal basis) that was precipitated with urea (Sigma Aldrich, ACS reagent) as described elsewhere.[231] Zirconium dioxide was made from zirconium nitrate hexahydrate (Sigma Aldrich 99.99% trace metal basis) that was precipitated with ammonium hydroxide. For both SnO_2 and ZrO_2, the remaining crystals were ground, washed with water, centrifuged and then dried at 120 °C overnight. All synthesized catalysts were calcined at 450 °C for 4 h in 500 ccm of air except for SnO_2 which was calcined at 300 °C.

5.2.2 Catalyst Characterization

A Micromeritics Accelerated Surface Area and Porosity (ASAP) 2020 system was used for N_2 physisorption followed by BET analysis.[166] Before analysis, samples were degassed at 110 °C and held at this temperature for 4 h. Adsorption− desorption measurements of nitrogen were carried out at −196 °C.

Powder XRD (X-ray Diffraction) patterns were obtained to verify crystal structure of synthesized catalysts. Measurements were taken on a Philips X'pert diffractometer equipped with an X'celerator module. Diffractograms were obtained with Cu Kα radiation for 2θ = 10−80° with a step size of 0.0167°

The quantification of Lewis and Brønsted acid sites on the above listed catalysts was done using *in-situ* pyridine adsorption followed by FT-IR spectroscopy. Measurements were done using Thermo Scientific Nicolet iS10 by collecting 64 scans for each spectrum with a resolution of 4 cm^{-1}. Self-supported catalyst wafers were prepared and loaded into an ultra-high vacuum setup where the sample was heated to 150 °C under high vacuum for 2 h. The sample then underwent an activation step at 450 °C for 1 h and then brought back down to 150 °C where pyridine was introduced at a pressure of 0.1 mbar for 30 min and then allowed to equilibrate for 1 h. The sample then underwent evacuation after which a spectrum was collected. To probe the strength of acid sites, the samples were subsequently heated to 250, 350, and 450 °C, and spectra of residual pyridine were obtained at 150 °C. Afterwards the sample was removed, a 6.45 mm diameter wafer was punched out and weighed to normalize acid site concentrations. Spectra were integrated around 1540 and 1440 cm^{-1} for Brønsted and Lewis acid sites, respectively. Molar extinction coefficients were taken from Tamura et al.[165]

5.2.3 SS-NMR Spectroscopy

Samples for SS-NMR spectroscopy measurements were prepared by incipient wetness impregnation. Initially, the catalyst was calcined at 450 °C in air for 4 h. Once cooled down, the samples were immediately removed from the furnace and about 0.5 g were impregnated with the aqueous erythrose solution on a watch glass and mixed around to form a slurry with a spatula. The watch glass was then placed in a desiccator connected to a membrane pump and dried overnight. The dried sample was then collected next morning and packed firmly into a 4 mm zirconia NMR rotor.

All SS-NMR spectroscopy measurements were carried out on a Bruker AVANCE III HD spectrometer operating at a proton frequency of 300.13 MHz. Samples were spun at the magic angle of 54.74° in a zirconia rotor with a VESPEL cap at a frequency of 10 kHz. After measurements were taken at 25 °C, the sample was heated in situ to 50 °C for 30 minutes before the next set of measurements were done. DPMAS and CPMAS measurements were collected using the corresponding pulse sequence shown in Figure 5.1. For DPMAS, a 5 μs 90° pulse was used with a 10 s recycle delay. For each spectrum, 1024 scans were collected and averaged. CPMAS spectra were collected using a ramped amplitude with a 5 μs 90° pulse and a 10 s recycle delay. For contact time experiments, the same CPMAS sequence was used, but instead of a ramp the magnetization transfer time was varied to the following values: 0.05, 0.1, 0.2, 0.3, 0.5, 0.7, 1, 1.2, 1.5, 2, 2.5, 3, 4, 6, and 8 ms. 256 scans were taken for each transfer time sequence, and the integrated area intensities for each moiety were plotted as a function of transfer time. The spectra were then fit using equation 1:

$$I(t) = \frac{I_0}{1-\frac{T(IS)}{T(I)_{1\rho}}}\left[\exp\left(\frac{-t}{T(I)_{1\rho}}\right) - \exp\left(\frac{-t}{T(IS)}\right)\right] \quad (1)$$

where t is the transfer time, I_0 is a constant, $T(I)_{1\rho}$ is the spin lattice relaxation time, T(IS) is the CP constant, and I(t) is the integrated intensity.

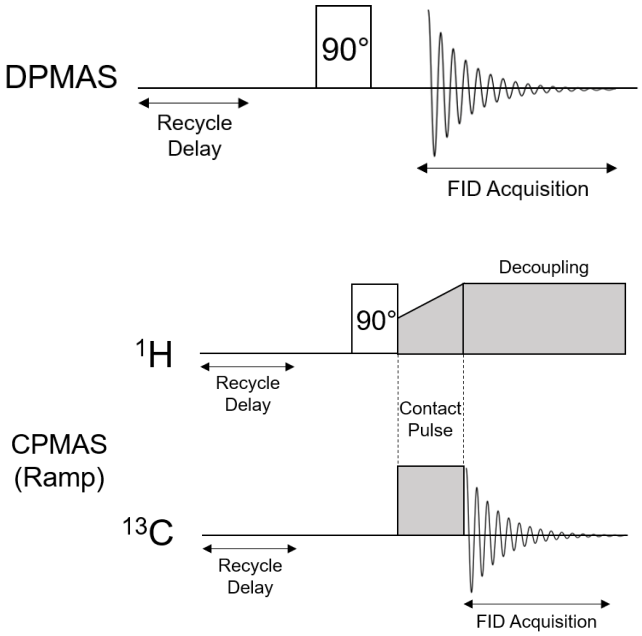

Figure 5.1 Standard pulse sequences used for DP and CP MAS experiments

Solution state ^{13}C NMR spectra were collected on a Bruker Avance III HD 500 MHz NMR instrument. An inverse-gated proton decoupling pulse sequence was applied with a 30° pulse width and an acquisition time of 1.1 s and a delay of 2 s. A total of 64 scans were collected for each spectrum.

5.3 Results

5.3.1 Characterization of Materials

Table 5.1 BET surface areas of materials used and amount of erythrose impregnated for NMR experiments

Sample	Surface Area (m^2/g)	Erythrose Loading (μmol/mg catalyst)	Erythrose Loading (μmol/m^2)
Al_2O_3	84	90	1070
CeO_2	64	40	625
Nb_2O_5	82	90	1100
SiO_2	70	40	570
SnO_2	120	70	583
TiO_2	60	130	2170
ZrO_2	80	40	500

XRD patterns from the synthesized materials, SnO_2 and ZrO_2, are shown in Figure D1 and are similar to reference patterns.[231,232] Table 5.1 shows the BET surface areas of the metal oxides and the respective amount of erythrose that was impregnated onto the sample. The impregnation amount was found by massing out catalyst and the amount of solution used to sufficiently wet the pores of the catalyst. Low loading of erythrose was used to ensure no surface crowding effects were occurring giving approximately $1/10^{th}$ surface coverage. This low loading was compensated by using fully enriched erythrose to avoid compromising NMR signal.

Results from infrared spectroscopy measurements of adsorbed pyridine are shown in Figure 5.2. Nb_2O_5 had the largest amount of both Brønsted and Lewis acid sites. Al_2O_3 also had significant Lewis acid sites (LAS) followed by CeO_2. They had an insignificant amount of Brønsted acid sites (BAS). TiO_2 had the next lowest amount of LAS and no measurable BAS,

while SnO_2 had the least LAS and no measurable BAS. Nb_2O_5 was the only material with a considerable amount of BAS.

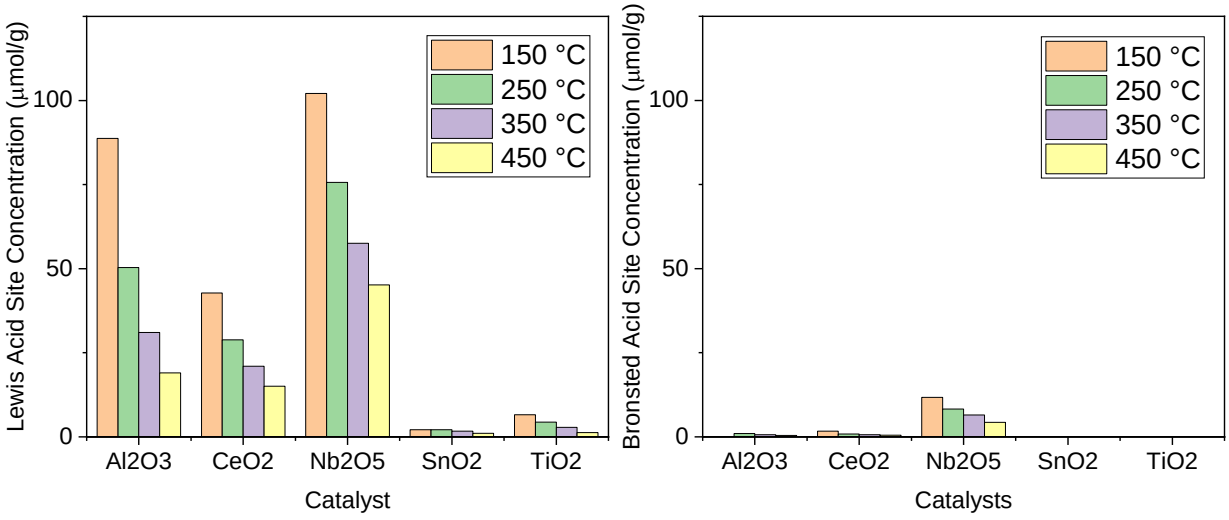

Figure 5.2 Quantification of Lewis and Brønsted acid site concentration using pyridine adsorption followed by infrared spectroscopy measurements

5.3.2 Solid State NMR Measurements – Surface Species Formation

5.3.2.1 Surface Species Formation on Oxidative Surfaces

^{13}C NMR spectra of fully enriched erythrose impregnated onto the catalysts obtained using the DP pulse sequence at 25 and 50 °C are shown in Figure 5.3. Several regions of interest are shaded to indicate nuclei of interest. The green shaded portion is the carboxyl region (marked as COO), blue shaded is the alkoxy region (marked as C-O), and red shaded is the aliphatic region. Any peaks in the COO region indicated a ring opening reaction of erythrose. This could be carboxyl groups, such as those present at 170 and 184 ppm shown in Figure 5.3, or an aldehydic or ketonic nuclei that resonates more up field (>200 ppm). The disappearance of a hemiacetal carbon peak between 95 and 110 ppm, depending on the material, is also indicative of a ring opening reaction occurring. This is the case for all materials studied, but the extent to which it is happening differs greatly depending on the material. On the more oxidative materials (CeO_2,

Nb_2O_5, SnO_2, and ZrO_2) the amount of carboxyl groups formed was higher than on non-oxidative materials (Al_2O_3, SiO_2, and TiO_2).

The spectrum of surface species on CeO_2 showed significant intensity of carboxyls relative to the C-O region and had no aliphatic carbons present. There was also a broad hemiacetal carbon peak at 104 ppm. Surface species on CeO_2 did not change at 50 ºC. The peaks for the carbon nuclei present on Nb_2O_5 were similar to the peaks on CeO_2 but there were aliphatic carbons present at 23 and 36 ppm. On Nb_2O_5 there was more of the carboxyl at 182 ppm relative to 172 ppm but on CeO_2 the opposite was detected. There was also slight presence of an aldehydic or ketonic carbon at 212 ppm on Nb_2O_5. Like species on CeO_2, the increase in temperature had no effect on the relative amount of each nuclei.

Spectra of surface species on SnO_2 and ZrO_2 were greatly influenced by the increase in temperature as evidenced by formation of new peaks and change in shape of those originally present. For surface species on SnO_2, there was slight carboxyl and aliphatic at 25 ºC along with very large presence of one hemiacetal peak at 101 ppm. After being heated to 50 ºC, the spectra of species on SnO_2 looked much different. The ratio of areas in hemiacetal carbon region to the C-O region decreased by over 90 %. This indicates significant ring opening is occurring at slightly elevated temperatures and is also evidenced by the greater presence of peaks in the carboxy land aliphatic carbon region. Interestingly, there was also a peak at 137 ppm that appears at 50 ºC in the region of olefinic and aromatic carbons. The broad peak in the C-O region at 25 ºC becomes more resolved when the temperature is increased and splits into two more resolved peaks. The changes of the surface species on ZrO_2 were similar to those on SnO_2 due to the temperature increase but to a lesser extent. Interestingly, the amount of carboxyl and aliphatic carbons present

on ZrO_2 were approximately equal, whereas for SnO_2 there is clearly more carboxyl present than aliphatic carbon at 50 °C.

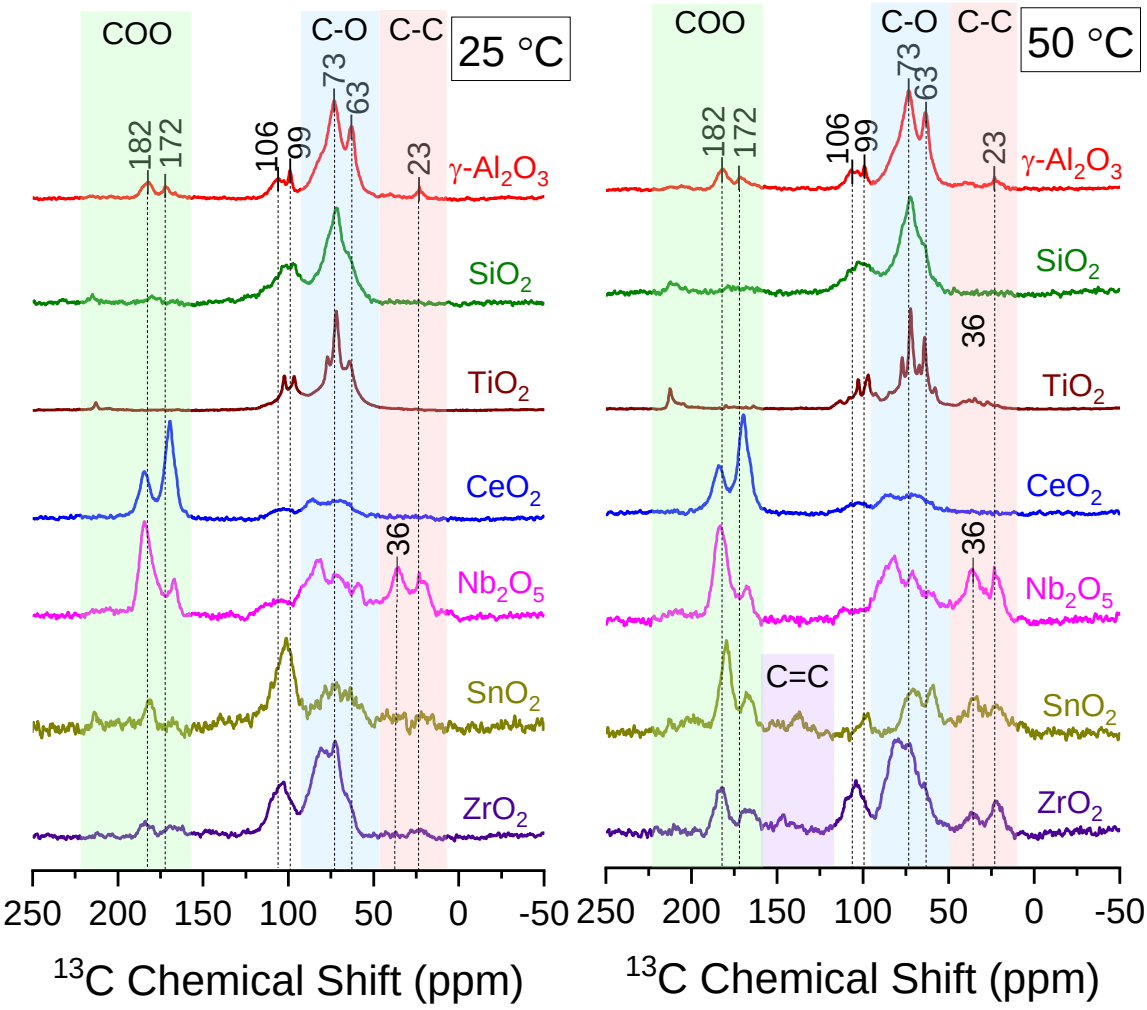

Figure 5.3 Solid State NMR ^{13}C spectra using DPMAS for erythrose adsorbed onto various metal oxide catalysts at 25 and 50 °C. Shaded regions are for various relevant carbon nuclei as noted at the top of the spectra

5.3.2.2 Surface Species Formation on Non-Oxidative Surfaces

For species on γ-Al_2O_3 there was a very low total peak area in the carboxyl region relative to the alkoxy (marked as C-O) region within the same spectra. On γ-Al_2O_3 there were two distinct hemiacetal carbon peaks at 99 and 106 ppm due to the presence of both the alpha and beta cyclic

hemiacetal forms of erythrose. There were also aliphatic carbons detected but like the carboxyl nuclei, there was not a significant amount. At 50 ºC, the relative amount of these surface species did not change. Species present on SiO_2 did not show much activity towards erythrose with only slightly presence of a carbonyl at 212 ppm. This peak increased when the sample was heated to 50 °C.

Like the surface species on SnO_2 and ZrO_2, those on TiO_2 were affected by the increase in temperature, but instead of significant change in the amount of certain carbons present, the peak resolution was greatly enhanced. In addition to the increase in area of the aldehyde peak at 212 pm and aliphatic carbons, the resolution of the peaks in the C-O region became sharper and more well-defined. The width of the peaks in the spectra of surface species on TiO_2 were the smallest by far. For a DPMAS spectra, this is indicative that the surface species will be weakly bound to the surface of the catalyst. This prompted further investigation into whether the sugar would easily be removed from the catalyst. The leftover dried TiO_2 sample was lixiviated with 1 mL of D_2O and 1 mL of DI water three times, and the supernatant was collected. This was also done for the γ-Al_2O_3 sample, and a comparison between the two and the starting erythrose solution is shown in Figure 5.4. There is clear presence of the original erythrose in the supernatant along with some product as evidenced by the carboxyl and aliphatic peaks. The supernatant from lixiviating γ-Al_2O_3 contained no carbon species at all suggesting the erythrose and respective surface species are strongly bond to its surface.

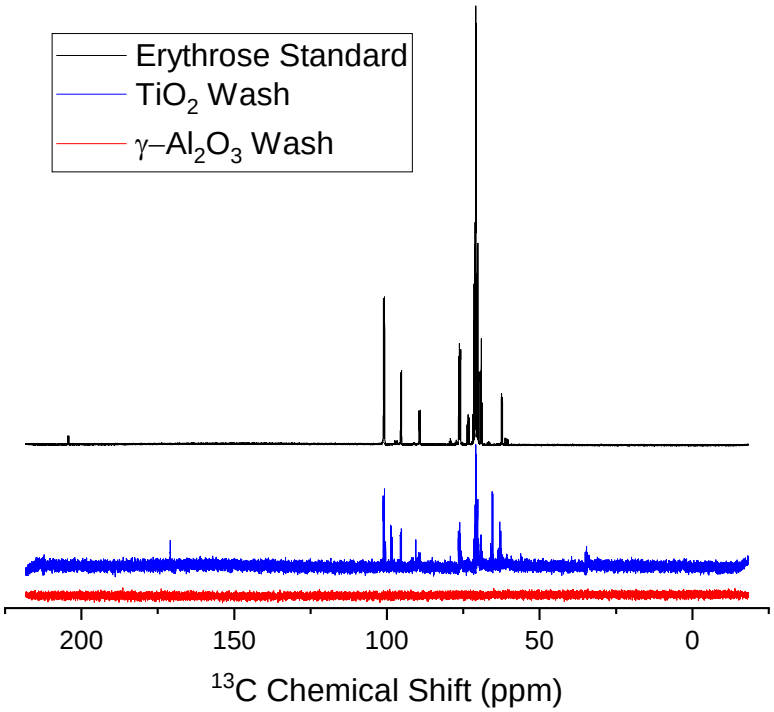

Figure 5.4 ^{13}C liquid state NMR spectra of erythrose standard solution and supernatant from lixiviation of TiO2 and γ-Al_2O_3 with D_2O

5.3.2.3 Tracking Carbonyl Migration

The following materials were not affected by temperature: γ-Al_2O_3, CeO_2, Nb_2O_5, and SiO_2. While SnO_2, TiO_2, and ZrO_2 were affected by the increase in temperature. To investigate whether the hemiacetal carbon was responsible for the formation of carboxyls, ^{13}C labelled erythrose at the hemiacetal position was impregnated onto both classes of materials. The CPMAS technique was used for samples that did not show new surface species at 50 °C and DPMAS for those that did are shown (Figure 5.5). The spectra were dominated by the peak of the hemiacetal carbon as it is the only enriched nucleus. For γ-Al_2O_3, there was clear presence of the carboxyl and aliphatic carbons in the same ratio as in Figure 5.3. This was also the same for surface species on CeO_2 and Nb_2O_5. Interestingly, however, there was a large amount of alkoxy carbons present on the surface of γ-Al_2O_3 but not on CeO_2 and Nb_2O_5. Moving to the temperature sensitive catalysts in Figure 5.5, as expected the hemiacetal carbon presence was totally depleted on SnO_2 after heating the

sample as seen in Figure 5.3. There was an unexpected strongly signal from the aliphatic carbon at 25 °C. For surface species on TiO_2, there was slight formation of carboxyl at 50 °C as expected but no formation of the carbonyl at 212 pm suggesting this moiety most likely forms from of the alkoxy carbons (Figure 5.3). Like the surface species on γ-Al_2O_3, the one on TiO_2 contained a significant amount of alkoxy carbon. Surface species on ZrO_2 exhibited small amounts of carboxyl and aliphatic carbon formation at 50 °C.

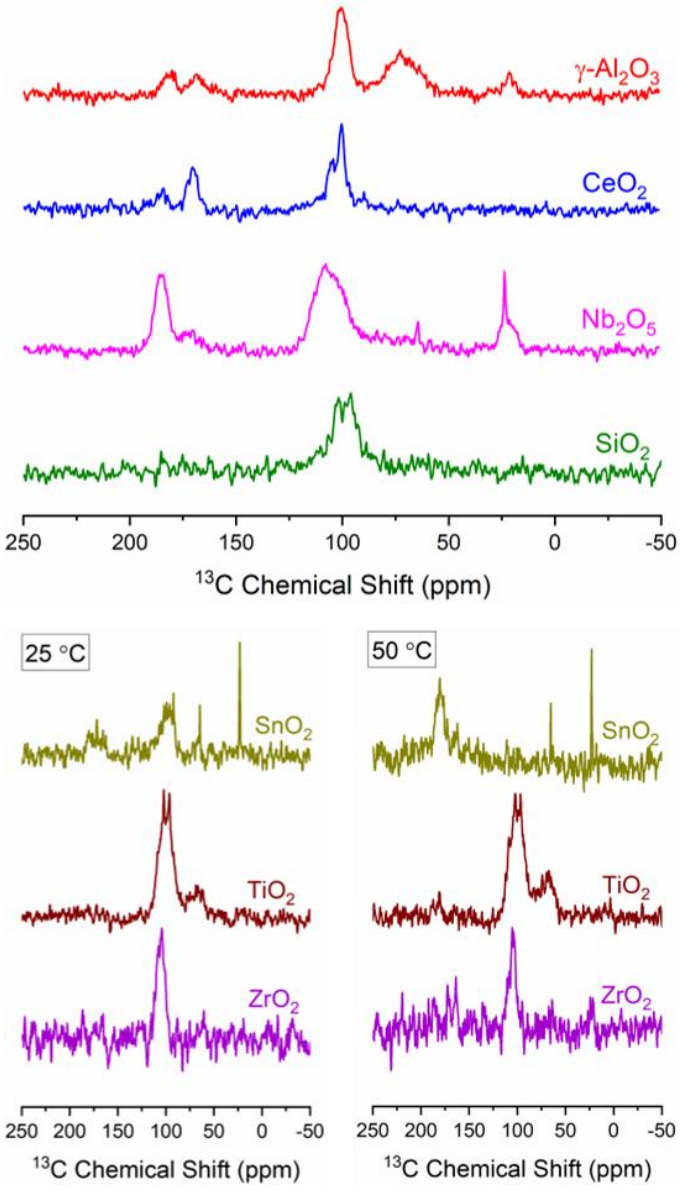

Figure 5.5 ^{13}C SS-NMR spectra of C1 labelled erythrose impregnated onto various metal oxides as written above the spectra. The top portion of spectra were done at 25 ºC

5.3.3 Solid State NMR Measurements – Relaxation and Mobility

$T_{1\rho}$ relaxation times obtained from fitting contact time data are shown in Table 5.2 and 5.3. Certain values were omitted either due to poor fitting or because the moiety was not present in the spectrum. Species marked as C-C are aliphatic carbon nuclei C-O are alkoxy carbon nuclei, HA are hemiacetal species, and COO are carboxyls.

Table 5.2 $T_{1\rho}$ values from fitted data at 25 °C in ms. The column titles are for corresponding moieties present with the following chemical shifts: (C-C-1) = 22 ppm, (C-C-2) = 35 ppm, (C-O1) = 61 ppm, (C-O2) = 73 ppm, (C-O3) = 84 ppm, (HA-1) = 96 ppm, (HA-2) = 106 ppm, (COO1) = 171 ppm and (COO2) = 184 ppm

Sample	C-C1	C-C2	C-O1	C-O2	C-O3	HA-1	HA-2	COO1	COO2
γ-Al_2O_3	-	-	6	9	4	4	-	-	2
CeO_2	-	-	5	7	11	15	-	5	10
Nb_2O_5	-	9	5	10	17	4	-	-	7
SnO_2	5	6	6	5	-	7	-	-	2
TiO_2	-	-	1	1	2	2	1	-	-
ZrO_2	-	7	6	6	-	-	-	-	2

Table 5.3 $T_{1\rho}$ values from fitted data at 50 °C in ms. The column titles are for corresponding moieties present with the following chemical shifts: (C-C-1) = 22 ppm, (C-C-2) = 35 ppm, (C-O1) = 61 ppm, (C-O2) = 73 ppm, (C-O3) = 84 ppm, (HA-1) = 96 ppm, (HA-2) = 106 ppm, (COO1) = 171 ppm and (COO2) = 184 ppm

Sample	C-C1	C-C2	C-O1	C-O2	C-O3	HA-1	HA-2	COO1	COO2
γ-Al_2O_3	-	-	6	10	6	11	-	-	0.8
CeO_2	-	-	3	6	-	8	-	5	0.7
Nb_2O_5	-	7	3	6	7	1	-	-	3
SnO_2	10	4	4	6	-	-	-	-	0.5
TiO_2	1	-	1	1	2	-	1	-	-
ZrO_2	-	5	6	12	-	-	-	-	2

The $T_{1\rho}$ value based on a carbon nucleus is a measure of molecular motion, where longer relaxation times indicate slower motion back to the original state and shorter times are faster motion back to equilibrium state. The $T_{1\rho}$ values for each moiety depend greatly on the surface onto which it is adsorbed. For example, the COO2 group had a $T_{1\rho}$ value of 2 ms on the surface of

γ-Al_2O_3, SnO_2, and ZrO_2 but values of 10 and 7 ms on CeO_2 and Nb_2O_5 at room temperature. Interestingly, the C-O1 group had either a $T_{1\rho}$ value of 5 or 6 ms but on TiO_2 this value was 1 ms. The other two C-O groups had much more variation in $T_{1\rho}$ values depending on the catalyst at 25 °C. The variation within relaxation times of all measured moieties on a certain material also varied greatly depending on the surface. For instance, relaxation times on TiO_2 were either 1 ms or 2 ms at 25 °C, whereas on CeO_2 the variation was from 5 to 15 ms. This demonstrates two things: 1) moieties on TiO_2 had the fastest average relaxation time compared to those on any other surface 2) the adsorption of erythrose onto TiO_2 is more uniform than CeO_2 or other catalysts. The latter statement is due to the uniformity in relaxation times across all moieties.

The effects of temperature increase on $T_{1\rho}$ relaxation times (Table 3) were significant and provide more insight into surface effects. The relaxation time of the COO2 group decreased significantly on all measured samples except ZrO_2. Most notably, the relaxation time for this group on CeO_2 dropped from 10 to 0.7 ms. Interestingly, however, the $T_{1\rho}$ relaxation time of the other carboxyl group measured on CeO_2 remained the same at 5 ms at 50 °C. All other $T_{1\rho}$ values on CeO_2 decreased as temperature increased. The surface also had significant effect on the direction of the relaxation times due to the temperature increase. For example, the $T_{1\rho}$ relaxation times across all moieties decreased on Nb_2O_5 at 50 °C. This is not the case on γ-Al_2O_3 where the values either stayed the same or increased except for the COO2 group. The $T_{1\rho}$ relaxation times for moieties on TiO_2 remained entirely unchanged at the elevated temperature suggesting that although there is a weak interaction due to fast relaxation times, there is some interaction with the surface.

There are several trends that appear from comparing the $T_{1\rho}$ relaxation times of the moieties across different materials. The decrease in $T_{1\rho}$ times for the downfield carboxyl (COO2) after increasing temperatures suggest this moiety is not interacting with the surface of all materials. It

is interesting to note that at 25 ºC the $T_{1\rho}$ value for COO2 varies from 2-10 ms with CeO_2 having the highest time and ZrO_2 the lowest. At 50 ºC, the value for relaxation time on CeO_2 drops to 0.7 ms suggesting it can freely move and is not bound to the surface. The value for the COO2 relaxation time on ZrO_2 does not change from the temperature increase meaning that it most likely is interacting with the surface but most likely is not strongly bound as the actual value of 2 ms is relatively short compared to the relaxation times for the various alkoxy groups measured.

For the materials that did not experience a change in surface species at 50 ℃, the upfield hemiacetal carbon group (HA-1) still had a $T_{1\rho}$ relaxation mechanism that could be well modeled. Those oxides, SnO_2 and TiO_2, which did see a significant change in surface species were not able to be well modeled. This results from the Arrhenius behavior exhibited on these materials in which more of the cyclic erythrose is reacting to form various open chain forms thus depleting the signal intensity for this moiety. This can also be seen in Figure 5.2 where the intensity of the HA-1 group decreases, especially on the SnO_2 surface. Interestingly for TiO_2, the downfield hemiacetal carbon group (HA-2) was still well modeled at 50 ℃ and its $T_{1\rho}$ relaxation time did not change. This indicates the HA-1 is undergoing ring opening while the HA-2 is still maintaining its confirmation most likely due to the site is it adsorbed onto.

5.4 Discussion

5.4.1 Reaction Pathways of Erythrose on Different Lewis Acidic Metal Oxides

In aqueous solution, erythrose exists as an equilibrium mixture with the cyclic hemiacetal (alpha and beta forms) as the predominant species along with the aldehyde and aldehyde hydrate forms[233] (Scheme 5.1). The free aldehyde can act as reactive center for many upgrading reactions of sugars to value-added chemicals and in acidic and basic conditions is in an equilibrium with the keto form, erythrulose. The breaking of the hemiacetal carbon bond in the ring and tracking

whether it remains as an aldehyde or transforms to another moiety is crucial to understanding the reaction pathway. As shown in Figure 5.5, the formation of carboxyl groups directly from the hemiacetal carbon indicate it is the most reactive of the carbons in the original cyclic form. The ring opening of erythrose is further evidenced by the presence of carboxyls in the ^{13}C NMR spectra (Figure 5.3). The extent of the relative amount of carboxyls present is strongly dependent on the surface the erythrose is impregnated. SiO_2 is a well-known catalytically inert material and thus there was minimal carboxyl formation on its surface. At 50 °C, the slight formation of an aldo/keto carbonyl group suggests increasing temperature assists in the ring opening process. The small fraction of ring open erythrose from solution may become stable when on a solid surface, but this driving force was not significant enough to create sufficient ring opened erythrose.

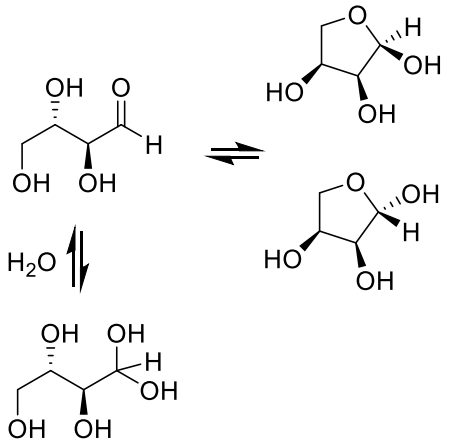

Scheme 5.1 Equilibrium forms of Erythrose in an aqueous environment

Interestingly, aliphatic carbon nuclei are not present on CeO_2, while Nb_2O_5 contained a significant amount at room temperature. SnO_2 and ZrO_2 also contained significant aliphatic carbons present at 50 °C. The presence of carboxyl and aliphatic carbons suggests that a type of disproportionation reaction is occurring on the surface. The proposed mechanism for this is shown in Scheme 5.2. For CeO_2, this pathway would end at the fourth pane where there is a carboxyl

intermediate stabilized on the surface and a carbon singly bonded oxygen species bound on the metal. This Cannizzaro-like mechanism would be base catalyzed and makes sense for a high oxygen storage capacity material like CeO_2.[196] The Cannizzaro reaction has been reported using CeO_2 based metals in alkaline solutions for the conversion of 5-hydroxymethylfurfural to 5-hydroxymethyl-2-furancarboxylic acid and 2,5-bishydroxymethylfuran.[234] For species in which aliphatic carbons are present, the reaction pathway continues as shown in Scheme 5.2. This pathway is known as the Tishchenko reaction and results in the formation of an ester from enolizable aldehydes. The Tishchenko reaction has been reported over various solid basic catalysts.[235] Since most catalysts tested in this study are Lewis acidic, this suggests a bifunctional mechanism is occurring where the metal is assisting in stabilizing one erythrose molecule while, another erythrose molecule is coordinated to a basic surface oxygen atom. Afterwards, the bonds to the surface are severed and the carbocation on the aldehydic carbon is neutralized by the electrophilic oxygen on the corresponding surface species. This is further evidenced by the surface species observed in Figure 5.5. The strong signal for the carboxyl and aliphatic carbons suggests these have to be from the original hemiacetal carbon and when the cycle is broken, the aldehyde is formed and proceeds to form the esterification product from the Tishchenko reaction as shown in Scheme 5.2.

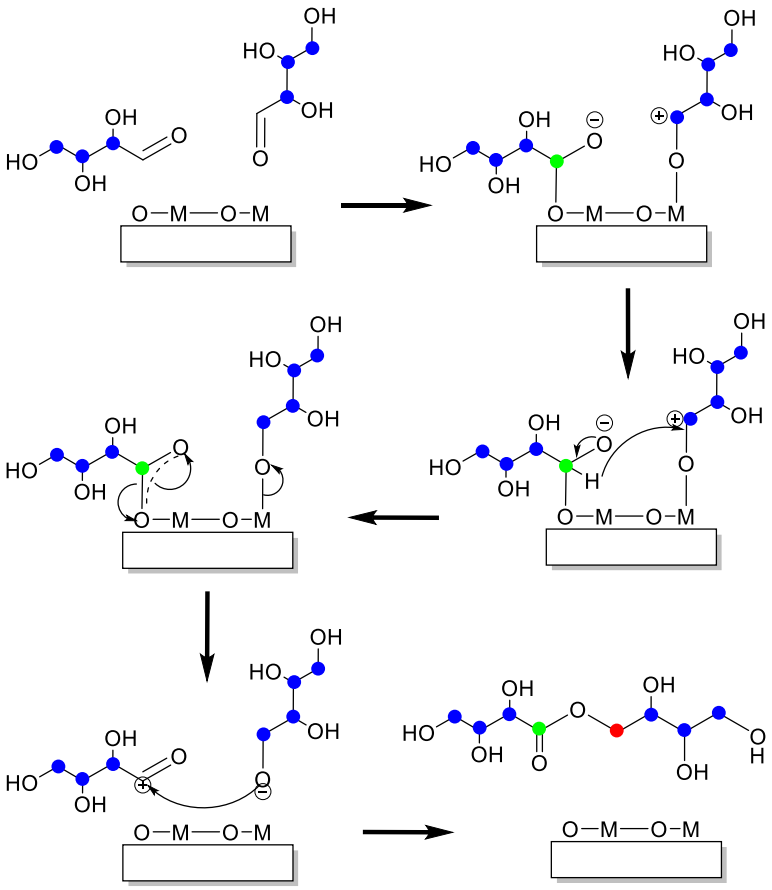

Scheme 5.2 Possible Cannizzaro/Tishchenko reaction pathway of erythrose on a generic metal oxide. Colored dots on carbons correspond to color shaded regions of functional groups within Figure 5.3.

The formation of an ester containing species from erythrose is surprising as erythrose typically has been observed to undergo retro-aldol condensation to glycolaldehyde.[236] This is most likely not occurring on these materials since there would be an aldo/keto carbonyl present and there is only slight signal in that region on SnO_2 and TiO_2. The role of water on the surface could be involved in changing the reaction path. The oxidative nature of the materials may also lead to predominantly carboxylated groups forming due to a high reactive oxygen surface. The hydrate form of erythrose may also be undergoing oxidation creating a carboxyl group. This is shown in Scheme 3. With the pair of peaks in the carboxyl region of the ^{13}C spectra, it is plausible that one

of these peaks is due to the oxidized hydrate form and the other is the from Cannizzaro/Tischenko reaction.

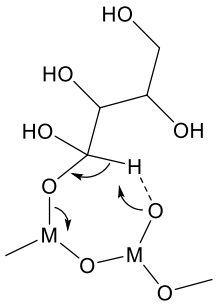

Scheme 5.3. Oxidation of hydrate form of erythrose to form a carboxylic acid on a metal oxide surface.

Most likely the aldo/keto species is due to isomerization of erythrose to erythrulose since the keto form is more stable than the aldehyde form. Rutile TiO_2 has also been shown to catalyze a similar isomerization of glucose to fructose.[203] The isomerization is most likely occurring on TiO_2 since the aldo/keto peak at 212 ppm (Figure 5.3) was very prominent, but for the C1 labelled erythrose this peak was not present (Figure 5.5), thus the carbonyl has migrated from the aldehyde on the labelled to the ketone on an unlabeled position. The presence of the olefinic carbon in the spectra of species on SnO_2 and ZrO_2 is most likely due to a retro-Michael dehydration in which the tertiary carbon has the loss of a leaving group in the form of water (Scheme 5.4). This retro-Michael mechanism was observed for erythrose on Sn-BEA in a batch system.[237] The olefinic carbon can also be from keto-enol tautomerization where the carbonyl has become an alkoxy. Tautomerization is an important step for retro-aldol condensation which has been observed for similar systems.[28,140,154]

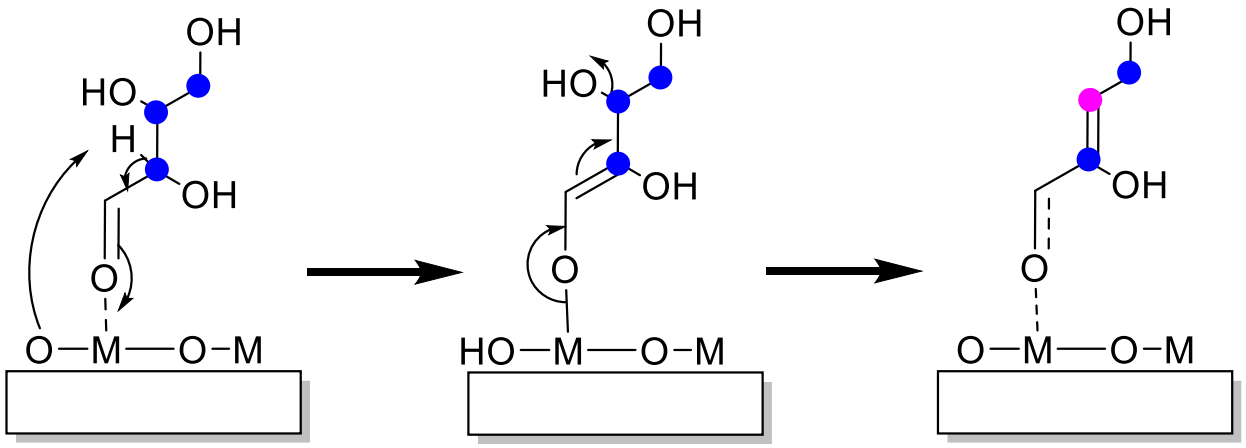

Scheme 5.4 Retro-Michael dehydration of ring opening erythrose on the surface of a metal oxide. Colored dots on carbons correspond to color shaded regions of functional groups within Figure 5.3.

At 50 ºC, the presence/increase of carbon species on SnO_2¸TiO_2 and ZrO_2 points to a kind of Arrhenius behavior exhibited on these materials. While for γ-Al_2O_3, CeO_2 and Nb_2O_5 the relative amount of each carbon remains the same. The slight increase from 25 to 50 ºC resulting in vastly different spectra is surprising. For the SnO_2 and ZrO_2, the retro-Michael reaction resulting in an olefinic carbon present at 150 ppm occurs at 50 ºC suggesting given the right surface, heat might be needed for this reaction to occur. The presence of aliphatic carbons with carboxyls also increased as for the temperature dependent materials meaning the Tishchenko route becomes feasible on certain surfaces at slightly elevated temperature. It is important to note that while these species exist on the surface there is no guarantee they will be able to desorb in this form and therefore corroborating kinetic studies are needed as future work.

Table 5.4 Summary of possible reactions of erythrose occurring on the many tested surfaces

Sample	Cannizzaro	Tishchenko	Dehydration	Isomerization
γ-Al_2O_3	-	X	-	-
CeO_2	X	-	-	-
Nb_2O_5	-	X	-	-
SiO_2	-	-	-	X
SnO_2	-	X	X	-
TiO_2	-	-	-	X
ZrO_2	-	X	X	-

5.4.2 Probing Mobility of Surface Species by $T_{1\rho}$ Relaxometry

The use of NMR relaxometry for insight into surface interactions such as adsorption and diffusion has received significant attention recently.[238–243] Gladden and coworkers have shown that the ratio of the longitudinal (T_1) to the transverse (T_2) relaxation times directly correlates to the adsorption strength for water on various metal oxides.[244] This study brings to the light the potential for using relaxation times as a metric for understanding adsorption strength. The current study seeks to accomplish a similar goal by using values for the $T_{1\rho}$ relaxation time to develop comparisons of the mobility of similar surface species on different materials. $T_{1\rho}$, also known as the spin-lattice relaxation time constant in the rotating frame, is like the T_2 relaxation time but in a spin locked state.[245] Thus, it also allows for measuring the time it takes for decay of the excited magnetization vector. By probing for $T_{1\rho}$ relaxation times at two different temperatures, one can understand which moieties or parts thereof are interacting with the surface in a strong or weak fashion and which are freely moving.

Although the $T_{1\rho}$ relaxation mechanism for the upfield carboxyl (COO1) could only be modeled well for species on the CeO_2 surface, it was shown to have a higher relative relaxation time and did not change at 50 ºC. This is still a valuable finding because it suggests two things about the COO1 group: (i) this carboxyl group is most likely the species attributed to the carboxyl product formed from the Cannizzaro like reaction shown in Scheme 2 and (ii) it is interacting with

the surface in a stronger fashion than the other carboxyl group. Although the COO2 group is present on CeO_2 without aliphatic carbons present, this is mostly due to the aliphatic carbon forming alkoxy groups instead. This again can be attributed to the high oxygen storage capacity of CeO_2 which can result in a kind of over oxidation of surface species.

The longer times for the alkoxy groups suggest these species are the groups primarily interacting with the surface of the oxides, specifically the C-O2 groups whose times do not significantly change at elevated temperatures. The C-O2 group on Nb_2O_5 and ZrO_2 is an exception to this and for both surfaces the relaxation times interestingly head in opposite directions. On ZrO_2, the rise in $T_{1\rho}$ for this species can be explained by surface heterogeneities[246] and migration of the moiety to another site on the surface during heating. For Nb_2O_5, the decrease in relaxation time is most likely due to this group being unbound to the surface and faster motion upon being heated. This is the case with all measured moieties on Nb_2O_5 indicating surface species will be able to desorb more easily relative to the other oxides.

The trend of moieties on TiO_2 not having a significant change in their $T_{1\rho}$ relaxation times but still having the lowest average relaxation time points to weak bonding interaction erythrose derived surface species have with the TiO_2 surface. This is corroborated from the very sharp and narrow peaks present in the TiO_2 DPMAS from Figure 5.2 which indicates very mobile groups. In addition, the supernatant obtained from lixiviation of impregnated TiO_2 (Figure 5.4) also provides evidence that there is some erythrose on the surface that is weakly bound. The peak of the aldo/keto group is indicative of a product at 50 °C, the only material to produce this signal. The implications from these results indicate TiO_2 may be a good candidate for erythrose upgrading. It exhibits Arrhenius behavior and desorbs from the surface relatively easily. By the Sabatier principle, these finding indicate TiO_2 might be a near of the optimum of activity and desorption. It also was able

to retain the highest loading of the erythrose (Table 1) making it more efficient although determining turnover frequency from future kinetic studies will help support this claim.

5.4.3 Descriptors for Performance of Lewis Acid Sites

Determining which factors define the activity, selectivity and stability of Lewis acidic catalysts is critical for choosing future catalysts based on similar characteristics. Electronegativity of metal atoms is one example of a useful descriptor that can be used to rationalize catalytic performance.[210] Using Pauling's definition of electronegativity, Shetty et al. concluded that molybdenum oxide supported on less electronegative oxide supports results in higher activity for hydrodeoxygenation of m-cresol.[247] Another potential descriptor of the electronic environment is the principle of hardness and softness, which was used by Bania et al. to explain that zeolite Y based materials with minimum hardness and maximum softness would have higher activity for oxidative coupling.[248] The ionic radius is yet another descriptor of LAS. Nguyen et al. suggested there was an optimal ionic radius of metal cations large enough for catalyzing the Bilik reaction more effectively.[249] These examples clearly demonstrate the role of relevant Lewis acid descriptors in explaining the activity and selectivity in reactions that are relevant to biomass conversion. This study considers the three aforementioned descriptors along with density of acid sites and other properties of the studied materials to provide clarity as to why certain reactions are occurring on specific metal oxides.

The values of hardness were considered for each metal, not taking into account the oxidation state or coordination.[27] This is certainly operating under the assumption that oxidation state does not affect these values for the metals, which most likely is not the case. No obvious trend can be ascertained for each metal and the surface species formed suggesting these descriptors may not be sufficient for describing these systems. The theory behind hardness and softness may

not hold up in this context and could possibly be explained by the fact erythrose (and possibly other sugars) are not ideal "hard" or "soft" analytes. Both the Mulliken and Pauling electronegativities were also considered as possible descriptors. Like the hardness values, the Mulliken electronegativity was considered for the metal itself.[27] The values of Pauling electronegativity considered were, however, taken in account using both oxidation and coordination number.[250] This did not seem to play much a role as, for both definitions, there is no obvious trend between electronegativity and surface species formed.

The fractional abundance of carboxyl nuclei as a function of ionic radii of the metals based on oxidation and coordination number are shown in Figure 5.6. The ionic radius of Si was by far the smallest at 0.26 Å and Ce was the largest at 0.87 Å. The trend shown is roughly exponential suggesting that increasing the size of the metal cation will catalyze the ring opening of erythrose and potentially other cyclic sugars. Having a larger metal atom may be necessary for catalyzing reactions of C4 molecules and above due to the larger site being able to accommodate biodentate configurations and/or more reactant.[251] Attempts have been made to implement larger metal atoms into relevant material systems to achieve these outcomes. Metal atoms exchanged into the framework of the BEA have been studied to understand the influence of the metal in a well-defined environment (zeolite).[252–255] Li and coworkers suggested the radius of the heteroatom is related to polarizability which affects distortion (geometry) of the active site.[252] Zr had the lowest distortion due to having the largest metal radius which resulted in the lowest energy barrier for glucose isomerization. Based on this conclusion and the activity of CeO_2 towards erythrose ring opening, if stable, a Ce-BEA catalyst would have similar activity or greater activity than Sn-BEA towards glucose upgrading.

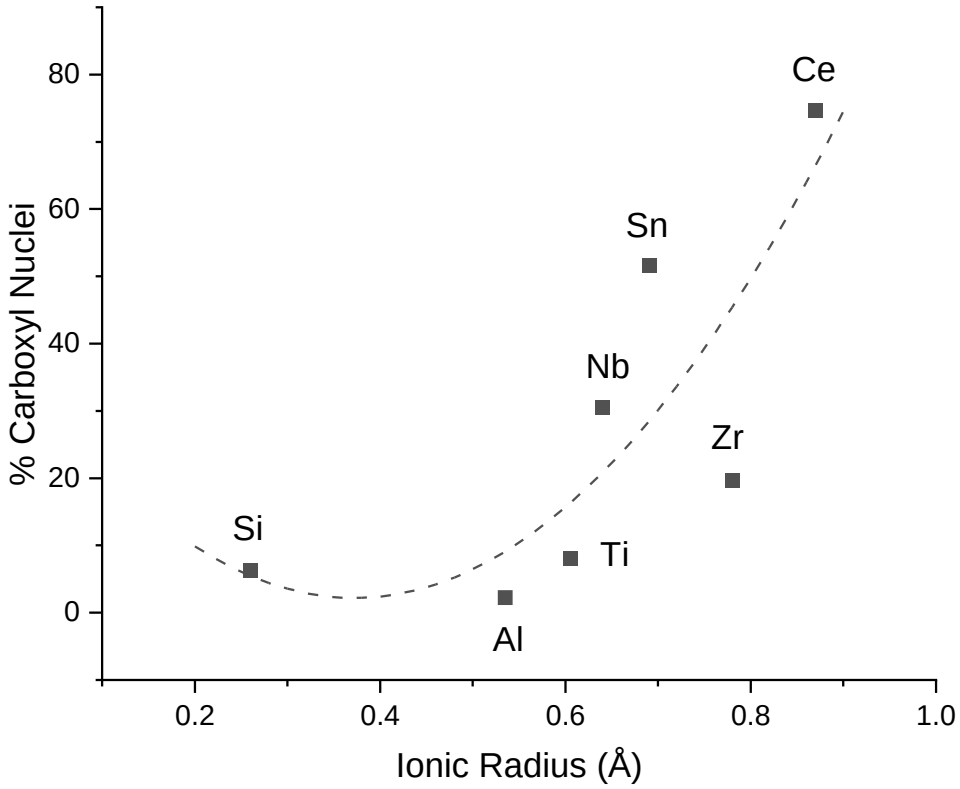

Figure 5.6 Percent carboxyl integrated area in ^{13}C DP-MAS vs. ionic radius of metal[256] based on their respective oxidation states/coordination in metal oxides tested. All integration done for 25 ºC spectra except for SiO_2, SnO_2, TiO_2, and ZrO_2. Coordination numbers were accounted for and based on the coordination in the oxide. The dashed line is to guide the eye.

The density of acid sites did not seem to play a significant role. Although CeO_2 and Nb_2O_5 had significantly high concentration of LAS, γ-Al_2O_3 had the lowest fraction abundance of carboxyl nuclei out of all samples even though it had a significantly high concentration of LAS (Figure 5.2). This suggests γ-Al_2O_3 might not be an ideal catalyst for sugar transformation even though it is active for other biomass relevant reactions such as dehydration.[97,210] For γ-Al_2O_3 to be valuable in a reaction system like this it would need either a dopant or some other catalyst that can engage in a ring opening mechanism with the sugar to begin the series of other relevant reactions hypothesized above. Another inherent characteristic of these materials to consider is the redox capability. CeO_2 is known to be very redox active which has shown to be impactful in catalyzing reactions.[109,257] CeO_2 also has a high oxygen storage capacity,[196] which can lead to having very

basic oxygen species on the surface which may also contribute to the high relative amount of carboxyl formation compared to the other materials tested here. The high oxygen storage capacity can also leave to over oxidation of products which may suggest it is not ideal for hydrodeoxygenation (HDO). CeO_2, however, is very reducible[258] which may be useful to achieve HDO in tandem with other ones described here. Nb_2O_5 has significant Brønsted acidic character to it while the other metal oxides do not and this could play a role in the ring opening of erythrose as has been shown for glucose on Nb_2O_5 elsewhere.[259] The Brønsted acidity is also necessary, in a cooperative manner with Lewis acidity, for the dehydration and isomerization of smaller sugars as shown for dihydroxyacetone to lactic acid.[260]

5.5 Conclusion

The reaction pathways of erythrose over Lewis acidic metal oxides is very dependent on the nature of material. SS-NMR revealed aliphatic, carboxyl, and olefinic nuclei that formed from erythrose at varying degrees. Nb_2O_5 created the most moieties which means it is most active. Since it was not affected by the increase in temperature, it can catalyze the ring opening of erythrose and other reactions at low temperatures making it ideal for sugar chemistry. This study is also one of the first to consider the interactions of a sugar on Lewis acidic metal oxides using NMR relaxometry. Alkoxy groups on all oxides had the longest average relaxation time suggesting they are interacting with the catalyst surface most strongly. TiO_2 had the shortest average $T_{1\rho}$ relaxation time and when the impregnated sample was washed, significant amount of species came off relative to γ-Al_2O_3. The short relaxation times of species on TiO_2 point it to being a weakly acidic material that may not deactiactivate as quickly but also not be as active. Ionic radius of the metal plays a role in the ability of erythrose to undergo a ring opening mechanism where a large cation

is beneficial for catalyzing the reaction. Redox activity is also an important property as the case with CeO_2.

Chapter 6 Final Conclusions and Recommendations for Future Work

6.1 Final Conclusions

The main theme of this thesis was to study how Lewis acids catalyze relevant reactions for biomass conversion. Specifically, how metal oxide catalysts that possess Lewis acidity can catalyze reactions, such as aldol condensation and isomerization. By taking a kinetic and surface science approach to this work, reaction mechanisms and surface interactions were elucidated. The systems studied in this work have provided critical insight into how Lewis acidic surfaces need to undergo dynamic changes to catalyze reactions like aldol condensation and esterification. A core understanding of how Lewis acid sites on oxides interact with certain oxygenated moieties was created in this work and serves as a knowledge basis that can be used to rationalize similar systems.

In Chapter 2, the effect of the reducible nature of MoO_3 on the aldol condensation of ethanol and acetaldehyde was investigated. Pretreating MoO_3 in O_2, N_2 and H_2 resulted in varying oxidation states of the Mo atoms. More harshly reduced MoO_3 was closer to the Mo (IV) oxidation state, while oxidative pretreatment kept the Mo oxidation state at Mo (VI). The more reduced sample was able to adsorb higher quantities of ethanol and acetaldehyde compared to the MoO_3 sample reduced more mildly using N_2. When the MoO_3 was more reduced, higher quantities of crotonaldehyde formed as well. This was hypothesized to be due to CUS formed from oxygen vacancies with the H_2 pretreated sample having the highest density of CUS. The mechanism of aldol condensation occurs through tautomerization of an adsorbed acetaldehyde molecule to the corresponding enolate with addition of another acetaldehyde molecule to form 3-hydroxybutanal followed by dehydration to crotonaldehyde.

Chapter 3 built off the work from Chapter 2 and addressed a major problem with the bare MoO_3 used in Chapter 2, the low surface area. MoO_3 was deposited onto two high surface area

supports, SiO_2 and Al_2O_3, and tested for aldol condensation of acetaldehyde. By adjusting the weight loading, the SiO_2 supported materials showed a monotonic increase in crotonaldehyde yield when the MoO_x loading increased. The same was not true for Al_2O_3 supported materials, where the lowest loading of MoO_x showed the best performance. The bare Al_2O_3 support showed decent activity for aldol condensation, and when Mo weight loading was increased to 20 wt% Mo the mass time yields were practically the same. This indicates that MoO_x can provide enhancement at low weight loadings, but at higher loadings, the Al active sites become quenched reducing conversion. Pyridine adsorption experiments followed by FTIR spectroscopy were used to quantify the concentration and strengths of the acid sites. It was concluded that the concentrations of medium and strong acid sites positively correlated with high production of crotonaldehyde.

Chapter 4 investigated how four different Lewis acidic metal oxides catalyze the retro-aldol condensation of two C4 probe molecules. The dehydration of 3-hydroxybutanal was shown to occur on γ-Al_2O_3 while on CeO_2, Nb_2O_5 and TiO_2 the retro-aldol condensation of 3-hydroxybutanal was observed. This means γ-Al_2O_3 is better suited for directed dehydration of a polyoxygenate compound while the other catalysts are able to coordinate larger molecules and catalyze C-C bond cleavage. Dehydration of 4-hydroxy-2-butanone to methyl vinyl ketone occurred on γ-Al_2O_3, CeO_2, and TiO_2 , which were strictly Lewis acidic. On the Brønsted and Lewis acidic Nb_2O_5 retro-aldol condensation of 4-hydroxy-2-butanone to acetone and formaldehyde occurred due to the ability of the catalyst to adsorb both the ketone and alcohol group of the adsorbate. Thus, bifunctional acidity is believed to be more beneficial for retro-aldol condensation of ketone and alcohol containing oxygenates.

In Chapter 5, erythrose upgrading was investigated using SSNMR spectroscopy. Erythrose derived surface species were observed on a variety of Lewis acidic metal oxides. Ring opening

was prominent on several catalysts at room temperature. One reaction mechanism that occurred was the Tischenko reaction in which primary aldehydes undergo coupling to form an ester. This occurred on Nb_2O_5 at room temperature and on SnO_2 and ZrO_2 at 50 ºC. Erythrose isomerization was only detected on TiO_2, suggesting this is the ideal catalyst tested for this reaction. The surface species adsorbed on TiO_2 were also the least strongly bound as determined by their peak width in the SSNMR spectra and through NMR relaxometry. This suggests that using TiO_2 as a catalyst for erythrose upgrading may lead to high throughput and not suffer significant deactivation. The atomic radius of the metal cation in the catalyst had a positive correlation to the amount of carboxyl groups present, an indication for the extent of ring opening that occurred.

6.2 Recommendations for Future Work

6.2.1 Determining the Reducibility of SnO_2 and its Consequences on Aldol Condensation

6.2.1.1 Characterization SnO_2 Reducibility

Based on the work shown in Chapter 2 and 3, reducing MoO_3 had clear advantages for adsorption of small oxygenates onto the surface due to creation of defects sites. Preliminary work using synthesized SnO_2 shows that reduction of the metal atom may not be entirely advantageous. Using the same SnO_2 synthesized for the work in Chapter 5, the effects of reduction on the metal center have already been underway. *In-situ* XAS measurements were carried out using high temperature reactor setup. SnO_2 was loaded into the cell and the sample was heated to 450 ºC under H_2 flow. The results from this experiment are displayed in Figure 6.1.

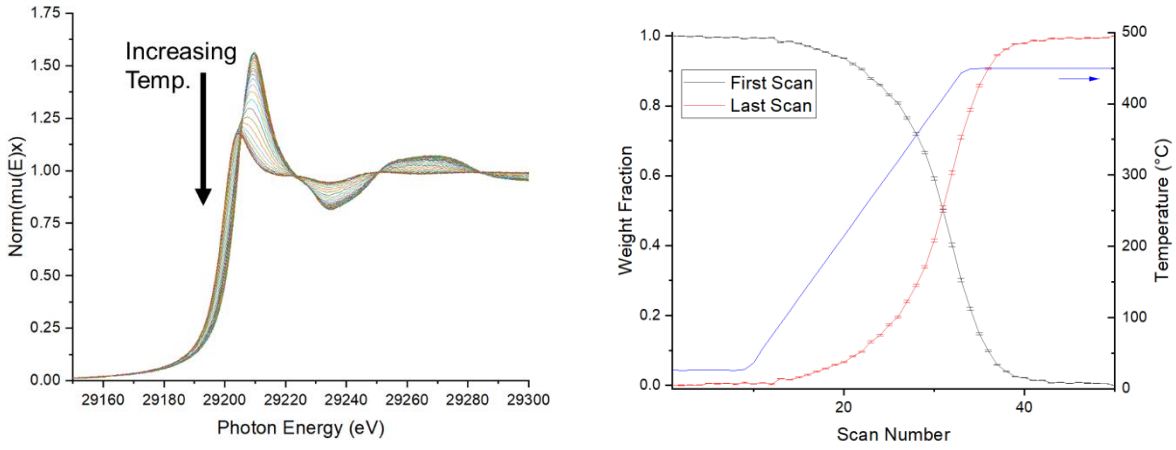

Figure 6.1 XANES spectra of SnO_2 during temperature ramp from room temperature to 450 °C under H_2 flow (left). Change in weight fraction of Sn (IV) and Sn (0) (black and red respectively) during fitting of XANES spectra as a function of sample temperature

These results indicate that, like MoO_3, SnO_2 can undergo severe reduction of the metal center through harsh reduction conditions. In this case, the oxide itself approaches a Sn (0) oxidation state. From Figure 6.1, the oxidation state began to decrease as the temperature approached 100 ºC. This suggests that using a lower reduction temperature, such as 200 ºC may create some defect Sn centers that can act as active sites like in the MoO_3 work.

XRD was used to further characterize the reduced SnO_2 (Figure 6.2). Diffractogram peaks are marked based on origin from Sn metal or SnO_2.[261] The results clearly indicate that the sample became almost entirely metallic after the same reduction step that was used in the XAS experiments. Future work should focus on adjusting the pretreatment procedure to find an optimum oxidation state in which some of the oxide state is preserved but vacancies are still created.

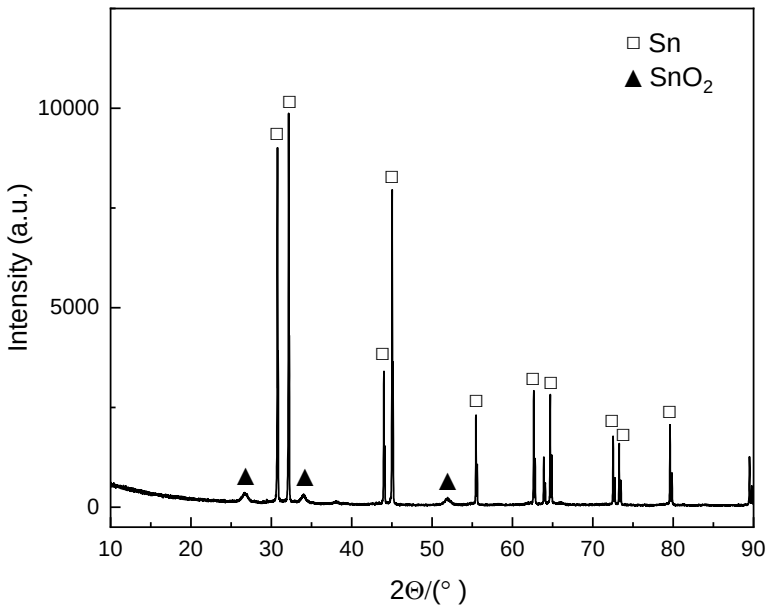

Figure 6.2 XRD Diffractogram of SnO2 after pretreated in 40 sccm H_2 at 450 ºC for 1 h

6.2.1.2 DFT Calculations of Small Oxygenate Adsorption on SnO_2

Adsorption energies of ethanol and acetaldehyde on the surface of a pristine and a reduced SnO_2 surface were calculated using DFT. A rutile SnO_2 slab with the 110-facet consisting of 32 atoms was constructed and all calculations were performed using Quantum Espresso and exchange-correlations interactions were treated with the BEEF-vdw functional. A 4x4x1 k-point basis set was employed with a 500 eV planewave cutoff. Values for adsorption energies were determined using the following equation,

$$E = E_{slab+ads} - E_{slab} - E_{ads}$$

where E is the adsorption energy and $E_{slab+ads}$, E_{slab}, and E_{ads} are the DFT energies from the adsorption complex, catalyst slab, and adsorbate respectively. To simulate a defect (oxygen vacancy), the bridging surface oxygen atom was removed and the geometry of the slab was re-optimized. Table 6.1 shows the calculated adsorption energies.

Table 6.1 DFT adsorption Energies of small oxygenates on pristine and defect containing SnO_2

Adsorbate	Pristine Surface (eV)	Defect Surface (eV)
Ethanol	-1.95	-1.34
Acetaldehyde	-1.08	-1.08

As can be seen, the adsorption of ethanol on a pristine SnO_2 was more favored on the reduced surface than the defect containing one. It must be noted that this energy was calculated using a constraint on the O-H bond of the alcohol because deprotonation by a surface oxygen was readily occurring during the initial geometry optimization. After the first set of optimization cycles, the constraint was removed and the system was allowed to re-relax. This, along with the lower adsorption energy of ethanol on the pristine surface, implies that SnO_2 has strong surface basicity. Removing an oxygen atom will reduce the overall basicity of the surface and thus reduce the strength of this interaction. Interestingly, the adsorption energy of acetaldehyde on both surfaces was the same. As seen with MoO_3, the creation of surface defects enhanced the propensity of aldehydes to adsorb onto its surface. The same cannot be said about SnO_2. While the adsorption energy was negative, there was no difference in the values themselves. This brings up an interesting notion about whether surface basicity plays a more dominant role than defect sites for the adsorption of aldehydes.

6.2.1.3 Future work for SnO_2

Future work for understanding the dynamic behavior of the SnO_2 surface and its interaction with various small oxygenates should be pursued. Initial results suggest that SnO_2 is heavily reducible and consists of active base centers that may act as active sites. As mentioned earlier, the pretreatment step should be investigated more heavily by combining XRD with *in-situ* UV-VIS spectroscopy. XRD patterns can show the beginning formation of crystalline metallic Sn domains. By using *in-situ* UV-VIS diffuse reflectance spectroscopy, bandgaps of SnO_2 at various

temperatures can be determined and then used to calculate the oxidation state of the Sn metal. This will provide clarity on how reduced the SnO_2 has become and can be used to study how SnO_2 behaves as a catalyst for aldol condensation of ethanol and acetaldehyde.

In addition to characterization, more experiments should be done to study how ethanol and acetaldehyde interact with SnO_2 and SnO_x. Like in Chapter 2, TPD-MS measurements should be used to measure how much ethanol and acetaldehyde are able to adsorb onto the surface after various pretreatments. At this stage, it is hypothesized that an oxidatively pretreated SnO_2 will adsorb more ethanol than a reductively pretreated SnO_2. For acetaldehyde, the effect of pretreatment temperature used needs to be further investigate. SnO_2 reduced at higher temperatures will have more defects to adsorb the oxygen of the aldehyde. While a SnO_2 that was reduced at lower temperatures will have more surface oxygen present which can attack the carbon of the aldehyde. This could lead to two different reaction pathways that needs to be studied more. Additionally, DRIFTS should be used to study the surface species that form from adsorbed ethanol and acetaldehyde. This will give insight into the reaction mechanism. Products identified from the DRIFTS spectra will corroborate those from the TPD-MS experiment. The DRIFTS experiments should also use a TPD step to see which surface species remain and can be used to verify which products are observed from the TPD-MS.

6.2.3 Kinetic Study of Erythrose Upgrading and PFG-NMR

Results in Chapter 5 provided strong evidence for coupling reactions of erythrose to larger C_8 species. Future kinetic studies will help confirm these findings through product identification and provide valuable insight into the reaction kinetics. Some work has already been carried out using a liquid flow reactor setup described elsewhere.[262] The results are displayed below (Figure 6.3). An initial concentration of 6 mM was used for the reactant, erythrose. After reaction there

was a slight change in the catalyst of the color, going from white to a slight tan color. This could possibly be due to the formation of humins. LCMS results indicated that the main product formed from the reaction is a C8 product with a mass of about 240. This suggests the product formed from the coupling of two erythrose molecules as hypothesized from Chapter 5. As temperature increased, the conversion increased. Future work should be on running reactions for the different catalysts tested in Chapter 5 and calculating important values like conversion and activation energies through construction of Arrhenius plots. Additionally, various reaction pathways can be deconvoluted. Special care should be given to limiting mass transfer limitations by adjusting flow rates of the product to make sure the conversion adjusts correspondingly. This will ensure the kinetics of the reaction are what is being controlling mechanism. Various particle size ranges can also be tested to make sure external mass transfer limitations are negligible.

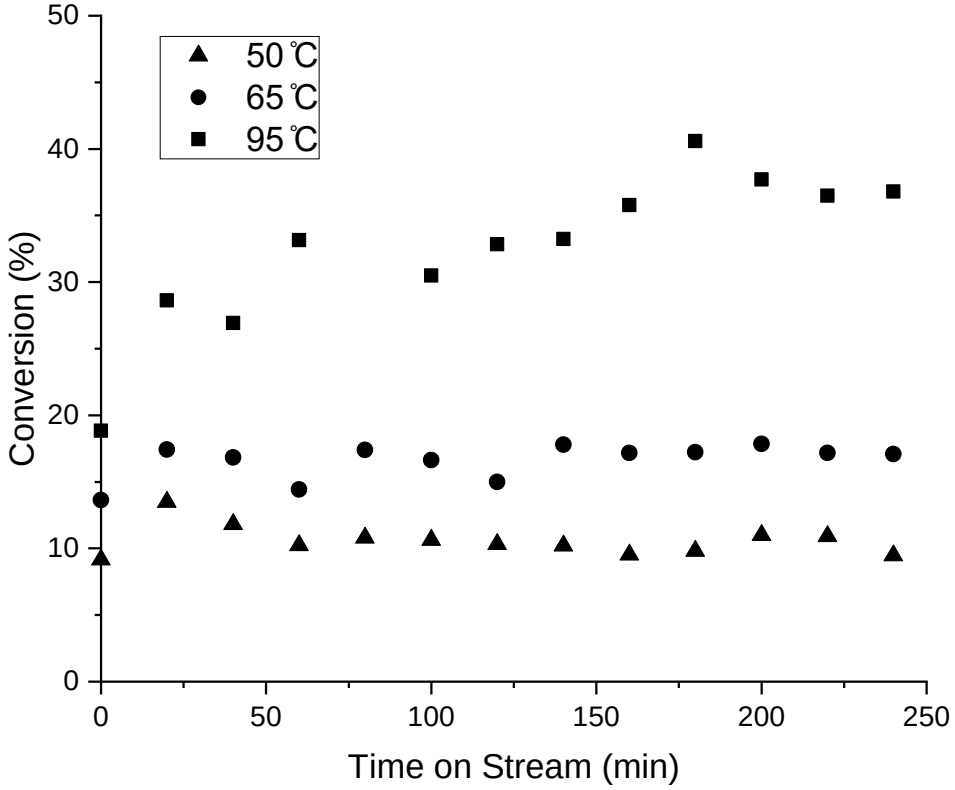

Figure 6.3 Erythrose conversion over Nb_2O_5 at various temperatures. W/F = 0.4 g•smL^{-1}

Along with preliminary kinetic studies, PFG-NMR studies have initially been conducted to measure the diffusivity of erythrose within relevant microporous materials. Fully ^{13}C labeled erythrose solution (0.175 M) was added to NMR tubes containing powders of highly crystalline microporous materials. Using a PFG-NMR pulse sequence, diffusivity of erythrose can be measured. The free diffusion of erythrose in solution was also measured to understand how the diffusion is affected within a porous network. Results are shown in Table 6.2.

Table 6.2 Diffusivity Values of Erythrose within Various Porous Materials

Material	Diffusivity (x 10^{-10} m^2/s)	Pore Size (Å)
MCM-41	1.6	25
SBA-15	1.6	57
Zeolite Y	3.9	7.4
N/A	8.5	N/A

These results indicate that clearly there was some diffusion hinderance of erythrose when it was introduced to the environment of a mesoporous and microporous material. The difference in diffusion between the silica-based materials (MCM-41 and SBA-15) and the silica-alumina based material (Zeolite Y) is surprising when strictly considering the pore sizes. It is possible that for Zeolite Y, the water in solution is the dominate adsorbate on the surface and erythrose is freer to move within a hydrated environment relative to the silica environment, which may have significant silanol nests that could hinder diffusion. These early results set up an interesting project that can focus on how sugars diffuse through the porous network of relevant heterogeneous catalysts. Changing the solvent from water to an alcohol may provide insight into whether the geometric environment is affecting diffusion or there are some interactions between the solvent and surface playing a role.

NMR relaxometry was also used to study the interactions of erythrose with other zeolites. It was shown by Gladden and coworkers that ratios of the T_1/T_2 relaxation times are directly related to the adsorption strength.[239,244] Based on the ratio of relaxation times, confinement effects and other geometric constraints of the zeolite are negligible, wheras surface interactions determine the strength of interaction.[244] The Si/Al ratio is an important factor for choosing zeolites to study and understanding how certain reactions are catalyzed. Thus, the effect of Si/Al ratio on the T_1/T_2 relaxation time was studied and results are shown in Figure 6.4.

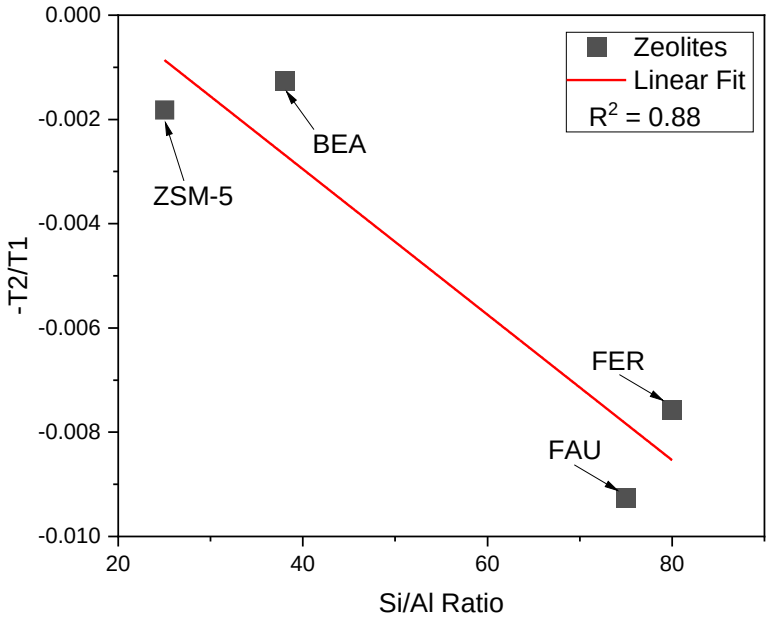

Figure 6.4 Relationship of Si/Al ratio from various zeolites versus $-T_2/T_1$

These results show that as the amount of Si is increased relative to Al, the ratio of $-T_2/T_1$ decreases. As Gladden and coworkers have shown for various heterogeneous systems, a lower value of $-T_2/T_1$ corresponds to weaker adsorption strength. Thus, it can be concluded that having more Al sites present in the catalyst will give a higher value of $-T_2/T_1$. This makes sense as having more Al sites in a zeolite framework can create more Lewis acid sites thus adsorbing more oxygenated functional groups than a Si site. Thus, Al sites will act as electron sinks and lead to

strong adsorption. This preliminary work provides very interesting insight into the surface interactions of erythrose with relevant crystalline materials. This technique would avoid the standard TPD-MS experiments which would suffer from reaction of adsorbed erythrose and sugar degradation which can occur at lower temperatures (100 °C). Future experiments with additional zeolite samples would provide statistical confidence in the above trend. Additionally, measuring zeolites with Si/Al ratios between 40 and 70 would provide more test points and confirm the hypothesis that having more Al sites gives a higher $-T_2/T_1$. Using zeolites with the same framework but different Si/Al ratios would also give solid evidence that it is the chemical nature of the material that is changing the adsorption interaction and not the geometry of the zeolite itself.

6.2.3 Surface Interactions of Erythrose on Metal Supported Catalysts

Building off the work from Chapter 5, the surface reactions of erythrose on other relevant heterogeneous catalysts should be investigated using SSNMR spectroscopy. Specifically, metal supported on oxide catalysts should be studied for erythrose upgrading. Cho et al. concluded that having both metal and acid sites for conversion of furfural to valeric acid was necessary for high performance and reducing catalyst deactivation.[263] This serves as motivation to study a similar system with erythrose. SSNMR ^{13}C spectra of erythrose on Pt/γ-Al_2O_3 and Pt/BEA systems and their supports are shown in Figure 6.5. There was slight increase in the intensity of carboxyl region and carbonyl region for the γ-Al_2O_3 based materials. This indicates that the Pt atom is having some added benefit in ring opening towards the ring-opening of erythrose. Looking at the spectra for the surface species on BEA, there is barely any difference between the addition of Pt and the bare support. Although there is very slight formation of carbonyl and carboxyl groups, this is almost negligible. There is, however, interesting differences between the two different supports. On γ-Al_2O_3 the shape of the spectra is much broader than the shape of the surface species on BEA. This

indicates that the erythrose on the surface is much more mobile within the zeolite framework then the γ-Al_2O_3. This result is interesting as it shows there is some additional benefit to incorporating Pt atoms with acidic catalysts. Repeating these experiments at higher temperatures to determine which groups form along with adjusting the Pt weight loading should be included as future work in this thrust.

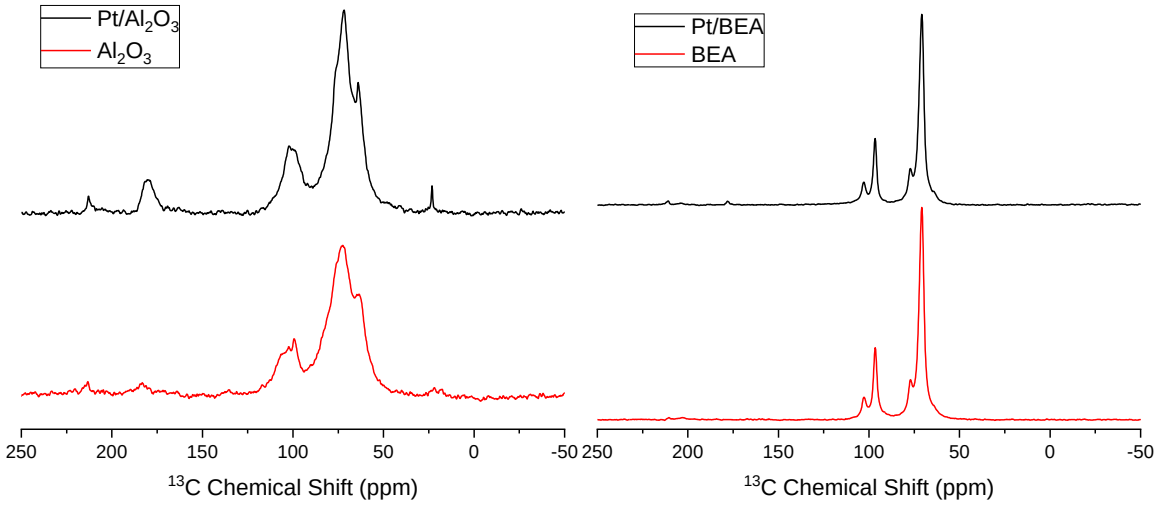

Figure 6.5 ^{13}C spectra of erythrose adsorbed onto the surface of Pt/γ-Al_2O_3 and Pt/BEA and supports

6.2.4 Surface Interactions of Glucose on Lewis Acidic Heterogeneous Catalysts

A main motivation behind the work of Chapter 5 was to understand the interactions of a model sugar compound on the surface of Lewis acidic heterogeneous catalysts. This was the primary reason to use erythrose for these studies was to reduce the complexity of data analysis. Given the strong understanding developed from Chapter 5 along with the optimized methodology, the logical next step would be to run similar experiments with glucose, the most abundant sugar in nature. Some early work was performed for determining the heat of adsorption of glucose on some metal oxides (Table 6.3). These measurements were done using a Calvet C80 Setaram Calorimeter

in which the sample cell consisted of hydrated catalyst in the inner cell and a 0.05 M glucose solution in the outer cell. The reference cell was the same without the catalyst present to account for the heat of solution resulting from mixing the two liquids. After a thermal equilibrium was reached, the samples were allowed to mix overnight and the final concentration was calculated using HPLC. The results for the final heats of adsorption are shown in Table 6.3 along with some values from similar studies.

Table 6.3 Heat of adsorption of glucose on several catalysts. Some values from literature are shown[264,265]

Material	ΔH_{ads} (kJ/mol)	Reference
MgO	-19.3	This Work
Nb_2O_5	-1.3	This Work
HY Zeolite	-77.4	264
MCM-41	-3.7	264
H-BEA	-8.7	265

The higher heat release during glucose adsorption on MgO as opposed to Nb_2O_5 indicates there is a stronger interaction between glucose and this sample. In the work in Chapter 5, Nb_2O_5 was shown to be active for the ring opening of erythrose and similar experiments should be done with glucose. This also indicates that since there was less heat released from glucose adsorbing onto Nb_2O_5, the relative amount of surface species formed from MgO may be greater in quantity. Future work should incorporate the same oxides tested in Chapter 5, and ^{13}C SSNMR spectroscopy measurements should be run to determine surface species.

Appendix A Supplementary Information for Chapter 2

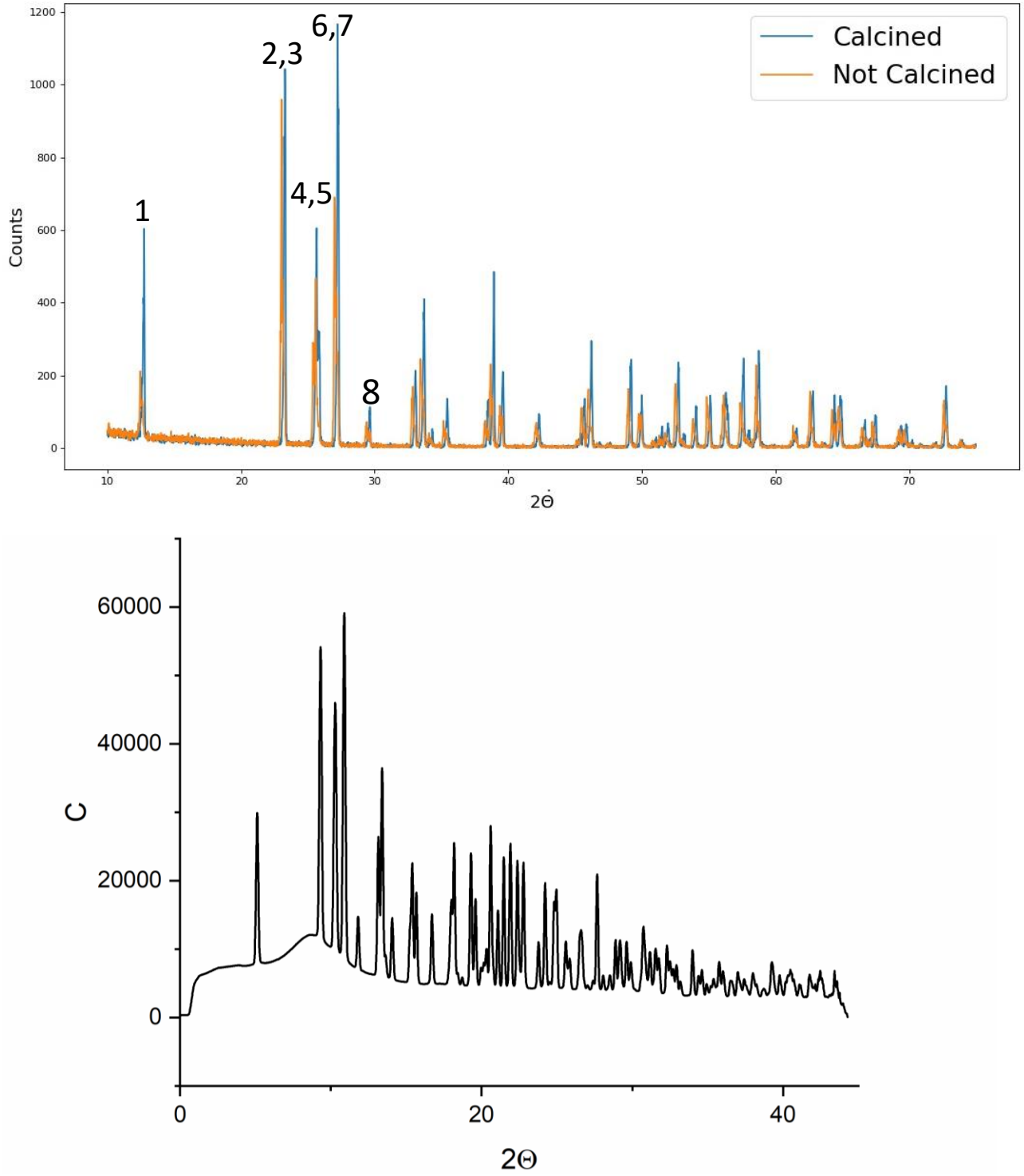

Figure A.1 (A) Diffractogram of before and after calcination of MoO_3. (B) after treatment at 450 C for 1 h in H_2.

Table A.1 D-spacing of the peaks labeled in Figure A1A for both the calcined and uncalcined samples

Peak No	d-spacing [Å] (Uncalcined)	d-spacing [Å] (Calcined)
1	7.10412	6.93498
2	3.86104	3.82878
3	3.81847	3.81305
4	3.50534	3.46951
5	3.47726	3.44036
6	3.29964	3.27346
7	3.26725	3.26343
8	3.03870	3.00851

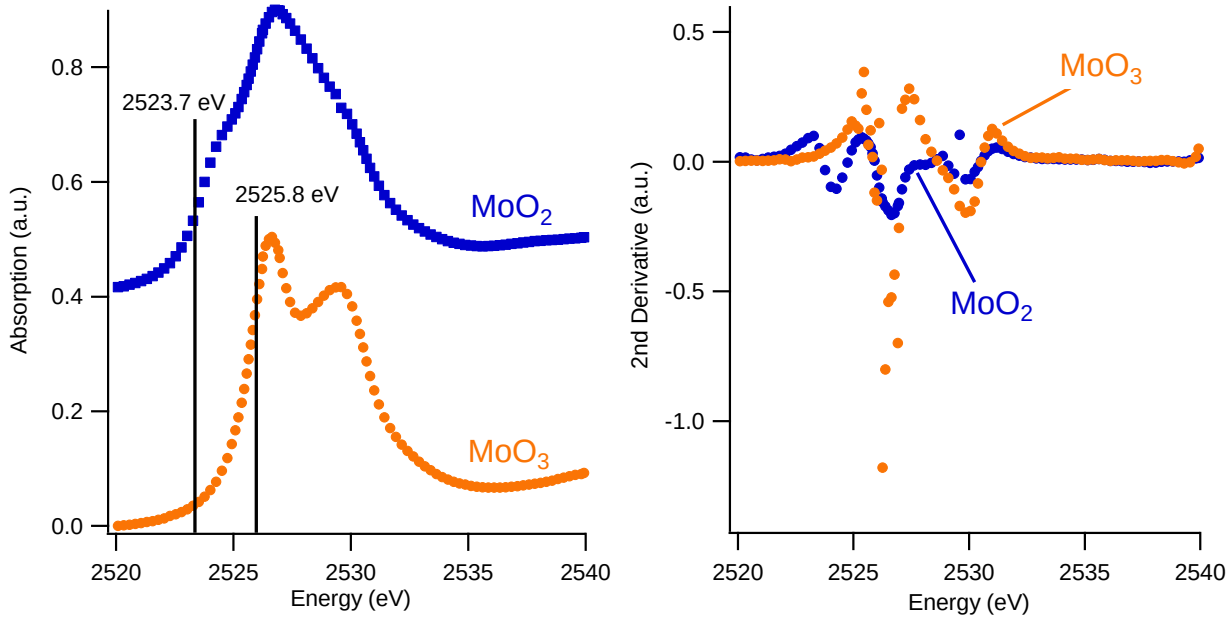

Figure A.2 Digitized XANES Mo L3 edge spectra (left) and 2nd derivative (right) of MoO_3 and MoO_2 from Kashiwabara et al.[69] Data was shifted up 4.9 eV in energy to align the MoO_3 spectra with the O_2 treated MoO_3 sample from this study.

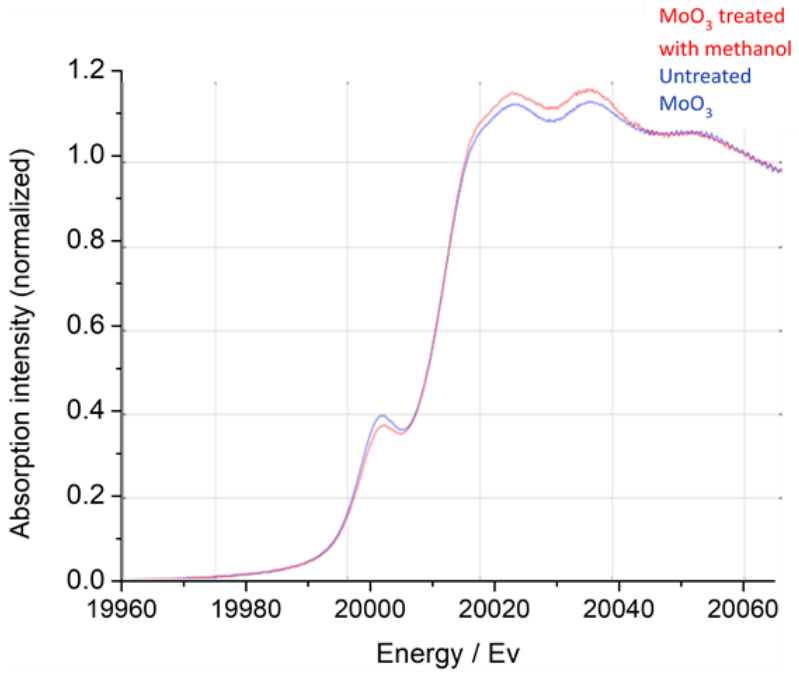

Figure A.3 Mo K-edge XANES spectra of MoO_3 before and after exposure to methanol

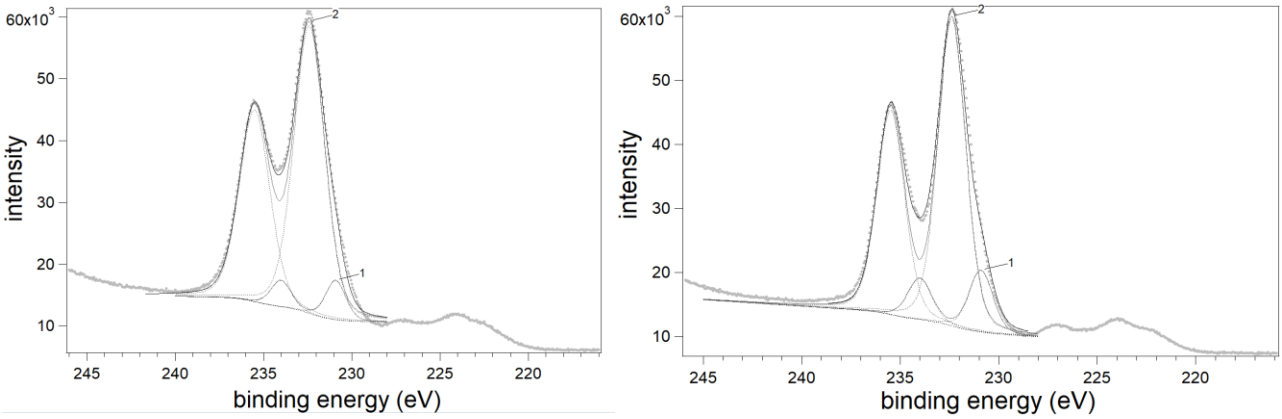

Figure A.4 X-ray photoelectron spectra and fits for Mo 3d in MoO_3 before (left) and after (right) exposure to methanol

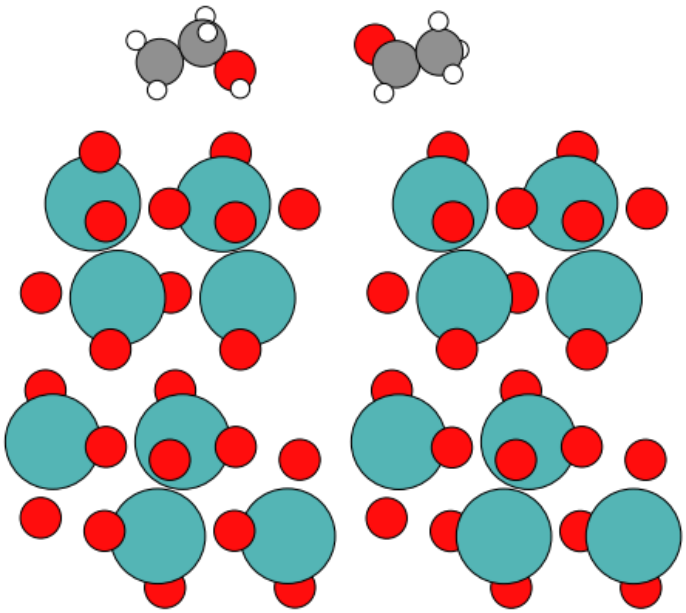

L to R: Ethanol and acetaldehyde on pristine MoO_3

Figure A.5 Adsorption geometries of ethanol and acetaldehyde on O-MoO_3. All atoms are represented by using their covalent radii

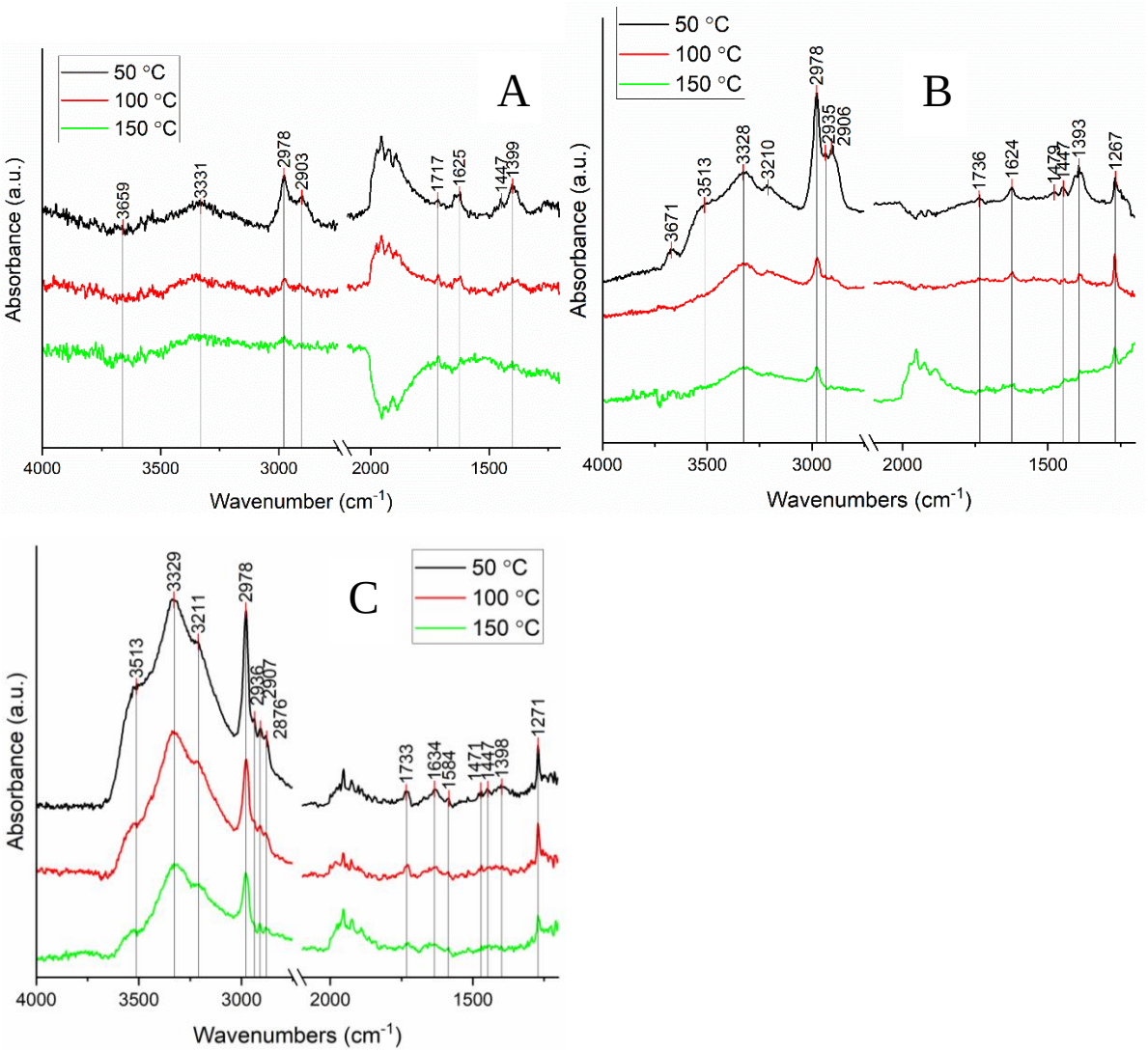

Figure A.6 DRIFTS spectra of ethanol adsorbed onto (A) R-MoO_x (B) I-MoO_x and (C) O-MoO_3

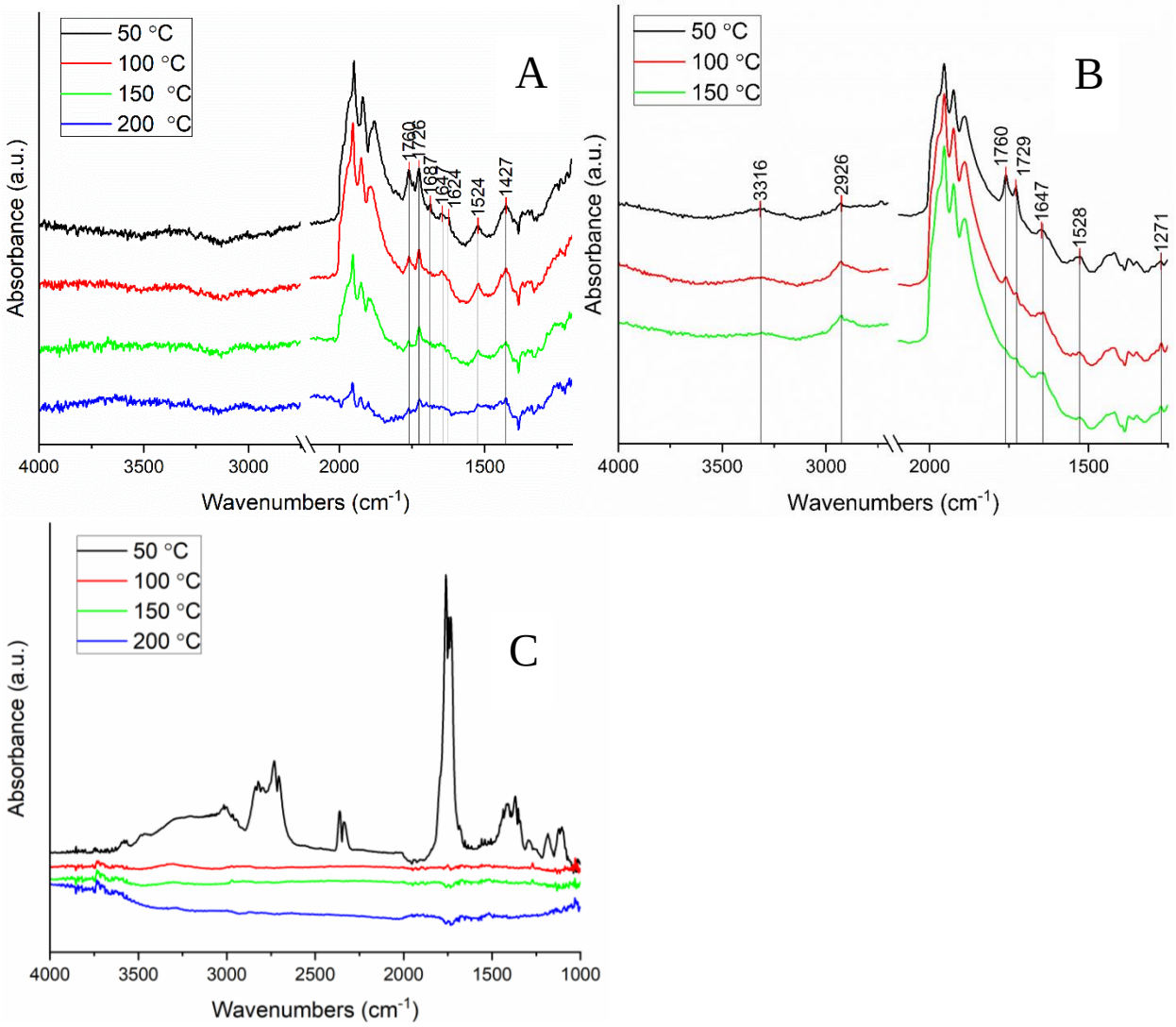

Figure A.7 DRIFTS spectra of acetaldehyde adsorbed onto (A) R-MoO_x (B) I-MoO_x (C) O-MoO_3

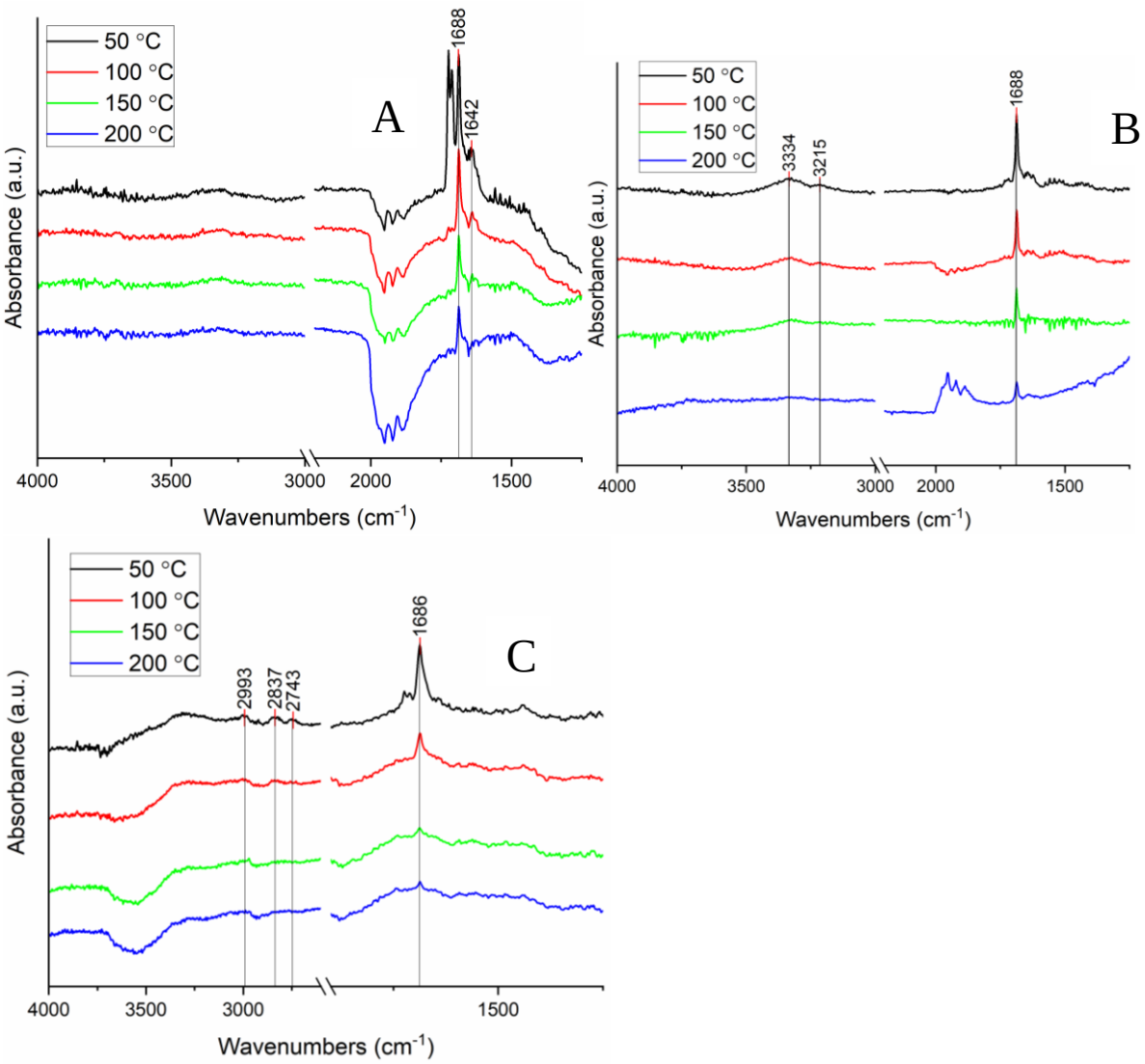

Figure A.8 DRIFTS spectra of crotonaldehyde adsorbed onto (A) R-MoO_x (B) I-MoO_x (C) O-MoO_3

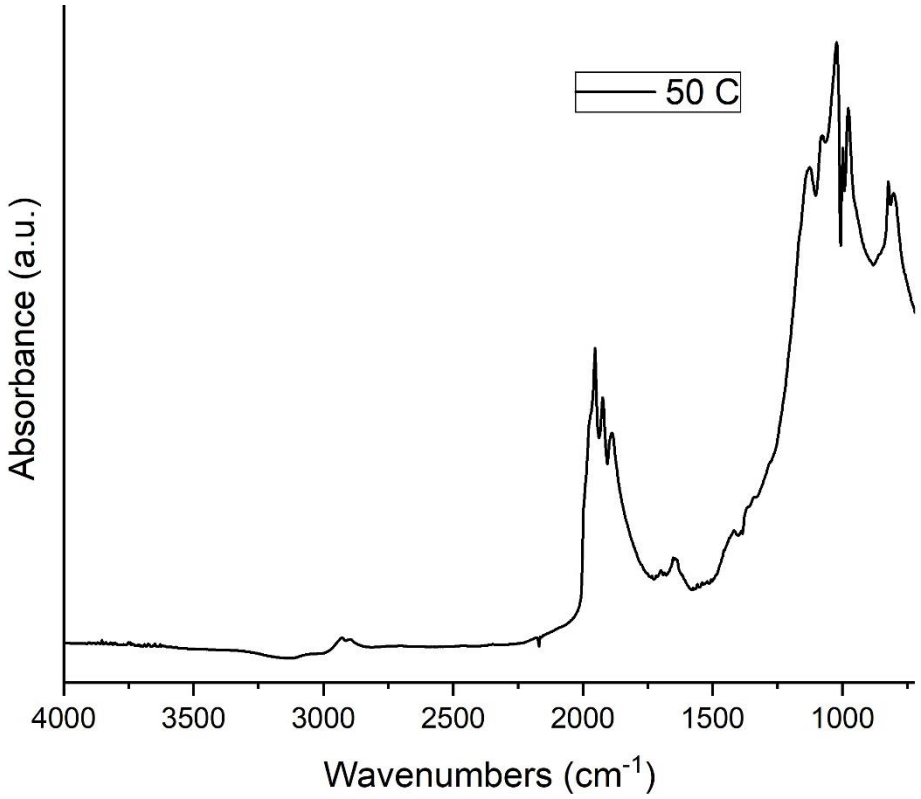

Figure A.9 DRIFTS spectra of MoO_3 at 50 ℃ after oxidative pretreatment

Table A.2 Vibrational Frequencies of ethanol on pristine MoO_3 and defect MoO_3

Pristine MoO_3 (cm^{-1})	Defect MoO_3 (cm^{-1})
50	50
50	50
50	61.6
50	87.9
58.4	121.7
132.4	182.9
270.6	253.0
358.2	357.6
410.9	394.0
779.8	792.1
853.0	817.1
1013.9	881.3
1024.7	1012.9
1093.1	1120.0
1256.7	1174.6
1352.1	1294.2
1380.2	1387.2
1407.6	1409.8
1457.2	1468.6
1489.7	1479.7
1411.0	1496.6
2988.4	3013.7
3010.3	3015.9
3029.4	3064.0
3075.8	3085.1
3135.9	3103.6
3691.9	3545.7

Table A.3 Vibrational Frequencies of acetaldehyde on pristine MoO_3 and defect MoO_3

Pristine MoO_3 (cm^{-1})	Defect MoO_3 (cm^{-1})
50	50
50	50
50	50
59.3	50
94.4	216.2
110.2	222.1
168.8	237.0
455.4	554.8
741.6	575.1
916.2	969.3
1069.	995.4
1106.8	1105.0
1353.7	1356.1
1395.9	1396.3
1447.9	1445.4
1482.1	1451.4
1678.5	1564.4
2858.7	2979.3
3022.0	3022.9
3093.1	3040.9
3119.8	3114.0

Table A.4 Vibrational Frequencies of crotonaldehyde on pristine MoO_3 and defect MoO_3

Pristine MoO_3 (cm^{-1})	Defect MoO_3 (cm^{-1})
50	50
50	50
50	50
50	38.5
50	126.1
56.0	149.4
86.9	203.3
136.0	216.7
175.9	246.8
220.3	301.1
455.9	484.7
530.1	596.3
652.6	672.7
799.8	782.6
841.4	891.5
951.1	971.0
1001.4	990.2
1093.8	1108.3
1132.4	1197.7
1178.0	1274.7
1259.2	1293.3
1311.8	1311.0
1326.7	1393.2
1420.3	1446.7
1463.3	1484.5
1669.2	1513.7
1722.2	1634.5
2240.3	2829.7
2880.6	2992.4
3011.7	3062.8
3074.8	3072.1
3093.3	3102.2
3125.9	3118.6

Table A.5 Ethanol TPD Total Molar Desorption Quantities

Ethanol TPDs		
	Moles Desorbed ($x10^{-8}$)	
	Inert	Reduced
Ethanol	34.9	210.3
Acetaldehyde	35.8	96.6
1,3-Butadiene	-	12.5
1-Butene	2.5	118.2
Crotonaldehyde	-	6.4
Total	73.2	444.0

Table A.6 Acetaldehyde TPD Total Molar Desorption Quantities

Acetaldehyde TPDs		
	Moles Desorbed ($x10^{-8}$)	
	Inert	Reduced
Acetaldehyde	35.4	188.9
1,3-Butadiene	4.9	12.5
1-Butene	1.4	4.7
Acetone	1.6	8.3
Crotonaldehyde	-	21.3
Total	43.3	235.7

Table A.7 Crotonaldehyde TPD Total Molar Desorption Quantities

Crotonaldehyde TPDs		
	Moles Desorbed ($x10^{-8}$)	
	Inert	Reduced
Crotonaldehyde	49.8	38.1
Acetaldehyde	18.8	24.4
Propene	4.6	87.6
Total	73.1	150.2

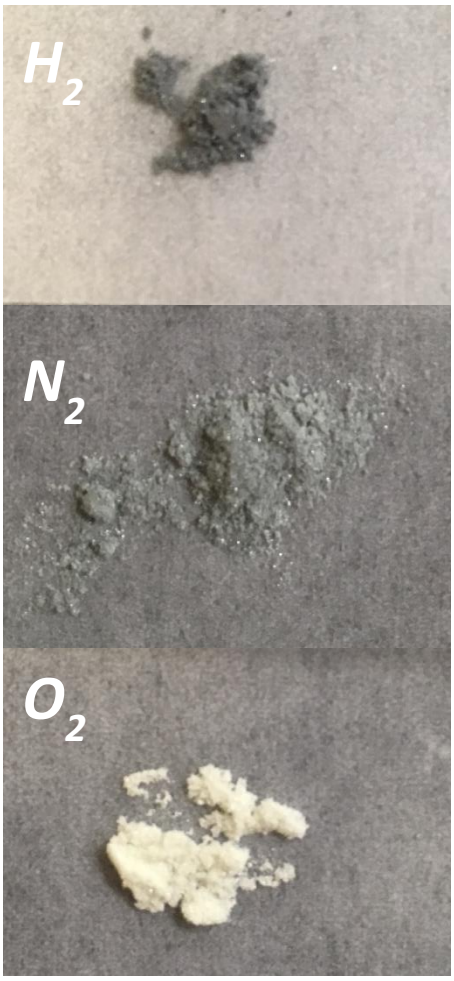

Figure A.10 MoO_3 powder after the various pretreatments at 450 C. Gas used during treatment is written

Appendix B Supplementary Information for Chapter 3

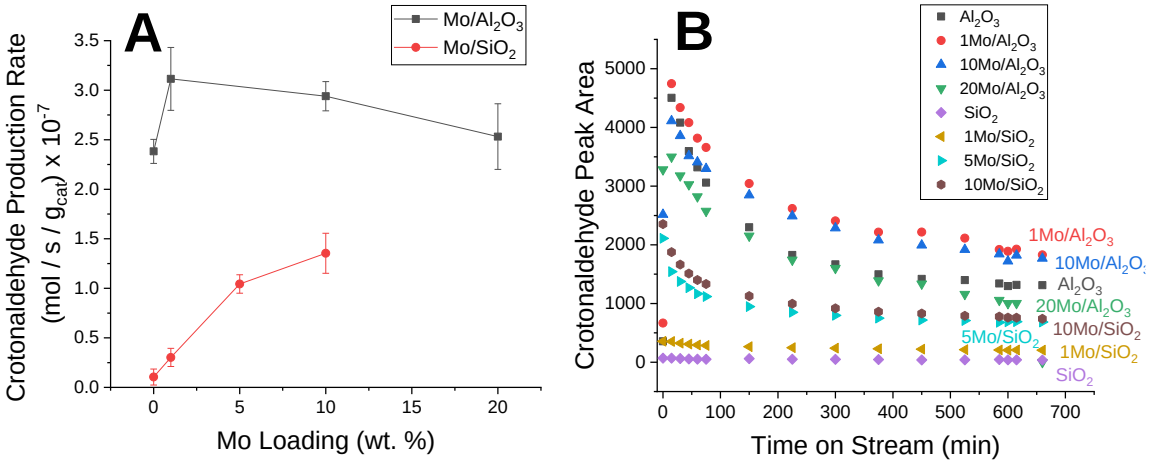

Figure B.1 Mass normalized crotonaldehyde formation rate after ~2.5 hours on stream at 300 °C (A) and time on stream profiles for various Mo supported catalysts (B). Data for all samples collected during the reaction of acetaldehyde at WHSV = 1.4 hr^{-1} after pretreatment in 36 sccm H_2 at 350 °C for one hour.

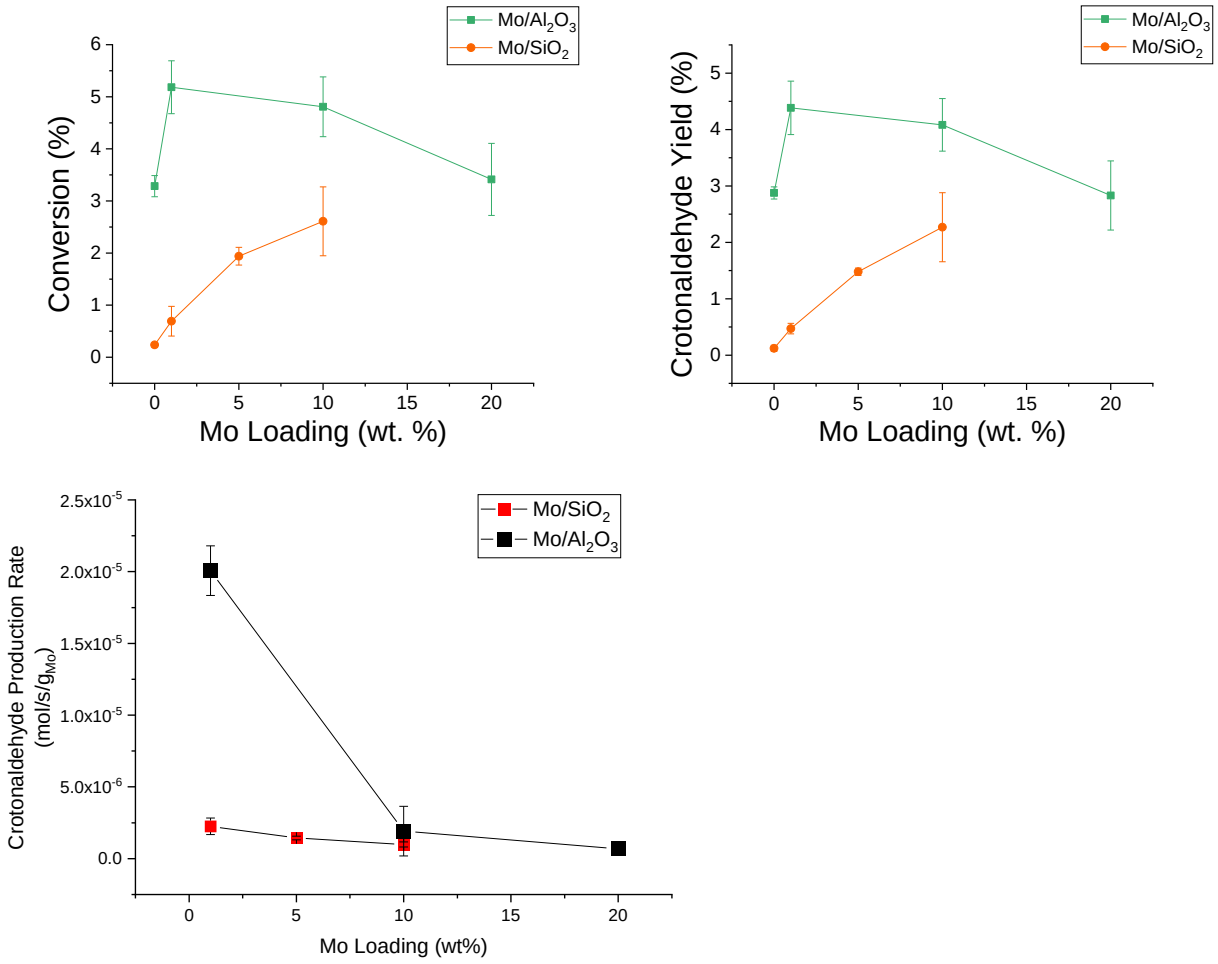

Figure B.2 Conversion (left) and yield (right) for the steady state reaction of acetaldehyde on various Mo-modified catalysts at WHSV = 1.4 h^{-1}. Samples were pretreated in 36 sccm H_2 at 350 °C for one hour, and data was collected after reaction at 300 °C for 10 hours. Crotonaldehyde production rate (bottom) normalized to mass of molybdenum present in catalyst.

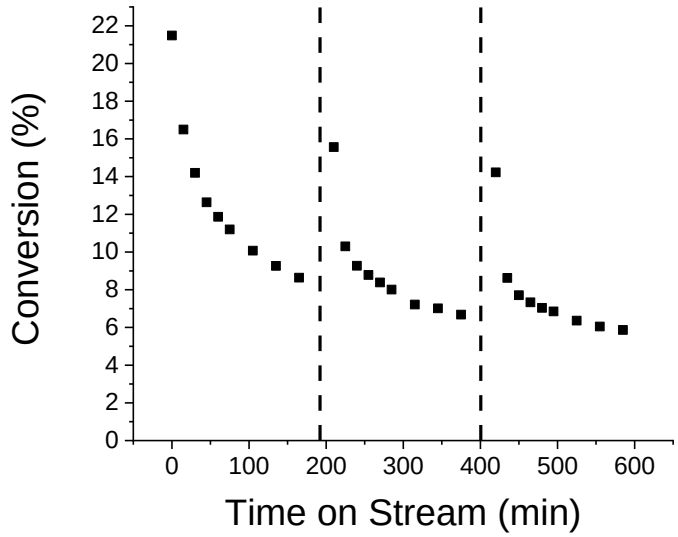

Figure B.3 Conversion vs time on stream for the aldol condensation of acetaldehyde at 300 °C on a 10Mo/Al_2O_3 catalyst. Sample was initially pretreated in H_2 at 350 °C for 1 hr. Dotted lines represent regeneration cycles, which involved treatment in H_2 at 350 °C for 30 min.

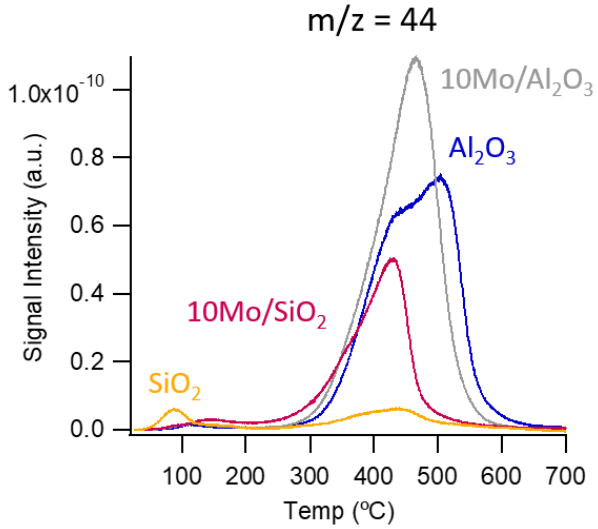

Figure B.4 CO_2 signal (m/z = 44) from spent catalysts during TPO after 11 hours on stream at 300 °C.

Table B.1 Integrated desorption areas associated with CO (m/z = 28) and CO_2 (m/z = 44) during TPO of spent, supported catalysts

	Relative Peak Areas (a.u.)	
Sample	*m/z = 28*	*m/z = 44*
$10Mo/Al_2O_3$	11.21	13.75
Al_2O_3	8.34	12.42
$10Mo/SiO_2$	5.15	6.24
SiO_2	0.66	1.36

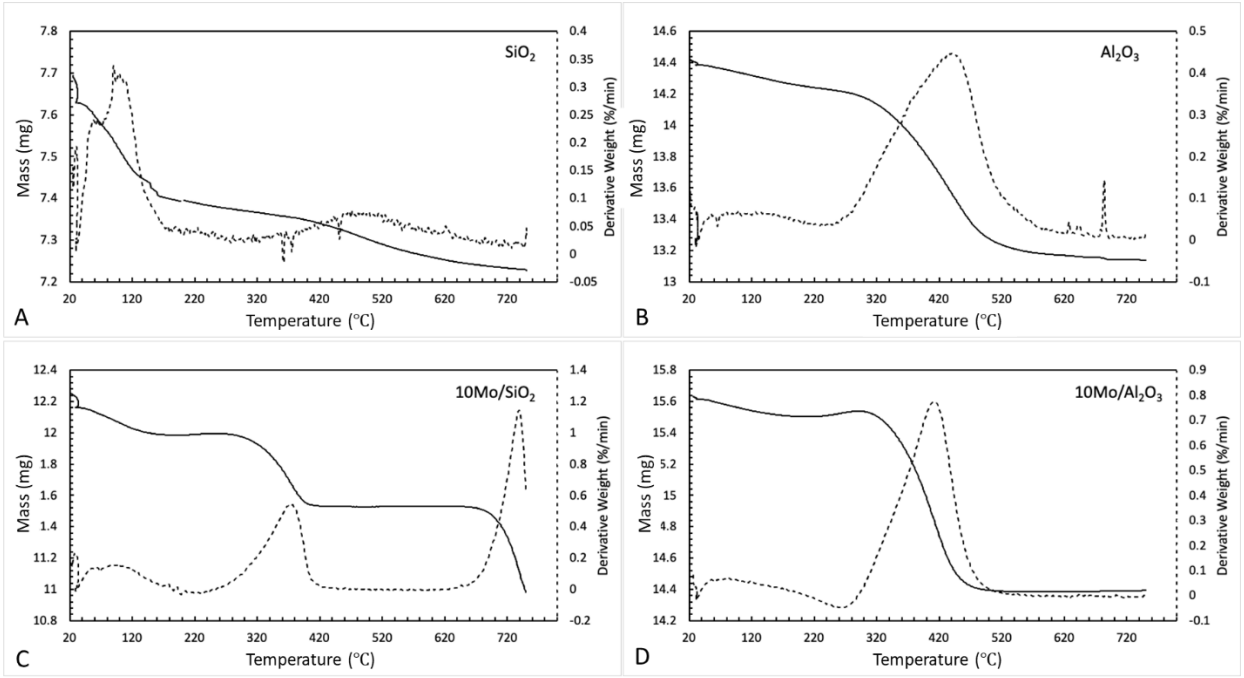

Figure B.5 TGA of SiO_2, Al_2O_3, $10Mo/SiO_2$ and 10 Mo/Al_2O_3 after reaction at 300 °C for 10 hours.

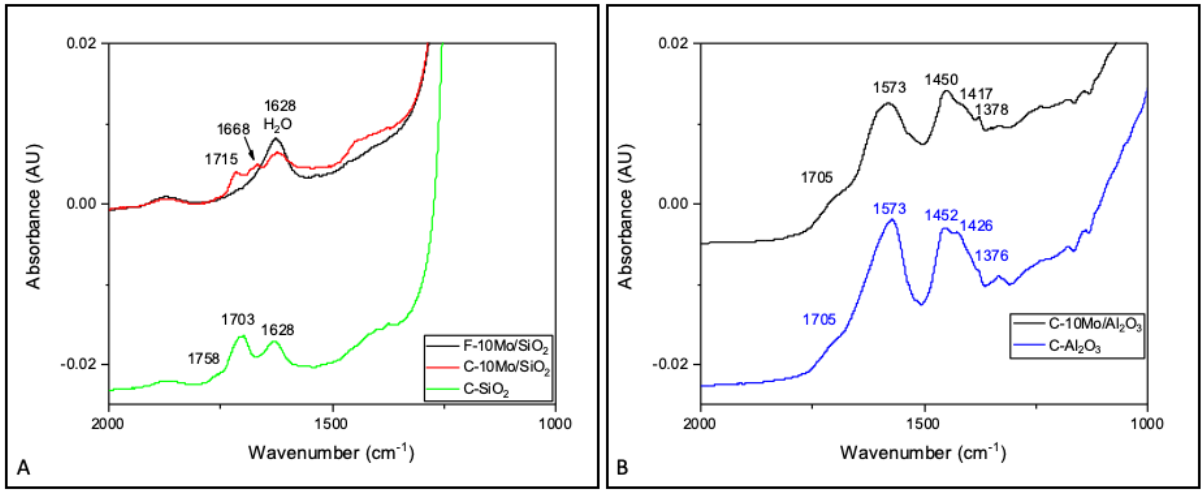

Figure B.6 ATR-FTIR of SiO_2 and $10Mo/SiO_2$ (panel A) and Al_2O_3 and $10Mo/Al_2O_3$ (panel B) after reaction at 300°C for 10 hours

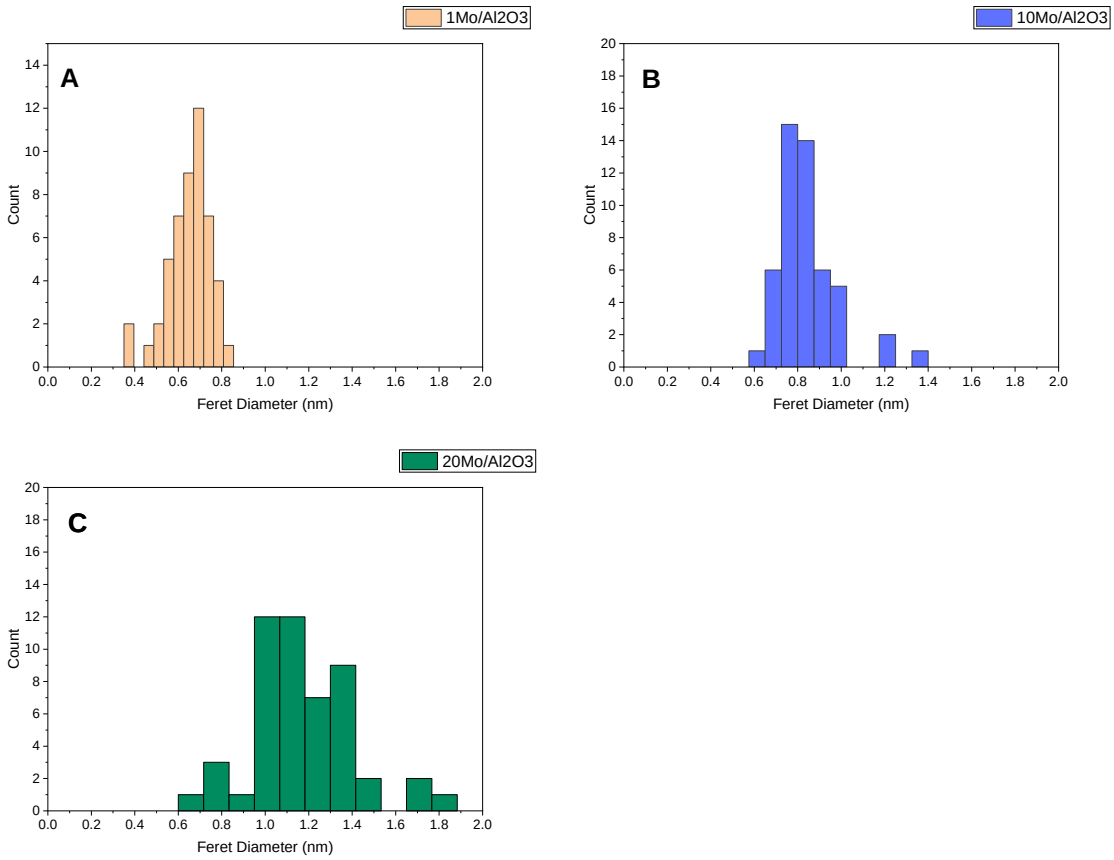

Figure B.7 Particle size distributions of $1Mo/Al_2O_3$ (A), $10Mo/Al_2O_3$ (B), and $20Mo/Al_2O_3$ (C)

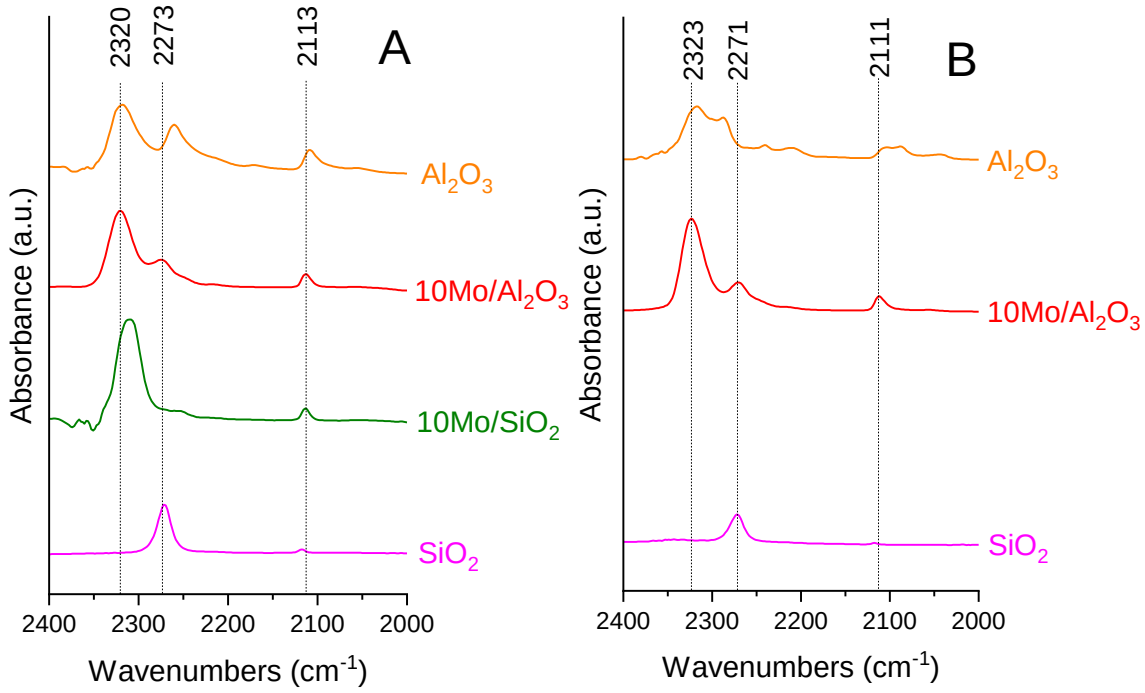

Figure B.8 Acetonitrile (d3) adsorption followed by FTIR spectroscopy of molybdenum supported catalysts before (A) and after (B) reduction.

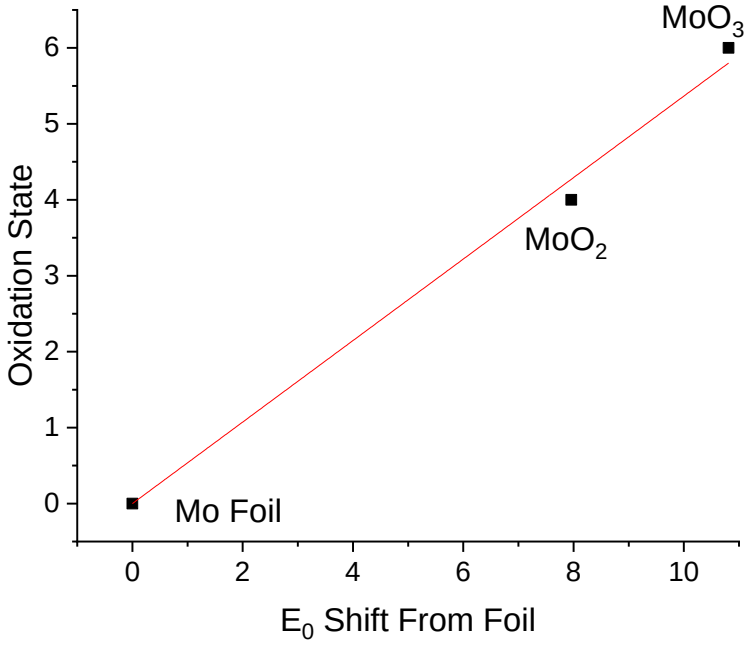

Figure B.9 Linear fit of oxidation state as a function of Mo XANES K edge energy relative to a Mo foil for MoO_3, MoO_2, and Mo foil standards.

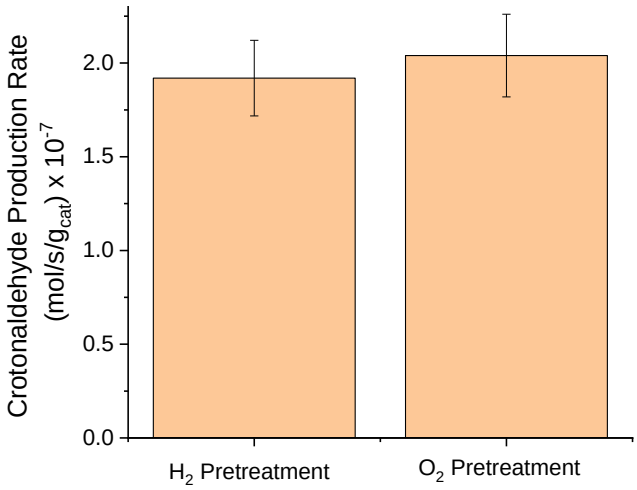

Figure B.10 Mass normalized crotonaldehyde formation rate during the steady state reaction of acetaldehyde on a 10Mo/Al_2O_3 sample pretreated with H_2 or O_2 at WHSV = 1.4 hr^{-1}. Pretreatment conditions involved 36 sccm H_2 or O_2 at 350 °C for one hour. Data was collected after reaction at 300 °C for 10 hours

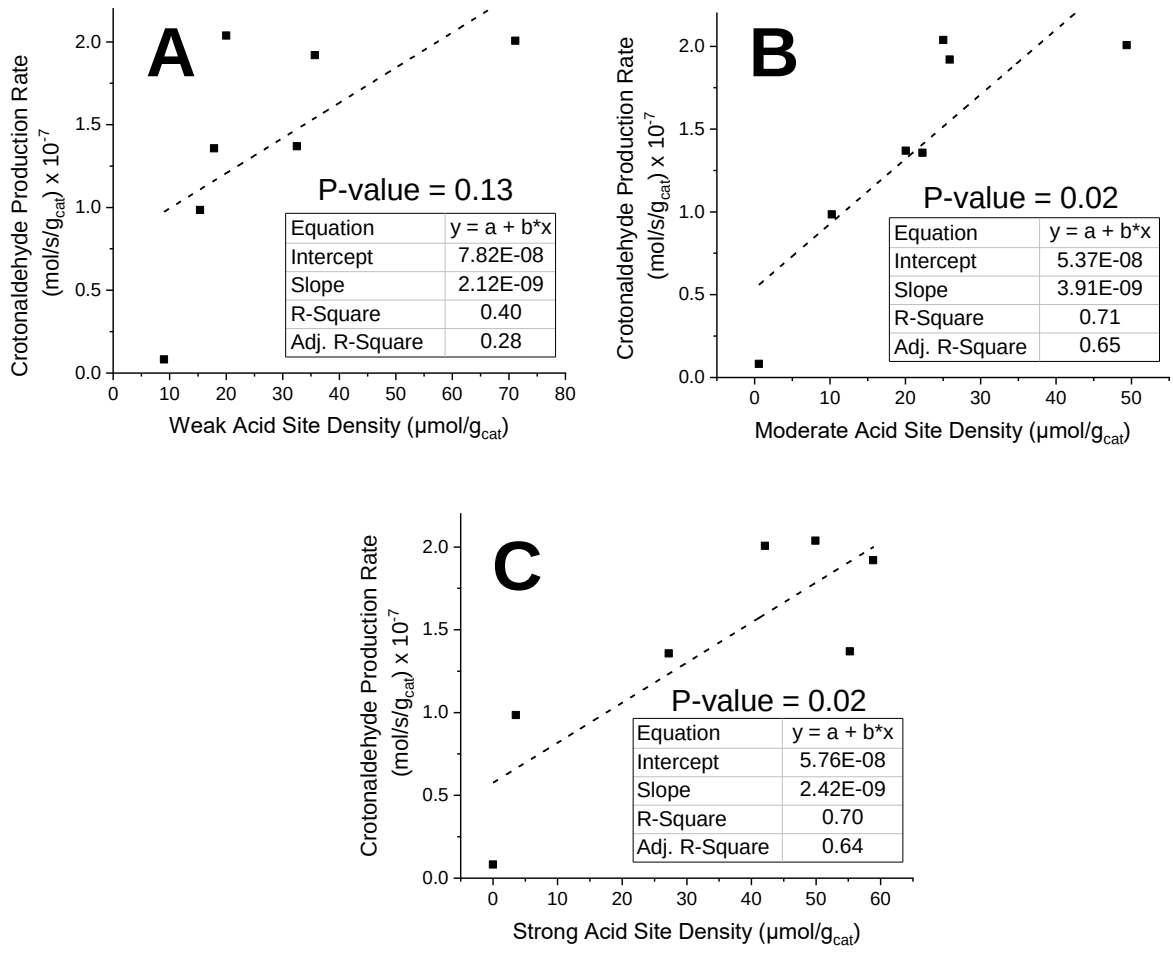

Figure B.11 Crotonaldehyde production rate from acetaldehyde plotted as a function of weak (A), medium (B), and strong (C) acid site densities for a series of Mo/Al_2O_3 and Mo/SiO_2 catalysts. The calculated P-values and R^2 values for a linear correlation between these two variables are displayed on each chart.

Appendix C Supplementary Information for Chapter 4

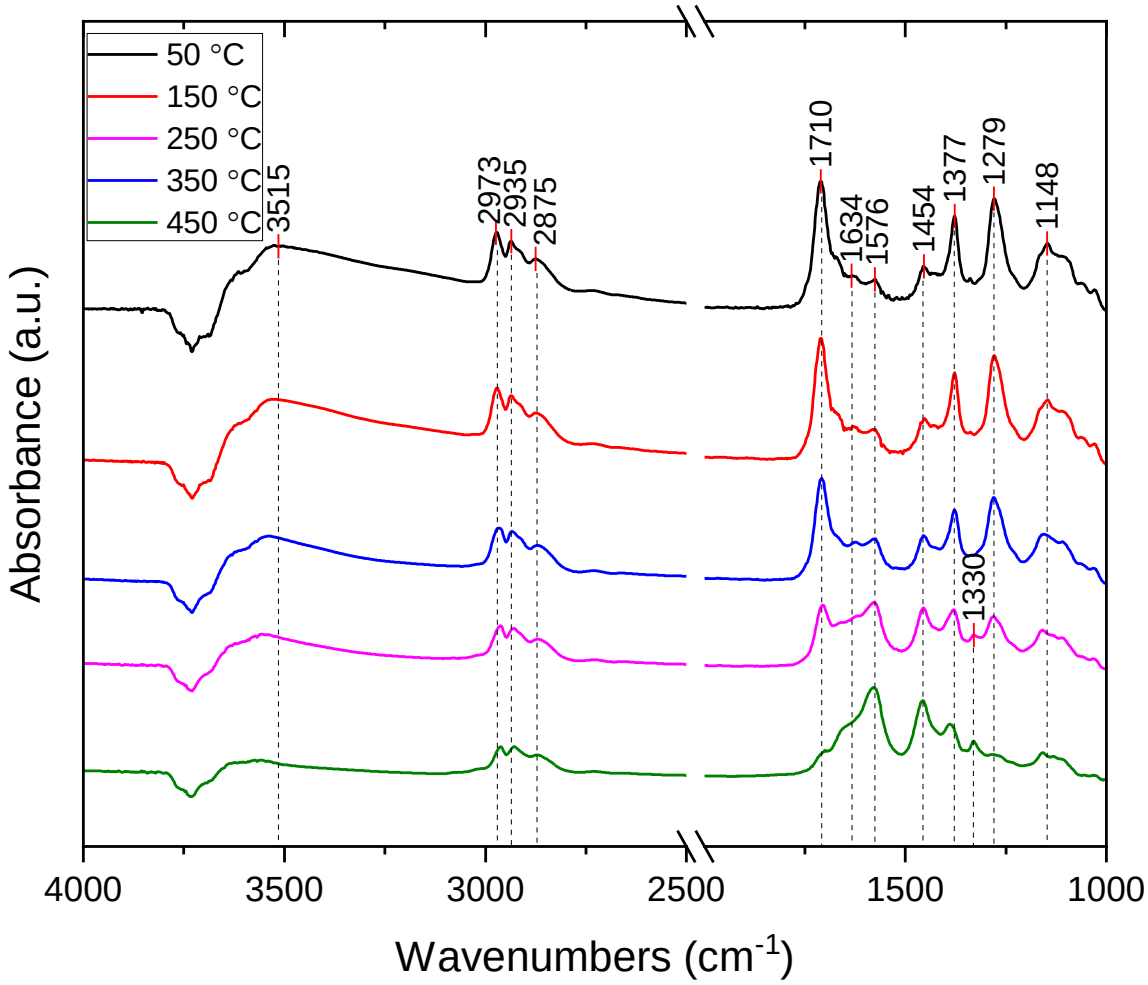

Figure C.1 FTIR Spectra of acetaldehyde adsorbed onto γ-Al_2O_3 followed by TPD

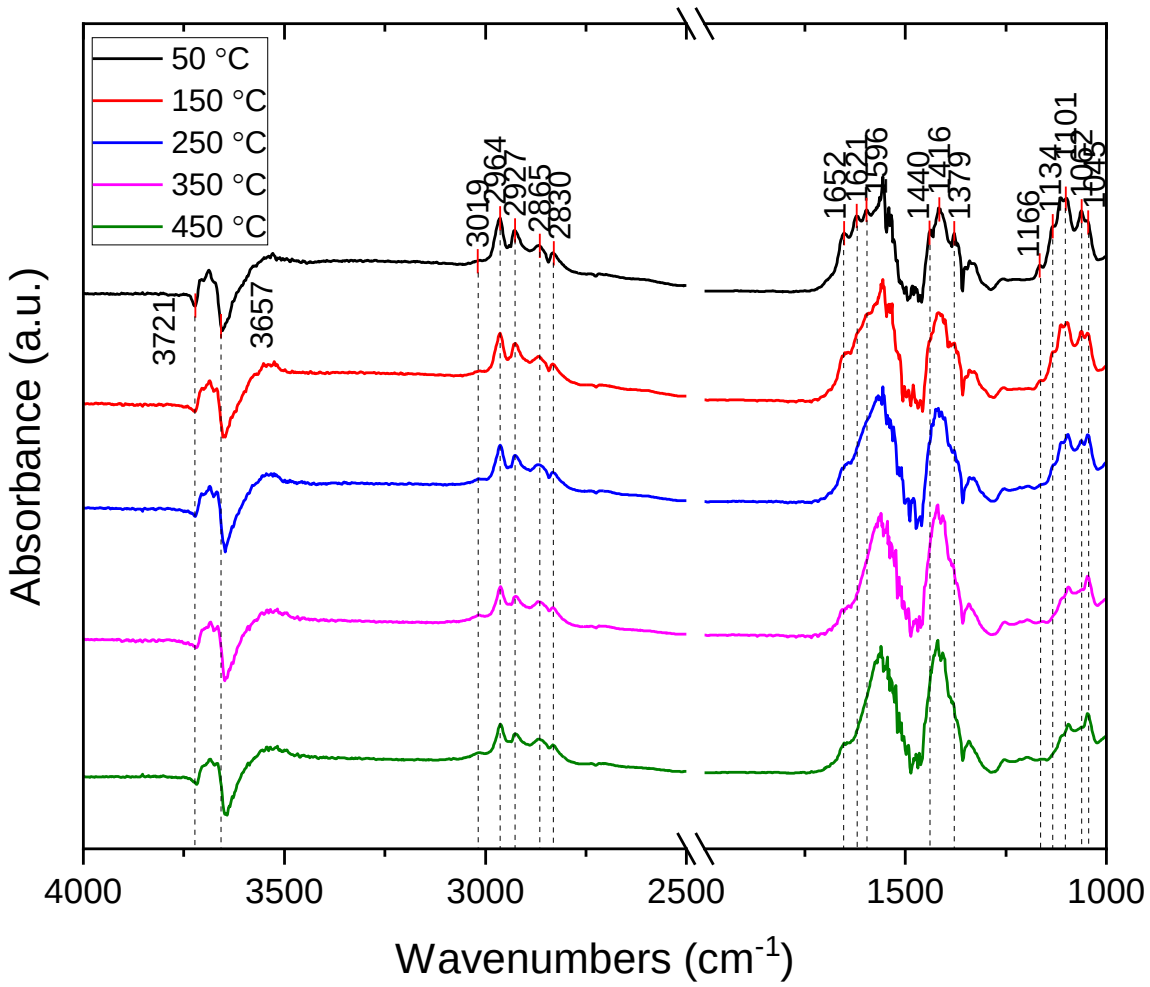

Figure C.2 FTIR Spectra of acetaldehyde adsorbed onto CeO_2 followed by TPD

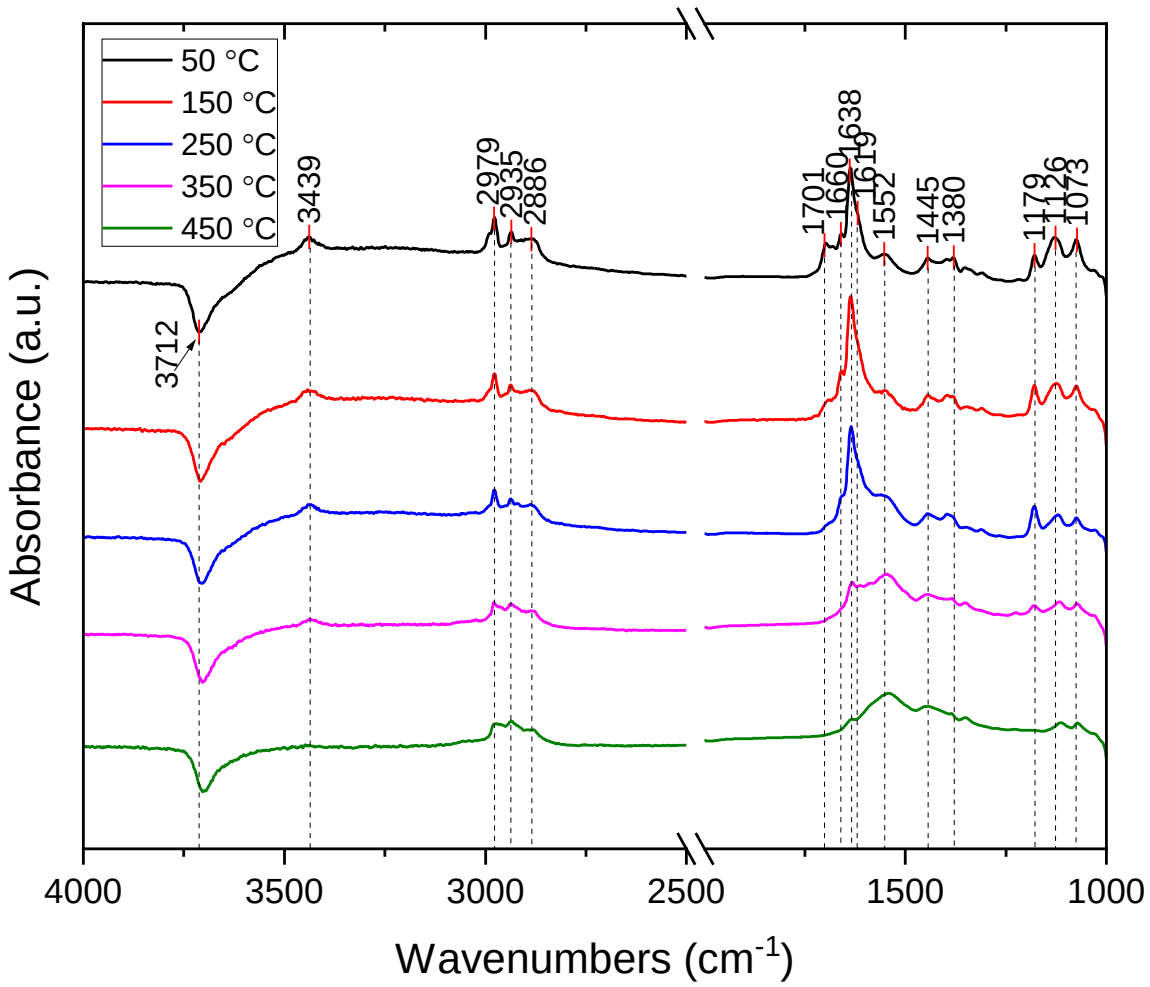

Figure C.3 FTIR Spectra of acetaldehyde adsorbed onto Nb_2O_5 followed by TPD

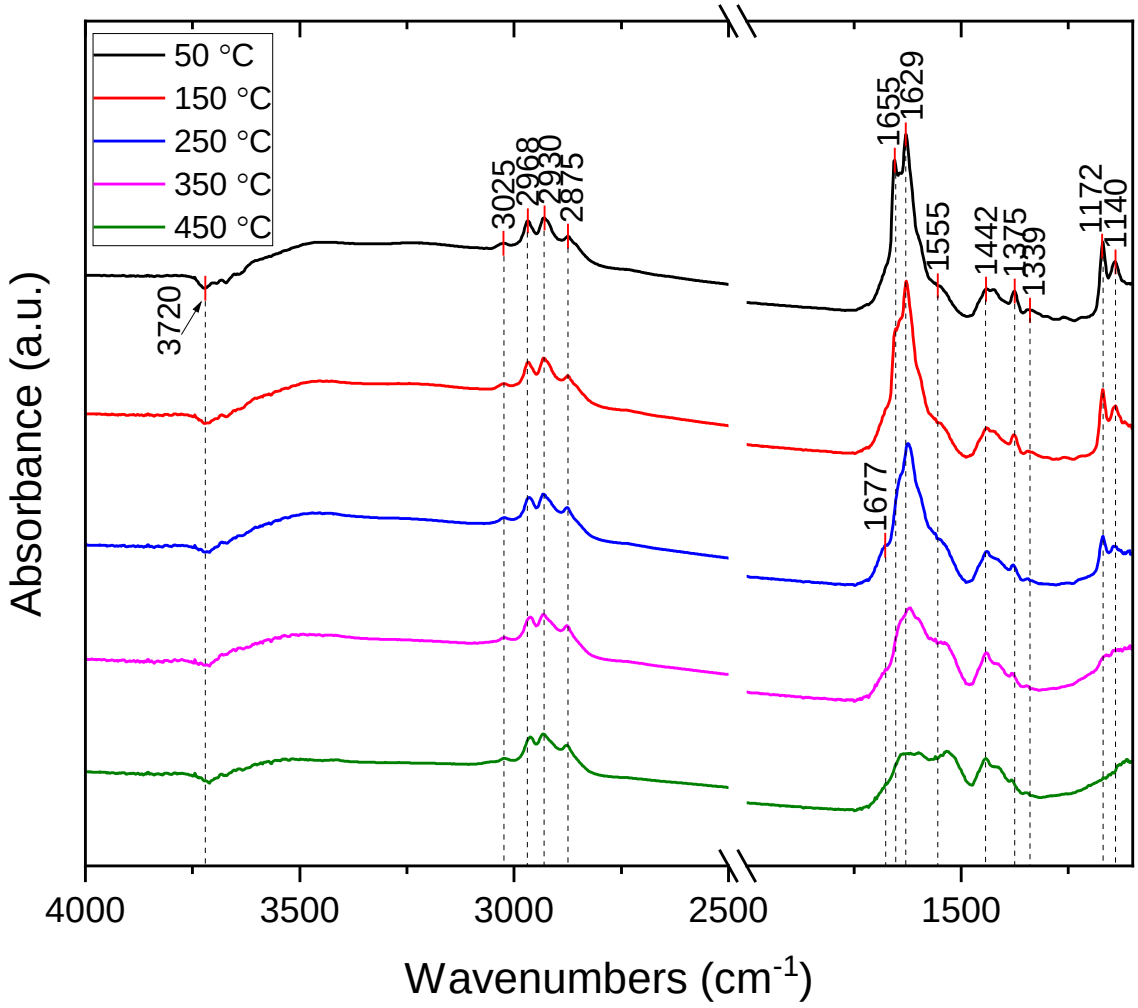

Figure C.4 FTIR Spectra of acetaldehyde adsorbed onto TiO_2 followed by TPD

Appendix D Supplementary Information for Chapter 5

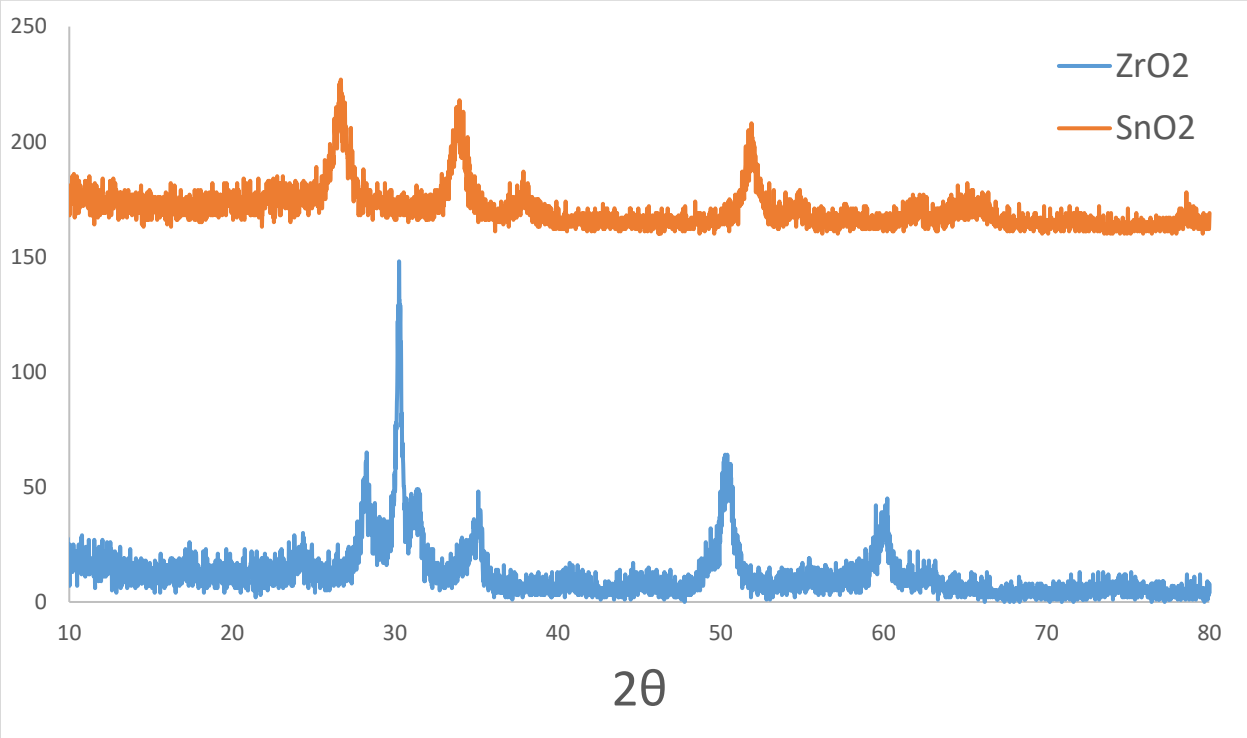

Figure D.1 XRD of synthesized SnO_2 and ZrO_2

References

(1) Spear, B. James Watt: The Steam Engine and the Commercialization of Patents. *World Pat. Inf.* **2008**, *30* (1), 53–58. https://doi.org/10.1016/j.wpi.2007.05.009.

(2) Flanigen, E. M. Chapter 2 Zeolites and Molecular Sieves an Historical Perspective. *Stud. Surf. Sci. Catal.* **1991**, *58* (C), 13–34. https://doi.org/10.1016/S0167-2991(08)63599-5.

(3) Topsøe, H.; Clausen, B. S.; Massoth, F. E. Hydrotreating Catalysis. In *Catalysis: Science and Technology*; Anderson, J. R., Boudart, M., Eds.; Springer Berlin Heidelberg: Berlin, Heidelberg, 1996; pp 1–269. https://doi.org/10.1007/978-3-642-61040-0_1.

(4) Armor, J. N. A History of Industrial Catalysis. *Catal. Today* **2011**, *163* (1), 3–9. https://doi.org/10.1016/j.cattod.2009.11.019.

(5) Vespa, J.; Armstrong, D. M.; Medina, L. *Demographic Turning Points for the United States: Population Projections for 2020 to 2060*; US Department of Commerce, Economics and Statistics Administration, US~…, 2018.

(6) Chen, Y.; Guo, F.; Wang, J.; Cai, W.; Wang, C.; Wang, K. Provincial and Gridded Population Projection for China under Shared Socioeconomic Pathways from 2010 to 2100. *Sci. Data* **2020**, *7* (1), 1–13. https://doi.org/10.1038/s41597-020-0421-y.

(7) Nations, U. No Title https://population.un.org/wpp/Graphs/DemographicProfiles/Line/900.

(8) U.S. Energy Information Administration. U.S. primary energy consumption by energy source, 2020 https://www.eia.gov/energyexplained/us-energy-facts/.

(9) Wang, J.; Bentley, Y. Modelling World Natural Gas Production. *Energy Reports* **2020**, *6*, 1363–1372. https://doi.org/10.1016/j.egyr.2020.05.018.

(10) Chu, S.; Cui, Y.; Liu, N. The Path towards Sustainable Energy. *Nat. Publ. Gr.* **2017**, *16* (1), 16–22. https://doi.org/10.1038/nmat4834.

(11) Nocera, D. G. Solar Fuels and Solar Chemicals Industry. *Acc. Chem. Res.* **2017**, *50* (3), 616–619. https://doi.org/10.1021/acs.accounts.6b00615.

(12) Veers, P.; Dykes, K.; Lantz, E.; Barth, S.; Bottasso, C. L.; Carlson, O.; Clifton, A.; Green, J.; Green, P.; Holttinen, H.; Laird, D.; Lehtomäki, V.; Lundquist, J. K.; Manwell, J.; Marquis, M.; Meneveau, C.; Moriarty, P.; Munduate, X.; Muskulus, M.; Naughton, J.; Pao, L.; Paquette, J.; Peinke, J.; Robertson, A.; Rodrigo, J. S.; Sempreviva, A. M.; Smith, J. C.; Tuohy, A.; Wiser, R. Grand Challenges in the Science of Wind Energy. *Science (80-.).* **2019**, *366* (6464). https://doi.org/10.1126/science.aau2027.

(13) Onda, A.; Ochi, T.; Yanagisawa, K. Selective Hydrolysis of Cellulose into Glucose over Solid Acid Catalysts. *Green Chem.* **2008**, *10* (10), 1033–1037. https://doi.org/10.1039/b808471h.

(14) Tricker, A. W.; Stellato, M. J.; Kwok, T. T.; Kruyer, N. S.; Wang, Z.; Nair, S.; Thomas, V. M.; Realff, M. J.; Bommarius, A. S.; Sievers, C. Similarities in Recalcitrant Structures of Industrial Non-Kraft and Kraft Lignin. *ChemSusChem* **2020**, *13* (17), 4624–4632.

https://doi.org/10.1002/cssc.202001219.

(15) 110th U.S. Congress. *ENERGY INDEPENDENCE AND SECURITY ACT OF 2007*; 2007.

(16) Langholtz, M.; Stokes, B.; Eaton, L. 2016 Billion-Ton Report: Advancing Domestic Resources for a Thriving Bioeconomy (Executive Summary). *Ind. Biotechnol.* **2016**, *12* (5), 282–289. https://doi.org/10.1089/ind.2016.29051.doe.

(17) Perlack, R. D.; Wright, L. L.; Turhollow, A. F.; Graham, R. L. *BIOMASS AS FEEDSTOCK FOR A BIOENERGY AND BIOPRODUCTS INDUSTRY: THE TECHNICAL FEASIBILITY OF A BILLION-TON ANNUAL SUPPLY*; Oak Ridge, Tennessee, 2005.

(18) Chandel, A. K.; Garlapati, V. K.; Singh, A. K.; Antunes, F. A. F.; da Silva, S. S. The Path Forward for Lignocellulose Biorefineries: Bottlenecks, Solutions, and Perspective on Commercialization. *Bioresour. Technol.* **2018**, *264* (June), 370–381. https://doi.org/10.1016/j.biortech.2018.06.004.

(19) Bridgwater, A. V. Review of Fast Pyrolysis of Biomass and Product Upgrading. *Biomass and Bioenergy* **2012**, *38*, 68–94. https://doi.org/10.1016/j.biombioe.2011.01.048.

(20) Kan, T.; Strezov, V.; Evans, T. J. Lignocellulosic Biomass Pyrolysis: A Review of Product Properties and Effects of Pyrolysis Parameters. *Renew. Sustain. Energy Rev.* **2016**, *57*, 1126–1140. https://doi.org/10.1016/j.rser.2015.12.185.

(21) Spivey, J. J.; Egbebi, A. Heterogeneous Catalytic Synthesis of Ethanol from Biomass-Derived Syngas. *Chem. Soc. Rev.* **2007**, *36* (9), 1514–1528. https://doi.org/10.1039/b414039g.

(22) Bermejo-Deval, R.; Assary, R. S.; Nikolla, E.; Moliner, M.; Roman-Leshkov, Y.; Hwang, S.-J.; Palsdottir, A.; Silverman, D.; Lobo, R. F.; Curtiss, L. A.; Davis, M. E. Metalloenzyme-like Catalyzed Isomerizations of Sugars by Lewis Acid Zeolites. *Proc. Natl. Acad. Sci.* **2012**, *109* (25), 9727–9732. https://doi.org/10.1073/pnas.1206708109.

(23) Román-Leshkov, Y.; Barrett, C. J.; Liu, Z. Y.; Dumesic, J. A. Production of Dimethylfuran for Liquid Fuels from Biomass-Derived Carbohydrates. *Nature* **2007**, *447* (7147), 982–985. https://doi.org/10.1038/nature05923.

(24) Jacques, C. V. Ø. Metal Oxides in Heterogeneous Oxidation Catalysis : State of the Art and Challenges for a More Sustainable World. **2019**, 577–588. https://doi.org/10.1002/cssc.201802248.

(25) Brown, I. D.; Skowron, A. Electronegativity and Lewis Acid Strength. *J. Am. Chem. Soc.* **1990**, *112* (9), 3401–3403. https://doi.org/10.1021/ja00165a023.

(26) Zhang, Y. Electronegativities of Elements in Valence States and Their Applications. 2. A Scale for Strengths of Lewis Acids. *Inorg. Chem.* **1982**, *21* (11), 3889–3893. https://doi.org/10.1021/ic00141a006.

(27) Pearson, R. G. Absolute Electronegativity and Hardness: Application to Inorganic Chemistry. *Inorg. Chem.* **1988**, *27* (4), 734–740. https://doi.org/10.1021/ic00277a030.

(28) Najmi, S.; So, J.; Stavitski, E.; McDermott, W. P.; Lyu, Y.; Burt, S. P.; Hermans, I.; Sholl, D. S.; Sievers, C. In-Situ IR Spectroscopy Study of Reactions of C3 Oxygenates on Heteroatom (Sn, Mo, and W) Doped BEA Zeolites and the Effect of Co-Adsorbed Water. *ChemCatChem* **2021**, *13*, 445–458. https://doi.org/10.1002/cctc.202001424.

(29) Román-Leshkov, Y.; Moliner, M.; Labinger, J. A.; Davis, M. E. Mechanism of Glucose Isomerization Using a Solid Lewis Acid Catalyst in Water. *Angew. Chemie - Int. Ed.* **2010**, *49* (47), 8954–8957. https://doi.org/10.1002/anie.201004689.

(30) Bermejo-Deval, R.; Orazov, M.; Gounder, R.; Hwang, S. J.; Davis, M. E. Active Sites in Sn-Beta for Glucose Isomerization to Fructose and Epimerization to Mannose. *ACS Catal.* **2014**. https://doi.org/10.1021/cs500466j.

(31) Orazov, M.; Davis, M. E. Tandem Catalysis for the Production of Alkyl Lactates from Ketohexoses at Moderate Temperatures. *Proc. Natl. Acad. Sci.* **2015**, *112* (38), 11777–11782. https://doi.org/10.1073/pnas.1516466112.

(32) Huber, G. W.; Iborra, S.; Corma, A. Synthesis of Transportation Fuels from Biomass: Chemistry, Catalysts, and Engineering. *Chem. Rev.* **2006**, *106* (9), 4044–4098. https://doi.org/10.1021/cr068360d.

(33) Corma Canos, A.; Iborra, S.; Velty, A. Chemical Routes for the Transformation of Biomass into Chemicals. *Chem. Rev.* **2007**, *107* (6), 2411–2502. https://doi.org/10.1021/cr050989d.

(34) Yue, H.; Zhao, Y.; Ma, X.; Gong, J. Ethylene Glycol: Properties, Synthesis, and Applications. *Chem. Soc. Rev.* **2012**, *41* (11), 4218–4244. https://doi.org/10.1039/c2cs15359a.

(35) Mäki-Arvela, P.; Simakova, I. L.; Salmi, T.; Murzin, D. Y. Production of Lactic Acid/Lactates from Biomass and Their Catalytic Transformations to Commodities. *Chem. Rev.* **2014**, *114* (3), 1909–1971. https://doi.org/10.1021/cr400203v.

(36) Caratzoulas, S.; Davis, M. E.; Gorte, R. J.; Gounder, R.; Lobo, R. F.; Nikolakis, V.; Sandler, S. I.; Snyder, M. A.; Tsapatsis, M.; Vlachos, D. G. Challenges of and Insights into Acid-Catalyzed Transformations of Sugars. *J. Phys. Chem. C* **2014**, *118* (40), 22815–22833. https://doi.org/10.1021/jp504358d.

(37) Moliner, M.; Roman-Leshkov, Y.; Davis, M. E. Tin-Containing Zeolites Are Highly Active Catalysts for the Isomerization of Glucose in Water. *Proc. Natl. Acad. Sci.* **2010**, *107* (14), 6164–6168. https://doi.org/10.1073/pnas.1002358107.

(38) Holm, M. S.; Saravanamurugan, S.; Taarning, E. Conversion of Sugars to Lactic Acid Derivatives Using Heterogeneous Zeotype Catalysts. *Science (80-.).* **2010**, *328* (5978), 602–605. https://doi.org/10.1126/science.1184246.

(39) Pearson, R. G. Hard and Soft Acids and Bases. *J. Am. Chem. Soc.* **1963**, *85* (22), 3533.

(40) Suarez, W.; Dijmesic, J. A.; Hill, C. G. Acidic Properties of Molybdena-Alumina for Different Extents of Reduction: Infrared and Gravimetric Studies of Adsorbed Pyridine. *J. Catal. w* **1985**, 408–421.

(41) Brown, I. D.; Skowron, A. Electronegativity and Lewis Acid Strength. *J. Am. Chem. Soc.* **1990**, *112* (9), 3401–3403. https://doi.org/10.1021/ja00165a023.

(42) Rellán-Piñeiro, M.; López, N. The Active Molybdenum Oxide Phase in the Methanol Oxidation to Formaldehyde (Formox Process): A DFT Study. *ChemSusChem* **2015**, *8* (13), 2231–2239. https://doi.org/10.1002/cssc.201500315.

(43) Miliordos, E.; Caratzoulas, S.; Vlachos, D. G. A Periodic-DFT Study of Retro-Aldol Fragmentation of Fuctose on MoO3. *Appl. Catal. A Gen.* **2017**, *530*, 75–82. https://doi.org/10.1016/j.apcata.2016.11.021.

(44) Rellan-Pineiro, M.; Garcia-Ratés, M.; Lopez, N. Mechanism for the Selective Epimerization of the Glucose Mannose Pair by Mo-Based Compounds: Towards Catalyst Optimization. *Green Chem.* **2017**, 5932–5939. https://doi.org/10.1039/C7GC02692G.

(45) Vohra, M.; Manwar, J.; Manmode, R.; Padgilwar, S.; Patil, S. Bioethanol Production: Feedstock and Current Technologies. *J. Environ. Chem. Eng.* **2014**, *2* (1), 573–584. https://doi.org/10.1016/j.jece.2013.10.013.

(46) Silveira, M. H. L.; Morais, A. R. C.; Da Costa Lopes, A. M.; Olekszyszen, D. N.; Bogel-Łukasik, R.; Andreaus, J.; Pereira Ramos, L. Current Pretreatment Technologies for the Development of Cellulosic Ethanol and Biorefineries. *ChemSusChem* **2015**, *8* (20), 3366–3390. https://doi.org/10.1002/cssc.201500282.

(47) Posada, J. A.; Patel, A. D.; Roes, A.; Blok, K.; Faaij, A. P. C.; Patel, M. K. Potential of Bioethanol as a Chemical Building Block for Biorefineries: Preliminary Sustainability Assessment of 12 Bioethanol-Based Products. *Bioresour. Technol.* **2013**, *135*, 490–499. https://doi.org/10.1016/j.biortech.2012.09.058.

(48) Barteau, M. A. Organic Reactions at Well-Defined Oxide Surfaces. *Chem. Rev.* **1996**, *96* (4), 1413–1430. https://doi.org/10.1021/cr950222t.

(49) Corson, B. B.; Jones, H. E.; Welling, C. E.; Hinckley, J. A.; Stahly, E. E. Butadiene from Ethyl Alcohol. Catalysis in the One-and Two-Stop Processes. *Ind. Eng. Chem.* **1950**, *42* (2), 359–373. https://doi.org/10.1021/ie50482a039.

(50) Ochoa, J. V.; Bandinelli, C.; Vozniuk, O.; Chieregato, A.; Malmusi, A.; Recchi, C.; Cavani, F. An Analysis of the Chemical, Physical and Reactivity Features of MgO-SiO2catalysts for Butadiene Synthesis with the Lebedev Process. *Green Chem.* **2016**, *18* (6), 1653–1663. https://doi.org/10.1039/c5gc02194d.

(51) Angelici, C.; Weckhuysen, B. M.; Bruijnincx, P. C. A. Chemocatalytic Conversion of Ethanol into Butadiene and Other Bulk Chemicals. *ChemSusChem* **2013**, *6* (9), 1595–1614. https://doi.org/10.1002/cssc.201300214.

(52) Chieregato, A.; Ochoa, J. V.; Bandinelli, C.; Fornasari, G.; Cavani, F.; Mella, M. On the Chemistry of Ethanol on Basic Oxides: Revising Mechanisms and Intermediates in the Lebedev and Guerbet Reactions. *ChemSusChem* **2015**, *8* (2), 377–388. https://doi.org/10.1002/cssc.201402632.

(53) Sun, Z.; Vasconcelos, A. C.; Bottari, G.; Stuart, M. C. A.; Bonura, G.; Cannilla, C.; Frusteri, F.; Barta, K. Efficient Catalytic Conversion of Ethanol to 1-Butanol via the

Guerbet Reaction over Copper- and Nickel-Doped Porous. *ACS Sustain. Chem. Eng.* **2017**, *5* (2), 1738–1746. https://doi.org/10.1021/acssuschemeng.6b02494.

(54) Toussaint, W. J.; Dunn, J. T.; Jachson, D. R. Production of Butadiene from Alcohol. *Ind. Eng. Chem.* **1947**, *39* (2), 120–125. https://doi.org/10.1021/ie50446a010.

(55) Bolin, T. B.; Wu, T.; Schweitzer, N.; Lobo-Lapidus, R.; Kropf, A. J.; Wang, H.; Hu, Y.; Miller, J. T.; Heald, S. M. In Situ Intermediate-Energy X-Ray Catalysis Research at the Advanced Photon Source Beamline 9-BM. *Catal. Today* **2013**, *205*, 141–147. https://doi.org/10.1016/j.cattod.2012.09.034.

(56) Ravel, B.; Newville, M. Synchrotron Radiation ATHENA, ARTEMIS, HEPHAESTUS: Data Analysis for X-Ray Absorption Spectroscopy Using IFEFFIT. *J. Synchrotron Rad* **2005**, *12*, 537–541. https://doi.org/10.1107/S0909049505012719.

(57) Baltrusaitis, J.; Mendoza-Sanchez, B.; Fernandez, V.; Veenstra, R.; Dukstiene, N.; Roberts, A.; Fairley, N. Generalized Molybdenum Oxide Surface Chemical State XPS Determination via Informed Amorphous Sample Model. *Appl. Surf. Sci.* **2015**, *326*, 151–161. https://doi.org/10.1016/j.apsusc.2014.11.077.

(58) Giannozzi, P.; Baroni, S.; Bonini, N.; Calandra, M.; Car, R.; Cavazzoni, C.; Ceresoli, D.; Chiarotti, G. L.; Cococcioni, M.; Dabo, I.; Dal Corso, A.; De Gironcoli, S.; Fabris, S.; Fratesi, G.; Gebauer, R.; Gerstmann, U.; Gougoussis, C.; Kokalj, A.; Lazzeri, M.; Martin-Samos, L.; Marzari, N.; Mauri, F.; Mazzarello, R.; Paolini, S.; Pasquarello, A.; Paulatto, L.; Sbraccia, C.; Scandolo, S.; Sclauzero, G.; Seitsonen, A. P.; Smogunov, A.; Umari, P.; Wentzcovitch, R. M. QUANTUM ESPRESSO: A Modular and Open-Source Software Project for Quantum Simulations of Materials. *J. Phys. Condens. Matter* **2009**, *21* (39), 395502. https://doi.org/10.1088/0953-8984/21/39/395502.

(59) Wellendorff, J.; Lundgaard, K. T.; Møgelhøj, A.; Petzold, V.; Landis, D. D.; Nørskov, J. K.; Bligaard, T.; Jacobsen, K. W. Density Functionals for Surface Science: Exchange-Correlation Model Development with Bayesian Error Estimation. *Phys. Rev. B - Condens. Matter Mater. Phys.* **2012**, *85* (23), 32–34. https://doi.org/10.1103/PhysRevB.85.235149.

(60) Rellán-Piñeiro, M.; López, N. A Coupled Density Functional Theory-Microkinetic Modeling for the Hydrodeoxygenation of Glycerol to Propylene on MoO3. *ACS Sustain. Chem. Eng.* **2018**, *6* (12), 16169–16178. https://doi.org/10.1021/acssuschemeng.8b02933.

(61) Coquet, R.; Willock, D. J. The (010) Surface of a-MoO3, a DFT +U Study. *Phys. Chem. Chem. Phys.* **2005**, *3* (010), 3819–3828.

(62) Rellán-Piñeiro, M.; Lopez, N. One Oxygen Vacancy, Two Charge States: Characterization of Reduced α - MoO 3 (010) through Theoretical Methods. *J. Phys. Chem. Lett.* **2018**, *3* (9), 2568–2573. https://doi.org/10.1021/acs.jpclett.8b00536.

(63) Pack, J. D.; Monkhorst, H. J. "special Points for Brillouin-Zone Integrations"-a Reply. *Phys. Rev. B* **1977**, *16* (4), 1748–1749. https://doi.org/10.1103/PhysRevB.16.1748.

(64) Bengtsson, L. Dipole Correction for Surface Supercell Calculations. *Phys. Rev. B - Condens. Matter Mater. Phys.* **1999**, *59* (19), 12301–12304. https://doi.org/10.1103/PhysRevB.59.12301.

(65) Bahn, S. R.; Jacobsen, K. W. An Object-Oriented Scripting Interface to a Legacy Electronic Structure Code. *Comput. Sci. Eng.* **2002**, *4* (3), 56–66. https://doi.org/10.1109/5992.998641.

(66) Brogaard, R. Y.; Henry, R.; Schuurman, Y.; Medford, A. J.; Moses, P. G.; Beato, P.; Svelle, S.; Nørskov, J. K.; Olsbye, U. Methanol-to-Hydrocarbons Conversion: The Alkene Methylation Pathway. *J. Catal.* **2014**, *314*, 159–169. https://doi.org/10.1016/j.jcat.2014.04.006.

(67) Delporte, P.; Meunier, F.́déric; Pham-Huu, C.; Vennegues, P.; Ledoux, M. J.; Guille, J. Physical Characterization of Molybdenum Oxycarbide Catalyst; TEM, XRD and XPS. *Catal. Today* **1995**, *23* (3), 251–267. https://doi.org/10.1016/0920-5861(94)00166-Y.

(68) Stiefel, E. I. Molybdenum Compounds. In *Kirk-Othmer Encyclopedia of Chemical Technology*; John Wiley & Sons, Inc.: Hoboken, NJ, USA, 2011; pp 1–24. https://doi.org/10.1002/0471238961.1315122519200905.a01.pub3.

(69) Kashiwabara, T.; Takahashi, Y.; Tanimizu, M.; Usui, A. Molecular-Scale Mechanisms of Distribution and Isotopic Fractionation of Molybdenum between Seawater and Ferromanganese Oxides. *Geochim. Cosmochim. Acta* **2011**, *75* (19), 5762–5784. https://doi.org/10.1016/j.gca.2011.07.022.

(70) Lede, E. J.; Requejo, F. G.; Pawelec, B.; Fierro, J. L. G. XANES Mo L-Edges and XPS Study of Mo Loaded in HY Zeolite. *J. Phys. Chem. B* **2002**, *106* (32), 7824–7831. https://doi.org/10.1021/jp014648p.

(71) Evans, J.; Frederick, J.; Mosselmans, W. L-Edge Studies on Molybdenum. *J. Phys. Chem* **1991**, *95*, 9673–9676.

(72) Aritani, H.; Tanaka, T.; Funabiki, T.; Yoshida, S.; Eda, K.; Sotani, N.; Kudo, M.; Hasegawa, S. Study of the Local Structure of Molybdenum-Magnesium Binary Oxides by Means of Mo L3-Edge XANES and UV-Vis Spectroscopy. *J. Phys. Chem.* **1996**, *100* (50), 19495–19501. https://doi.org/10.1021/jp9615464.

(73) Bare, S. R. Surface Structure of Highly Dispersed MoO 3 on MgO Using in Situ Mo L 3-Edge XANES †. *Langmuir* **1998**, *14*, 1500–1504.

(74) George, G. N.; Cleland, W. E.; Enemark, J. H.; Kipke, C. A.; Roberts, S. A.; Smith, B. E.; Cramer, S. P. L-Edge Spectroscopy of Molybdenum Compounds and Enzyme. *J. Am. Chem. Soc.* **1990**, *112* (7), 2541–2548. https://doi.org/10.1021/ja00163a010.

(75) Bare, S. R.; Mitchell, G. E.; Maj, J. J.; Vrieland, G. E.; Gland, J. L. Local Site Symmetry of Dispersed Molybdenum Oxide Catalysts: XANES at the Mo L2,3-Edges. *J. Phys. Chem* **1993**, *97* (22), 6048–6053.

(76) De Groot, F. M. F.; Hu, Z. W.; Lopez, M. F.; Kaindl, G.; Guillot, F.; Tronc, M. Differences between L3 and L2 X-Ray Absorption Spectra of Transition Metal Compounds. *J. Chem. Phys.* **1994**, *101* (8), 6570–6576. https://doi.org/10.1063/1.468351.

(77) Choy, J. H.; Kim, D. K.; Demazeau, G.; Jung, D. Y. LIII-Edge XANES Study on Unusually High Valent Iridium in a Perovskite Lattice. *J. Phys. Chem.* **1994**, *98* (25), 6258–6262. https://doi.org/10.1021/j100076a005.

(78) Cramer, S. P.; Eccles, T. K.; Kutzler, F. W.; Hodgson, K. O.; Mortenson, L. E. Molybdenum X-Ray Absorption Edge Spectra. The Chemical State of Molybdenum in Nitrogenase. *Journal of the American Chemical Society*. March 1976, pp 1287–1288. https://doi.org/10.1021/ja00421a053.

(79) Wong, J.; Lytle, F. W.; Messmer, R. P.; Maylotte, D. H. K-Edge Absorption Spectra of Selected Vanadium Compounds. *Phys. Rev. B* **1984**, *30* (10), 5596–5610. https://doi.org/10.1103/PhysRevB.30.5596.

(80) Asakura, H.; Shishido, T.; Yamazoe, S.; Teramura, K.; Tanaka, T. Structural Analysis of Group V, VI, and VII Metal Compounds by XAFS. *J. Phys. Chem. C* **2011**, *115* (48), 23653–23663. https://doi.org/10.1021/jp2034104.

(81) Yamamoto, T. Assignment of Pre-Edge Peaks in K-Edge x-Ray Absorption Spectra of 3d Transition Metal Compounds: Electric Dipole or Quadrupole? *X-Ray Spectrometry*. John Wiley and Sons Ltd November 2008, pp 572–584. https://doi.org/10.1002/xrs.1103.

(82) De Groot, F. M. F.; Hu, Z. W.; Lopez, M. F.; Kaindl, G.; Guillot, F.; Tronc, M. Differences between L3 and L2 X-Ray Absorption Spectra of Transition Metal Compounds. *J. Chem. Phys.* **1994**, *101* (8), 6570–6576. https://doi.org/10.1063/1.468351.

(83) Lede, E. J.; Requejo, F. G.; Pawelec, B.; Fierro, J. L. G. XANES Mo L-Edges and XPS Study of Mo Loaded in HY Zeolite. *J. Phys. Chem. B* **2002**, *106* (32), 7824–7831. https://doi.org/10.1021/jp014648p.

(84) Nakamura, K.; Eda, K.; Sotani, N. Heat Treatment of Hydrogen Molybdenum Bronze in an Oxygen-Free Atmosphere. Formation of a Defect Structure and Attempt to Carry Out a Catalytic Reaction. *Bull. Chem. Soc. Jpn.* **1998**, *71* (9), 2063–2070.

(85) Ressler, T.; Jentoft, R. E.; Wienold, J.; Günter, M. M.; Timpe, O. In Situ XAS and XRD Studies on the Formation of Mo Suboxides during Reduction of MoO3. *J. Phys. Chem. B* **2000**, *104* (27), 6360–6370. https://doi.org/10.1021/jp000690t.

(86) Lv, M.; Xie, W.; Sun, S.; Wu, G.; Zheng, L.; Chu, S.; Gao, C.; Bao, J. Activated-Carbon-Supported K-Co-Mo Catalysts for Synthesis of Higher Alcohols from Syngas. *Catal. Sci. Technol.* **2015**, *5* (5), 2925–2934. https://doi.org/10.1039/c5cy00083a.

(87) Choi, J. G.; Thompson, L. T. XPS Study of As-Prepared and Reduced Molybdenum Oxides. *Appl. Surf. Sci.* **1996**, *93* (2), 143–149. https://doi.org/10.1016/0169-4332(95)00317-7.

(88) Bronkema, J. L.; Bell, A. T. Mechanistic Studies of Methanol Oxidation to Formaldehyde on Isolated Vanadate Sites Supported on High Surface Area Zirconia. *J. Phys. Chem. C* **2008**, *112* (16), 6404–6412. https://doi.org/10.1021/jp7110692.

(89) Araña, J.; Garriga I Cabo, C.; Doña-Rodríguez, J. M.; González-Díaz, O.; Herrera-Melián, J. A.; Pérez-Peña, J. FTIR Study of Formic Acid Interaction with TiO 2 and TiO 2 Doped with Pd and Cu in Photocatalytic Processes. *Appl. Surf. Sci.* **2004**, *239* (1), 60–71. https://doi.org/10.1016/j.apsusc.2004.04.039.

(90) Kilos, B.; Bell, A. T.; Iglesia, E. Mechanism and Site Requirements for Ethanol Oxidation on Vanadium Oxide Domains. *J. Phys. Chem. C* **2009**, *113*, 2830–2836.

(91) Del Arco, M.; Carriazo, D.; Gutiérrez, S.; Martín, C.; Rives, V. An FT-IR Study of the Adsorption and Reactivity of Ethanol on Systems Derived from Mg2Al-W7O246-Layered Double Hydroxides. *Phys. Chem. Chem. Phys.* **2004**, *6* (2), 465–470. https://doi.org/10.1039/b309070a.

(92) Appel, L. G.; Silva, C. G.; Zonetti, P. C.; Rodrigues, C. P.; Gaspar, A. B. Chemicals from Ethanol—The Acetone One-Pot Synthesis. *Appl. Catal. A Gen.* **2013**, *458*, 111–118. https://doi.org/10.1016/j.apcata.2013.03.028.

(93) Yee, A.; Morrison, S. J.; Idriss, H. A Study of the Reactions of Ethanol on CeO 2 and Pd / CeO 2 by Steady State Reactions , Temperature Programmed Desorption , and In Situ FT-IR. *J. Catal.* **1999**, *186*, 279–295.

(94) Madhavaram, H.; Idriss, H. Acetaldehyde Reactions over the Uranium Oxide System. *J. Catal.* **2004**, *224* (2), 358–369. https://doi.org/10.1016/j.jcat.2004.03.018.

(95) Vohs, J. M.; Barteau, M. A. DEHYDRATION AND DEHYDROGENATION OF ETHANOL AND 1-PROPANOL ON THE POLAR SURFACES OF ZINC OXIDE. *Surf. Sci.* **1989**, *221*, 590–608.

(96) Kaichev, V. V; Chesalov, Y. A.; Saraev, A. A.; Yu, A.; Knop-gericke, A.; Andrushkevich, T. V; Bukhtiyarov, V. I. Redox Mechanism for Selective Oxidation of Ethanol over Monolayer V 2 O 5 / TiO 2 Catalysts. *J. Catal.* **2016**, *338*, 82–93. https://doi.org/10.1016/j.jcat.2016.02.022.

(97) Golay, S.; Doepper, R.; Renken, A. In-Situ Characterisation of the Surface Intermediates for the Ethanol Dehydration Reaction over g -Alumina under Dynamic Conditions. *Appl. Catal. A Gen.* **1998**, *172*, 97–106.

(98) Yu, Z.; Chuang, S. S. C. In Situ IR Study of Adsorbed Species and Photogenerated Electrons during Photocatalytic Oxidation of Ethanol on TiO 2. *J. Catal.* **2007**, *246*, 118–126. https://doi.org/10.1016/j.jcat.2006.11.022.

(99) Foo, G. S.; Wei, D.; Sholl, D. S.; Sievers, C. Role of Lewis and Brønsted Acid Sites in the Dehydration of Glycerol over Niobia. *ACS Catal.* **2014**, 3180–3192. https://doi.org/10.1021/cs5006376.

(100) Jentoft, J. C.; Schmelz, H.; Knozinger, H. Preparation of Selective Catalytic Reduction Catalysts via Milling and Thermal Spreading. *Appl. Catal. A Gen.* **1997**, *161*, 167–182.

(101) Vuurman, M. A.; Stufkens, D. J.; Oskam, A.; Deo, G.; Wachs, I. E. Combined Raman and IR Study of MOx-V2O5/Al2O3(MOx= MoO3, WO3, NiO, CoO) Catalysts under Dehydrated Conditions. *J. Chem. Soc. - Faraday Trans.* **1996**, *92* (17), 3259–3265. https://doi.org/10.1039/FT9969203259.

(102) Rasko, J.; Kiss, J. Adsorption and Surface Reactions of Acetaldehyde. *Appl. Catal. A Gen.* **2005**, *287*, 252–260. https://doi.org/10.1016/j.apcata.2005.04.003.

(103) Lochar, V.; Drobná, H. FTIR Study of the Interaction of Crotonaldehyde and Maleic Anhydride with V 2 O 5 and MoO 3. *Appl. Catal. A Gen.* **2004**, *269*, 27–31. https://doi.org/10.1016/j.apcata.2004.03.054.

(104) De Jesús, J. C.; Zaera, F. Adsorption and Thermal Chemistry of Acrolein and Crotonaldehyde on Pt(111) Surfaces. *Surf. Sci.* **1999**, *430* (1), 99–115. https://doi.org/10.1016/S0039-6028(99)00406-9.

(105) Zhu, L.; Lu, J. Q.; Chen, P.; Hong, X.; Xie, G. Q.; Hu, G. S.; Luo, M. F. A Comparative Study on Pt/CeO 2 and Pt/ZrO 2 Catalysts for Crotonaldehyde Hydrogenation. *J. Mol. Catal. A Chem.* **2012**, *361–362*, 52–57. https://doi.org/10.1016/j.molcata.2012.05.002.

(106) Englisch, M.; Jentys, A.; Lercher, J. A. Structure Sensitivity of the Hydrogenation of Crotonaldehyde over Pt/SiO2 and Pt/TiO2. *J. Catal.* **1997**, *166* (1), 25–35. https://doi.org/10.1006/jcat.1997.1494.

(107) Xu, J.; Wu, P.; Ye, E. C.; Yuan, B. F.; Feng, Y. Q. Metal Oxides in Sample Pretreatment. *TrAC - Trends Anal. Chem.* **2016**, *80*, 41–56. https://doi.org/10.1016/j.trac.2016.02.027.

(108) Krishnakutty, N.; Vannice, M. A. The Effect of Pretreatment on Pd/C Catalysts: I. Adsorption and Absorption Properties. *Journal of Catalysis*. 1995, pp 312–326. https://doi.org/10.1006/jcat.1995.1213.

(109) Schimming, S. M.; Foo, G. S.; Lamont, O. D.; Rogers, A. K.; Yung, M. M.; D'Amico, A. D.; Sievers, C. Kinetics of Hydrogen Activation on Ceria-Zirconia. *J. Catal.* **2015**, *329*, 335–347. https://doi.org/10.1016/j.jcat.2015.05.027.

(110) Liang, Z.; Jiang, D.; Fang, G.; Leng, W.; Tu, P.; Tong, Y.; Liu, L.; Ni, J.; Li, X. Catalytic Enhancement of Aldol Condensation by Oxygen Vacancy on CeO 2 Catalysts. *ChemistrySelect* **2019**, *4* (14), 4364–4370. https://doi.org/10.1002/slct.201900712.

(111) Schaub, R.; Thostrup, P.; Lopez, N.; Lægsgaard, E.; Stensgaard, I.; Nørskov, J. K.; Besenbacher, F. Oxygen Vacancies as Active Sites for Water Dissociation on Rutile TiO2(110). *Phys. Rev. Lett.* **2001**, *87* (26), 266104-1-266104–4. https://doi.org/10.1103/PhysRevLett.87.266104.

(112) Puigdollers, A. R.; Schlexer, P.; Tosoni, S.; Pacchioni, G. Increasing Oxide Reducibility: The Role of Metal/Oxide Interfaces in the Formation of Oxygen Vacancies. *ACS Catal.* **2017**, *7* (10), 6493–6513. https://doi.org/10.1021/acscatal.7b01913.

(113) Xiao, X.; Bergstrom, H.; Saenger, R.; Johnson, B.; Sun, R.; Peterson, A. The Role of Oxygen Vacancies in Biomass Deoxygenation by Reducible Zinc/Zinc Oxide Catalysts. *Catal. Sci. Technol.* **2018**, *8* (7), 1819–1827. https://doi.org/10.1039/c7cy02535a.

(114) Prasomsri, T.; Nimmanwudipong, T.; Román-Leshkov, Y. Effective Hydrodeoxygenation of Biomass-Derived Oxygenates into Unsaturated Hydrocarbons by MoO 3 Using Low H 2 Pressures. *Energy Environ. Sci* **2013**, *6*, 1732–1738. https://doi.org/10.1039/c3ee24360e.

(115) Schimming, S. M.; Lamont, O. D.; König, M.; Rogers, A. K.; D'Amico, A. D.; Yung, M. M.; Sievers, C. Hydrodeoxygenation of Guaiacol over Ceria-Zirconia Catalysts. *ChemSusChem* **2015**, *8* (12), 2073–2083. https://doi.org/10.1002/cssc.201500317.

(116) Zhao, C.; Watt, C.; Kent, P. R.; Overbury, S. H.; Mullins, D. R.; Calaza, F. C.; Savara, A.; Xu, Y. Coupling of Acetaldehyde to Crotonaldehyde on CeO 2– x (111): Bifunctional Mechanism and Role of Oxygen Vacancies. *J. Phys. Chem. C* **2018**, *123*, 8273–8286. https://doi.org/10.1021/acs.jpcc.8b08535.

(117) Calaza, F. C.; Xu, Y.; Mullins, D. R.; Overbury, S. H. Oxygen Vacancy-Assisted Coupling and Enolization of Acetaldehyde on CeO2(111). *J. Am. Chem. Soc.* **2012**, *134* (43), 18034–18045. https://doi.org/10.1021/ja3074243.

(118) Chu, D.; Zhao, C. Reduced Oxygen-Deficient CuWO4 with Ni Catalyzed Selective Hydrogenolysis of Cellulose to Ethylene Glycol. *Catal. Today* **2018**, No. July, 0–1. https://doi.org/10.1016/j.cattod.2018.10.006.

(119) Román-Leshkov, S.; Prasomsri, T.; Shetty, M.; Murugappan, K.; Ro An-Leshkov, Y. Insights into the Catalytic Activity and Surface Modification of MoO 3 during the Hydrodeoxygenation of Lignin-Derived Model Compounds into Aromatic Hydrocarbons under Low Hydrogen Pressures. *Energy Environ. Sci.* **2014**, *7*, 2660–2669.

(120) Nolte, M. W.; Zhang, J.; Shanks, B. H. Ex Situ Hydrodeoxygenation in Biomass Pyrolysis Using Molybdenum Oxide and Low Pressure Hydrogen. *Green Chem.* **2015**, *18* (1), 134–138. https://doi.org/10.1039/c5gc01614b.

(121) Bligaard, T.; Nørskov, J. K.; Dahl, S.; Matthiesen, J.; Christensen, C. H.; Sehested, J. The Brønsted–Evans–Polanyi Relation and the Volcano Curve in Heterogeneous Catalysis. *J. Catal.* **2004**, *224*, 206–217. https://doi.org/10.1016/j.jcat.2004.02.034.

(122) Medford, A. J.; Vojvodic, A.; Hummelshøj, J. S.; Voss, J.; Abild-Pedersen, F.; Studt, F.; Bligaard, T.; Nilsson, A.; Nørskov, J. K. From the Sabatier Principle to a Predictive Theory of Transition-Metal Heterogeneous Catalysis. *J. Catal.* **2015**, *328*, 36–42. https://doi.org/10.1016/j.jcat.2014.12.033.

(123) Idriss, H.; Seebauer, E. G. Reactions of Ethanol over Metal Oxides. *J. Mol. Catal. A Chem.* **2000**, *152*, 201–212.

(124) Takezawa, N.; Hanamaki, C.; Kobayashi, H. The Mechanism of Dehydrogenation of Ethanol on Magnesium Oxide. *J. Catal.* **1975**, *38* (1–3), 101–109. https://doi.org/10.1016/0021-9517(75)90067-6.

(125) Mudiyanselage, K.; Al-Shankiti, I.; Foulis, A.; Llorca, J.; Idriss, H. Reactions of Ethanol over CeO2 and Ru/CeO2 Catalysts. *Appl. Catal. B Environ.* **2016**, *197*, 198–205. https://doi.org/10.1016/j.apcatb.2016.03.065.

(126) Tatibouet, J. M.; German, J. E. A Structure-Sensitive Oxidation Reaction: Methanol on Molybdenum Trioxide Catalysts. *J. Catal.* **1981**, *72* (2), 375–378. https://doi.org/10.1016/0021-9517(81)90022-1.

(127) Oyama, S. T.; Zhang, W. True and Spectator Intermediates in Catalysis: The Case of Ethanol Oxidation on Molybdenum Oxide As Observed by in Situ Laser Raman Spectroscopy. *J. Am. Chem. Soc.* **1996**, *118*, 7173–7177.

(128) Smith, R. L. The Structural Evolution of the MoO3 (010) Surface during Reduction and Oxidation Reactions. **1998**.

(129) Zhang, W.; Desikan, A.; Oyama, S. T. Effect of Support in Ethanol Oxidation on Molybdenum Oxide. *J. Phys. Chem.* **1995**, *99* (39), 14468–14476. https://doi.org/10.1021/j100039a039.

(130) Seman, M.; Kondo, J. N.; Domen, K.; Radhakrishnan, R.; Oyama, S. T. Reactive and Inert Surface Species Observed during Methanol Oxidation over Silica-Supported Molybdenum Oxide. *J. Phys. Chem. B* **2002**, *106* (50), 12965–12977. https://doi.org/10.1021/jp0263828.

(131) Pomalaza, G.; Capron, M.; Ordomsky, V.; Dumeignil, F. Recent Breakthroughs in the Conversion of Ethanol to Butadiene. *Catalysts* **2016**, *6* (12), 203. https://doi.org/10.3390/catal6120203.

(132) Sun, J.; Wang, Y. Recent Advances in Catalytic Conversion of Ethanol to Chemicals. *ACS Catal.* **2014**, *4* (4), 1078–1090. https://doi.org/10.1021/cs4011343.

(133) Jones, M. D. Catalytic Transformation of Ethanol into 1,3-Butadiene. *Chem. Cent. J.* **2014**, *8* (1), 1–5. https://doi.org/10.1186/s13065-014-0053-4.

(134) Kung, H. H. Chapter 4 Surface Coordinative Unsaturation. In *Transition Metal Oxides Surface Chemistry and Catalysis*; Delmon, B., Yates, J. ., Eds.; Elsevier Science Publishing Company Inc.: New York, NY, 1991; pp 53–71.

(135) Mann, A. K. P.; Wu, Z.; Calaza, F. C.; Overbury, S. H. Adsorption and Reaction of Acetaldehyde on Shape-Controlled CeO2 Nanocrystals: Elucidation of Structure-Function Relationships. *ACS Catal.* **2014**, *4* (8), 2437–2448. https://doi.org/10.1021/cs500611g.

(136) Chen, T. L.; Mullins, D. R. Adsorption and Reaction of Acetaldehyde over CeOX(111) Thin Films. *J. Phys. Chem. C* **2011**, *115* (8), 3385–3392. https://doi.org/10.1021/jp110429s.

(137) Chong, S. V.; Idriss, H. Reactions of Acetaldehyde on UO2(111) Single Crystal Surfaces. Evidence of Benzene Formation. *J. Vac. Sci. Technol. A Vacuum, Surfaces, Film.* **2002**, *19* (4), 1933–1937. https://doi.org/10.1116/1.1371321.

(138) Wang, S.; Goulas, K.; Iglesia, E. Condensation and Esterification Reactions of Alkanals, Alkanones, and Alkanols on TiO2: Elementary Steps, Site Requirements, and Synergistic Effects of Bifunctional Strategies. *J. Catal.* **2016**, *340*, 302–320. https://doi.org/10.1016/j.jcat.2016.05.026.

(139) Rekoske, J. E.; Barteau, M. A. Competition between Acetaldehyde and Crotonaldehyde during Adsorption and Reaction on Anatase and Rutile Titanium Dioxide. *Langmuir* **1999**, *15* (6), 2061–2070. https://doi.org/10.1021/la9805140.

(140) Idriss, H.; Diagne, C.; Hindermann, J. P.; Kiennemann, A.; Barteau, M. A. Reactions of Acetaldehyde on CeO2 and CeO2-Supported Catalysts. *J. Catal.* **1995**, *155*, 219–237.

(141) Zhang, J.; Liu, X.; Sun, M.; Ma, X.; Han, Y. Direct Conversion of Cellulose to Glycolic Acid with a Phosphomolybdic Acid Catalyst in a Water Medium. *ACS Catal.* **2012**, *2* (8), 1698–1702. https://doi.org/10.1021/cs300342k.

(142) McGlade, C.; Ekins, P. The Geographical Distribution of Fossil Fuels Unused When Limiting Global Warming to 2°C. *Nature* **2015**, *517* (7533), 187–190. https://doi.org/10.1038/nature14016.

(143) Salvi, B. L.; Subramanian, K. A.; Panwar, N. L. Alternative Fuels for Transportation

Vehicles: A Technical Review. *Renew. Sustain. Energy Rev.* **2013**, *25*, 404–419. https://doi.org/10.1016/j.rser.2013.04.017.

(144) Huber, G. W.; Cortright, R. D.; Dumesic, J. A. Renewable Alkanes by Aqueous-Phase Reforming of Biomass-Derived Oxygenates. *Angew. Chemie* **2004**, *116* (12), 1575–1577. https://doi.org/10.1002/ange.200353050.

(145) Chheda, J. N.; Dumesic, J. A. An Overview of Dehydration, Aldol-Condensation and Hydrogenation Processes for Production of Liquid Alkanes from Biomass-Derived Carbohydrates. *Catal. Today* **2007**, *123* (1–4), 59–70. https://doi.org/10.1016/j.cattod.2006.12.006.

(146) Serrano-Ruiz, J. C.; Dumesic, J. A. Catalytic Routes for the Conversion of Biomass into Liquid Hydrocarbon Transportation Fuels. *Energy Environ. Sci.* **2011**, *4* (1), 83–99. https://doi.org/10.1039/c0ee00436g.

(147) Dutta, A.; Iisa, M. K.; Talmadge, M.; Mukarakate, C.; Griffin, M. B.; Tan, E. C.; Wilson, N.; Yung, M. M.; Nimlos, M. R.; Schaidle, J. A.; Wang, H.; Thorson, M.; Hartley, D.; Klinger, J.; Cai, H. *Ex Situ Catalytic Fast Pyrolysis of Lignocellulosic Biomass to Hydrocarbon Fuels: 2019 State of Technology and Future Research*; 2020.

(148) Taifan, W. E.; Bučko, T.; Baltrusaitis, J. Catalytic Conversion of Ethanol to 1,3-Butadiene on MgO: A Comprehensive Mechanism Elucidation Using DFT Calculations. *J. Catal.* **2017**, *346*, 78–91. https://doi.org/10.1016/j.jcat.2016.11.042.

(149) Di Cosimo, J. I.; Apesteguía, C. R.; Ginés, M. J. L.; Iglesia, E. Structural Requirements and Reaction Pathways in Condensation Reactions of Alcohols on MgyAlOx Catalysts. *J. Catal.* **2000**, *190* (2), 261–275. https://doi.org/10.1006/jcat.1999.2734.

(150) Kozlowski, J. T.; Davis, R. J. Sodium Modification of Zirconia Catalysts for Ethanol Coupling to 1-Butanol. *J. Energy Chem.* **2013**, *22* (1), 58–64. https://doi.org/10.1016/S2095-4956(13)60007-8.

(151) Zhang, H.; Ibrahim, M. Y. S.; Flaherty, D. W. Aldol Condensation among Acetaldehyde and Ethanol Reactants on TiO2: Experimental Evidence for the Kinetically Relevant Nucleophilic Attack of Enolates. *J. Catal.* **2018**, *361*, 290–302. https://doi.org/10.1016/j.jcat.2018.02.030.

(152) Young, Z. D.; Hanspal, S.; Davis, R. J. Aldol Condensation of Acetaldehyde over Titania, Hydroxyapatite, and Magnesia. *ACS Catal.* **2016**, *6* (5), 3193–3202. https://doi.org/10.1021/acscatal.6b00264.

(153) Ordomsky, V. V.; Sushkevich, V. L.; Ivanova, I. I. Study of Acetaldehyde Condensation Chemistry over Magnesia and Zirconia Supported on Silica. *J. Mol. Catal. A Chem.* **2010**, *333* (1–2), 85–93. https://doi.org/10.1016/j.molcata.2010.10.001.

(154) Najmi, S.; Rasmussen, M.; Innocenti, G.; Chang, C.; Stavitski, E.; Bare, S. R.; Medford, A. J.; Medlin, J. W.; Sievers, C. Pretreatment Effects on the Surface Chemistry of Small Oxygenates on Molybdenum Trioxide. *ACS Catal.* **2020**, *10* (15), 8187–8200. https://doi.org/10.1021/acscatal.0c01992.

(155) Tian, H.; Wachs, I. E. Molybdena Local Structural Determination in Different

Environments : Aqueous Solutions , Bulk Mixed Oxides and Supported MoOx Catalysts. *J. Phys. Chem. C* **2010**, *2* (Vi), 6. https://doi.org/10.1021/jp103269w.

(156) Yao, R.; Herrera, J. E.; Chen, L.; Chin, Y. H. C. Generalized Mechanistic Framework for Ethane Dehydrogenation and Oxidative Dehydrogenation on Molybdenum Oxide Catalysts. *ACS Catal.* **2020**, *10* (12), 6952–6968. https://doi.org/10.1021/acscatal.0c01073.

(157) Cheng, E.; Notestein, J. Catalytic Dehydrogenation of Isobutane over Supported MoOx/K-Al2O3. *J. Catal.* **2021**, *397*, 212–222. https://doi.org/10.1016/j.jcat.2021.03.032.

(158) Harlin, M. E.; Backman, L. B.; Krause, A. O. I.; Jylhä, O. J. T. Activity of Molybdenum Oxide Catalyst in the Dehydrogenation of N-Butane. *J. Catal.* **1999**, *183* (2), 300–313. https://doi.org/10.1006/jcat.1999.2413.

(159) Abello, M. C.; Gomez, M. F.; Ferretti, O. Mo/γ-Al2O3 Catalysts for the Oxidative Dehydrogenation of Propane. Effect of Mo Loading. *Appl. Catal. A Gen.* **2001**, *207* (1–2), 421–431. https://doi.org/10.1016/S0926-860X(00)00680-3.

(160) Setnička, M.; Tišler, Z.; Kubička, D.; Bulánek, R. Activity of Molybdenum Oxide Catalyst Supported on Al2O3, TiO2, and SiO2 Matrix in the Oxidative Dehydrogenation of n-Butane. *Top. Catal.* **2015**, *58* (14–17), 866–876. https://doi.org/10.1007/s11244-015-0453-2.

(161) Zhao, H.; Song, H.; Chou, L.; Zhao, J.; Yang, J.; Yan, L. Insight into the Structure and Molybdenum Species in Mesoporous Molybdena-Alumina Catalysts for Isobutane Dehydrogenation. *Catal. Sci. Technol.* **2017**, *7* (15), 3258–3267. https://doi.org/10.1039/c7cy00975e.

(162) Boufaden, N.; Akkari, R.; Pawelec, B.; Fierro, J. L. G.; Said Zina, M.; Ghorbel, A. Dehydrogenation of Methylcyclohexane to Toluene over Partially Reduced Mo-SiO2 Catalysts. *Appl. Catal. A Gen.* **2015**, *502*, 329–339. https://doi.org/10.1016/j.apcata.2015.05.026.

(163) Yu, M.; Qu, W.; Xu, S.; Wang, L.; Liu, B.; Zhang, L.; Peng, J. Interfacial Stability, Electronic Property, and Surface Reactivity of α-MoO3/γ-Al2O3 Composites: DFT and DFT + U Calculations. *Comput. Mater. Sci.* **2018**, *153* (March), 217–227. https://doi.org/10.1016/j.commatsci.2018.06.046.

(164) Handzlik, J.; Ogonowski, J. Structure of Isolated Molybdenum(VI) and Molybdenum(IV) Oxide Species on Silica: Periodic and Cluster DFT Studies. *J. Phys. Chem. C* **2012**, *116* (9), 5571–5584. https://doi.org/10.1021/jp207385h.

(165) Tamura, M.; Shimizu, K.; Satsuma, A. General Comprehensive IR Study on Acid / Base Properties of Metal Oxides. *Appl. Catal. A Gen.* **2012**, *433–434*, 135–145. https://doi.org/10.1016/j.apcata.2012.05.008.

(166) Brunauer, S.; Emmett, P. H.; Teller, E. Adsorption of Gases in Multimolecular Layers. *J. Am. Chem. Soc.* **1938**, *60* (2), 309–319. https://doi.org/10.1021/ja01269a023.

(167) Barrett, E. P.; Joyner, L. G.; Halenda, P. P. The Determination of Pore Volume and Area Distributions in Porous Substances. I. Computations from Nitrogen Isotherms. *J. Am.*

Chem. Soc. **1951**, *73* (2), 373–380.

(168) Bartholomew, C. H. Mechanisms of Catalyst Deactivation. *Appl. Catal. A Gen.* **2001**, *212* (1–2), 17–60. https://doi.org/10.1016/S0926-860X(00)00843-7.

(169) Hill, W.; Miessner, H.; Öhlmann, G. Fourier Transform Infrared Study of the Adsorption and of Reactions of Acetaldehyde on Dispersed Silica. *J. Chem. Soc. Faraday Trans. I* **1989**, *85* (3), 691–697. https://doi.org/10.1039/F19898500691.

(170) Socrates, G. *Infrared and Raman Characteristic Group Frequencies*; 2001. https://doi.org/10.1002/jrs.1238.

(171) Carosso, M.; Vottero, E.; Morandi, S.; Manzoli, M.; Ferri, D.; Fovanna, T.; Pellegrini, R.; Piovano, A.; Groppo, E. Deactivation of Industrial Pd/Al2O3 Catalysts by Ethanol: A Spectroscopic Study. *ChemCatChem* **2021**, *13* (3), 900–908. https://doi.org/10.1002/cctc.202001615.

(172) Seki, T.; Nakajo, T.; Onaka, M. The Tishchenko Reaction: A Classic and Practical Tool for Ester Synthesis. *Chemistry Letters*. The Chemical Society of Japan 公益社団法人 日本化学会 August 2006, pp 824–829. https://doi.org/10.1246/cl.2006.824.

(173) Biradar, A. V.; Umbarkar, S. B.; Dongare, M. K. Transesterification of Diethyl Oxalate with Phenol Using MoO 3/SiO2 Catalyst. *Appl. Catal. A Gen.* **2005**, *285* (1–2), 190–195. https://doi.org/10.1016/j.apcata.2005.02.028.

(174) Bañares, M. A.; Fierro, J. L. G.; Moffat, J. B. The Partial Oxidation of Methane on MoO3/SiO2 Catalysts: Influence of the Molybdenum Content and Type of Oxidant. *J. Catal.* **1993**, *142* (2), 406–417. https://doi.org/10.1006/jcat.1993.1218.

(175) Chakrabarti, A.; Wachs, I. E. Molecular Structure-Reactivity Relationships for Olefin Metathesis by Al2O3 -Supported Surface MoOx Sites. *ACS Catal.* **2018**, *8*, 949–959. https://doi.org/10.1021/acscatal.7b03598.

(176) Pelmenschikov, A. G.; Van Santen, R. A.; Jänchen, J.; Meijer, E. CD3CN as a Probe of Lewis and Bronsted Acidity of Zeolites. *J. Phys. Chem.* **1993**, *97* (42), 11071–11074. https://doi.org/10.1021/j100144a028.

(177) Escalona Platero, E.; Peñarroya Mentruit, M.; Morterra, C. Fourier Transform Infrared Spectroscopy Study of CD3CN Adsorbed on Pure and Doped γ-Alumina. *Langmuir* **1999**, *15* (15), 5079–5087. https://doi.org/10.1021/la981654c.

(178) Chakrabarti, A.; Wachs, I. E. Activation Mechanism and Surface Intermediates during Olefin Metathesis by Supported MoO x /Al 2 O 3 Catalysts. *J. Phys. Chem. C* **2019**, *123* (19), 12367–12375. https://doi.org/10.1021/acs.jpcc.9b02426.

(179) Xiao, L. P.; Wang, S.; Li, H.; Li, Z.; Shi, Z. J.; Xiao, L.; Sun, R. C.; Fang, Y.; Song, G. Catalytic Hydrogenolysis of Lignins into Phenolic Compounds over Carbon Nanotube Supported Molybdenum Oxide. *ACS Catal.* **2017**, *7* (11), 7535–7542. https://doi.org/10.1021/acscatal.7b02563.

(180) Prasomsri, T.; Shetty, M.; Murugappan, K.; Román-Leshkov, Y. Insights into the Catalytic Activity and Surface Modification of MoO 3 during the Hydrodeoxygenation of

Lignin-Derived Model Compounds into Aromatic Hydrocarbons under Low Hydrogen Pressures. *Energy Environ. Sci.* **2014**, *7* (8), 2660–2669. https://doi.org/10.1039/c4ee00890a.

(181) Rajagopal, S.; Marini, H. J.; Marzari, J. A.; Miranda, R. Silica-Alumina-Supported Acidic Molybdenum Catalysts - TPR and XRD Characterization. *J. Catal.* **1994**, *147* (2), 417–428. https://doi.org/10.1006/jcat.1994.1159.

(182) Tian, H.; Roberts, C. A.; Wachs, I. E. Molecular Structural Determination of Molybdena in Different Environments: Aqueous Solutions, Bulk Mixed Oxides, and Supported MoO3 Catalysts. *J. Phys. Chem. C* **2010**, *114* (33), 14110–14120. https://doi.org/10.1021/jp103269w.

(183) Hu, H.; Wachs, I. E.; Bare, S. R. Surface Structures of Supported Molybdenum Oxide Catalysts: Characterization by Raman and Mo Ls-Edge XANES. *J. Phys. Chem* **1995**, *99*, 10897–10910.

(184) Saraeian, A.; Burkhow, S. J.; Jing, D.; Smith, E. A.; Shanks, B. H. Catalyst Property Effects on Product Distribution during the Hydrodeoxygenation of Lignin Pyrolysis Vapors over MoO 3 /γ-Al 2 O 3 . *ACS Sustain. Chem. Eng.* **2021**, *9* (19), 6685–6696. https://doi.org/10.1021/acssuschemeng.1c00295.

(185) Rekoske, J. E.; Barteau, M. A. Kinetics, Selectivity, and Deactivation in the Aldol Condensation of Acetaldehyde on Anatase Titanium Dioxide. *Ind. Eng. Chem. Res.* **2011**, *50* (1), 41–51. https://doi.org/10.1021/ie100394v.

(186) Busca, G. Acid Catalysts in Industrial Hydrocarbon Chemistry. *Chem. Rev.* **2007**, *107* (11), 5366–5410. https://doi.org/10.1021/cr068042e.

(187) Caratzoulas, S.; Davis, M. E.; Gorte, R. J.; Gounder, R.; Lobo, R. F.; Nikolakis, V.; Sandler, S. I.; Snyder, M. A.; Tsapatsis, M.; Vlachos, D. G. Challenges of and Insights into Acid-Catalyzed Transformations of Sugars. *J. Phys. Chem. C* **2014**, *118* (40), 22815–22833. https://doi.org/10.1021/jp504358d.

(188) Mei, J.; Mao, J.; Chen, Z.; Yuan, S.; Li, H.; Yin, H. Mechanism and Kinetics of 4-Hydroxy-2-Butanone Formation from Formaldehyde and Acetone under Supercritical Conditions and in High-Temperature Liquid-Phase. *Chem. Eng. Sci.* **2015**, *131*, 213–218. https://doi.org/10.1016/j.ces.2015.03.025.

(189) Chang, Y. C.; Ko, A. N. Vapor Phase Reactions of Acetaldehyde over Type X Zeolites. *Appl. Catal. A Gen.* **2000**, *190* (1–2), 149–155. https://doi.org/10.1016/S0926-860X(99)00293-8.

(190) Digne, M.; Sautet, P.; Raybaud, P.; Euzen, P.; Toulhoat, H. Use of DFT to Achieve a Rational Understanding of Acid-Basic Properties of γ-Alumina Surfaces. *J. Catal.* **2004**, *226* (1), 54–68. https://doi.org/10.1016/j.jcat.2004.04.020.

(191) Jenness, G. R.; Christiansen, M. A.; Caratzoulas, S.; Vlachos, D. G.; Gorte, R. J. Site-Dependent Lewis Acidity of γ-Al2O3 and Its Impact on Ethanol Dehydration and Etherification. *J. Phys. Chem. C* **2014**, *118* (24), 12899–12907. https://doi.org/10.1021/jp5028349.

(192) Roy, S.; Mpourmpakis, G.; Hong, D.-Y.; Vlachos, D. G.; Bhan, A.; Gorte, R. J. Mechanistic Study of Alcohol Dehydration on Γ-Al2O3. *ACS Catal.* **2012**, *2* (9), 1846–1853. https://doi.org/dx.doi.org/10.1021/cs300176d |.

(193) Dixit, M.; Kostetskyy, P.; Mpourmpakis, G. Structure-Activity Relationships in Alkane Dehydrogenation on γ-Al2O3: Site-Dependent Reactions. *ACS Catal.* **2018**, *8* (12), 11570–11578. https://doi.org/10.1021/acscatal.8b03484.

(194) Cholewinski, M. C.; Dixit, M.; Mpourmpakis, G. Computational Study of Methane Activation on γ-Al2O3. *ACS Omega* **2018**, *3* (12), 18242–18250. https://doi.org/10.1021/acsomega.8b02554.

(195) Zaki, M. I.; Hasan, M. A.; Pasupulety, L. Surface Reactions of Acetone on Al2O3, TiO2, ZrO2, and CeO2: IR Spectroscopic Assessment of Impacts of the Surface Acid-Base Properties. *Langmuir* **2001**, *17* (3), 768–774. https://doi.org/10.1021/la000976p.

(196) Trovarelli, A. Structural and Oxygen Storage/Release Properties of CeO2-Based Solid Solutions. *Comments Inorg. Chem.* **1999**, *20* (4–6), 263–284. https://doi.org/10.1080/02603599908021446.

(197) Nishikawa, J.; Miyazawa, T.; Nakamura, K.; Asadullah, M.; Kunimori, K.; Tomishige, K. Promoting Effect of Pt Addition to Ni/CeO2/Al2O3 Catalyst for Steam Gasification of Biomass. *Catal. Commun.* **2008**, *9* (2), 195–201. https://doi.org/10.1016/j.catcom.2007.05.045.

(198) Lu, Y.; Li, S.; Guo, L. Hydrogen Production by Supercritical Water Gasification of Glucose with Ni/CeO2/Al2O3: Effect of Ce Loading. *Fuel* **2013**, *103*, 193–199. https://doi.org/10.1016/j.fuel.2012.04.038.

(199) Jing, Y.; Xin, Y.; Guo, Y.; Liu, X.; Wang, Y. Highly Efficient Nb2O5 Catalyst for Aldol Condensation of Biomass-Derived Carbonyl Molecules to Fuel Precursors. *Chinese J. Catal.* **2019**, *40* (8), 1168–1177. https://doi.org/10.1016/S1872-2067(19)63371-1.

(200) Luo, S.; Falconer, J. L. Acetone and Acetaldehyde Oligomerization on TiO2 Surfaces. *J. Catal.* **1999**, *185* (2), 393–407. https://doi.org/10.1006/jcat.1999.2511.

(201) Idriss, H.; Barteau, M. A. Selectivity and Mechanism Shifts in the Reactions of Acetaldehyde on Oxidized and Reduced TiO2(001) Surfaces. *Catal. Letters* **1996**, *40* (3–4), 147–153. https://doi.org/10.1007/BF00815275.

(202) Idriss, H.; Kim, K. S.; Barteau, M. A. Carbon—Carbon Bond Formation via Aldolization of Acetaldehyde on Single Crystal and Polycrystalline Tio2 Surfaces. *Journal of Catalysis*. 1993, pp 119–133. https://doi.org/10.1006/jcat.1993.1012.

(203) Watanabe, M.; Aizawa, Y.; Iida, T.; Nishimura, R.; Inomata, H. Catalytic Glucose and Fructose Conversions with TiO2 and ZrO2 in Water at 473 K: Relationship between Reactivity and Acid-Base Property Determined by TPD Measurement. *Appl. Catal. A Gen.* **2005**, *295* (2), 150–156. https://doi.org/10.1016/j.apcata.2005.08.007.

(204) Yuan, Y.; Brady, C.; Annamalai, L.; Lobo, R. F.; Xu, B. Ga Speciation in Ga / H-ZSM-5 by in-Situ Transmission FTIR Spectroscopy. *J. Catal.* **2021**, *393*, 60–69. https://doi.org/10.1016/j.jcat.2020.11.004.

(205) Goguet, A.; Meunier, F. C.; Tibiletti, D.; Breen, J. P.; Burch, R. Spectrokinetic Investigation of Reverse Water-Gas-Shift Reaction Intermediates over a Pt/CeO2 Catalyst. *J. Phys. Chem. B* **2004**, *108* (52), 20240–20246. https://doi.org/10.1021/jp047242w.

(206) Ichikawa, N.; Sato, S.; Takahashi, R.; Sodesawa, T. Synthesis of 3-Buten-2-One from 4-Hydroxy-2-Butanone over Anatase-TiO2 Catalyst. *Catal. Commun.* **2005**, *6* (1), 19–22. https://doi.org/10.1016/j.catcom.2004.10.004.

(207) Luo, S.; Falconer, J. L. Aldol Condensation of Acetaldehyde to Form High Molecular Weight Compounds on TiO2. *Catal. Letters* **1999**, *57* (3), 89–93. https://doi.org/10.1023/A:1019003817314.

(208) Katayama, Y.; Okanishi, T.; Muroyama, H.; Matsui, T.; Eguchi, K. Enhanced Supply of Hydroxyl Species in CeO 2 - Modi Fi Ed Platinum Catalyst Studied by in Situ ATR-FTIR Spectroscopy. **2016**. https://doi.org/10.1021/acscatal.6b00108.

(209) Lin, H.; Long, J.; Gu, Q.; Zhang, W.; Ruan, R.; Li, Z.; Wang, X. In Situ IR Study of Surface Hydroxyl Species of Dehydrated TiO 2: Towards Understanding Pivotal Surface Processes of TiO 2 Photocatalytic Oxidation of Toluene. *Phys. Chem. Chem. Phys.* **2012**, *14* (26), 9468–9474. https://doi.org/10.1039/c2cp40893g.

(210) Copeland, J. R.; Santillan, I. A.; Schimming, S. M.; Ewbank, J. L.; Sievers, C. Surface Interactions of Glycerol with Acidic and Basic Metal Oxides. *J. Phys. Chem. C* **2013**, *117* (41), 21413–21425. https://doi.org/10.1021/jp4078695.

(211) Román-Leshkov, Y.; Davis, M. E. Activation of Carbonyl-Containing Molecules with Solid Lewis Acids in Aqueous Media. *ACS Catal.* **2011**, *1* (11), 1566–1580. https://doi.org/10.1021/cs200411d.

(212) Pihko, P. M. Activation of Carbonyl Compounds by Double Hydrogen Bonding: An Emerging Tool in Asymmetric Catalysis. *Angew. Chemie - Int. Ed.* **2004**, *43* (16), 2062–2064. https://doi.org/10.1002/anie.200301732.

(213) Carchini, G.; López, N. Adsorption of Small Mono- and Poly-Alcohols on Rutile TiO2: A Density Functional Theory Study. *Phys. Chem. Chem. Phys.* **2014**, *16* (28), 14750–14760. https://doi.org/10.1039/c4cp01546k.

(214) Scaranto, J.; Giorgianni, S. A Quantum-Mechanical Study of CO Adsorbed on TiO2: A Comparison of the Lewis Acidity of the Rutile (1 1 0) and the Anatase (1 0 1) Surfaces. *J. Mol. Struct. THEOCHEM* **2008**, *858* (1–3), 72–76. https://doi.org/10.1016/j.theochem.2008.02.027.

(215) Sievers, C.; Noda, Y.; Qi, L.; Albuquerque, E. M.; Rioux, R. M.; Scott, S. L. Phenomena Affecting Catalytic Reactions at Solid–Liquid Interfaces. *ACS Catal.* **2016**, *6* (12), 8286–8307. https://doi.org/10.1021/acscatal.6b02532.

(216) Nakagawa, Y.; Kasumi, T.; Ogihara, J.; Tamura, M.; Arai, T.; Tomishige, K. Erythritol: Another C4 Platform Chemical in Biomass Refinery. *ACS Omega* **2020**. https://doi.org/10.1021/acsomega.9b04046.

(217) Pearson, R. G. Hard and Soft Acids and Bases. *J. Am. Chem. Soc.* **1963**, *85* (22), 3533–3539. https://doi.org/10.1021/ja00905a001.

(218) Foti, A.; Musumarra, G.; Trovato-salinaro, A.; Scire, S.; Barresi, V.; Fortuna, C. G.; Strazzulla, G.; Condorelli, D. F.; Doria, V. a; Chimiche, S. OPLS Discriminant Analysis: Combining the Strengths of PLS-DA and SIMCA Classificatio. *J. Chemom.* **2007**, No. September, 398–405. https://doi.org/10.1002/cem.

(219) Cleaves, H. J.; Scott, A. M.; Hill, F. C.; Leszczynski, J.; Sahaide, N.; Hazenf, R. Mineral–Organic Interfacial Processes: Potential Roles in the Origins of Life. *Chem. Soc. Rev* **2012**, *41* (16), 5459–5472.

(220) Wang, J. Electrochemical Glucose Biosensors. *Chem. Rev.* **2008**, 57–69. https://doi.org/10.1016/B978-012373738-0.50005-2.

(221) *BIOPHYSICO-CHEMICAL PROCESSES OF ANTHROPOGENIC ORGANIC COMPOUNDS IN ENVIRONMENTAL*; Xing, B., Senesi, N., Huang, P. M., Eds.; John Wiley & Sons, Inc., 2011.

(222) Rahman, M.; Ahammad, A. J. S.; Jin, J.; Ahn, S. J.; Lee, J. A Comprehensive Review of Glucose Biosensors Based on Nanostructured Metal-Oxides. *Sensors* **2010**, *10*, 4855–4886. https://doi.org/10.3390/s100504855.

(223) Shi, H.; Lercher, J. A.; Yu, X. Y. Sailing into Uncharted Waters: Recent Advances in the in Situ Monitoring of Catalytic Processes in Aqueous Environments. *Catal. Sci. Technol.* **2015**, *5* (6), 3035–3060. https://doi.org/10.1039/c4cy01720j.

(224) David D. Lawas, Hans-Maecus L. Bitter, A. J. Solid-State NMR Spectroscopy Correlation St Ru Ctu Dyna Re Cs Solid-State NMR Spectroscopic Methods in Chemistry. *Angew. Chem. Int. Ed. Engl.* **2002**, *41*, 3096.

(225) Lapina, O. B. Modern SsNMR for Heterogeneous Catalysis. *Catal. Today* **2017**, *285*, 179–193. https://doi.org/10.1016/j.cattod.2016.11.005.

(226) Klinowski, J. Solid-State NMR Studies of Molecular Sieve Catalysts. *Chem. Rev.* **1991**, *91* (7), 1459–1479. https://doi.org/10.1021/cr00007a010.

(227) Kolodziejski, W.; Klinowski, J. Kinetics of Cross-Polarization in Solid-State NMR: A Guide for Chemists. *Chem. Rev.* **2002**, *102* (3), 613–628. https://doi.org/10.1021/cr000060n.

(228) Qi, L.; Alamillo, R.; Elliott, W. A.; Andersen, A.; Hoyt, D. W.; Walter, E. D.; Han, K. S.; Washton, N. M.; Rioux, R. M.; Dumesic, J. A.; Scott, S. L. Operando Solid-State NMR Observation of Solvent-Mediated Adsorption-Reaction of Carbohydrates in Zeolites. *ACS Catal.* **2017**, *7* (5), 3489–3500. https://doi.org/10.1021/acscatal.7b01045.

(229) Schaefer, J.; Stejskal, E. O.; Buchdahl, R. Magic-Angle 13C NMR Analysis of Motion in Solid Glassy Polymers. *Macromolecules* **1977**, *10* (2), 384–405. https://doi.org/10.1021/ma60056a031.

(230) Okolie, C.; Lyu, Y.; Kovarik, L.; Stavitski, E.; Sievers, C. Coupling of Methane to Ethane, Ethylene, and Aromatics over Nickel on Ceria–Zirconia at Low Temperatures. *ChemCatChem* **2018**, *10* (12), 2700–2708. https://doi.org/10.1002/cctc.201701892.

(231) Hagemeyer, A.; Hogan, Z.; Schlichter, M.; Smaka, B.; Streukens, G.; Turner, H.; Volpe,

A.; Weinberg, H.; Yaccato, K. High Surface Area Tin Oxide. *Appl. Catal. A Gen.* **2007**, *317* (2), 139–148. https://doi.org/10.1016/j.apcata.2006.09.040.

(232) Sathyaseelan, B.; Manikandan, E.; Baskaran, I.; Senthilnathan, K.; Sivakumar, K.; Moodley, M. K.; Ladchumananandasivam, R.; Maaza, M. Studies on Structural and Optical Properties of ZrO2nanopowder for Opto-Electronic Applications. *J. Alloys Compd.* **2017**, *694*, 556–559. https://doi.org/10.1016/j.jallcom.2016.10.002.

(233) Risley, J. M.; Van Etten, R. L. Kinetics of Oxygen Exchange at the Anomeric Carbon Atom of D-Glucose and d-Erythrose Using the Oxygen-18 Isotope Effect in Carbon-13 Nuclear Magnetic Resonance Spectroscopy. *Biochemistry* **1982**, *21* (25), 6360–6365. https://doi.org/10.1021/bi00268a007.

(234) Miao, Z.; Zhang, Y.; Pan, X.; Wu, T.; Zhang, B.; Li, J.; Yi, T.; Zhang, Z.; Yang, X. Superior Catalytic Performance of Ce1-XBixO2-δ Solid Solution and Au/Ce1-XBixO2-δ for 5-Hydroxymethylfurfural Conversion in Alkaline Aqueous Solution. *Catal. Sci. Technol.* **2015**, *5* (2), 1314–1322. https://doi.org/10.1039/c4cy01060d.

(235) Seki, T.; Kabashima, H.; Akutsu, K.; Hattori, H.; Tachikawa, H. Mixed Tishchenko Teaction over Solid Base Catalysts. *J. Catal.* **2001**, *204* (2), 393–401. https://doi.org/10.1006/jcat.2001.3414.

(236) Sasaki, M.; Goto, K.; Tajima, K.; Adschiri, T.; Arai, K. Rapid and Selective Retro-Aldol Condensation of Glucose to Glycolaldehyde in Supercritical Water. *Green Chem.* **2002**, *4* (3), 285–287. https://doi.org/10.1039/b203968k.

(237) Van De Vyver, S.; Odermatt, C.; Romero, K.; Prasomsri, T.; Román-Leshkov, Y. Solid Lewis Acids Catalyze the Carbon-Carbon Coupling between Carbohydrates and Formaldehyde. *ACS Catal.* **2015**, *5* (2), 972–977. https://doi.org/10.1021/cs5015964.

(238) Robinson, N.; Robertson, C.; Gladden, L. F.; Jenkins, S. J.; D'Agostino, C. Direct Correlation between Adsorption Energetics and Nuclear Spin Relaxation in a Liquid-Saturated Catalyst Material. *ChemPhysChem* **2018**, *19* (19), 2472–2479. https://doi.org/10.1002/cphc.201800513.

(239) Weber, D.; Mitchell, J.; Mcgregor, J.; Gladden, L. F. Comparing Strengths of Surface Interactions for Reactants and Solvents in Porous Catalysts Using Two-Dimensional NMR Relaxation Correlations. *J. Phys. Chem. C* **2009**, *113* (16), 6610–6615. https://doi.org/10.1021/jp811246j.

(240) D'Agostino, C.; Feaviour, M. R.; Brett, G. L.; Mitchell, J.; York, A. P. E.; Hutchings, G. J.; Mantle, M. D.; Gladden, L. F. Solvent Inhibition in the Liquid-Phase Catalytic Oxidation of 1,4-Butanediol: Understanding the Catalyst Behaviour from NMR Relaxation Time Measurements. *Catal. Sci. Technol.* **2016**, *6* (21), 7896–7901. https://doi.org/10.1039/c6cy01458e.

(241) Bernin, D.; Topgaard, D. NMR Diffusion and Relaxation Correlation Methods: New Insights in Heterogeneous Materials. *Curr. Opin. Colloid Interface Sci.* **2013**, *18* (3), 166–172. https://doi.org/10.1016/j.cocis.2013.03.007.

(242) Ahola, S.; Zhivonitko, V. V.; Mankinen, O.; Zhang, G.; Kantola, A. M.; Chen, H. Y.;

Hilty, C.; Koptyug, I. V.; Telkki, V. V. Ultrafast Multidimensional Laplace NMR for a Rapid and Sensitive Chemical Analysis. *Nat. Commun.* **2015**, *6*, 1–7. https://doi.org/10.1038/ncomms9363.

(243) Ahola, S.; Telkki, V. V. Ultrafast Two-Dimensional NMR Relaxometry for Investigating Molecular Processes in Real Time. *ChemPhysChem* **2014**, *15* (8), 1687–1692. https://doi.org/10.1002/cphc.201301117.

(244) D'Agostino, C.; Mitchell, J.; Mantle, M. D.; Gladden, L. F. Interpretation of NMR Relaxation as a Tool for Characterising the Adsorption Strength of Liquids inside Porous Materials. *Chem. - A Eur. J.* **2014**, *20* (40), 13009–13015. https://doi.org/10.1002/chem.201403139.

(245) Deese, A. J.; Dratz, E. A.; Hymel, L.; Fleischer, S. Proton NMR T1, T2, and T1 Rho Relaxation Studies of Native and Reconstituted Sarcoplasmic Reticulum and Phospholipid Vesicles. *Biophys. J.* **1982**, *37* (1), 207–216. https://doi.org/10.1016/S0006-3495(82)84670-5.

(246) Geppi, M.; Mollica, G.; Borsacchi, S.; Veracini, C. A. Solid-State NMR Studies of Pharmaceutical Systems. *Appl. Spectrosc. Rev.* **2008**, *43* (3), 202–302. https://doi.org/10.1080/05704920801944338.

(247) Shetty, M.; Murugappan, K.; Prasomsri, T.; Green, W. H.; Román-Leshkov, Y. Reactivity and Stability Investigation of Supported Molybdenum Oxide Catalysts for the Hydrodeoxygenation (HDO) of m-Cresol. *J. Catal.* **2015**, *331*, 86–97. https://doi.org/10.1016/j.jcat.2015.07.034.

(248) Bania, K. K.; Bharali, D.; Viswanathan, B.; Deka, R. C. Enhanced Catalytic Activity of Zeolite Encapsulated Fe(III)-Schiff-Base Complexes for Oxidative Coupling of 2-Napthol. *Inorg. Chem.* **2012**, *51* (3), 1657–1674. https://doi.org/10.1021/ic201959g.

(249) Nguyen, H.; Nikolakis, V.; Vlachos, D. G. Mechanistic Insights into Lewis Acid Metal Salt-Catalyzed Glucose Chemistry in Aqueous Solution. *ACS Catal.* **2016**, *6* (3), 1497–1504. https://doi.org/10.1021/acscatal.5b02698.

(250) Li, K.; Xue, D. Estimation of Electronegativity Values of Elements in Different Valence States. *J. Phys. Chem. A* **2006**, *110* (39), 11332–11337. https://doi.org/10.1021/jp062886k.

(251) Rai, N.; Caratzoulas, S.; Vlachos, D. G. Role of Silanol Group in Sn-Beta Zeolite for Glucose Isomerization and Epimerization Reactions. *ACS Catal.* **2013**, *3* (10), 2294–2298. https://doi.org/10.1021/cs400476n.

(252) Li, Y. P.; Head-Gordon, M.; Bell, A. T. Analysis of the Reaction Mechanism and Catalytic Activity of Metal-Substituted Beta Zeolite for the Isomerization of Glucose to Fructose. *ACS Catal.* **2014**, *4* (5), 1537–1545. https://doi.org/10.1021/cs401054f.

(253) Yang, G.; Zhou, L.; Han, X. Lewis and Brönsted Acidic Sites in M 4+-Doped Zeolites (M = Ti, Zr, Ge, Sn, Pb) as Well as Interactions with Probe Molecules: A DFT Study. *J. Mol. Catal. A Chem.* **2012**, *363–364*, 371–379. https://doi.org/10.1016/j.molcata.2012.07.013.

(254) Bregante, D. T.; Flaherty, D. W. Periodic Trends in Olefin Epoxidation over Group IV

and v Framework-Substituted Zeolite Catalysts: A Kinetic and Spectroscopic Study. *J. Am. Chem. Soc.* **2017**, *139* (20), 6888–6898. https://doi.org/10.1021/jacs.7b01422.

(255) Gunther, W. R.; Michaelis, V. K.; Griffin, R. G.; Roman-Leshkov, Y. Interrogating the Lewis Acidity of Metal Sites in Beta Zeolites with 15N Pyridine Adsorption Coupled with MAS NMR Spectroscopy. *J. Phys. Chem. C* **2016**, *120* (50), 28533–28544. https://doi.org/10.1021/acs.jpcc.6b07811.

(256) Shannon, R. D. Revised Effective Ionic Radii and Systematic Studies of Interatomic Distances in Halides and Chalcogenides. *Acta Crystallogr. Sect. A* **1976**, *32* (5), 751–767. https://doi.org/10.1107/S0567739476001551.

(257) Saqer, S. M.; Kondarides, D. I.; Verykios, X. E. Catalytic Oxidation of Toluene over Binary Mixtures of Copper, Manganese and Cerium Oxides Supported on γ-Al2O3. *Appl. Catal. B Environ.* **2011**, *103* (3–4), 275–286. https://doi.org/10.1016/j.apcatb.2011.01.001.

(258) Trovarelli, A. Catalytic Properties of Ceria and CeO2-Containing Materials. *Catal. Rev. - Sci. Eng.* **1996**, *38* (4), 439–520. https://doi.org/10.1080/01614949608006464.

(259) Nakajima, K.; Baba, Y.; Noma, R.; Kitano, M.; Kondo, J. N.; Hayashi, S.; Hara, M. Nb 2 O 5 3 NH 2 O as a Heterogeneous Catalyst with Water-Tolerant Lewis Acid Sites. *J. Am. Chem. Soc.* **2011**, 4224–4227. https://doi.org/10.1021/ja110482r.

(260) Nakajima, K.; Hirata, J.; Kim, M.; Gupta, N. K.; Murayama, T.; Yoshida, A.; Hiyoshi, N.; Fukuoka, A.; Ueda, W. Facile Formation of Lactic Acid from a Triose Sugar in Water over Niobium Oxide with a Deformed Orthorhombic Phase. *ACS Catal.* **2018**, *8* (1), 283–290. https://doi.org/10.1021/acscatal.7b03003.

(261) Hu, R.; Sun, W.; Zeng, M.; Zhu, M. Dispersing SnO2 Nanocrystals in Amorphous Carbon as a Cyclic Durable Anode Material for Lithium Ion Batteries. *J. Energy Chem.* **2014**, *23* (3), 338–345. https://doi.org/10.1016/S2095-4956(14)60156-X.

(262) Innocenti, G.; Papadopoulos, E.; Fornasari, G.; Cavani, F.; Medford, A. J.; Sievers, C. Continuous Liquid-Phase Upgrading of Dihydroxyacetone to Lactic Acid over Metal Phosphate Catalysts. *ACS Catal.* **2020**, *10* (20), 11936–11950. https://doi.org/10.1021/acscatal.0c03761.

(263) Cho, H. J.; Kim, D.; Li, S.; Su, D.; Ma, D.; Xu, B. Molecular-Level Proximity of Metal and Acid Sites in Zeolite-Encapsulated Pt Nanoparticles for Selective Multistep Tandem Catalysis. *ACS Catal.* **2020**, *10* (5), 3340–3348. https://doi.org/10.1021/acscatal.9b03842.

(264) Lourvanij, K.; Rorrer, G. L. Reaction Rates for the Partial Deh y Dration of Glucose to Organic Acids in Solid-Acid , Molecular-Sieving Catal y St Powders. *J. Chem. Technol. Biotechnol.* **1997**, *50*.

(265) Leon, M.; Swift, T. D.; Nikolakis, V.; Vlachos, D. G. Adsorption of the Compounds Encountered in Monosaccharide Dehydration in Zeolites. *Langmuir* **2013**, *29*, 6597–6605.